Electrochemical Studies of the Oxygen Reduction Reaction: Platinum and Platinum Bimetallic Single Crystal Electrodes

A thesis submitted to Cardiff University for the degree of Philosophiae Doctor

Ashley Brew M.Sc.
DEPARTMENT OF CHEMISTRY CARDIFF UNIVERSITY

Acknowledgements

Firstly I would like to thank my supervisor, Professor Gary A. Attard, for his support and guidance throughout my PhD. His contagious enthusiasm for research has been a constant source of motivation.

There are many people in the Electrochemical Surface Science research group at Cardiff University with whom I have worked that I would like to thank: specifically Dr Mujib Ahmed for providing CV and RDE training and support at the start of my PhD, Jinyu Ye for his assistance with STM and CV studies and Katherine Hunter for her assistance in carrying out CV studies. Other group members that I would like to thank are: Dr Shaoliang Guan, Dr Peter Jenkins and Oliver Donovan-Sheppard. I would also like to thank all the undergraduate students that I have worked with, in particular Patrick Bergstrom-Mann and Kate Silby for their assistance with particular projects. Thanks must also go to Dr David Morgan for carrying out XPS analysis as well as all technical staff at Cardiff University for their services.

I would finally like to thank my mum, sister and step-dad for their kind support and my partner Lauren Mattingley for her love and support throughout my PhD.

Publications

Gary A. Attard, Jin-Yu Ye, Ashley Brew, David Morgan, Patrick Bergstrom-Mann, Shi-Gang Sun, **Characterisation and electrocatalytic activity of PtNi alloys on Pt{111} electrodes formed using different thermal treatments**, J. Electroanal. Chem., 716 (2014) 106-11

Gary A. Attard, Ashley Brew, Jin-Yu Ye, David Morgan, Shi-Gang Sun, **Oxygen Reduction Reaction Activity on Pt{111} Surface Alloys**, ChemPhysChem, 15 (2014) 2044-51

Gary A. Attard, Ashley Brew, **Cyclic voltammetry and oxygen reduction activity of the Pt{110}-(1×1) surface**, J. Electroanal. Chem. 747 (2015) 123-9

Other Publications

Fengjie Xia, Mu Pan, Shichun Mu, Richard Malpass-Evans, Mariolino Carta, Neil B. McKeown, Gary A. Attard, Ashley Brew, David J. Morgan, Frank Marken, **Polymers of intrinsic microporosity in electrocatalysis: Novel pore rigidity effects and lamella palladium growth**, Electrochimica Acta 128 (2014) 3-9

Gary A. Attard, Ashley Brew, Katherine Hunter, Jonathan Sharman, Edward Wright, **Specific adsorption of perchlorate anions on Pt{hkl} single crystal electrodes**, Phys. Chem. Chem. Phys., 16 (2014) 13689-98

Contents

Important Symbols and Abbreviations

Symbols

Symbol	Description	Units
A	Electrode Area	cm^{-2}
α	Symmetry factor	-
C	Capacitance	F
C_{DL}	Double layer capacitance	F
δ	Diffusion layer thickness	nm
D	Diffusion coefficient	cm^2s^{-1}
E	Applied potential	V
E_B	Electron binding energy	eV
E_{eq}	Equilibrium potential	V
E^o	Standard half-cell potential	V
$E_{1/2}$	Half wave potential	V
E_{cell}	Cell potential	V
F	Faraday's constant	9.649×10^4 C mol^{-1}
η	Overpotential	V
η_{max}	Maximum energy efficiency	-
η_{Carnot}	Carnot efficiency	-
θ/θ_{ad}	Adsorbate coverage	-
I	Tunnelling current	A
i_{DL}	Double layer charging current	A
i_{net}	Net (observed) current	A
i_{ox}	Oxidative current (anodic)	A
i_{Red}	Reductive current (cathodic)	A
j	Diffusional flux/current density	$mol^{-2}s^{-1}$/A cm^{-2}
j_{lim}	Limiting current density	A cm^{-2}
j_{net}	Net current density	A cm^{-2}
j_{trans}	Kinetic current density	A cm^{-2}
j_0	Exchange current density	A cm^{-2}
k^o	Rate constant at E_{eq}	-

m_T	Mass transport coefficient	cm s^{-1}
n	Number of electrons	-
P	Partial pressure	atm
R	Gas constant	8.314 J K^{-1} mol^{-1}
R_e	Reynold's number	-
T	Temperature	K
ν	Sweep rate	Vs^{-1}
V	Potential	V
ϕ	Work function	eV
ω	Rotation speed	Hz/rpm

Abbreviations

CV	Cyclic voltammetry/cyclic voltammogram
DMFC	Direct methanol fuel cell
DFT	Density functional theory
EV	Electric vehicle
FAFC	Formic acid fuel cell
fcc	Face centred cubic
FCEV	Fuel cell electric vehicle
GHG	Greenhouse gas
HEV	Hybrid electric vehicle
hcp	Hexagonal close packed
HHV	Higher heating value
HOR	Hydrogen oxidation reaction
HPORR	Hydrogen peroxide oxidation-reduction reaction
H_{UPD}	Hydrogen underpotential deposition
ICE	Internal combustion engine
IHP	Inner Helmholtz plane
LHV	Lower heating value
LEED	Low energy electron diffraction

NP	Nanoparticle
OHP	Outer Helmholtz plane
ORR	Oxygen reduction reaction
PEM	Proton exchange membrane
PEMFC	Proton exchange membrane fuel cell
PZC	Point of zero charge
PZTC	Point of zero total charge
RDE	Rotating disk electrode
RHE	Reversible hydrogen electrode
RRDE	Rotating ring disk electrode
STM	Scanning Tunnelling Microscopy
TTW	Tank-to-wheel
UHV	Ultra high vacuum
UPD	Underpotential deposition
WTW	Well-to-wheel
XPS	X-ray photoelectron spectroscopy

1 Chapter One – Introduction

1.1 Fossil Fuels and the Need for Research into Alternative Fuels

Since before the industrial revolution, the burning of fossil fuels such as petroleum, natural gas, coal and peat has been performed by humans to create heat for purposes such as keeping warm in colder climates, cooking, creating clean drinking water and the forging of weapons over the millennia. This relatively small scale use of large, but finite, resources had negligible effect on the global climate. As a result of the industrial revolution, world population and energy consumption has risen dramatically. It had taken all of human history until 1927 to reach a world population of 2 billion, but less than 50 years to add the next 2 billion and 25 years to add the next 2 billion people [1]. This growing population's thirst for energy has been, and is being, quenched mainly by coal, oil and natural gas. What seemed once an inexhaustible energy supply is now being used at a rate many orders of magnitude faster than its creation over millions of years. This consumption is now having an effect on many of the physical processes of the planet. So much so that there is debate amongst scientists on whether or not we can be considered to be in a new geological epoch, called the Anthropocene, due to human activity having significant impact on Earth's ecosystems [2].

Issues resulting from the consumption rate of fossil fuels are multi-faceted, but mainly fall into two categories, environment and economic-political issues. The famous and controversial hockey stick graphs, which show how global average temperature has changed throughout history, illustrate the major effect that burning fossil fuels have on the environment. Studies on global temperature over the last 11,000 years show that during this time there has been two periods with higher than present global average temperature (for example during the medieval warm and early Holocene periods) [3]. Importantly though, they show that the *rate* of temperature increase since the industrial revolution is faster than any other time over the last 11,000 years [3], it seems also likely that it is unprecedented over the last million years (if not more) as previous temperature changes occurred over thousands of years.

Correlation between the rapid increase in fossil fuel consumption over the last 200 years and the onset of dramatic global climate change in the same period does not by itself imply that the latter is the cause of the previous, but the mechanism connecting the two is understood and agreed upon. It is now known that human consumption of fossil fuels has affected the global

climate by the mechanism thus described. Gases such as CO_2, methane etc., are released when fossil fuels are burned, these adsorb infra-red radiation (heat) from the Sun and prevent its escape from the atmosphere. This property is why these gases are known as greenhouse gases (GHGs). In the second half of the twentieth century, burning of fossil fuels has greatly increased the levels of these gases in the atmosphere, increased the planet's ability to contain heat and therefore increased global temperature [4]. The effect of GHGs on the heat escaping the planet can be seen on the outgoing long-wave radiation spectra of the Earth [5]. CO_2 and global temperature have also been studied in detail over thousands of years by comparing CO_2 captured in ice, which signifies historical atmospheric CO_2 concentration, with the oxygen isotope ratio of polar ice, which relates to the historical water temperature of oceans [6]. Historical atmospheric CO_2 levels, which are known accurately for the last 800,000 years [6], correlate well with the global average temperature over the same time period. These studies show that changes in Earth's orbit triggered initial temperature increases in the past, which resulted in the release of CO_2 from the oceans. This GHG emission greatly amplified the temperature increase due to the greenhouse effect ("positive feedback") and that the warming would not have been as great, had so much CO_2 not been released into the atmosphere [7]. The current level of CO_2 in the atmosphere, which reached 400ppm in 2014, is higher than any level found during the 800,000 years examined, which fluctuated between ~200ppm and ~300ppm [6]. Geochemical records indicate that the last time CO_2 concentration equalled the current levels may have been over 20 million years ago [8]. Some of the environmental effects of the current sudden climate change are as follows; loss of Artic ice [9], rising sea levels [10], increasing ocean acidity [11], lowering ocean oxygen concentrations [12], increasing frequency of extreme weather events [13], increasing extinction rates [14] and decreasing crop yields [15]. Each of these also have a plethora of knock-on effects, too many to list. Also, there are many direct environmental problems from the use of fossil fuels, such as oil spills, smog, acid rain etc.

The political and economic issues, associated with continued fossil fuel usage and current climate change, are complex and will not be covered in detail here. One such issue though is that of a nation's energy (in)dependence, which can be highlighted by the Russian-Ukrainian gas crisis of 2009 (the EU imports a large percentage of its energy from outside the union, much from the fossil fuel rich Russia). This crisis showed that reliance on another nation's energy production can cause strong geopolitical tensions. The strain of which has the accompanying risks of war, local conflicts etc.

In many nations unconventional oil and gas is now routinely released from rocks by injecting high pressure water and sand through a drill hole in order to create small fractures which release the fuel, a process known as fracking. This has allowed the retrieval of shale gas that was previously uneconomical and technologically unfeasible to obtain. This is being seen in many countries that are rich in such resources as an opportunity to reduce their reliance on imported energy and therefore decrease energy dependence and its associated problems. Although it has been shown in some studies that natural gas derived from fracking may produce lower amounts of GHGs than coal (by about 50%) [16], other studies have shown that Shale gas produces higher GHG emissions than coal over a 20 year time scale and similar levels to coal over a 100 year period [17]. The different results in various studies derive from what percentage of methane is considered to leak from the well in the fracking process [18]. In a recent study on the implications of shale gas development for climate change, it was concluded that "shale gas will likely not substantially change global GHG concentrations on its own: policy and a range of competitive low-GHG energy options are the key factors" [18].

By focusing research on low-GHG technologies, competition with fossil fuel energy sources may be increased. All GHG emitting sectors could lower their contribution to global climate change by adopting "green", low carbon, technologies. The work in this thesis is related to the potential that fuel cell vehicles have to reduce the GHG impact of the transport sector. In 2010, the transport sector was responsible for ~27% of all CO_2 emissions in Europe, second only to the CO_2 emissions from electricity production [19]. Within the transport sector, road transport contributes the most to emissions and is therefore an area that requires greater adoption of low carbon technologies. Biofuel vehicles, hybrid electric vehicles (HEVs), electric vehicles (EVs) and fuel cell electric vehicles (FCEVs) are such technologies.

1.1.1 The Role of Fuel Cell Electric Vehicles (FCEVs) in an Alternative Fuel Future

In analysing and comparing low carbon transport technologies, it is important to consider not only the method the technology uses to run the driveshaft, but also aspects relating to the energy carrier. Important aspects may be the initial extraction/production of the energy carrier, its subsequent transport, distribution and storage, and its final consumption within the vehicle. This beginning to end, life-cycle analysis of a vehicle technology is known as a well-to-wheel

(WTW) analysis. When only the consumption of the energy carrier within the vehicle is analysed this is known as a tank-to-wheel (TTW) analysis. Both WTW and TTW analyses have been performed upon all vehicle technologies in regards to parameters such as energy efficiency, GHG emissions and fossil fuel use (see reference [20] for an up to date analysis of the impact of automotive fuels and powertrains in the European context). Due to the different parts of the life cycle that these analyses consider, vehicle technologies may have very different TTW and WTW impacts. For example, a vehicle technology may have very low TTW GHG emissions if the consumption of the energy carrier within the vehicle is clean and efficient, but if the production, transport, distribution and storage of the energy carrier creates large amounts of GHGs, the vehicle technology's WTW GHG emissions could be high. The same principle is true for other parameters such as energy efficiency.

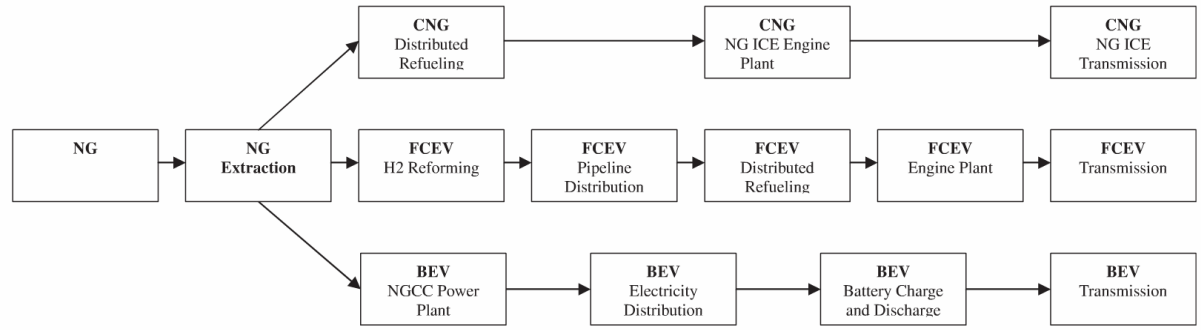

Figure 1. Example fuel chains used for complete cycle, well-to-wheel analysis of vehicle impact. Compressed natural gas (CNG) vehicle, fuel cell electric vehicle (FCEV) and battery electric vehicle (BEV) fuel chains using natural gas are shown here [21].

Through WTW studies, it has been shown that, compared with other technologies, both BEVs and FCEVs can greatly reduce GHG emissions [22, 23]. The percentage reduction, though, depends critically on how the energy carrier is obtained. For FCEVs, this percentage can range from an increase in GHG emissions of 60% for liquid H_2 produced via electrolysis, through to a 100% reduction for a number of other H_2 production methods [22]. One study has shown that in north America the natural gas → hydrogen → fuel cell vehicle process compared to the petroleum → gasoline → internal combustion vehicle process would give (per mile travelled) a 41% reduction in total primary energy use, a 56% reduction in greenhouse gases, and a 100% reduction in petroleum use [24, 25]. Therefore reductions in vehicle impact may be observed for hydrogen FCEVs even when non-renewable sources of hydrogen are used. In a similar logic, the environmental impact of BEVs is heavily dependent on the electricity mix of the source, which varies greatly from country to country [23]. Countries that have a high

percentage of fossil fuels contributing to their electricity mix will not see the environmental benefits of electric vehicles (for example Poland, see figure below), whereas countries such as France, which has a large percentage of nuclear power contributing to its electricity mix [23], will. The level of renewables in the electricity mix also has a major effect on the environmental impact of hydrogen FCEVs, especially when the hydrogen is produced via electrolysis [25].

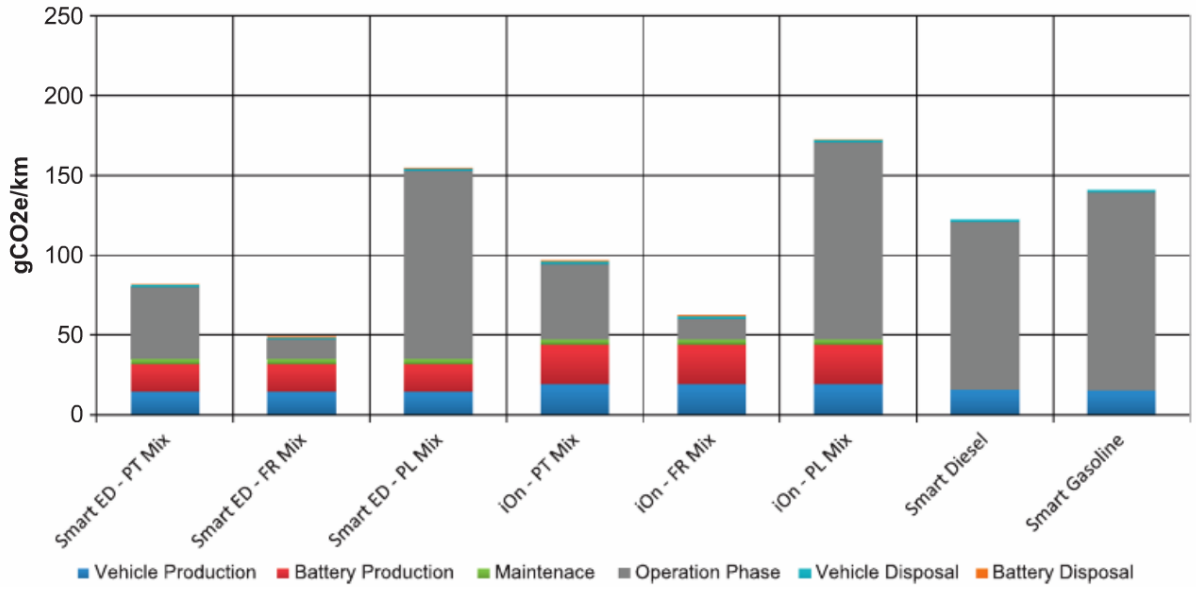

Figure 2. GHG intensity per km travelled for some subcompact vehicles. Smart electric drive (ED), iOn, Smart Diesel and Smart Gasoline vehicles are compared. The GHG intensity of the electric vehicles are shown with respect to the electricity mix of three different countries; PT = Portuguese, FR = French and PL = Polish electricity mix. Reprinted from reference [23].

As it has been shown that BEV and FCEV technologies are both capable of great reductions in energy use, fossil fuel use and GHG emissions compared to conventional combustion engine vehicles, it then comes down to other aspects of both technologies in deciding the future of the automobile industry. Both technologies have drawbacks which inhibit them from obtaining commercial acceptance and also which are the focus of a great amount of current research. In regards to BEVs, one of the problems is the relatively long recharging times. A full charge is performed overnight and a couple of hours are needed for a partial charge. These times are inconvenient when compared to the minutes needed to refuel other vehicle types. Also, the contribution of the weight of the battery to the total vehicle mass is greatly increased for vehicles with a higher mileage range, meaning that BEVs tend to have much lower mileage ranges compared to other technologies. Estimates show that for a 100 mile range a BEV with a base mass of 1250kg, the battery system contributes about 130kg. For a 300 mile BEV range, a 1250kg vehicle would require a battery system of 500kg [26]. Battery technology is

continually improving, off the back of advancements in personal device technology such as laptops, phones etc., with one goal of research being to increase battery technology's low specific energy (kWh/kg) in order to combat the weight and mileage issues described here. Another goal of research into battery technology is to decrease charging times. Very quick full recharge times of less than 1 minute have been claimed with some battery technologies such as aqueous lithium systems [27]. Even if such recharge times were possible, large amounts of energy would be required from the grid [28] for each BEV being charged and active cooling of the battery may be required [26]. It is therefore possible that BEVs based on Li-ion batteries may be fundamentally restricted to serving the purpose of short term trips that would not require intermediate refuelling. Such BEVs could still contribute towards the future green automobile fleet by offering low impact transport for short journeys, for example within cities. Most road journeys that are taken are of such length and the gasoline cars that BEVs would be replacing are less efficient the lower their speed, such as speeds driven within cities.

In comparison to BEVs, hydrogen FCEVs demonstrate efficiency at the 300 mile range due to the lower weight of the fuel cell compared to the battery system. The weight of the fuel cell system within a FCEV is 150kg heavier than the battery of a BEV at the 100 mile range but crucially the fuel cell system does not scale in weight so dramatically with mileage range. Therefore at the 300 mile range the fuel cell system contributes 200-300kgs less than the battery system. [26]

There are two main factors inhibiting the commercial acceptance of FCEVs, both of which are the focus of current research. The first issue is that the price of FCEVs, which is high largely due to the large amount of expensive platinum utilised at the electrodes of the fuel cell [26]. Multiple avenues are being investigated in response to this issue and are showing promise, such as the development of thin film catalysts [29] and platinum alloys [30], which produce higher current at a given potential. Even non platinum-group [31] metals and non-metal catalysts [32] are being investigated. The second issue lies with the storage, transportation and distribution of hydrogen. These can have a dramatic effect on FCEV's WTW impact, therefore multiple avenues are again being investigated to create hydrogen storage and transport methods that have minimal impact on energy use and the environment. A complete discussion of these problems is outside the scope of this thesis.

It seems likely, due to BEV's and FCEV's complementary strengths and weaknesses, that one single technology is unlikely to gain a monopoly. The future of the automobile fleet across the

world will likely consist of a mixture of alternative fuel technologies, at least as the fleet bridges from old, carbon intensive ICE vehicles to low carbon vehicles. BEV and FCEVs will likely have a continually increasing share of the fleet as their prices decrease, as has been predicted [19]. Also, it has been suggested that plug-in hybrid and BEVs could provide the stepping stones to a future hydrogen economy, due to the components common between hybrid and electric vehicles and those also common between BEV and FCEVs [33]. As each alternative fuel technology develops and improves, the investment in each should be constantly reviewed with focus being on dramatically improving the current state of the environment and environmental stability in the long term.

1.1.2 An Overview of Proton Exchange Membrane Fuel Cells (PEMFCs)

A fuel cell is an electrochemical cell that converts chemical energy from a fuel directly into electrical energy. It does this through a chemical reaction between a fuel and an oxidising agent, usually oxygen. The development of the first hydrogen fuel cell (known at the time as a gaseous voltaic battery) was mentioned in a journal in 1838 by Sir William Grove [34, 35] and detailed later in 1942 [36].

Before the invention of the fuel cell, the process of converting electrical energy into chemical energy was well known. For example, it had been noticed that electricity could be used to cause a reaction which released gas if electrodes were placed in water. This was known at the time to be the splitting of water molecules into hydrogen and oxygen, electrolysis. Grove wondered if the same thing could be performed in reverse: if hydrogen and water could be combined at separate electrodes to create electricity, which was the stimulus for the first experiments which proved that this could be done. Hydrogen and oxygen were bubbled separately over platinum wire electrodes in contact with a sulphuric acid solution, the sulphuric acid solution acted to conduct protons between the two electrodes and the gases were consumed at each electrode (see figure 3, below) [35, 36]. Although the exact mechanism for the process was not understood, electricity and water were produced from these first crude fuel cells, confirming the hypothesis and paving the way for our modern understanding of electrochemistry.

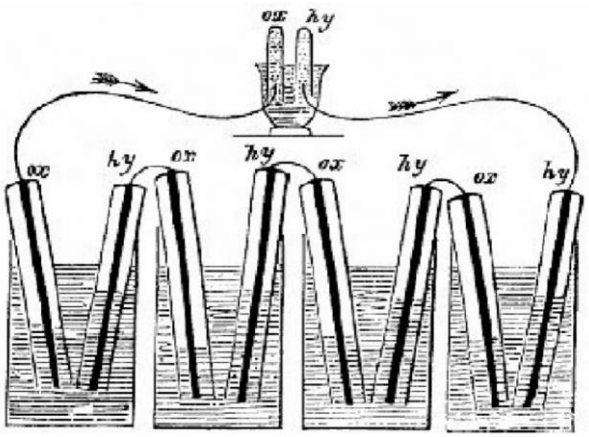

Figure 3. The first fuel cell. (Originally printed in Grove, W. R. (1838). On a new voltaic combination. Philosophical Magazine and Journal of Science 13, 430.) [35, 37]

The rise of the steam engine in the early 19th century, and later the combustion engine, meant that the fuel cell was not fully appreciated until the mid-to-late 20th century. In the middle of the 20th century General Electric (GE) invented the proton exchange membrane (PEM) fuel cell, which used a solid electrolyte known as Nafion® that had superior properties to previous solid electrolytes. At this point fuel cell's high cost limited their use to space missions and other specialist applications. The recent reduction in the cost of fuel cells, as a result of initial research in the late 80s by Ballard Power Systems, has meant that they could lead to an economical, green alternative to fossil fuel reliant vehicles. [37]

Fuel cells vary in the type of fuel they utilise. For example, formic acid is the fuel used in formic acid fuel cells (FAFCs) and methanol in direct-methanol fuel cells (DMFCs). FCEVs that have hydrogen as their fuel utilise in what is known as a proton exchange membrane fuel cell (PEMFC). Figure 4, below, is a basic illustration of a modern PEMFC. Fuel cells also vary in the type of electrolyte used (the part of the fuel cell which allows charge to travel between the two electrodes of the cell). Aqueous alkaline solutions, molten acids and molten carbonates are some of the electrolytes used in various fuel cell technologies. A PEMFC utilises a solid polymer electrolyte.

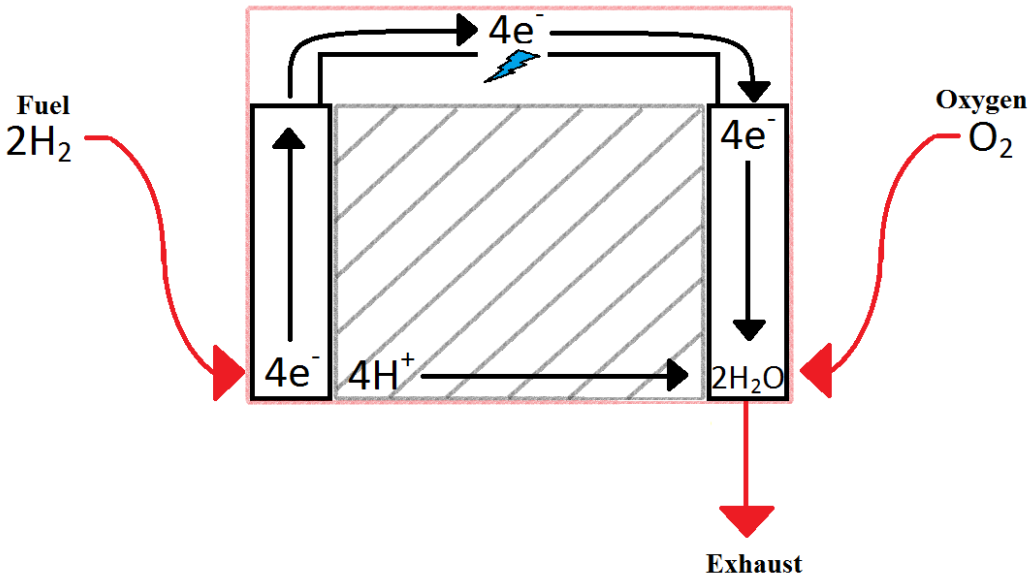

Figure 4. A basic illustration of a proton exchange membrane fuel cell (PEMFC). The hydrogen oxidation reaction (HOR) is shown on the left electrode, the anode, and the oxygen reduction reaction (ORR) is shown on the right electrode, the cathode. The PEM of the FC is shown in the centre of this illustration by diagonal lines. Exhaust = H_2O.

Current is produced in a PEMFC device as a result of oxidation and reduction reactions which take place at the anode and cathode respectively. Reactants are supplied continuously and therefore current is maintained as long as reactant supply is not interrupted. This is where the main difference between a fuel cell and a battery lies: a battery relies on a fixed store of reactants, which is recharged when depleted. The hydrogen oxidation reaction (HOR) at the anode forms protons and electrons (reaction 1). These are separated from each other by a central proton exchange membrane (PEM), usually Nafion®, a sulfonated tetrafluoroethylene based polymer. This is negatively charged, conducting protons but not electrons, therefore enabling the protons to travel through the PEM and forcing the electrons through an external circuit, powering connected devices. Electrons arriving at the cathode on the opposite end of the cell reduce oxygen through a reaction also involving protons (reaction 2). Both electrodes constitute an electrically conducting carbon support decorated with catalysts for the reactions. The overall reaction (reaction 3) shows that PEMFCs produce only water as waste, the exhaust in a FCEV, and also shows that the maximum obtainable output for a single cell as shown in figure 3 is 1.23V, considering the difference in equilibrium potentials for the HOR and ORR.

$$H_2\,(g, 1\ \text{atm}) \rightarrow\ 2H^+\,(aq, 1\ \text{M}) + 2e^-\quad E^o = 0\text{V}$$

Reaction 1. The hydrogen oxidation reaction (HOR). [37]

$$O_2\,(g, 1\text{ atm}) + 4e^- + 4H^+(aq, 1\text{ M}) \rightarrow 2H_2O \quad E^o = 1.23\text{ V}$$

Reaction 2. The oxygen reduction reaction (ORR). [37]

$$H_2 + \frac{1}{2}O_2 \rightarrow H_2O \quad E_{cell} = 1.23\text{V}$$

Reaction 3. Overall reaction from reactions 1 and 2. [37]

According to the first law of thermodynamics, the energy input to a system must balance with the total energy output (total of useful and waste output: equation 1, below). This equation can be used to define the maximum energy efficiency of a process according to equation 2. Therefore the efficiency of any energy conversion device, such as a fuel cell or a combustion engine, is the ratio of the useful energy output to the energy input. In regards to a PEMFC, the enthalpy of combustion of hydrogen (286 $kJmol^{-1}$) is the energy input and 1.23V is the energy output in volts. This corresponds, through using the equation $\Delta G = -nFE$, to a Gibbs free energy of 237.1$kJmol^{-1}$ and enables the maximum efficiency of the PEMFC to be calculated, as is shown in the specific form of equation 2. This is 83% at 298K using hydrogen's higher heating value (HHV) as the input energy Q_{in} [37]. The HHV is the amount of heat released in combusting 1 mol of hydrogen at 298K and having the product, water vapour, return to 298K, condensing in the process. Calculations using hydrogen's lower heating value (LHV), in which the temperature of water vapour is only returned to 423K (150 Celsius), give a hydrogen fuel cell a higher efficiency of ~95%, as the latent heat of vaporisation of water vapour is assumed to be unrecoverable. These efficiencies correspond to a maximum thermodynamic limit on the performance of a PEMFC: even with zero energy losses elsewhere, through processes such as electrical resistance and reaction inefficiencies at the electrodes, the percentage efficiency of a hydrogen fuel cell cannot be increased above these values.

$$Q_{in} = W_{out} + Q_{out}$$

Equation 1. Energy balance equation. Q_{in} is the energy input to the system and W_{out} and Q_{out} are the mechanical work output and the waste heat output respectively.

$$\eta_{max} = \frac{W_{out}}{Q_{in}}$$

$$\eta_{max} = \frac{\Delta G_f^0}{\Delta H_f^0} = \frac{237.1\text{ kJ/mol}}{286\text{ kJ/mol}} = 83\%$$

Equation 2. General equation (top) for the maximum energy efficiency (η_{max}) of a process [38]. Specific equation (bottom) for the maximum energy efficiency of a hydrogen fuel cell operating at 298K, using hydrogen's higher heating value (HHV, ΔH_f^0) and the Gibbs free energy (ΔG_f^0) of the reaction. [37]

At both electrodes, catalysts decorating the carbon support are required to aid the reaction of both hydrogen oxidation and oxygen reduction. This is done in order to minimise the energy loss associated with these reactions and therefore maximise efficiency. Platinum is used at the anode, which efficiently catalysis the HOR with minimal energy loss [39]. At the cathode, the best catalyst of the pure metals for the ORR is also platinum [40], which does not efficiently catalyse the reaction. Even with an order of magnitude greater mass of platinum than that which is needed at the anode, a large activation energy barrier remains and energy is therefore lost at this electrode [26]. The energy loss at the cathode is the biggest contributor to efficiency loss within a PEMFC. This efficiency loss is reflected in the operating voltage of fuel cells, which is approximately 0.8V, far from the 1.23V theoretically possible. Due to the expense of platinum, improving the cathode catalyst's efficiency would have a dual benefit; that of increasing the power output of fuel cells and also of decreasing the cost of PEMFC vehicles.

The equivalent efficiency limit for a heat engine, such as a gasoline engine within a vehicle is known as the Carnot efficiency limit, the equation for which is shown below (equation 3). Its physical meaning is that some energy from the high temperature heat source is converted to useful work and the rest is dumped into the low temperature heat sink.

$$\text{Carnot Efficiency } (\eta_{Carnot}) = \frac{W_{out}}{Q_{in}} = \frac{T_1 - T_2}{T_1} \; or \; 1 - \frac{T_2}{T_1}$$

Equation 3. The Carnot efficiency equation. Used to calculate the efficiency limit of a heat engine. [37, 38]

For a gasoline engine the low temperature heat sink, T_2, would be the exhaust at ~50ºC, the lowest possible temperature being ambient temperature. The maximum temperature within the combustion engine is T_1. From equation 3 it can be seen that to achieve a high Carnot efficiency, T_1 must be very high or T_2 very low. Although 100% efficiency would only be observed for an engine with an infinite T_1 or a T_2 of absolute zero, it would be wrong to state that this equation implies that an ideal heat engine is less efficient than an ideal fuel cell. A comparison of fuel cells to the Carnot cycle has shown that an internal combustion engine (ICE) utilising the combustion reaction between H_2 and O_2 has the same thermodynamic maximum efficiency as a fuel cell utilising H_2 and O_2 for an electrochemical reaction [38]. In reference [38] the question "…if fuel cells have the same maximum efficiency as a heat engine,

then how can fuel cells be more efficient in practice?" was posed. The answer, succinctly given, was "…that if a fuel cell is compared to a heat engine of the same theoretical efficiency, then the fuel cell will not be limited in practice by having to deal with the high temperature of the heat engine. Heat engines cannot operate at the maximum combustion temperature, because of the materials problems of handling the working fluid. Therefore, heat engines are forced to accept operating losses that fuel cells, operating at a much lower temperature, can avoid." Due to this, and other issues, gasoline and diesel road vehicles of all sizes have lower thermal efficiencies than FCEVs, between 20-40% [41]. One area of ICE research is on developing engine materials to cope with the high temperatures needed to increase efficiency.

1.2 Background and History of Catalysis, Electrochemistry and Electro-catalysis

The history of catalysis has been split into periods which have been detailed in "A brief history of catalysis" [42]. These periods shall be summarized here, interspersed with electrochemistry and electro-catalysis history.

The 1st period of catalysis stretched from the dawn of civilisation to the early 19th century, where the main catalytic process exploited was the fermentation of sugar to alcohol by yeast [42], although it was not appreciated that catalysis was occurring. The mechanism of this, and of other catalytic processes, was therefore unrealised and unexplored.

Similarly, before the 19th century, electrochemical processes had not been identified and electrochemistry did not exist as a field of chemistry. This was because previous centuries had been spent trying to understanding the phenomena of electricity and magnetism. In trying to understand electricity, Alessandro Volt planted the seeds for electrochemistry as a new field by making the first battery in 1800 [43]. He made this by alternatively stacking silver and zinc disks atop each other, separating each layer by moistened cardboard, proving that electricity flows between two different metals. We know now that this occurs due to the metals' difference in potential. The unit of potential is the Volt, in memory of Alessandro.

It was not until the early 1800's that electricity was being used to cause chemical reactions, through electrolysis of water [43] and electroplating of metals, although, there was no understanding of the connection between electricity and chemistry. Humphrey Davy first commented on this interaction by stating that electricity produced in electrolytic cells was caused by chemical reactions. Michael Faraday quantified this interaction by discovering the two laws of electrochemistry; "the amount of a substance deposited on each electrode of an electrolytic cell is directly proportional to the amount of electricity passing through the cell" and "the quantities of different elements deposited by a given amount of electricity are in the ratio of their chemical equivalent weights" [44]. This discovery, of the proportionality between electricity and chemical reactions, established the field of electrochemistry and enabled its future quantitative study. William Grove's experiments the late 1830's (chapter 1.1.2) proved that these laws were also applicable in reverse [36]; namely, reactions between chemicals can produce an amount of electricity proportional to the amount of chemicals consumed.

From the 1850's electrochemistry found great use industrially. Through electrolysis, pure aluminium, sodium and chlorine, were produced [45]. Also, a greater understanding of electrochemical processes was gained by the work of many scientists such as Johann Hittorf (who discovered that ion movement is responsible for electric current), Wilhelm Ostwald (who contributed to our understanding of electrolyte solutions) and Hermann Nernst (famous for his namesake equation of the electromotive force).

The 2nd period of catalysis started with the first systematic observations and investigation of processes that were later classified as catalysis [42]. Although other scientists had discovered some fundamental concepts of catalysis in the early 1800's, Jöns Jacob Berzelius summarized their work and, along with his own findings, keenly identified a "catalytic force" that took place in disparate reactions under investigation at the time. He provided an early definition of catalysis, translated as "reactions that are accelerated by substances that remain unchanged after the reaction" [46]: a useful definition to this day. With the help of other chemical concepts that were being laid down, the understanding of catalysis matured, and toward the end of this period George Lemoine discovered that "a catalyst… cannot change the position of the equilibrium, it can only alter the rate at which it is reached" [42], a key concept in modern catalysis. This process of enlightenment into catalytic phenomena defined this period.

After the worth of catalysts was realised (also after the framework of understanding had been gained in the 2nd period) the 3rd period of catalysis began and catalysts were used for many processes by industry near the end of the 19th century [42]. In the 1920's, Eric Rideal found that catalysts may be applied to electrochemical reactions and the term electro-catalysis was coined in 1936 by Kobozev [47]. Although, it was not until decades later that electro-catalysts were used by industry.

Later periods of catalysis were associated with what problems and issues catalysts were applied to and what commodities were made using catalysis throughout the 20th century [42]. Throughout this century, and to this day, catalysts were used for the derivation of various fuels (e.g. catalytic cracking), the creation of ammonia for fertilisers, polymerisation, and for the synthesis of many other commodity chemicals. Catalysis's value in producing fine and speciality chemicals was also being exploited through the production of agricultural pesticides to combat crop loss and the production of pharmaceuticals to treat disease [48]. They were also periods in which many more crucial insights into catalysis were gained, for example, the Langmuir-Hinshelwood kinetic theory for catalysis and the Sabatier principle.

During the 2nd half of the 20th century electro-catalysis became more than an academic field as it was appreciated by industry that the electricity consumption of electrolysis could be reduced by the right choice of electrode catalyst. Electro-catalysts reduce the overpotential (the "extra" potential, above or below the equilibrium potential) required to create the same current, and therefore the same amount of chemical product, as the un-catalysed reaction [47]. Also during the 20th century, with the move towards the electronic age, many techniques have been devised that can probe the electrode-electrolyte interface [43]. One of these techniques being voltammetry, where the potential is controlled at an electrode-electrolyte interface and any resulting current measured. One use of such a technique is to evaluate the efficiency of electro-catalysts.

Catalysis is now being used ever increasingly to battle with the modern issues of climate change and environmental damage: therefore environmental catalysts are ever growing in their demand. The first of these go back over 50 years, when the catalytic converter was first developed to consume the harmful local emissions at the exhaust of fossil fuel vehicles [48]. As GHGs are also emitted from the exhaust of these vehicles, the catalytic converter has evolved over time to increasingly minimise the escape of these pollutants from vehicles. In response to increasing climate concerns though, fossil fuel vehicles are beginning to be replaced by BEVs and in the future FCEVs will be more prevalent, which do not require a catalytic converter. Catalysts will still have their place in the future of automobiles though, due to the requirement of electro-catalysts for the reactions in FCEVs.

1.2.1 Electrode Kinetics and the Butler-Volmer Equation

Consider an electrode-electrolyte interface. If the electrode is a metal then it has strongly overlapping orbitals and energy levels existing as a continuum, therefore the energy of the electrons can be increased by increasing the applied voltage (see figure 5, below), which affects the Fermi-level of the metal. If the electrode is in contact with a solution containing reducible species, the Fermi-Level of the electrode may be increased enough to reduce them. An electron is transferred from the metal to the solution species' lowest unoccupied molecular orbital (LUMO) and it is reduced. The reverse may also occur: the Fermi-level can be reduced so that it may oxidise solution species, an electron would then jump from the solution species's highest occupied molecular orbital (HOMO) to the metal. The difference between the energy levels of

the metal and the solution species dictate whether the electron transfer is thermodynamically favourable, but not its kinetics. Electrode kinetics describes how the rate of electron transfer at an electrode surface is affected by, amongst other factors, the applied voltage.

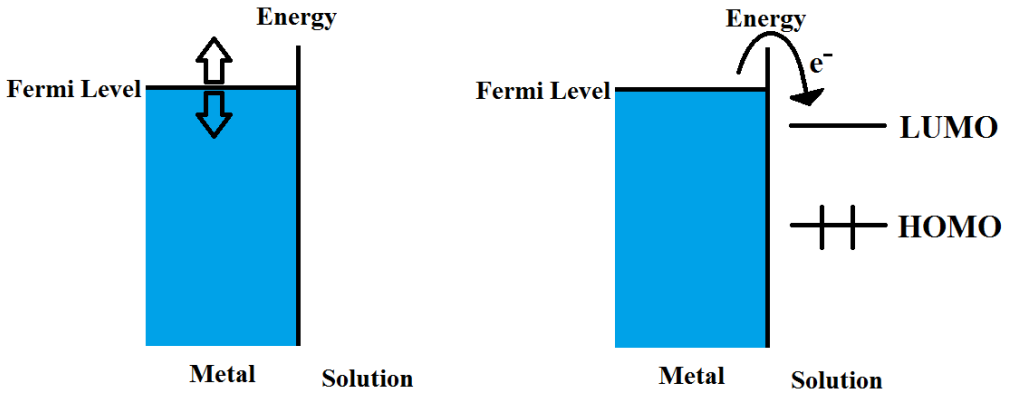

Figure 5. An illustration of the continuous electron levels of a metal in contact with a solution, left. The same metal in contact with a solution containing reducible species, right.

The reduction reaction illustrated above can be written as the reaction

$$O + e^- \leftrightarrow R \qquad (1)$$

"O" represents the oxidised form of the solution species and "R" the reduced. The rates of the forward, reduction R_{red}, and backward, oxidation R_{ox}, reactions are given by

$$R_{Red} = k_{red}[O] \qquad R_{ox} = k_{ox}[R] \qquad (2)$$

Where k_{red} and k_{ox} are the rate constants of reduction and oxidation and [O] and [R] are the concentrations of the species *O* and *R* respectively. As well as monitoring this reaction by the changing concentration of either *O* or *R*, it can also be monitored by the electrical current at the electrode surface, *i*, as this is the rate of electron transfer. The cathodic, reductive, current (i_{red}) and anodic, oxidative, current (i_{ox}) are then expressed as

$$i_{Red} = nFAk_{red}[O]_s \qquad i_{ox} = nFAk_{ox}[R]_s \qquad (3)$$

Where *n*, *F* and *A* are the number of electrons transferred in the reaction, Faraday's constant, and the electrode area respectively. $[O]_s$ and $[R]_s$ are the concentration of species *O* and *R* at the electrode surface. The net rate of reaction (R_{net}) is the rate of the forward reaction minus the rate of the backward and therefore the net (observed) current (i_{net}), is the combination of the reductive and oxidative currents according to equation 5.

$$R_{net} = R_{red} - R_{ox} = k_{red}[O] - k_{ox}[R] \quad (4)$$

$$i_{net} = i_{red} - i_{ox} = nFAk_{red}[O]_s - nFAk_{ox}[R]_s \quad (5)$$

Rate constants vary with temperature according to the Arrhenius rate equation.

$$k = Ae^{-E_a/RT} \quad (6)$$

Here E_a is the activation energy of the reaction, R the gas constant, T the temperature in Kelvin, and A the pre exponential factor, also known as the frequency factor, representing the attempts made at overcoming the activation energy barrier. Because rate constants k_{red} and k_{ox} are also affected by the applied potential (for example with k_{red} becoming bigger with increasing negative potential), electrode kinetics must describe the effect of potential (E) upon rate, as the Arrhenius equation does with temperature. To achieve this, the Butler-Volmer equation of electrochemical kinetics has been derived. Which, for the 1 electron transfer above, has the equation.

$$i_{net} = i_0 \left(e^{\frac{\alpha F(E-E_{eq})}{RT}} - e^{-\frac{(1-\alpha)F(E-E_{eq})}{RT}} \right) \quad (7)$$

Where E_{eq} is the equilibrium potential for the reaction and E the potential applied to the electrode surface. i_0 is the exchange current, which represents the current flowing both ways at E_{eq} (i_{red} or i_{ox}, where there is zero net current). i_0 has equation

$$i_0 = FAk^o[R]_b{}^{\alpha}[O]_b{}^{(1-\alpha)} \quad (8)[49]$$

Where $[R]_b$ and $[O]_b$ are the bulk concentrations of R and O respectively and k^o is the rate constant for the reaction at E_{eq}. α is what is known as the symmetry factor. The physical meaning of terms α and 1-α in equations 7 and 8 are to do with the position of the activation energy peak for the reaction along the reaction coordinate. α in the above equation is the position of the activation energy peak along the reaction coordinate of the anodic (oxidation) reaction. Therefore 1- α represents this peak's position along the reaction coordinate of the cathodic (reduction) reaction. A value for α of 0.5 (1 - α = 0.5) signifies that the peak for the activation energy barrier of both the reduction and oxidation reactions is exactly half way along the reaction coordinate, between reactant and products. Therefore exactly half of the energy from the potential drop at the electrode-electrolyte interface is used to push the

reaction, as the reaction coordinate is downhill thereafter. Values of α different to 0.5 imply an asymmetry in the reaction coordinate; the peak of the activation energy barrier lying closer to reactants or products. For these situations the proportion of the energy from the potential drop used is different for the oxidation and reduction reactions.

As $(E - E_{eq})$ in equation 7 is the difference between the equilibrium and applied potential, it is commonly replaced with the symbol η, which is known as the overpotential. Also, it is common to divide equation 7 by the electrode area to gain the most common form of the Butler-Volmer equation, shown in equation 9.

$$j_{net} = j_0 \left(e^{\frac{\alpha F \eta}{RT}} - e^{-\frac{(1-\alpha) F \eta}{RT}} \right) \quad (9)[50]$$

Here, j_0 is the exchange current density and j_{net} the net current density. j_0 is vitally important in electrocatalysis as it describes the ability of an electrocatalyst to catalyse a reaction; the better the catalyst the higher its j_0 and larger currents can be observed close to the E_{eq} for the reaction. The effect of exchange current density on the current-potential response is shown in figure 6 below. High values of j_0 are observed for fast, well-catalysed, reactions such as the HOR in PEMFCs. The complimentary ORR, due to its slow kinetics over even the most active catalysts, has a j_0 several orders of magnitude lower than this.

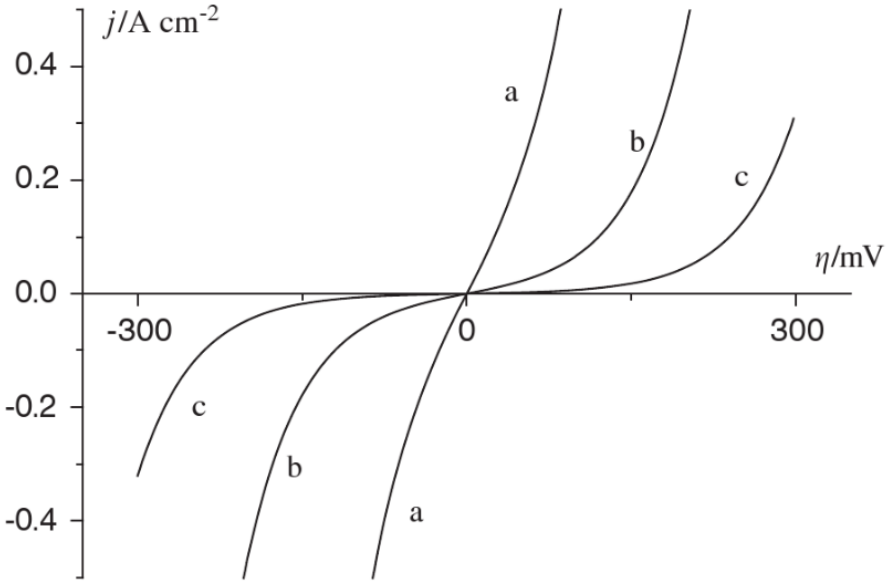

Figure 6. Influence of the exchange current density, j_0, on the j-η response when n = 1 and $\alpha = 0.5$. j_0 = (a) 0.1, (b) 0.01 and (c) 0.001 A cm^{-2}. [50]

To overcome this low j_0, a penalty is paid for by the ORR in terms of overpotential, η. For a reaction with high j_0 (the HOR) a small overpotential is needed to maintain a particular current, whereas for a reaction with a small j_0 (the ORR) a very large overpotential is needed to maintain the same current. Therefore, in PEMFCs, the ORR requires a much larger overpotential to match the current from the HOR, resulting in power (energy) loss. This is illustrated below.

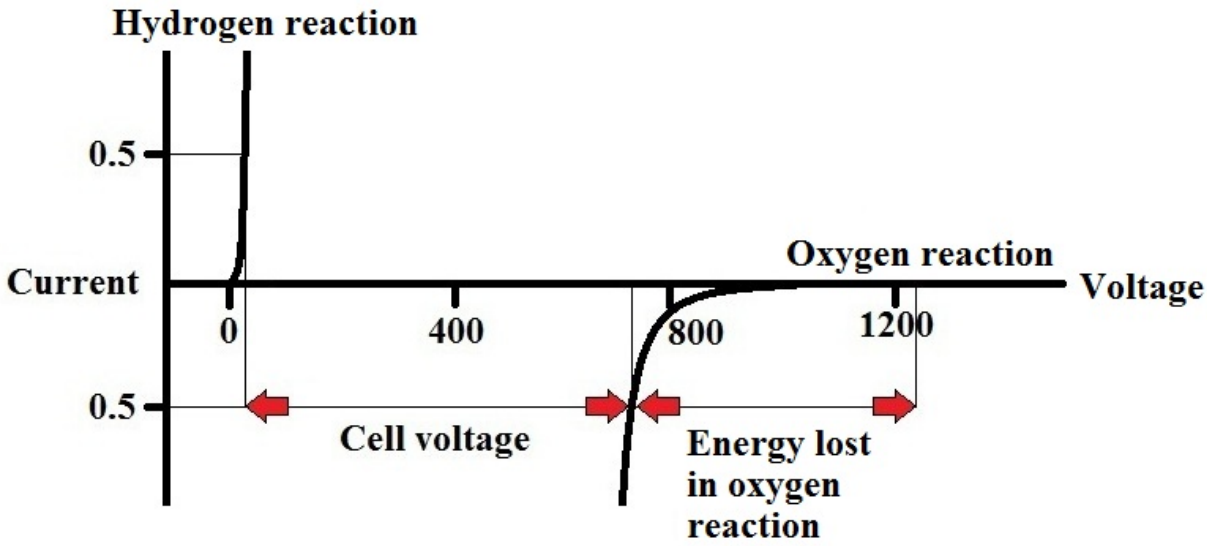

Figure 7. Illustration of the efficiencies of both the HOR and the ORR. On this scale E^0 for the ORR = 1230mV and E^0 for the HOR = 0mV. Here it is shown that a much larger overpotential is needed from the ORR to maintain the arbitrary current of 0.5 than the HOR.

1.2.2 Adsorption

Catalysis often occurs through the intermediate formation of bonds between reactant and catalyst, a pre-requisite of which is reactant adsorption upon the catalyst. Therefore an understanding of adsorption is paramount in catalysis. IUPAC defines adsorption as an "increase in the concentration of a substance at the interface of a condensed and a liquid or gaseous layer owing to the operation of surface forces" [51]. This preferential concentration of species at the interface is the direct result of surface energy requirements. Surface atoms, compared to the bulk, are under co-ordinated. There is therefore excess energy at the surface compared to the bulk, known as surface energy. To relieve this energy the surface may relax, reconstruct or adsorb external species.

Heterogeneous catalysis occurs at the electrodes of PEMFCs: solid phase catalysts catalyse the reaction of dissolved hydrogen and oxygen. The adsorption processes that occur here are therefore at the solid electrode/liquid electrolyte interface (see next chapter). Firstly, the gas-solid interface shall be considered in order to illustrate some key aspects of adsorption processes.

Two types of adsorption have been classified, physisorption and chemisorption. Physisorption is characterised by weak interactions between adsorbate (e.g. gas molecule) and adsorbent (e.g. a solid catalyst surface), whereas chemisorption is characterised by stronger interactions between the two. Chemisorption is also characterised by a chemical reaction between the adsorbent and adsorbate (therefore electron transfer) and the formation of true bonds. Physisorption is a Van der Waals interaction, the adsorbing species barely perturbed. These aspects are reflected in their adsorption enthalpies, generally <35 kJ mol^{-1} adsorption enthalpies are observed for physisorption and >35 kJ mol^{-1} for chemisorption. [52]

The subject of this thesis is the ORR at metal electrodes, therefore let's consider a gaseous oxygen molecule approaching a metal surface. The following diagram, of the type developed by Lennard-Jones [53] in the 20s and 30s, shows the potential energy of unbound molecular oxygen and bound atomic oxygen as a function of distance perpendicular to the metallic surface.

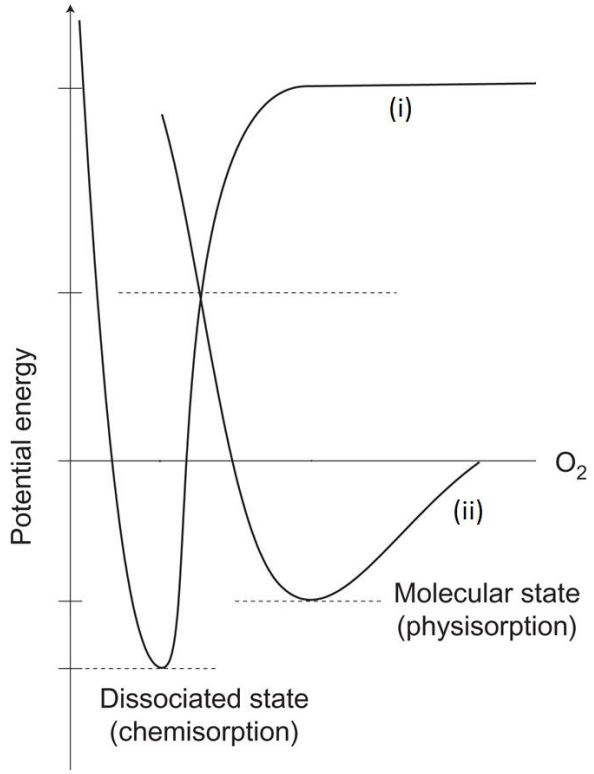

Figure 8. One-dimensional energy diagram for dissociative adsorption [52]. Adapted from [54]

At infinite distance from the surface an individual oxygen molecule exhibits zero potential energy as it is indistinguishable from the bulk gaseous molecules. At a certain distance, commensurate with Van der Waals interactions, molecule-surface interactions begin. Oxygen enters a physisorption well of negative potential energy, a process with no activation barrier. For the molecule to approach closer than this requires energy input, reflected by the exponential increase in potential energy from right to left in curve (ii)**.** Once a certain oxygen-metal distance is reached, overlap between metal d-band and oxygen anti-bonding orbitals can occur (known as back-donation) and the strong oxygen double bond may be dissociated. The process then progresses to curve (i) and atomic oxygen is bound to the metal in a chemisorption well, which may fulfil surface energy requirements. [52]

The depth of the physisorption and chemisorption wells (as well as the shapes of the curves i and ii) depend on the identity of both the metal and the gaseous molecule, due to the metal's surface energies requirements and the gaseous molecule's ability to fulfil these requirements through adsorption. The shape and depth of the wells also denote whether there is an activation barrier for molecular dissociation. If curves (i) and (ii) intersect above the zero energy line then there is an activation energy barrier to overcome whereas the dissociation is barrierless if this intersection occurs below the line.

The Lennard-Jones' diagram does offer some enlightenment into the kinetics observed for adsorption, but it is a simplification. In reality, the depth of both potential wells is a function of adsorbate coverage, due to the effect that lateral interactions, such as Coulombic interactions, have on adsorption enthalpy. Also, many other parameters contribute to the variation in magnitude of the activation energy barrier, including the relative orientation of the incoming molecule with respect to the surface, its rotational and vibrational energy, and its position above a particular site (directly above or between atoms) at the point of impact. [52]

To account for the complexities associated with adsorption, adsorption isotherms have been developed. An adsorption isotherm describes the adsorbate coverage as a function of pressure for gasses and concentration for liquids. The simplest, and first developed, isotherm being the linear adsorption isotherm, in which the amount of surface adsorbate is linearly proportional to pressure through the equation

$$\theta = k_H P \qquad (1)$$

Here θ is the coverage, k_H is known as Henry's adsorption constant and P is the partial pressure of the adsorbant. This simple isotherm is not useful at high adsorbate coverage [55] as it does not account for adsorbate-adsorbate interactions. Nevertheless, at low adsorbate coverage, where such interactions may be negligible, this isotherm simulates observed adsorption behaviour [56].

Except at low pressures, surface coverage does not increase linearly with pressure or concentration [56]. The Freundlich adsorption isotherm [57] is one isotherm which describes adsorption non-linearly. It is mathematically expressed

$$log\,\frac{x}{m} = \log(K) + \frac{1}{n}\log(P) \qquad (2)$$

x is the mass of adsorbate, m the mass of adsorbent, P the pressure of the adsorbate. K and n are constants for a particular adsorbent and adsorbate at a given temperature. P may also be replaced by concentration, C, for a solution adsorbate. The Freundlich adsorbtion isotherm is criticised for having no fundamental thermodynamic basis since it does not reduce to Henry's law at low concentrations [58].

The Langmuir adsorption isotherm [59] is another early developed isotherm that has a number of assumptions, such as there being no interactions between adsorbate molecules, all adsorption sites are equivalent, and that only monolayer coverage is exhibited. Although these are clearly unrealistic assumptions, the Langmuir adsorption isotherm produces good agreement with a wide variety of experimental data and is probably the best known and most widely used adsorption isotherm [58]. In solution, the Langmuir adsorption isotherm is used to model H_{upd} formation on Pt{111} [60]. The Langmuir equation showing surface coverage as a function of pressure is

$$\theta = \frac{\alpha P}{1+\alpha P} \qquad (3)$$

Here, α is a constant relating to the binding energy of adsorption and the other terms have their usual meanings described above. The Langmuir adsorption isotherm has also been modified to account for the formation of multilayers through the BET (Brunauer-Emmett-Teller) isotherm [61]. The straight line form of which is

$$\frac{P}{\nu(P_0-P)} = \frac{1}{\nu_{mon}c} + \frac{P(c-1)}{P_0\nu_{mon}c} \qquad (4)[61]$$

where c is the BET constant, P_0 the vapour pressure of the adsorbate, v the volume of the adsorbed layer at standard temperature and pressure. v_{mon} is v at monolayer coverage.

In order to account for adsorbent-adsorbent interactions the Tempkin isotherm [62] has also been derived from the Langmuir model. This model assumes that the heat of adsorption decreases linearly with coverage due to these interactions [63].

Since the discovery of the early isotherms summarised above, a plethora of isotherms have been developed to account for many nuances of adsorption at a variety of different interfaces. A recent review of the state of the modelling of adsorption isotherm systems can be found here [63].

1.2.3 The Electrical Double Layer

The previous section mainly focussed on adsorption at the gas-solid interface. Here, the structure of the solid electrode/liquid (aqueous) electrolyte interface shall be discussed.

When a metal electrode is placed in contact with an electrolyte a potential difference is set up across the interface. The electrode will therefore be either positively or negatively charged with respect to the electrolyte. The electrolyte, interrupted by the electrode, will respond in various ways to the presence of this charged surface. Mainly, electrostatic interactions occur between the electrode and electrolyte. Ions of opposite charge are concentrated at the interface and dipole moments of the solvent molecules may be orientated towards the electrode. Therefore a structure, distinct to the bulk electrolyte, exists at the electrode electrolyte interface. Due to the charge at the electrode along with the opposite charge in solution, this interfacial structure is known as the electrical double layer. Many models have been developed and refined over the years to describe the electrical double layer. [64]

The first model of the electrical double layer was proposed in 1853 by German scientist Hermann von Helmholtz [65]. In the Helmholtz model the double layer is considered as two layers of charge separated by a fixed distance, analogous to a capacitor [64]. The, let's say, negative charge at the electrode is exactly cancelled out by the layer of positive ions from the electrolyte and the potential drop at the interface is abrupt and linear. The composition of the electrolyte is the same as the bulk at a short distance from the electrode. In this model it is assumed that that the ions approach the electrode up to a distance, known as the Outer

Helmholtz Plane (OHP), which is limited by the ion's solvation shell. Also it is assumed that a layer of solvation lies between the electrode and the ions. [50]

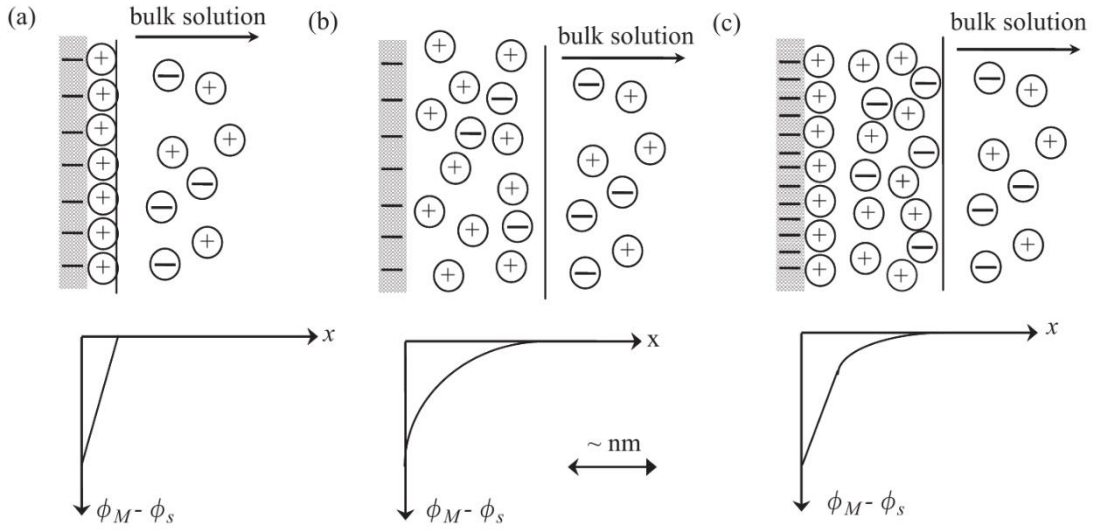

Figure 9. Schematic representation of the (a) Helmholtz, (b) Guoy-Chapman and (c) Stern models for the electrical double layer at an electrode/electrolyte interface. Below each model are the resulting distributions in the potential perpendicular to the surface. [50]

The capacitance of the double layer from the Helmholtz model is the same as a parallel plate capacitor and therefore has the equation:

$$C = \frac{\sigma}{V} = \frac{\varepsilon\varepsilon_0}{d} \tag{1}$$

where ε is the dielectric constant between the plates, ε_0 is the electric constant, V is the potential difference between the plates in volts, σ is the charge held on the plates and d is the distance between the plates. The differential capacitance, the change in charge with voltage, for a parallel plate capacitor is constant, as seen through the following equation

$$\sigma = \frac{\varepsilon\varepsilon_0}{d} V \qquad \frac{d\sigma}{dV} = \frac{\varepsilon\varepsilon_0}{d} \tag{2}$$

Therefore the Helmholtz model for the electrical double layer predicted the same ($\frac{\varepsilon\varepsilon_0}{d}$) value for the differential capacitance and capacitance. However, it was later observed that the differential capacitance of the double layer is not constant, as it varies with potential. This factor was then accounted for in the Guoy-Chapmann model [66] by the inclusion of a diffuse layer. In this model, the ions at the electrode surface are dispersed by Brownian motion. The

electrode charge is not cancelled by a single layer of opposite charge at the electrode surface, but by a diffuse layer of ions that are highest in concentration close to the electrode and decrease in concentration with distance. The Guoy-Chapmann model correctly simulates the capacitance observed at potentials close to the point of zero charge (PZC) and also in solutions with low ionic concentration. However, at potentials further from the PZC and at high ionic concentration this model does match observed behaviour. [64]

The next development in modelling of the electrical double layer came from Otto Stern in 1924 [67]. In the Stern model the Helmholtz and the Gouy-Chapman model are combined. Ions are considered to approach up to the point of the OHP as in the Helmholtz model and this can account for some of the potential drop at the electrode-electrolyte interface. The rest of the potential drop occurs throughout a diffuse layer, per the Gouy-Chapman model. In this hybrid model the potential drop is linear between the electrode and the OHP, where a certain amount of ions are immobilised, and is non-linear in the diffusion layer, where ions are spread diffusely through Brownian motion (see figure 9(c)). It must be noted here that the diffusion layer described in this section is different to the diffusion layer discussed later, which is to do with the flow of reactant to the electrode surface. [64]

The capacitance in the Stern model is the total of the capacitance in both the Helmholtz and Gouy-Chapman, diffuse, layers. Considering that these are capacitors in series, the capacitance is then

$$\frac{1}{C} = \frac{1}{C_H} + \frac{1}{C_G} \qquad (3)$$

This model is applicable to a greater variety of situations than the Helmholtz and Gouy-Chapman models alone. At high electrolyte concentrations equation 3 simplifies to the Helmholtz model and at low concentrations it simplifies to the Gouy-Chapman model. The Stern model, however, does not simulate the differential capacitance of solutions containing ions which may “specifically” adsorb (discussed below), as it does not account for such a phenomenon.

The next model of the double layer was proposed by Grahame in 1947 [68]. The Grahame model is distinct from those discussed thus far in that some ions are considered able to approach closer to the electrode surface than the OHP, the previous point of closest approach. This was postulated to occur by an ion losing its solvation shell and making direct contact with the

electrode surface. This closer plane of approach was called the inner Helmholtz plane (IHP). Ions that adsorb to the IHP are known as "specifically adsorbed" since this action is particular to certain chemical species. Through specific adsorption, negatively charged solution species, such as Cl^- or I^-, may specifically adsorb on a negative electrode surface. This is due to the weakly bound hydration shell that surrounds them. Small positively charged ions common to electrolyte solutions, such as Na^+, often exhibit a strongly bound hydration layer and rarely specifically adsorb. These aspects mean that, in a solution containing negatively charged ions in contact with a negatively charged electrode, the potential between the electrode and the IHP may actually drop to more negative values, before increasing linearly between the IHP and the OHP. [64]

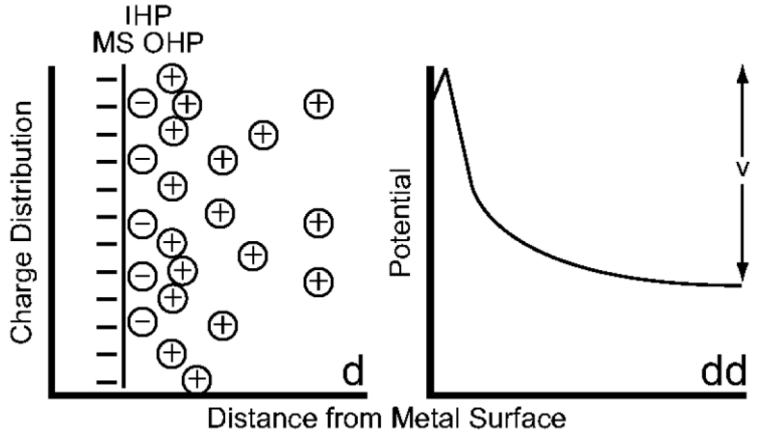

Figure 10. Grahame model of the double layer at the electrode/electrolyte interface. Charge distribution vs. distance, left, and potential variation vs. distance, right. MS = metal surface, IHP = inner Helmholtz plane, OHP = outer Helmholtz plane. Reprinted from [64]

The final major contribution to our current understanding (except modern, statistical mechanics based models) of the electrical double layer came from the Bockris-Devanathan-Muller (BDM) model [69]. This model modifies that of the Stern model by considering that solvent molecules are orientated by the electric field of the electrode. The IHP in this model consists of specifically adsorbed species along with a layer of orientated solvent molecules. The second, third, etc. layers of solvent molecules are orientated to a progressively less degree by the charged electrode. Due to this orientation, this model predicts a dielectric constant for the solution which varies throughout the electrical double layer. For water as the solvent the dielectric constant varies from approximately 6 for in the first layer, to approximately 30 in the second, approaching the bulk value in successive layers [64].

1.3 The Surface Atomic Structure of Metals

Adsorption upon metal surfaces and catalytic activity are highly dependent on the arrangement of atoms exposed to the adsorbent. For example specific adsorption, discussed in the previous section, is dependent not only upon the identity of the solution species but also upon the arrangement of atoms at the electrode surface. This is because alignment of orbitals and bonding depend upon both these factors. Most prepared metals, although exhibiting a regular bulk structure, do not exhibit a regular surface structure. Their surfaces are made of a variety of sites, such as flat regions, steps and defects, which differ in their local atomic arrangement and have different electronic properties [52]. The local activity for a catalytic reaction may therefore vary over the whole surface as some areas may not have the ideal properties for catalysis. For the ORR catalyst in fuel cells such a scenario is a waste of platinum that could be more optimally used if the whole surface exhibited optimal activity. Therefore the relationship between particular surface atomic arrangements and ORR activity must be understood, as it is this fundamental understanding which informs which atomic arrangements have highest activity. Shape controlled nanoparticle catalysts may then be made which contain the maximum amount of these sites.

The metals used in this work have a face centred cubic (fcc) bulk structure. The surface structure reflects this underlying bulk structure. The identification of different surfaces shall be discussed in the following sections.

1.3.1 The Miller Index and Microfacet Notation Systems

Consider the face-centred cubic, fcc, structure below. One corner of this unit cell may be defined as the origin and the x, y and z axis are labelled. The unit cell dimension is the shortest distance between two corners of the cell and has units a. The distance from the origin to the next atom in the x, y or z axis is therefore 1a.

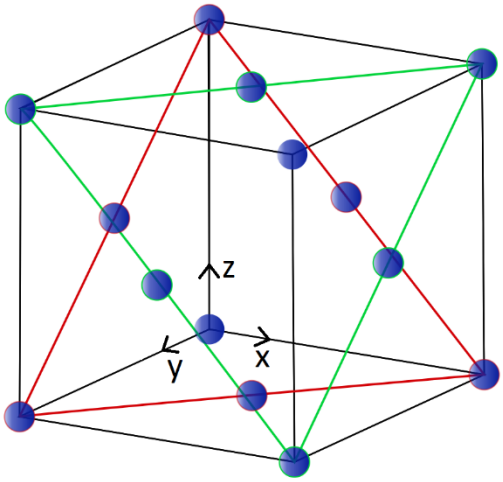

Figure 11. Face-centred cubic crystal lattice structure. Adapted from Wikimedia Commons image (http://commons.wikimedia.org/wiki/File:Face-centered_cubic_crystal_lattice.svg).

The fcc structure can be cut at any plane within the unit cell, creating an exposed surface with a unique atomic arrangement. This plane is defined by a series of three numbers, four in the case of a hexagonal close-packed (hcp) unit cell, collectively known its Miller index. The Miller index identifies the surface atomic structure that would be made from a cut at this plane. To determine the Miller index, firstly identify the x, y and z coordinates that the plane intercepts as fractions of the unit cell dimension, a. For example, let's take a plane which intercepts at ½a in the x axis, 1a in the y axis and ∞a in the z (an ∞ intercept represents a plane running parallel to that axis and which therefore does not cross it). The next step (the final one in this case) in achieving the Miller index for the plane is to take the reciprocal of the numbers above; (1/[1/2], 1/1, 1/∞) = (2,1,0). The Miller index for this plane is therefore (210). [52]

If after the previous step the results are still fractions, then all the reciprocals must be multiplied by an appropriate number, as Miller indices must consist of whole numbers. For example, if after the reciprocals were taken the result (1, 1/2, 1/2) was achieved, then every number would be multiplied by 2 to give the Miller index (211). Likewise, if the index is not in its simplest form after taking the reciprocal, then every number must be divided by an appropriate number, as Miller indices are the simplest numeric representation of the plane. For example, the numbers of the index (842) would be halved to make the Miller index (421). If the plane intercepts at a negative point in one of the axis then a bar is placed above the relative value. For example, the index for the plane intercepting at ½, -1, ∞ would have the Miller index $(2\bar{1}0)$ rather than (2,-1,0).

The three numbers in the Miller index plane are denoted generally by the letters *h*, *k* and *l*. With regards to notation, parenthesis, (), are used to denote a single plane whereas braces, {}, are used to denote a family of planes. A family of planes are those which are equivalent due to symmetry features of the unit cell. For example the planes (100), (010), (001), $(\bar{1}00)$, $(0\bar{1}0)$ and $(00\bar{1})$ exhibit identical atomic arrangements and are recognised as a family of planes as {100}.

If *h*, *k* and *l* in the Miller index are all either 1 or 0, then a cut through the crystal for that plane will form an atomically flat surface, with no steps or kinks. There are three such surfaces for fcc structures, {111}, {100} and {110}, illustrated below. The {111} plane exhibits a hexagonal atomic arrangement with 6 fold symmetry. The atoms of the {100} plane are packed in a cubic fashion with 4 fold symmetry and the {110} plane exhibits atoms packed rectangular, with 2 fold symmetry.

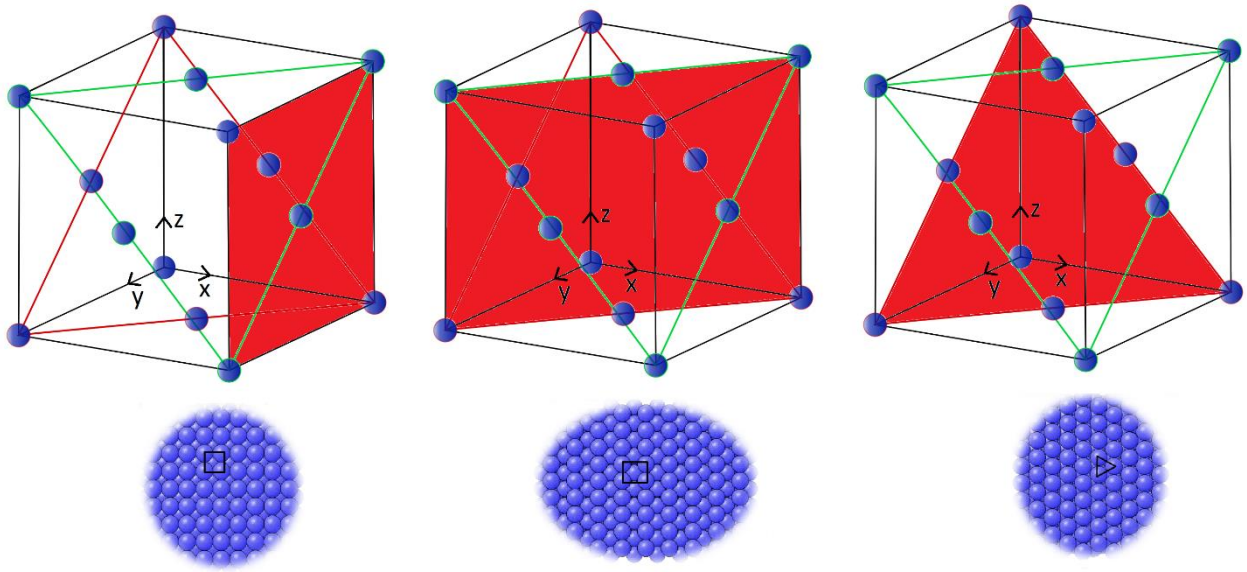

Figure 12. Base plane atomic arrangements of the fcc system. From left to right, (100), (110) and (111). Adapted from Wikimedia Commons image (http://commons.wikimedia.org/wiki/File:Face-centered_cubic_crystal_lattice.svg).

Miller index planes with one or more numbers that are greater than 1 are known as high Miller index planes. As detailed above, these planes intercept at fractional values of the unit cell's axis. These surfaces contain flat areas, which have an atomic arrangement of one of the three base planes. Flat areas of high index planes are known as terraces and are separated by monoatomic steps. The (13,1,1) surface for example contains terraces of (100) atoms separated by (111) steps.

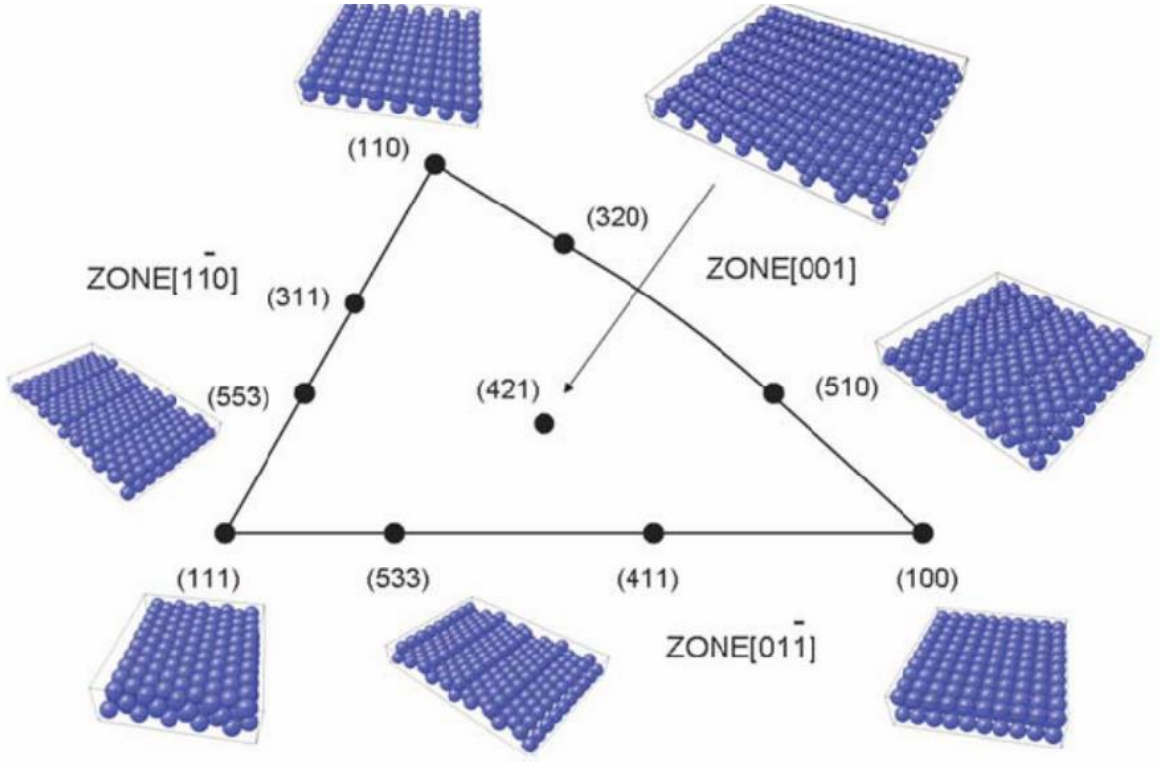

Figure 13. Unit stereographic triangle of fcc single-crystal surfaces and their corresponding surface atomic arrangements. [70]

All the high Miller index planes may be represented on a triangle where the vertices (poles) represent the basal planes. This is known as the stereographic triangle of the fcc system. Stepped surfaces are represented along the sides of the triangle. The further away from the poles one travels, the shorter the terrace of a particular base plane and the higher the density of steps. Many high index surfaces also exhibit kinks in the steps. Kinked surfaces are represented by the area within the stereographic triangle.

Another notation system, useful for denoting stepped surfaces, is the microfacet system [71]. The (755) surface for instance contains (111) terraces that are 6 atoms wide separated by (100) steps, in microfacet notation this is written 6(111) x (100). This system can be helpful in visualising the surface. There are also rules for converting between the microfacet and Miller index notation systems for stepped surfaces. For example, the series of surfaces with microfacet notation n(111) x (100), where n is the number of atoms in the terrace, is written (n+1,n-1,n-1) in Miller index notation. The turning point of the zones occur where n=2 in their microfacet notation. This is the point where the length of terrace and step is equal (2 atoms). This is illustrated by the (311) surface, which in microfacet notation may be written as either 2(111) x (100) or 2(100) x (111).

Zone	Miller index (n≥2)	Microfacet notation
$[01\bar{1}]$	$(n+1, n-1, n-1)$	$n(111)\times(100)$
	$(2n-1, 1, 1)$	$n(100)\times(111)$
$[1\bar{1}0]$	$(n+1, n+1, n-1)$	$n(111)\times(110)$
	$(2n-1, 2n-1, 1)$	$n(110)\times(111)$
[001]	$(n, n-1, 0)$	$n(110)\times(100)$
	$(n, 1, 0)$	$n(100)\times(110)$

Figure 14. Relationship between the Miller index notation and microfacet notation systems. [72]

1.4 Electrochemical Techniques

There are a variety of electrochemical techniques that may be used to study the electrode-electrolyte interface. In most cases, a three electrode electrochemical cell is required for quantitative analysis. The electrode that possesses the surface under examination is known as the working electrode (WE), the reference electrode (REF) is used as a reference for potential control, and the counter electrode (CE) completes the electrical circuit by allowing charge to flow between itself and the working electrode. A machine which uses these three electrodes to control the potential at the working electrode and which measures the current passed between the working electrode and the electrolyte is known as a potentiostat. A basic illustration of the circuit of a potentiostat is shown in figure 15. An amperostat, also known as a galvanostat, does the reverse to a potentiostat: it is capable of controlling the current flow and measures the potential.

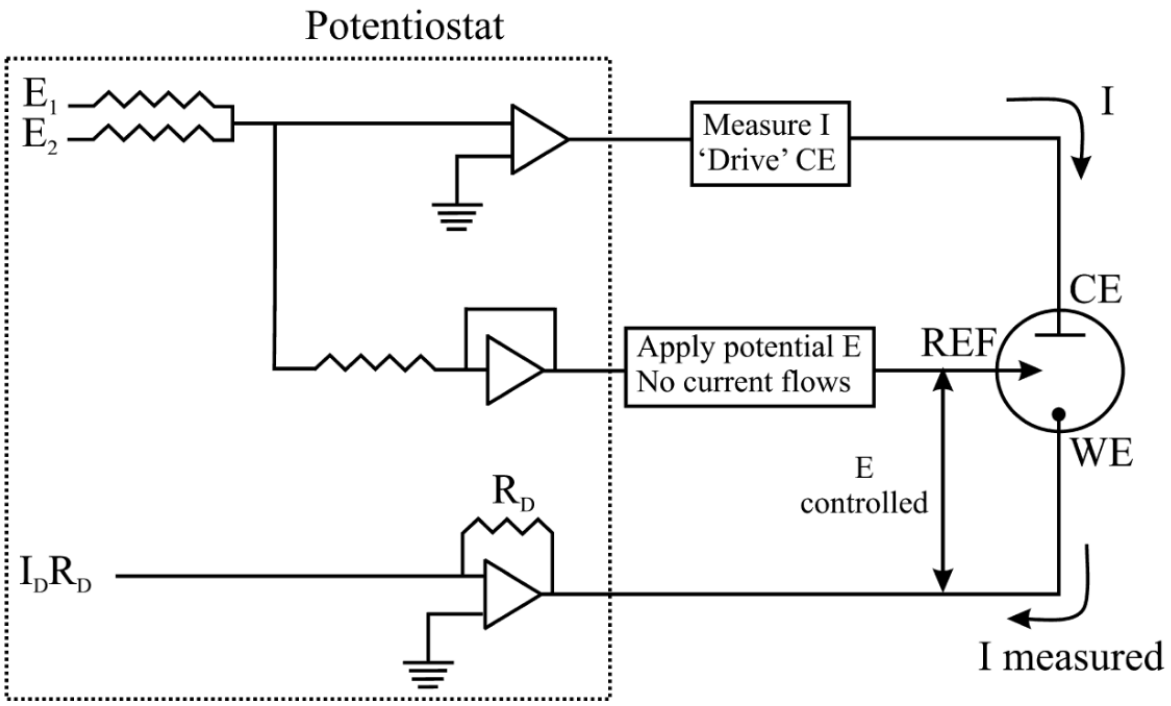

Figure 15. A basic representation of the circuit of a potentiostat controlling a three electrode electrochemical cell. [73]

Coulometric techniques make use of the devices described above and contain two technique subsets, potentiostatic and amperostatic coulometry. Potentiostatic coulometry involves holding the potential of the working electrode at a constant value and measuring the resulting

current flow at the interface with time. Amperostatic coulometry pulls a constant current at the working electrode and measures its changing potential with time.

The above coulometric techniques are part of the major family of dynamic electrochemical techniques. These are techniques in which current is allowed to flow through the electrolyte solution, as opposed to static techniques in which it is restricted. Figure 16 shows a family tree of interfacial electrochemical techniques. The first branching of the tree relates to whether the current, *i*, is allowed to flow through the cell or not (static or dynamic techniques). The second branching, within the dynamic techniques family, relates to whether potential or current control (potentiostatic or amperostatic coulometry) is involved. [74]

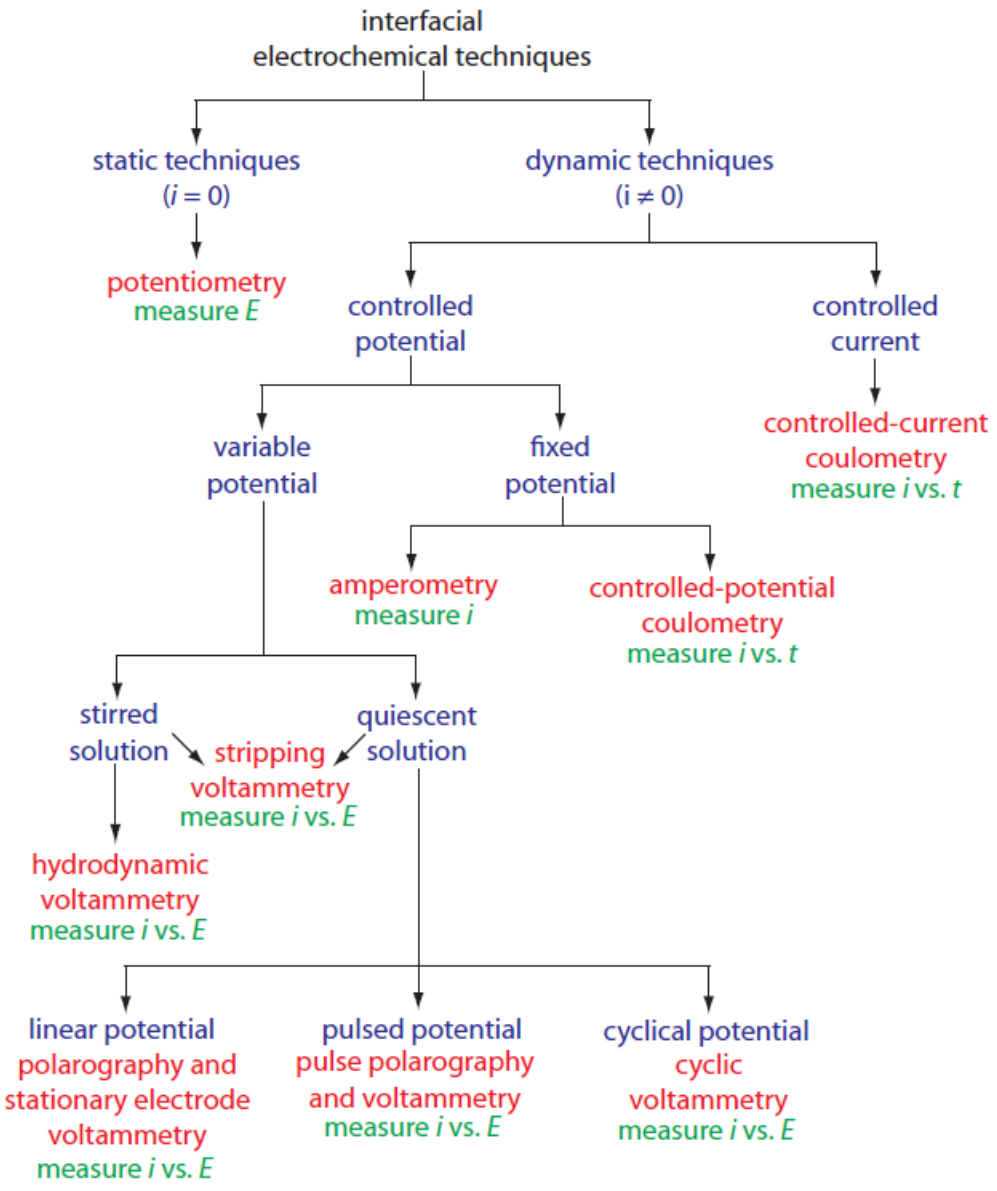

Figure 16. The family tree of electrochemical techniques. The techniques themselves are shown in red, their experimental conditions are shown in blue, and their analytical responses are shown in green. [74]

The static technique potentiometry is useful in measuring the potential of an electrochemical cell. Potentiometry finds use in pH meters because their working electrode potential depends upon concentration of protons [74].

Coulometric techniques can be used to measure an analyte's concentration by measuring the charge passed, *Q*, in coulombs, in completely oxidising or reducing the species. This charge is then related to its concentration through Faraday's Law. [74, 75]

$$Q = nFN_A \quad (1)$$

where *n* equals the number of electrons transferred per mole of electrons, *F* is Faraday's constant, and N_A is the number of moles of analyte. In potentiostatic coulometry, the current, *i*, is measured with time, *t*. Current is converted to charge through the relationship

$$Q = it \quad (2)$$

The charge passed after complete hydrolysis of the analyte is then the integral of equation 2 with respect to time,

$$Q = \int_{t_0}^{t_e} i(t)\, dt \quad (3) \text{ [75]}$$

where t_0 is the time at the start of the reaction and t_e is the time after complete electrolysis. Equation 1 is then used to calculate the concentration of the electrolysed species. Note that a suitable potential must be chosen which will continue to cause electrolysis of the species whilst its concentration diminishes. This is because the reduction potential of the species changes with its concentration according to the Nernst equation. Also, a potential must be chosen that does not cause reactions with other species in the electrolyte or the electrolyte itself. This is so that as close to 100% of the current passed is associated with the reaction of the species of interest. [50, 75]

The current vs. time curve observed in potentiostatic coulometry shows that there is an exponential decay of current. This is because at t_0 there is a high concentration of species at the electrode surface. After consumption of species at times $>t_0$ more species must diffuse to the electrode surface before it may be electrolysed. A depletion layer therefore grows from the surface, more correctly known as the diffusion layer (diffusion is discussed in the following

sections). If conditions are not correct then the current may essentially reach zero, not due to complete electrolysis of species, but due to depletion of the species only at the electrode surface. In such experiments, in order to carry out complete electrolysis of the analyte and therefore accurately determine its concentration this effect needs to be diminished. This is done by using a high surface area electrode, stirring the solution and by using a small volume of analyte. By manipulation of these parameters, virtually all analyte may be electrolysed at the electrode surface in a practical time frame. [50, 73]

The other techniques within the family tree involve measuring a current response as a function of a potential which is varied over time (the way in which the potential is changed as a function of time is known as the experiments' potential waveform). The simplest of these is chronoamperometry, in which the potential is at first held at a particular value, then, after a set time, is stepped to another value. The potentials may be chosen so that the first does not cause electrolysis of the analyte and the second does.

The subset of electrochemical techniques which are of import to the work presented here are voltammetric techniques. These techniques are similar to chronoamperometry, in that the current is measured as a function of a varied potential. Voltammetric techniques differ from chronoamperometry in that they have more complex potential waveforms: the potential is changed not as a simple stepping of one value to another. One example of a voltammetric technique is linear sweep voltammetry (LSV), in which the potential between the working and reference electrode is swept smoothly between one potential value and another. There are many types of pulsed potential voltammetry which exhibit complex potential waveforms, for example normal pulse, differential pulse, staircase, and square-wave polarography.

Another, technically voltammetric technique, not shown on the family tree, is electrochemical impedance spectroscopy (EIS). This powerful technique is increasingly being used in the analysis of fuel cell devices. Briefly, in this technique a sinusoidal potential is applied to the working electrode and the resulting sinusoidal current signal is recorded. The disparity between the applied potential wave and the resultant current wave can give information on the resistance and capacitance aspects of the system.

This myriad of potential waveforms available to electrochemists means that many aspects of reaction kinetics may be probed by the appropriate choice of experimental conditions. All of the above techniques may be performed under quiescent or hydrodynamic solution control,

also enabling exploitation of diffusional aspects of reaction species. Cyclic voltammetry (CV) is the voltammetric technique which is paramount to the work carried out in this study.

1.4.1 Mass Transport in Electrochemistry

In chapter 1.2, the relationship between the potential applied to an electrode in contact with an electrolyte and the current density for a redox reaction occurring at the interface was discussed and the relevant equations derived. In deriving these equations, the current density was shown to be dependent upon the surface concentration of the redox species at any potential different to the equilibrium value. Therefore, a true description of the current density needs to take into account how the reactant species is delivered to the electrode surface and how product is removed once formed. It also requires a description of how the concentration profiles of products and reactants at the electrode surface change with time. The concentration profile at the electrode surface during chronoamperometry and voltammetry was discussed in chapter 1.4 and only diffusion was considered. It shall be shown here that the current response of a reaction at an electrode surface is highly dependent on mass transport effects.

Mass transport may be split into three categories; diffusion, convection and migration. Diffusion, as noted previously, is the movement of a species due to a gradient in concentration [50]. Diffusion occurs by the movement of species from a high to a low concentration and occurs naturally in order to spread out any concentration variations. Concentration gradients are created during electrochemical reactions due to the consumption of reactants and creation of products at the electrode surface and therefore diffusion is the main mode of mass transport to consider during voltammetry.

Adolf Fick derived equations to describe diffusion in 1855 [76]. Fick's first law of diffusion describes the rate of diffusion parallel to the electrode and may be written

$$j = -D\frac{\partial c}{\partial x} \qquad (1)[73]$$

where D (units of cm^2s^{-1}) is the species' diffusion coefficient and $\frac{\partial c}{\partial x}$ is the concentration gradient at the point of interest. *j*, here, is known as the diffusional flux and has units of $mol^{-2}s^{-1}$ [50]. The negative value signifies that diffusion occurs from high to low concentration. This equation shows that a large concentration drop at the electrode surface results in a high

diffusional mass transport. Fick's second law of diffusion describes how the concentration changes with time and is written

$$\frac{\partial c}{\partial t} = D\frac{\partial^2 c}{\partial x^2} \qquad (2)[73]$$

Convection is the movement of a species due to external mechanical forces [50]. There are many ways in which convection may be achieved, for example by rotation of the electrode or by flowing electrolyte over the electrode surface. Natural convection can also occur due to the random vibrations in a laboratory environment [50]. Controlled convection is often used in order to elucidate reaction parameters as it can be described mathematically. The final mode of mass transport is migration, which is the transport of charged solution particles attracted or repelled by a charged surface. Reactants and products are often charged species and may therefore be affected by migration. To minimise this affect, a large excess of electrolyte is used in electrochemical experiments and it is the electrolyte ions that carry the majority of charge through solution. As migration is not an important mass transport issue to consider in most electrochemical studies, the effect of diffusion and convection shall be the focus of later sections.

1.4.1.1 Diffusion in Chronoamperometry

Firstly, let's consider the influence of mass transport on the Faradaic current for the reaction below under investigation using chronoamperometry.

$$O + e^- \leftrightarrow R$$

In this explanation both oxidised (O) and reduced (R) forms of the solution species are considered to not adsorb upon the electrode surface. Consider also that we are interested in the forward reaction, reducing species O to R, and that there is no R in solution at the start of reaction. The reaction starts with a switch in potential, from one which does not cause reaction of O, to a negative potential which completely reduces species O at the electrode surface. At the beginning of the reaction, at t=0, the concentration of O at the surface is equal to the bulk concentration (at t=0, $[O]_s = [O]_b$). After a short period of time, all of O at the surface is reduced and its surface concentration becomes zero (at t>0, $[O]_s = 0$). A concentration gradient then exists between $[O]_s$ and $[O]_b$ which draws more O towards the electrode for further

reaction (The reverse occurs with R; at times just after t=0 there is a high $[R]_s$ and $[R]_b$ = 0, drawing R away from the electrode surface). This process, of transport of a species due to the presence of a concentration gradient, is known as diffusion. Therefore, at t>0 the current observed for the reduction of O is dependent upon its rate of diffusion to the electrode surface. The layer between the electrode surface, where [O] = 0, and the beginning of the bulk solution, where [O] = $[O]_b$, is known as the *Nernst diffusion layer*. The width of the diffusion layer has the symbol δ. It is defined as the thickness that the diffusion layer would have if the concentration profile were a straight line coinciding with the tangent to the true concentration profile at the interface, and that straight line were extended up to the point where the bulk concentration is reached [51]. Figure 17 clarifies this idea, where 1 on the x axis equals δ. [50, 73, 75, 77]

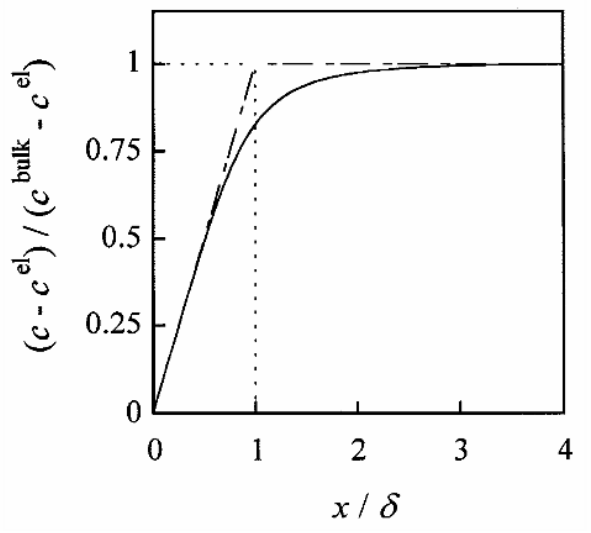

Figure 17. Concentration profile as a function of distance from the electrode surface in units of diffusion layer thickness δ. c=concentration, c^{el}=concentration at the electrode surface (zero), c^{bulk}=bulk analyte concentration. [78]

From Fick's 1st law of diffusion the diffusional flux, *j*, across this layer can therefore be written

$$j = D_O \frac{\partial [O]}{\partial x} \qquad \text{(at } x = 0, [O] = 0) \qquad \therefore \qquad j = D_O \frac{[O]_b}{\delta} \qquad (1)$$

where D_O is the coefficient of diffusion for species O and x the distance from the electrode surface. D_O and δ may be combined to form the mass transport coefficient, m_T, of species O [73] and the equation is then written

$$j = m_T [O]_b \qquad (m_T = \frac{D_O}{\delta}) \qquad (2)$$

If the potential is held at the same reducing value, O is consumed and the diffusion layer, δ, grows with time and therefore the flux of O to the electrode surface decreases. Assuming that convection or migration do not contribute to the mass transport of O towards the electrode, the diffusion layer will continue to grow until all of O in the reaction vessel is consumed. In reality the diffusion layer reaches a limiting value before this point, due to natural convection of O in the bulk solution. As the concentration of O at the surface in the above scenario is zero, the current observed for the reduction of O is considered transport limited and depends upon the mass transport coefficient, m_T, rather than the rate constant k_{red}.

$$i_{red} = \frac{nFAD_O[O]_b}{\delta} \quad \text{or} \quad i_{red} = nFAm_T[O]_b \qquad (3)\ [73]$$

The Cottrell equation, below, describes the current response with time after stepping to a potential which completely reacts a species at the electrode surface. It is derived using Fick's second law of diffusion.

$$i_{red} = \frac{nFA\sqrt{D_O}[O]_b}{\sqrt{\pi t}} \qquad (4)\ [73]$$

1.4.1.2 Diffusion in Cyclic Voltammetry

Cyclic voltammetry (CV) is an extension of LSV in which the potential at the working electrode is cycled linearly between low ($E_{initial}$) and high (E_{final}) values as illustrated below. Due to the pattern created in the potential (E) vs. time (t) plot in figure 18, this waveform is known as the sawtooth potential waveform. The gradient of this waveform denotes the scan rate of the experiment (V/t), which is kept constant throughout.

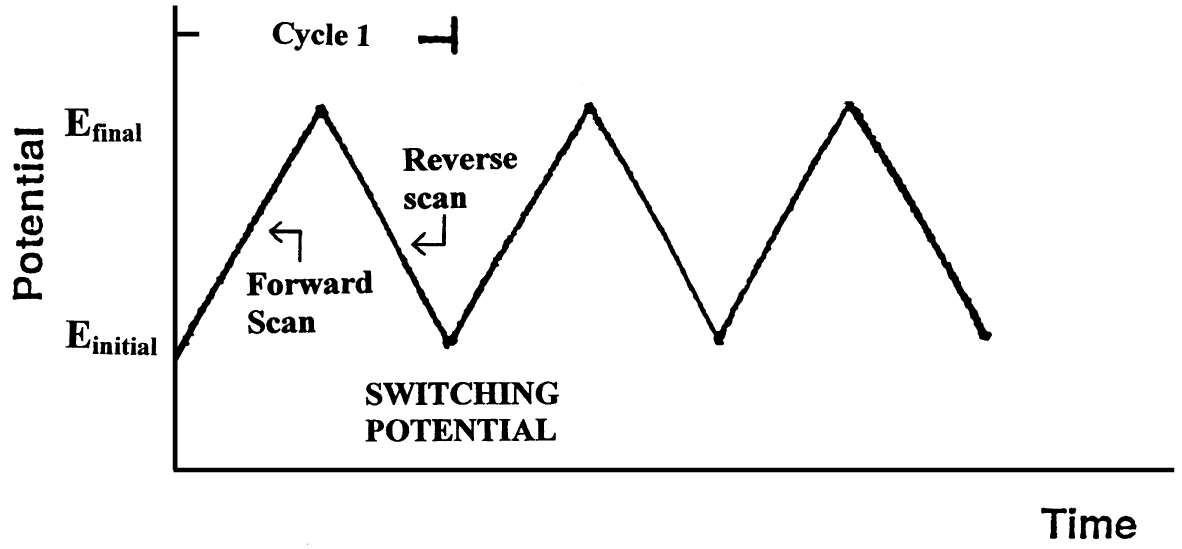

Figure 18. Sawtooth potential waveform of a cyclic voltammetry (CV) experiment. [77]

The "readout" of a CV experiment shows applied potential on the x axis and resulting current flow on the y axis. The system parameters of a typical experiment are set up so that oxidation reactions at the electrode interface give rise to a positive current and reduction reactions give rise to negative current. The current response on the y axis is routinely divided by the working electrode's electro-active area so that different sized electrodes may be compared. Therefore current density, j (Acm^{-2}), is usually plotted on the y axis rather than current (A).

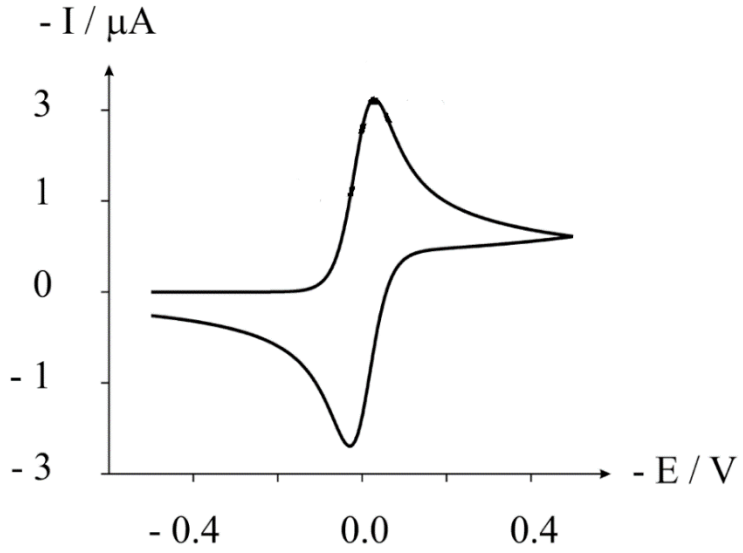

Figure 19. A possible CV response for the oxidation and reduction of solution species upon the application of the potential waveform in figure 18. Adapted from reference [73].

Other than Faradaic processes, current in CV experiments may result from non-Faradaic processes: in which no electron transfer occurs at the electrode-electrolyte interface. Non-Faradaic current occurs because of the capacitive nature of the electrode-electrolyte interface and is to do with movement of ions, which occurs in response to the changing charge on the electrode surface as its potential is swept. Consider a working electrode surface with a particular amount of positive charge upon it. Due to electroneutrality there is equal negative charge held in the solution side of the double layer. Increasing the potential at the electrode in a positive potential sweep increases the charge at the electrode surface. To maintain electroneutrality the concentration of negative ions in the double layer must increase. These new ions join the electrolyte double layer from the bulk solution. Flow of current due to this phenomenon is known as double layer charging. [50]

Double layer charging current, i_{DL}, is directly proportional to CV scan rate and electrode area and is represented by the equation

$$i_{DL} = C_{DL} A \nu \qquad (1)$$

where $\nu (Vs^{-1})$ is the scan rate of the voltammetric experiment, A(cm^2) the electrode area and C_{DL} (farad, F) is the double layer capacitance.

A typical CV experiment of an electrode in contact with an electrolyte gives a current response resulting from both non-Faradaic and Faradaic processes. In most cases it is the Faradaic processes that are of interest in electrocatalytic investigations, therefore non-Faradaic charging current must be deducted from the overall current response so that only Faradaic current remains. In platinum electrochemistry, the double layer charging is routinely deducted from the whole current response by a rectangular baseline subtraction. Although this assumes a constant capacitance throughout the CV and is therefore a simplification, this treatment is useful in attaining electrochemical surface areas of electrode surfaces. Attempts at identifying how exactly the capacitance changes with electrode potential for a Pt{111} electrode in contact with a perchloric acid electrolyte can be found here [79, 80]. These studies illustrate the complexities in deconvoluting non-Faradaic and Faradaic processes for a reactive surface such as platinum.

The Faradaic current response for a voltammetric technique such as CV is more complex than the potential described step above. Let's consider using CV to examine the reduction of O as before. The voltage is initiated at some value that is insignificant to reduce O, $E_{Initial}$. The

voltage then heads towards E_{Final}, a value chosen which drives the reaction of O rapidly. This is performed at sweep rate, ν. Upon reaching a potential value which causes species O to react, current increases exponentially; due to effect of overpotential on the rate constant for the reaction (see 1.2). After this initial exponential increase, the current continues to increase, albeit less than exponentially. A peak in the current is then observed. This peak occurs when the effect of the increasing overpotential balances with the decreasing concentration of O at the electrode surface as it is consumed. At higher potentials the current decreases, as it is now dependent upon the rate of diffusion of O to the surface (i.e. there is a large constant diffusion layer thickness). [50, 73]

For the 1 electron, reversible (i.e. a reaction which can be driven with minimal overpotential) reduction of O, the peak current (i_p) is proportional to the scan rate according to the Randles-Sevcik equation at 298K

$$i_p = 0.4463FA[O]_b\sqrt{\left(\frac{F\nu D_O}{RT}\right)} \qquad (2)[73]$$

where F is Faraday's constant, A the electrode area, $[O]_b$ the bulk concentration of O, ν the scan rate, D_O the diffusion coefficient of O, R the gas constant and T the temperature. This illustrates a major distinction between the behaviour of Faradaic and non-Faradaic current in response to scan rate. Faradaic current has a square root dependence upon scan rate whereas capacitive charging has a linear dependency. Therefore, capacitive charging scales greater with scan rate and can mask Faradaic responses at high scan rates.

After reaching E_{Final} in CV, the potential is turned around. At the start of the reverse sweep a reduction current is still observed as the potential is still sufficient to reduce species O at a diffusion limiting level. After the current reaches levels which may react R, oxidation current rises as R is consumed at the electrode surface. The processes described above happen in reverse: oxidation current increases exponentially, before peaking and then decreasing due to the consumption of R at the electrode surface.

The table and CV below, illustrate some of the diagnostic tests that may be performed in order to differentiate between reversible and irreversible (requiring significant overpotential to push the reaction) couples.

Diagnostic tests for the form of the cyclic voltammetric responses for a reversible and irreversible couple O/R at 298 K.

Experimental measurable	*Reversible couple*	*Irreversible couple*
$\Delta E_p = E_p^a - E_p^c$	$\frac{59}{n}$ mV	$> \frac{59}{n}$ mV and f(k_s, ν)
$E_p - E_{p/2}$	$\frac{59}{n}$ mV	$\frac{48}{\alpha n}$ mV
$\left\lvert \frac{j_p^c}{j_p^a} \right\rvert$	1	1
E_p	Independent of ν	Dependent on ν
j_p	Proportional to $\nu^{1/2}$	Proportional to $\nu^{1/2}$

Table 1 Diagnostic tests for the form of the cyclic voltammetric responses for a reversible and irreversible couple O/R at 298K. [50]

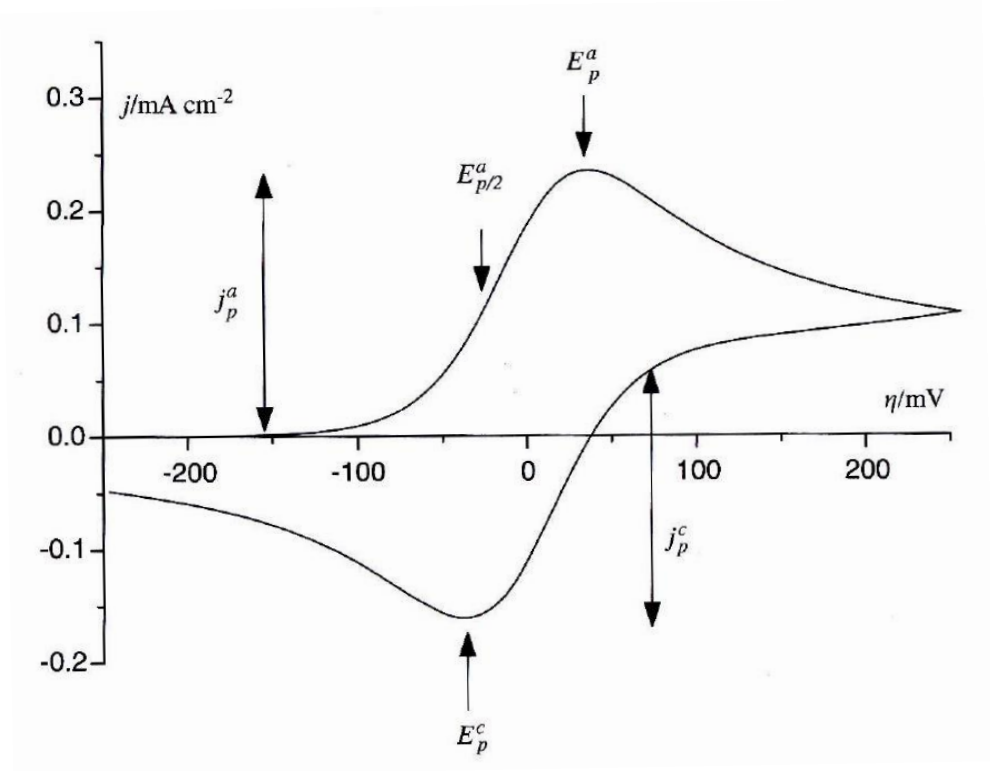

Figure 20. Cyclic voltammogram to define the symbols used in the table above. [50]

Finally the current response for the cyclic voltammetry involving the formation of surface-bound species shall be discussed (adsorption), as this is a major feature of platinum single crystal electrochemistry discussed in the next section. The key difference between reactions

forming surface bound species and reaction which do not is that the current observed at potentials beyond the peak is different. If (as in the O/R couple) R is surface bound, at large negative potentials the current will return to zero and not to a diffusion limiting value, as the reaction is ultimately limited by the number of sites available for adsorption of R on the electrode surface. The figure below illustrates the cyclic voltammetry of the oxidation and reduction of surface bound species at the reversible and irreversible kinetic limits. The differences between these and the CV in figure 20 are obvious. In most real scenarios the current before and after the peak reaches not zero, but the capacitive charging baseline current. The table below illustrates the diagnostic tests for CV responses involving adsorption. Many differences between reactions involving adsorption and those without adsorption can be seen. For example the peak-to-peak separation, ΔE_p, for a reversible couple with surface adsorption is 0mV compared to $^{59}/_{n}$mV without surface adsorption.

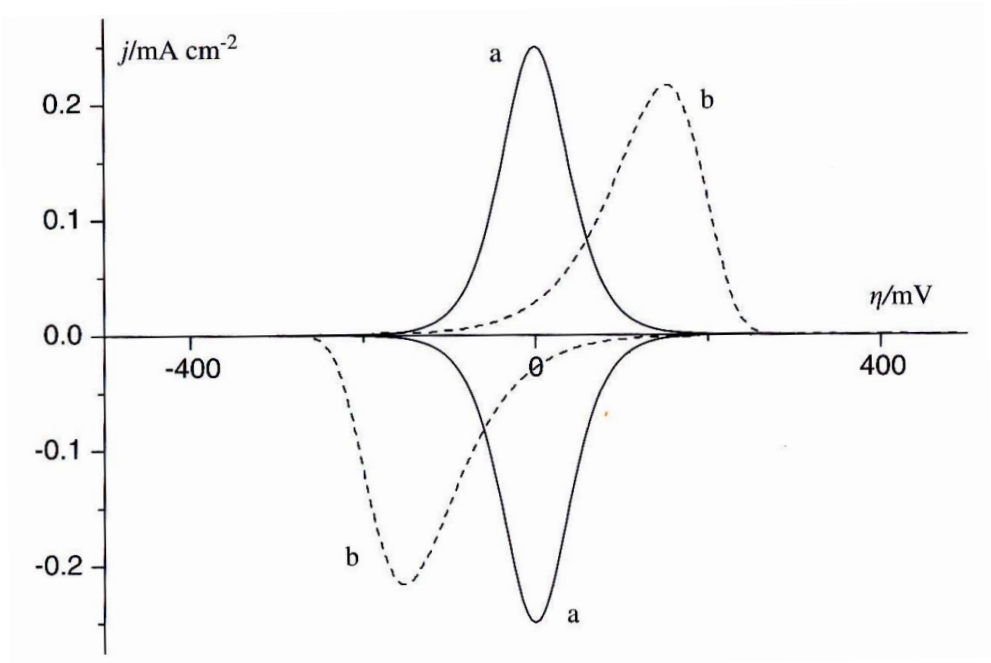

Figure 21. CVs for the reversible, (a), and irreversible, (b), O/R couples. These involve the oxidation and reduction of bound species. Note that non-Faradaic charging processes are not included in this simulation. [50]

Diagnostic tests for the form of the cyclic voltammetric responses for a reversible and irreversible couple O/R when O and/or R are surface bound at 298 K.

Experimental measurable	*Reversible couple*	*Irreversible couple*
$\Delta E_p = E_p^a - E_p^c$	0 mV	>0 mV and f(k_s,ν)
$\left\|\frac{j_p^c}{j_p^a}\right\|$	1	1
E_p	Independent of ν	Function of ν
j_p	Proportional to ν	Proportional to ν
q_p	$q_p^a = q_p^c$	$q_p^a = q_p^c$
Peak shape	Symmetrical	Symmetrical but broader

Table 2 Diagnostic tests for the form of the cyclic voltammetric responses for a reversible and irreversible couple O/R when O and/or R adsorbed at the electrode surface at 298K. [50]

1.4.1.3 Hydrodynamic Effects in Voltammetry

During a stationary voltammetry experiment a peak shape is usually observed for oxidation or reduction. At potentials higher than the peak potential a limiting current may be observed which is lower than the peak current. This limiting current depends upon the width of the diffusion layer δ (as well as rate of reaction, scan rate etc.), which at high overpotentials will not continue to grow indefinitely, but will maintain a stable diffusion layer thickness due to natural convection. The simulated voltammetry [81] in the illustration below (left, figure 22) shows that for large diffusion layer thicknesses this peak shape will be clearly observed. Upon decreasing the diffusion layer thickness the diffusion limiting current at high potentials is seen to increase due to the higher level of diffusional flux at the interface. This results in a transition from a peak shaped curve to a sigmoidal one at the smallest diffusion layer thickness.

The thickness of the diffusion layer may be decreased in reality by the use of hydrodynamic electrodes, where the flow of electrolyte to the electrode surface is controlled. This forced convection decreases the maximum diffusion layer thickness compared to natural convection, as its effect is much stronger. Figure 24 shows that when using a rotating disc electrode (RDE) a fourfold increase in rotation rate halves the diffusion layer thickness. [73]

An example of controlling the diffusion layer thickness of a reaction is shown below (figure 23, right) for the reduction of O_2 to peroxide. A RDE (described below) is used for

hydrodynamic control and a range of rotation rates are used. The stationary voltammetry of this reaction (0rpm) shows a peak shape. At 100rpm, the diffusion layer thickness has been reduced and therefore the diffusion limiting current is greatly increased, but a peak is still present. At 400rpm the reaction curve has become completely sigmoidal. The experimental results in figure 23, from 0rpm to 400rpm, mirror the simulated ones in figure 22.

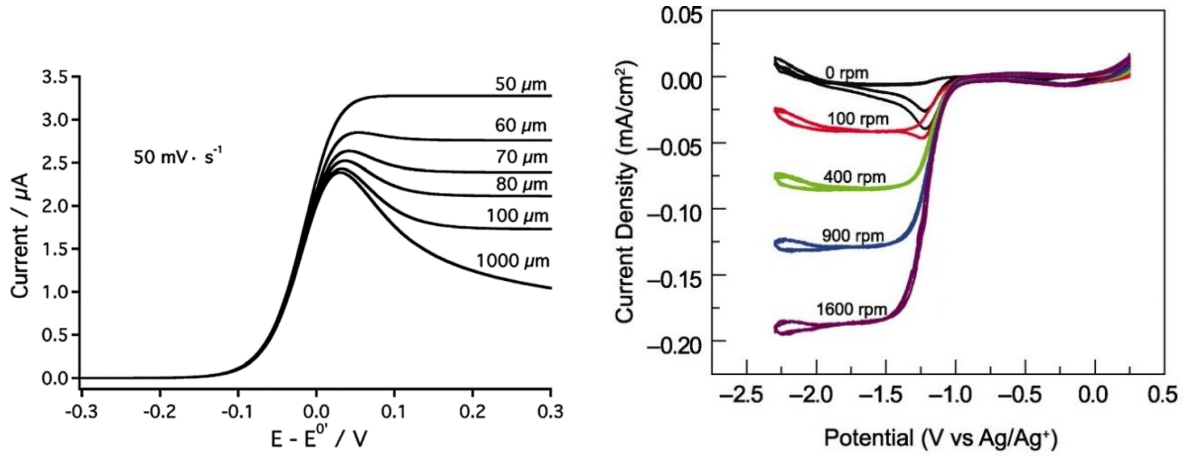

Figure 22, left. Simulated linear sweep voltammograms in which the scan rate is fixed but the thin-layer (double-layer) thickness is varied [81]. Figure 23, right. Rotating-disk electrode measurements of O_2 reduction to peroxide [82].

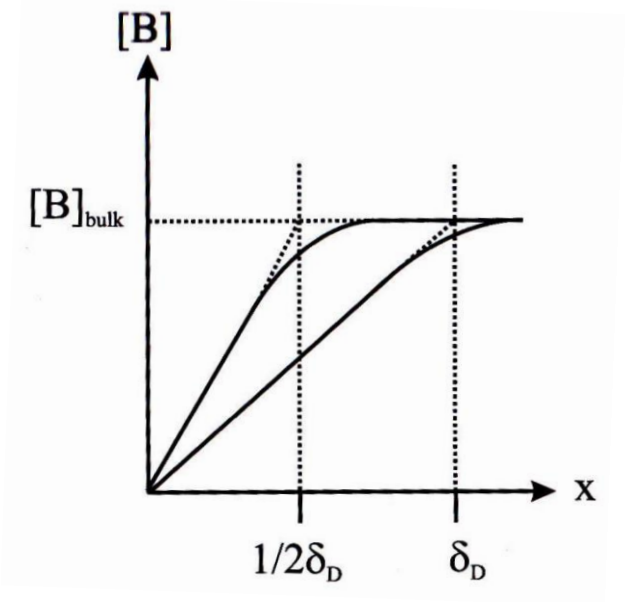

Figure 24. A fourfold increase in rotation speed halves the diffusion layer thickness [73].

1.4.1.3.1 The Rotating Disc Electrode (RDE)

A rotating disc electrode consists of a disc electrode surrounded by an electrically insulating and chemically inert material. This is placed into solution and through rotation of the electrode the electrolyte is pulled towards its surface. The flow of the electrolyte is laminar (i.e. occurring in perpendicular layers with no transfer of material between the layers) if the rotation rate is not set above a certain value and flow speed depends upon the rotation rate of the electrode. The diffusion layer thickness is controlled predictably by the equation

$$\delta = \frac{1.61\nu^{1/6}D^{1/3}}{\omega^{1/2}} \quad (1)\ [50]$$

Here, ν is the kinematic viscosity (viscosity to density ratio), D is the coefficient of diffusion of the species and ω is the rotation speed of the electrode in Hz.

Reynold's number (R_e), named after Osbourne Reynold's work in the 1880s [83], is a dimensionless number that can be used to define the experimental parameters at which predictable laminar flow is maintained. Reynold's number is defined as the ratio of inertial to viscous forces [73]. Equations describing this number can be derived for many flow systems, for the RDE system R_e is described by equation (2).

$$R_e = \frac{\omega r^2}{\nu} \quad (2)\ [73]$$

Here, r is the radius of the electrode. Laminar flow has been found to occur at Reynold values of 2×10^3 [73]. Above this value turbulent flow occurs, which is unpredictable. Equation (2) shows that higher viscosity materials can be made to flow at higher rates before breaking down into turbulent flow. The rotation rates used in the study of the oxygen reduction reaction in aqueous solutions are far below this limit.

Once the material hits the surface of the electrode it cannot continue in a straight line and is thrown outwards according to figure 25.

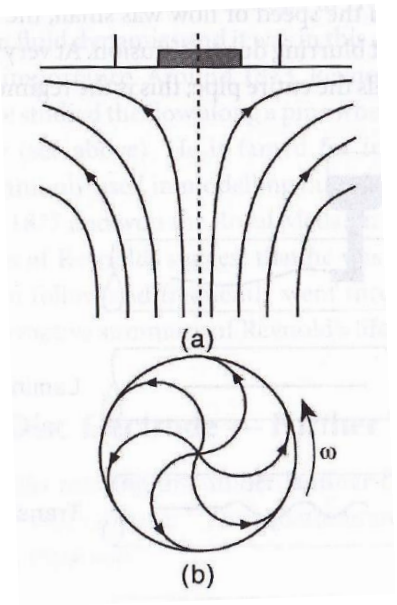

Figure 25. Schematic diagram of the flow pattern created by the rotating disc electrode. (a) View from the side showing how the solution is pumped towards the disc, then thrown outwards. (b) Solution flow close to the electrode surface, viewed from below. [73]

The current for a reduction reaction was defined in equation 3, chapter 1.4.1.1, as

$$i_{red} = \frac{nFAD_O[O]_b}{\delta} \quad (3)$$

Which is relevant at large overpotentials, where the surface concentration of O is zero. As the diffusion layer is controlled by the RDE, substituting equation (1) into this expression gives the value of the limiting current ($i_{red,lim}$) as a function of measurable quantities.

$$i_{red,lim} = 0.62nAFD_O^{2/3}[O]_b\omega^{1/2}\nu^{-1/6} \quad (4)\ [84]$$

Divided by the area, A, this is known as the limiting current density, j_{lim}. This equation is known as the Levich equation.

For irreversible redox reactions, such as oxygen reduction/water oxidation, the reduction and oxidation waves are separated by a large potential range where only double layer charging current is observed. For the oxygen reduction reaction, the complete transition from the reduction occurring under kinetic control (at low overpotentials) to the reaction occurring under diffusion control (at high overpotentials) can be observed, as well as a mixed kinetic-diffusion controlled regime at intermediate potentials. An expression may be derived which describes the current, *I*, throughout this transition.

$$\frac{1}{I} = \frac{1}{nFAk[O]_b} + \frac{1}{-0.62nFAD_O{}^{2/3}[O]_b\omega^{1/2}\nu^{-1/6}} \quad (5)\ [84]$$

Where $nFAk[O]_b$ is the kinetic current obtainable, were there no mass transport limitations. This equation is more commonly written in the following form,

$$\frac{1}{j} = \frac{1}{j_{trans}} + \frac{1}{j_{lim}} \quad (6)\ [84]$$

Here, j_{trans} is the kinetic current density, j_{lim} the mass transport limited current density and j the observed current density. j_{trans} contains the rate constant for the reaction, k, which depends on the applied potential as described previously. j_{lim} is constant at a particular rotation rate and is therefore potential independent. Equation (7) tells us that at low overpotentials, where the current density is small, the j_{trans} term dominates as the reaction is under pure kinetic control, i.e. $\frac{1}{j_{lim}}$ can be ignored at low current density. Within this potential range the observed current is the real kinetic current for the reaction, i.e. at low j, $j=j_{trans}$. At high overpotentials, k becomes large, $\frac{1}{j_{trans}}$ becomes insignificant compared to $\frac{1}{j_{lim}}$ and the reaction is under complete diffusion control (at high j, $j=j_{lim}$). At intermediate potentials neither terms can be cancelled out and the observed current density is less than the kinetic current density due to some inhibition caused by diffusion. The kinetic current density, j_{trans}, throughout this mixed kinetic-diffusion regime can be obtained through rearranging equation (6)

$$j_{trans} = \frac{jj_{lim}}{j_{lim}-j} \quad (7)\ [84]$$

and applying this equation to the current density, j, obtained experimentally.

Alternatively, j_{trans} may be found by carrying the reaction out at various rotation rates, ω. By plotting $\frac{1}{j}$ vs. $\frac{1}{\omega^{1/2}}$ (according to equation 5) and extrapolating $\frac{1}{\omega^{1/2}}$ to zero, the current density at infinite rate of diffusion is found, j_{trans}.

There are a couple of advantages of performing the first method to calculate j_{trans}. The major one being that only a single voltammetry at one rotation rate needs to be performed. Equation (7) is then applied to the data set to obtain j_{trans} at every potential. Feliu et. al. [84] have performed both of the above methods and compared the j_{trans} results obtained. Both procedures gave identical results in a wide potential range, shown below.

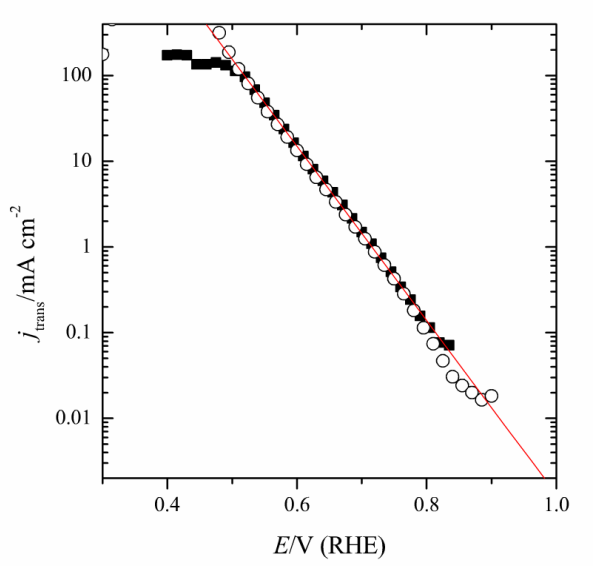

Figure 26. j_{trans} values vs. potential calculated for a Pt(111) electrode in 0.5 M H_2SO_4. Black squares are values calculated from the intercept of the plot of $\frac{1}{j}$ vs. $\frac{1}{\omega^{1/2}}$, using equation (6). Empty circles are values calculated by applying Eq. (8) to the curve at 3000 rpm. [84]

Once the above analysis has been performed on ORR data from the RDE, parameters such as the Tafel slope, from the gradient, and the exchange current density, from the current density extrapolated to 1.23V, can be obtained from the j_{trans} vs. potential plot.

1.4.1.3.2 The Rotating Ring Disc Electrode (RRDE)

The rotating ring disc electrode (RRDE) is similar in design to the RDE as it also contains a disc electrode that is surrounded by an insulating layer. Past this insulating layer the RRDE contains a ring electrode and there is a final insulating layer past the ring. The design of this electrode is shown in figure 27.

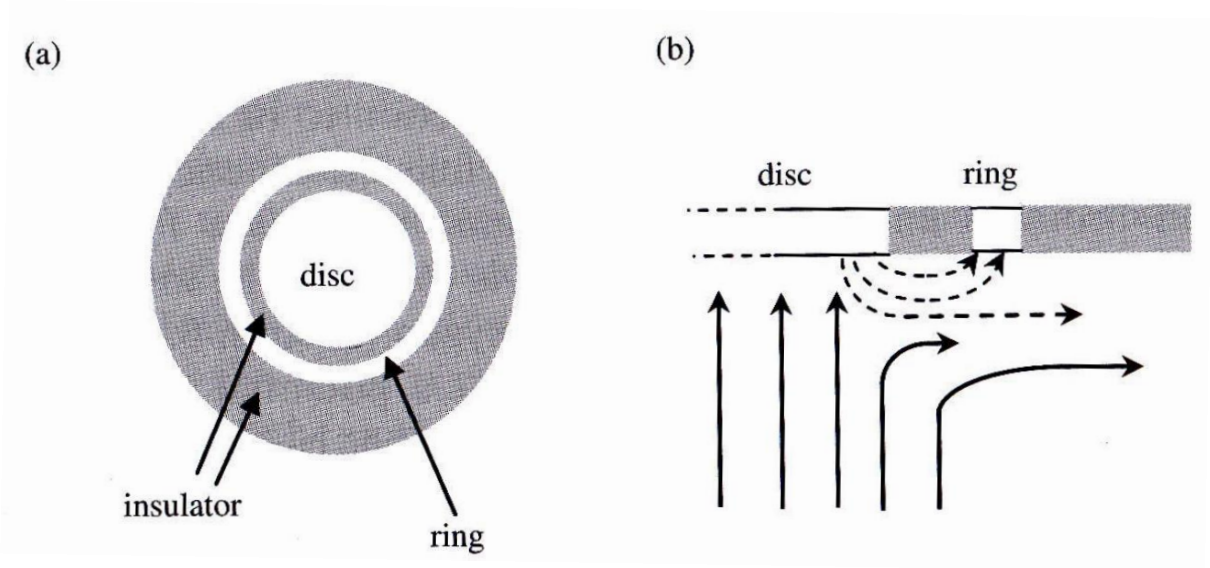

Figure 27. (a) View of the rotating disk electrode (RRDE) from below and (b) solution flow pattern at the RRDE. [50]

The laminar flow for the RRDE is the same as the RDE. The dashed arrows in figure 27 (b) show that reaction intermediates formed at the disk surface may be transported to the ring and react. Therefore RRDE enables a more detailed study of electrode reactions than RDE alone. Not all the reaction intermediate formed at the disk surface is detected at the ring though, as much is flung out into solution. This is accounted for by measuring the disk's collection efficiency, N, defined as the fraction of a completely stable species formed at the disk that is detected at the ring [50]. Collection efficiencies usually range from 20-40% and can be tested easily. As RRDEs can be made with a range of geometries, with different thicknesses of ring, disk and insulating layers, it is important to test each RRDE for its collection efficiency.

The potential at the disk and ring electrodes are controlled and manipulated separately. A common RRDE experimental design is to have the ring potential held and to perform CV at the disk. The potential of the ring is set so as not to react with the reactant in solution but only with a reaction intermediate. The RRDE is very commonly used in this way to analyse the oxygen reduction reaction. Hydrogen peroxide is an ORR reaction intermediate that can be detected at the disk electrode in the following way. A platinum polycrystalline (or single crystalline) disk electrode is used and is swept between 0 and 1V (vs. RHE) so as to monitor the reduction of oxygen. A polycrystalline platinum ring is used which is set at 1V or above. Any transient hydrogen peroxide formed at the disk is thrown out towards the ring electrode. The ring electrode is held ≥1V so that any H_2O_2 is instantly oxidised and is therefore measured at the ring as an oxidation current. Figure 28, below, shows a RRDE study of the oxygen

reduction reaction over Pt{111} in contact with acid electrolyte [85]. Hydrogen peroxide is commonly detected at the ring when the disk is at potentials corresponding to H_{UPD} (see next section), therefore a large ring current is usually observed at low potentials for the ORR [85, 86]. Hydrogen adsorption seems to decrease the number of sites which are available for breaking the O-O bond necessary for the four-electron reduction pathway [85]. Hydrogen peroxide is also produced in the ORR at potentials above H_{UPD} in alkaline electrolyte [86] and when halogen anions are present in acid electrolyte [87, 88].

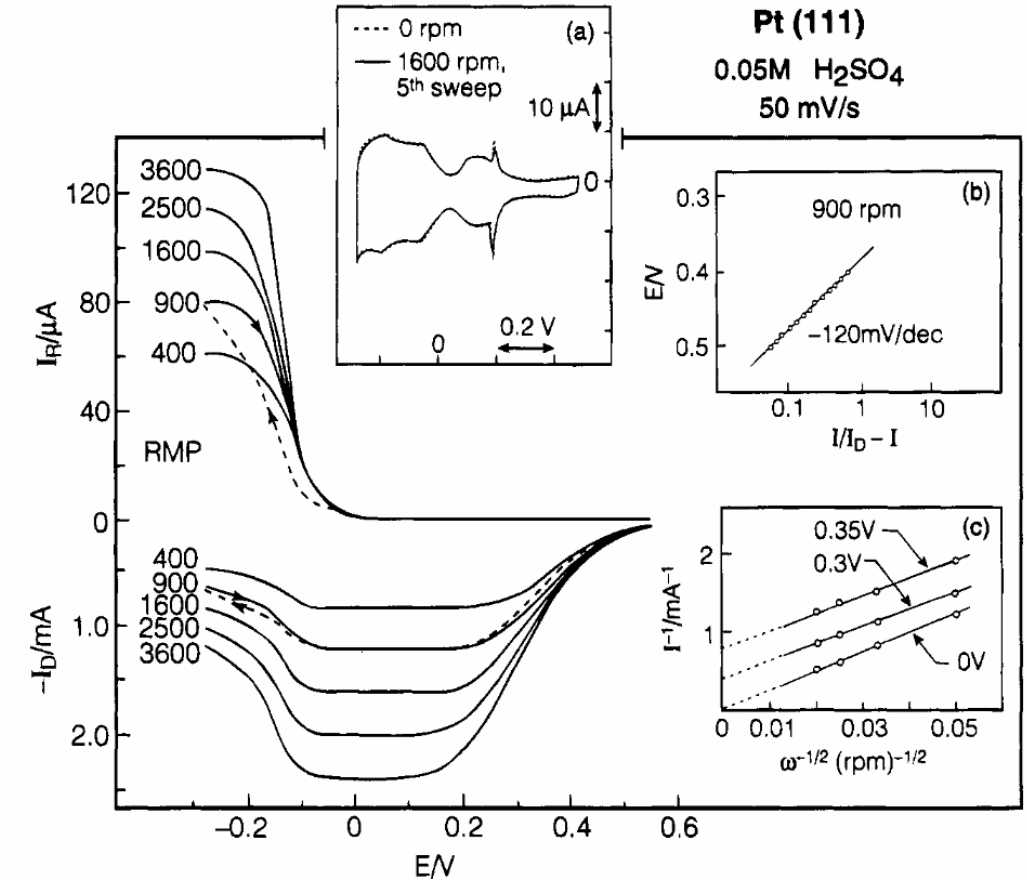

Figure 28. Disk (l_D) and ring (I_R) currents during oxygen reduction on Pt(111) in 0.05 M H_2SO_4 at a sweep rate of 50 mV/s (ring potential=0.95V): (-) positive-going sweeps; (- - -) negative-going sweep at 900 rpm. (a) Cyclic voltammetry of Pt(111) in the RRDE assembly in oxygen-free electrolyte with and without rotation. (b) Tafel plot at 900 rpm. (c) Levich plot at various electrode potentials. [85]

1.4.2 CV of Well-Defined Platinum Single Crystal Electrodes

It is important in all electrochemical studies that a "reproducible electrode surface" is used. What is meant by this is that the electrode must be prepared in such a way that the same surface is obtained every time. This is vitally important as electrode reactions may be catalysed by different sites to varying degrees; in the case of solid metal electrodes, terrace, step or kink sites. If the electrode is not reproducible or the sites not quantified, structure activity relationships and a true understanding of the electrode processes will be impossible to obtain.

Before studies on single crystal electrodes began, a method for the production of reproducible polycrystalline platinum electrode surfaces was created. This involved applying multiple voltammetric scans to the surface, between the onset of hydrogen evolution and oxygen evolution [89-91]. As a result, the reproducible CV of polycrystalline platinum was obtained in various acid electrolytes [89]. An example of a CV of polycrystalline platinum in 1M $HClO_4$ is shown in figure 29 below.

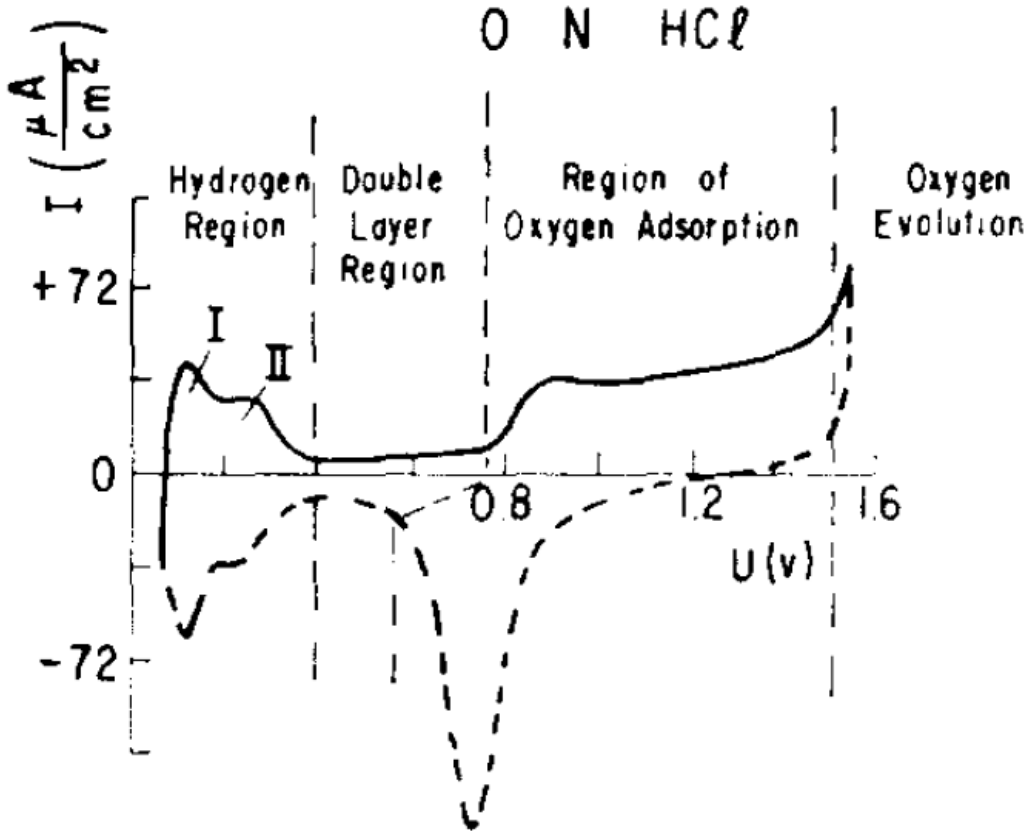

Figure 29. CV of polycrystalline platinum in 1M $HClO_4$ showing the various regions. Sweep rate 30mV/sec. Solid line – anodic sweep, dashed line – cathodic sweep. [89]

The multiple features observed at potentials between 0.4V vs. RHE and just higher than the potential of hydrogen evolution (the "hydrogen region") were generally understood as the adsorption-desorption of protons in solution. The reaction occurring being

$$H^+ + e^- \Leftrightarrow H_{ads} \quad (1)\ [89]$$

In most cases two peaks were observed in this potential range for hydrogen adsorption-desorption, depending on the electrolyte solution [89]. These were observed at two distinct potentials, implying that hydrogen binding occurred in a weak and strong mode, corresponding to the leftmost (0.12V vs. RHE) and rightmost (0.27V vs RHE) peaks respectively. In some studies a third peak at an intermediate potential of 0.22V was also observed [90, 92]. This whole area is also known as the hydrogen underpotential deposition, H_{UPD}, region, as it is the deposition of hydrogen at potentials "under" the E^0 for hydrogen evolution. The integrated charge for all the peaks in the H_{UPD} region was shown to be approximately 210μC/cm^2 and could be used to compare electrode surfaces with different areas and roughness [93].

The second region of note in figure 29 is the "double layer region". In this region only capacitive charging occurs and therefore is of little interest usually. The final potential range, between ~0.8V vs. RHE and the onset of oxygen evolution, was associated with platinum oxidation to form hydroxides/oxides [90]. In this range a relatively flat oxidation process was observed in the positive scan, although some peaks could be discerned [90]. In the negative scan, reduction of oxidised platinum takes place and appears as a single sharp reduction peak at lower potentials than the oxidation process. This platinum oxidation/reduction asymmetry (irreversibility) could be lowered if the upper potential limit was reduced [90, 94]. This led to the conclusion that easily reducible species such as OH are formed early in the oxidation. The process of Pt surface oxidation, although still not completely understood, can be expressed as the following [95]

$$Pt + H_2O \rightarrow PtOH + H^+ + e^- \quad 0.85\text{-}1.10\text{V} \quad (2)$$

$$PtOH \xrightarrow{Place\ Exchange} PtO + H^+ + e^- \quad 1.10\text{-}1.40\text{V} \quad (3)$$

$$PtO + H_2O \rightarrow PtO_2 + 2H^+ + 2e^- \quad >1.4\text{V} \quad (4)$$

The first attempt at making single crystal platinum electrodes for electrochemical analysis was performed by Fritz G. Will in 1964 [96]. To create the crystals high purity platinum (99.999%) was heated in an electron beam and orientated, cut to expose the required face, polished, then annealed in vacuum to approximately 800K and finally sealed into lime glass so that only the polished face was exposed. Exact details of the experimental Fritz used can be found here [96]. Despite the meticulous cleaning of electrolytes and exact preparation of electrodes, cycling of the electrodes between 50-1550mV vs. RHE (as above) had to be performed in order to obtain reproducible results. Through his procedure, the CV response of polycrystalline platinum was compared to the responses of prepared Pt{111}, {100} and {110} electrodes in sulphuric acid electrolyte. Although preparing these crystals still involved cycling them to high potentials, a procedure Fritz acknowledged may change the surfaces, features in the H_{UPD} region were identified. The two H_{UPD} peaks were observed to occur at the same potentials on the polycrystalline as the single crystalline surfaces, with the lower potential peak being largest for Pt{110} and the one at higher potentials being larger for Pt{100}. Through this work, the low potential H_{UPD} peak was correctly assigned to the presence of {110} sites on the surface of polycrystalline platinum and the higher peak to the presence of {100} sites.

A great advancement in the making of single crystal platinum electrodes was gained upon the advent of the flame annealing procedure, developed by J. Clavilier and R. Durand [97]. This procedure involved heating the prepared electrode to ~1600K in a gas oxygen flame, catalytically oxidising surface impurities, and quenching the crystal with ultra-pure water whilst still at a relatively high temperature. A droplet of ultra-pure water remained attached to the electrode surface upon removal, protecting it in transfer to the electrochemical cell. The CVs obtained from this procedure were markedly different to those obtained without the flame annealing procedure, especially in the case of Pt{111}, shown below. The CV response of Pt{111} obtained from Clavilier and Durand's annealing procedure is known to be the correct, characteristic response for a well ordered Pt{111} crystal with (1x1) surface atomic structure.

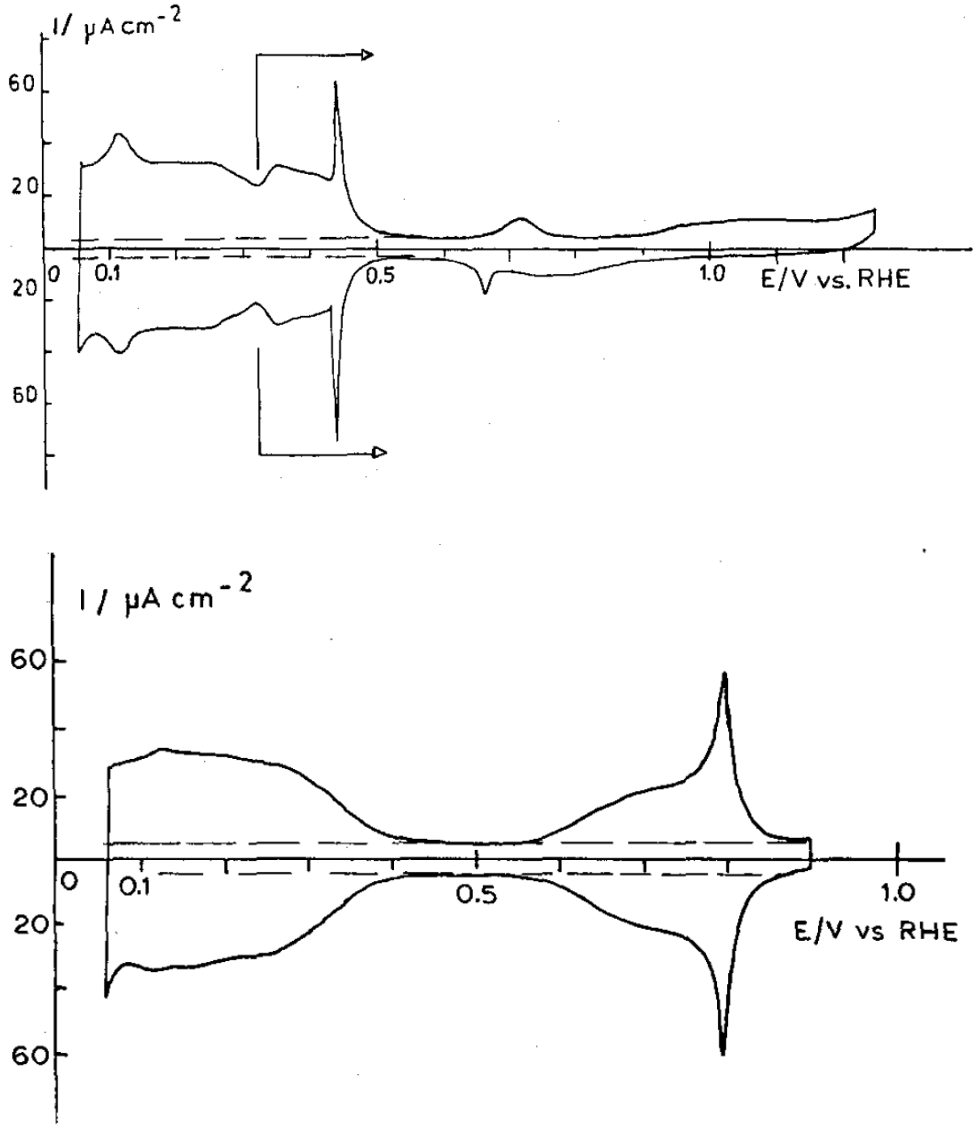

Figure 30. CV of Pt{111} single crystal electrodes prepared by the Clavilier and Durand flame annealing procedure. Above, 0.5 M H_2SO_4, below 0.1 M $HClO_4$; sweep rate 50mV s^{-1}. [97, 98]

There has been one small change in the flame annealing procedure since it was devised. In general, after flaming the crystal to remove impurities, it is now common that the crystal is transferred to cool in a particular gaseous atmosphere before quenching in ultra-pure water. This is because the cooling ambient is now known, after many studies [99-102], to be a determining factor in the arrangement of atoms in the surface atomic layer.

The accuracy and reproducibility of the flame annealing method has enabled the systematic study of many electrochemical reactions as a function of atomic arrangement: true structure-activity relationships are now able to be investigated. After a particular surface is made and flame annealed, CV is commonly performed and the response compared against the literature. If the response is that expected for the surface-electrolyte combination, the study may continue.

The ability of CV to distinguish between prepared platinum surfaces is shown in figure 31, where unique voltammetry is observed for every surface in the [Ptn(111)x(110)] series in sulphuric acid.

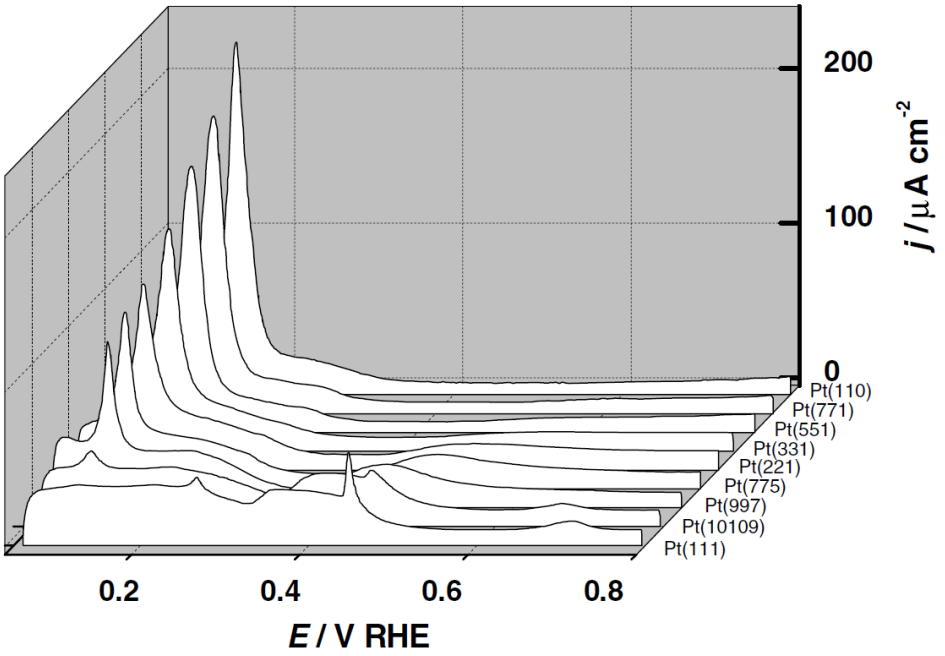

Figure 31. Voltammetric profiles of selected Pt(*hkl*) electrodes in 0.5M H_2SO_4. Scan rate: 50 mVs^{-1}. Only the positive scan is shown. [103]

As well as enabling a fundamental understanding of electrochemical reactions, the use of single crystals has enabled an understanding of nanoparticle catalysts [72, 104] and has led to ideas for their improvement [72, 105].

1.4.2.1 CV of Platinum Nanoparticles

The CV of platinum nanoparticles may be understood from the single crystal voltammetric responses mentioned in the previous section. Platinum nanocubes, for example, have (100) faces exposed, and exhibit voltammetry in common with Pt(100) and [Ptn(100)x(111)] single crystals, namely the sharp peak at 0.27V and the broader peak at ~0.35V (vs. RHE) for (111) steps and (100) terraces respectively (figure 33) [106]. Tetrahedrons/Octahedrons have (111) sites exposed and exhibit a response at 0.12V vs. RHE due to the (111)x(111) step, as is also seen on [Ptn(111)x(111)] single crystals [107]. It is also possible to observe sulphate adsorption on (111) terrace sites in the CV of tetrahedral/octahedral Pt nanoparticles [107]. Other shapes

of nanoparticles exhibit varying proportions of (111), (100) or (110) sites and therefore exhibit cyclic voltammetry that is just as characteristic as those observed for single crystals. A stereographic triangle, similar to one usually drawn for single crystals, may be made for nanoparticles bound by different crystal planes [72]. Figure 32 shows such a triangle.

Although voltammetry may be used to identify the relative proportions of the crystallographic faces exposed to the electrolyte, its weakness lies in that similar voltammetry may be seen for some nanoparticles that are actually quite different in shape or size. For example, all nano-cuboids are terminated by (100) faces. Therefore perfectly cube shaped nanoparticles and extended nano-cuboid nanoparticles would appear identical through CV. Therefore, it is common that other techniques such as transmission electron microscopy (TEM) are used in combination with CV.

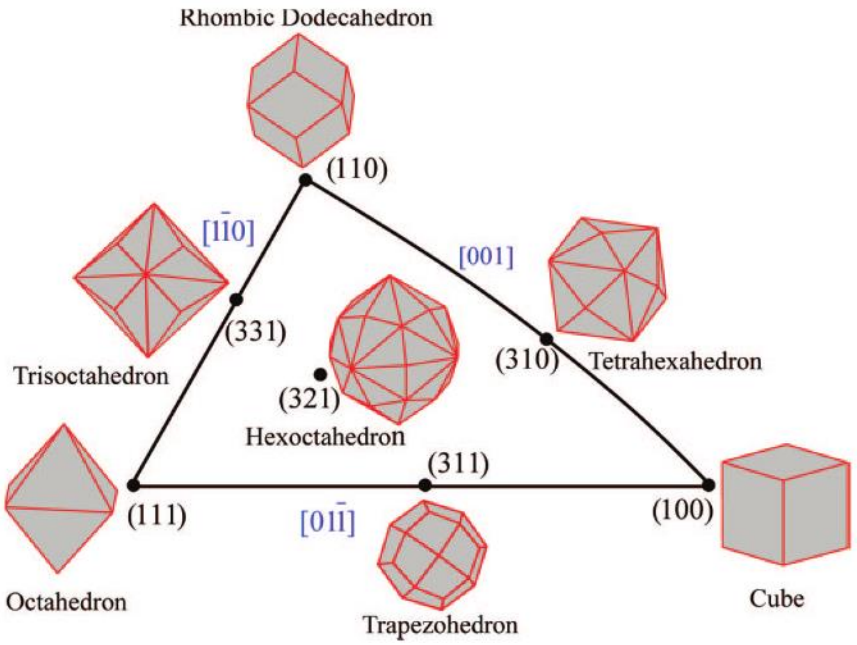

Figure 32. Unit Stereographic triangle of polyhedral nanocrystals bounded by different crystal planes. [72]

Platinum single crystals cannot be used to investigate changes in properties that may be observed as a result of dimensions on the nano-scale. Nevertheless, studies may utilise results obtained from single crystal experiments in order to create more active nanoparticle catalysts. In one study, it was shown that ammonia oxidation almost exclusively occurs on Pt{100} sites on single crystals [108], whereas Pt{111} and Pt{110} surfaces had virtually no activity. As a direct result of these findings it was shown in a subsequent study that nanoparticles with the

highest amount of (100) sites had the best activity for this reaction [106]. The CVs of the nanoparticles used in this study are shown in figure 33.

In the case of the ORR, Pt{111} has been shown to have higher activity than Pt{100} in perchloric acid [109] and lower activity in sulphuric acid [84] in single crystal studies. The same trends were found in Pt NPs, where (111) site rich NPs exhibited higher activity than those (100) rich in perchloric acid but had lower activity in sulphuric acid [107].

The collaboration of work on platinum single crystals with NPs is crucial, as it helps with the goal of creating highly active catalysts at low catalyst loading.

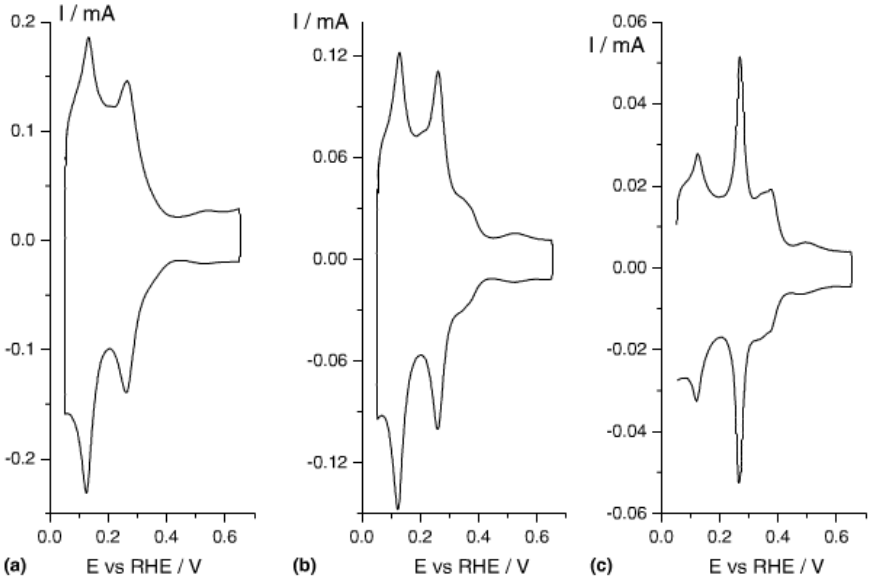

Figure 33. Voltammograms of platinum nanoparticles with increasing (100) site contribution from left to right. [106]

In trying to incorporate the highest amount of active sites into catalysts, the field of platinum nanoparticle and nanostructure synthesis has seen great development, especially in the last two decades. Synthesis methods are becoming ever more exact and sophisticated so that greater control can be achieved over the arrangement of atoms exposed to reactants. Although a review of these methods is outside the scope of this work, it is worth mentioning that an increasing range of exotic shapes and structures such as nano-frames [110], cages and rings [111] are now obtainable through directed nanoparticle synthesis.

1.5 Alloy Catalysts

The term bimetal commonly refers to a case where two different metals are joined but their atoms do not mix. This is in contrast to an alloy where there is mixture of the component metals' atoms. The term "bi-metallic alloy" is also commonly used to mean a binary alloy. Bi-metallic and alloy catalysts can exhibit many unique properties which are not present in either of the component metals, such as enhanced activity, selectivity, poison tolerance and stability. In an effort to understand and exploit the properties of these catalysts, there has been considerable work over the last decades in elucidating their structural, electronic and chemical properties.

There are two basic types of alloys, substitutional and interstitial, with different bulk distributions of component metals. Substitutional alloys exhibit substitution of the solute metal (also known as minority or secondary metal) atoms with the base (primary) metal atoms. This alloy type commonly occurs between metals with similarly sized atoms. Interstitial alloys usually occur when the solute metal atoms are smaller than the base metal. The solute metal atoms are then contained within the crystalline structure of the base metal, between its atoms. Of these two alloy types, only substitutional alloys shall be detailed here, as interstitial alloys were not used in this work.

Bi-metallic and alloy NP catalysts have been the focus of much research [29, 30, 112] in relation to PEMFCs as they offer high activity for oxygen reduction compared to Pt NPs (greater reduction currents are observed at a particular potential, half wave potential is pushed to positive values and, due to a lower platinum requirement, higher mass activities per weight platinum are observed over such catalysts). Some bi-metallic and alloy catalysts also have preferred properties for the anodic reaction, hydrogen oxidation. For example, high CO tolerance, which is found in hydrogen gas feeds and is a common catalyst poison, is observed by the use of certain alloys [113].

Alloys can exhibit surface properties that are different to that of the bulk. Firstly, a distinct surface vs. bulk geometry may be observed [114]. This could be by the contraction of atoms in the outermost layers, reconstruction of the surface, or by surface segregation of one metal [114-116]. The surface geometry of an alloy catalyst can have an effect on reactions due to the ensemble effect, i.e. "the rate at which an elementary reaction step proceeds on the surface of a given catalyst will depend on… the availability of specific atomic groupings that can provide

the number of surface atoms necessary for chemisorption, by acting as active sites (atomic ensemble effects)" [117]. Many factors control the surface geometry of alloys, the main driving force for its occurrence being to increase surface coordination and reduce surface free energy.

Due to the complex surface structure of alloy systems, their surface electronic properties may vary greatly compared to the monometallic case [30, 118]. Electronic structure in alloys may change due to charge transfer between elements in atomic ensembles [119]; known as the ligand effect [118]. This inevitably occurs in concert with strain effects, where there is a contraction of atomic spacing, leading to greater overlap of atomic orbitals (and vice versa) [120]. Surface electronic perturbation may be small for alloys which only exhibit a subtle difference in surface geometry but massive for alloys which exhibit 100% surface enrichment of one element or complete surface atomic rearrangement.

As heterogeneous catalysis is a surface phenomenon, a complete description of the first few atomic layers of an alloy catalyst as well as the bulk structure is needed to understand catalytic activity. Techniques such as low energy electron diffraction (LEED) [121], x-ray adsorption spectroscopy (XAS)/ultraviolet photoemission spectroscopy (UPS) [30] and surface x-ray scattering (SXS) [122] have been used to elucidate surface properties of many alloys. These techniques are often used in combination with density functional theory (DFT) [30, 123] in order to try to find so called "descriptors" for catalytic activity: i.e. fundamental properties which correlate with catalytic activity. For example, investigations into the oxygen reduction reaction have found that binding energies of the catalyst surface with reaction intermediates OH and O (ΔE_{OH} and ΔE_{O}) correlate well with activity[30, 124] and that this correlation holds well for both mono-metallic [124] and alloy catalysts [30]. ΔE_{OH} and ΔE_{O} are controlled by the *d*-band centre of the metal/alloy [30] and therefore this is a descriptor for ORR activity according to the Sabatier principal: optimum intermediate binding (controlled by the *d*-band centre) is required so that the reaction is neither poisoned by strongly binding intermediates nor forms intermediates that are too weakly bound to continue to react. Knowledge about descriptors can be used to design catalysts that have ideal properties for catalysis, as factors such as *d*-band position can be controlled by alloy catalyst synthesis methods by exploiting the ligand effect and surface segregation.

1.5.1 Surface Segregation in Pt Based Binary Alloys and its Effect on Oxygen Reduction

The surface segregation of platinum based binary alloys, especially PtNi alloys, and its effect on catalysis is well studied [30, 116, 121, 122, 125, 126]. In 1985, through the use of LEED, Gaultier *et. al.* first found that surface enrichment of platinum atoms in the topmost layer relative to the bulk Pt concentration was present in PtNi alloys with a range of compositions [116, 126]. The $PtNi_9${111} alloy was found to exhibit surface segregation of platinum so that the top most atomic layer contained 30% (3 times the bulk concentration) platinum [121]. A 1:1 PtNi{111} alloy was found to exhibit 88 atomic % platinum [125] in the first layer and the Pt_3Ni{111} alloy exhibited a pure platinum (99% +/- 1%) top-most layer [126]. In all cases a compositional oscillation was observed with surface depth: the second layer being deprived of platinum relative to the bulk and (for PtNi and Pt_3Ni) the third layer being platinum rich. This oscillatory behaviour was found to dampen with depth until the bulk alloy atomic composition was reached. This platinum enrichment, along with oscillatory behaviour, was also observed the {100} PtNi alloy surfaces. The {110} alloys exhibited an inverse behaviour in the surface composition, strong Ni enrichment. The surface composition profiles of the base pane PtNi alloys obtained by Gauthier and Baudoing are shown in the figure below. Studies have shown that other platinum alloys, such as Pt_3Fe{111} and Pt_3Co{111} [30], also exhibit a pure platinum outermost layer with a platinum-depleted second layer.

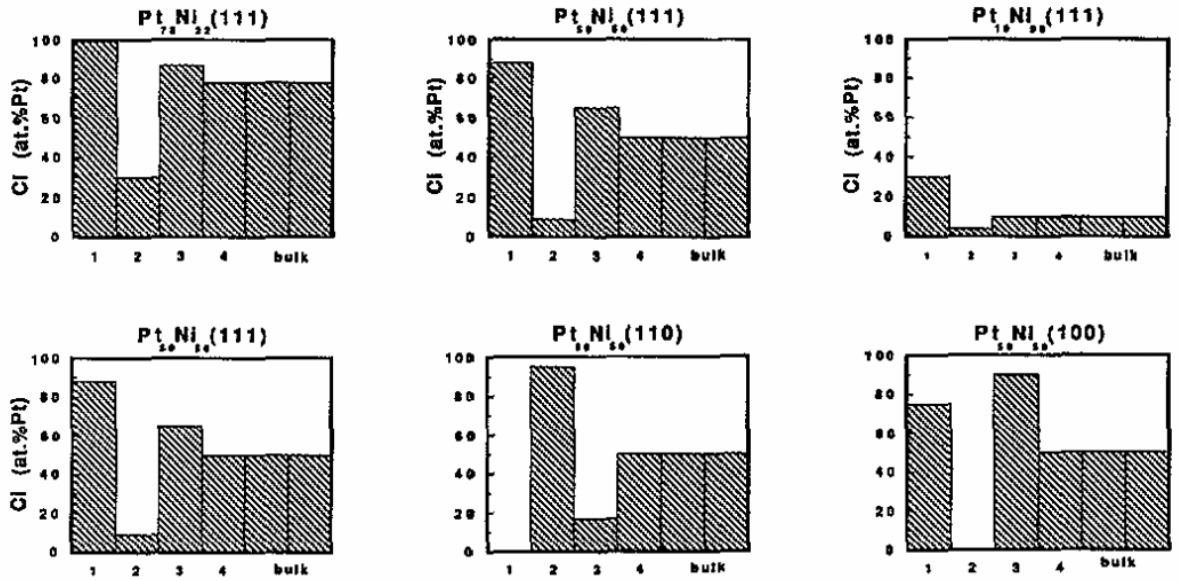

Figure 34. Summary of the results obtained by LEED surface crystallographic studies on platinum-nickel fcc random substitutional alloys. (Gauthier and Baudoing 1990) [116]

It has been shown that by depositing Ni on Pt{111} at 300K, a Ni-Pt-Pt{111} monolayer structure forms [127]. Carrying out the deposition procedure at 600K results in the formation of a Pt-Ni-Pt{111} sandwich structure [128], with nickel only being present in the second atomic layer. In this case the nickel has moved from top to second layer and illustrates the driving force of the above alloys to form a Pt enriched top layer followed by a Ni enriched second layer. Theoretical and experimental studies have shown that exposure of these types of structures to hydrogen or oxygen can influence surface composition. Hydrogen exposure favours the Pt-3d-Pt{111} sandwich structure whereas oxygen favours the 3d-Pt-Pt{111} surface [112, 129, 130].

Surface hydrogen, OH or oxide can also be formed electrochemically and therefore the surface segregation profile could change with potential. The surface composition of the top-layer-Pt-enriched Pt_3Ni{111} system has been analysed during CV. The surface alloy structure and segregation profile was found to be stable between 0.05-1V (vs RHE), with only a contraction of the surface Pt layer upon adsorption of oxygenated species at high potentials [122].

In the last 15 years, interest in the effect of surface segregation in electrocatalysis has increased, as PtM alloys (where for example M=Fe, Co or Ni) have increased activity when compared to pure platinum for the oxygen reduction reaction [30]. Markovic *et. al.* first found that Pt_3Ni and Pt_3Co alloy catalysts had increased activity for oxygen reduction when they were prepared in such a way as to form a pure platinum top-layer, which he called a “Pt-skin” [131, 132]. Catalysts with a surface layer composition matching the bulk alloy composition were prepared by argon ion etching of a bulk alloy and were found to have higher activity than polycrystalline platinum, but not as high as the Pt-skin surfaces. The Pt-skin catalysts were prepared by annealing the etched alloy. This was the first time that an electrocatalyst’s high activity for the ORR could be associated with a segregation effect. [131]

The high activity of the Pt-skin surface was associated with weaker Pt-OH_{ads} interaction on the electronically modified monoatomic layer of Pt atoms [132] according to the ligand effect. Pt-OH_{ads} was assumed to be a site blocking species (θ_{ad}) which lowered the reaction kinetics according to the equation;

$$j = nFKc_{O_2}(1-\theta_{ad})^{x}\exp\left(-\frac{\beta FE}{RT}\right)\exp\left(-\frac{\mathrm{g}\Delta G_{ad}}{\mathrm{RT}}\right) \qquad (1)\ [122]$$

CV of the Pt-skin catalysts showed that at high potentials their coverage of OH was lower than over pure platinum[132]. Also it showed that the potential onset of OH formation was higher for the Pt-skin surfaces. This is illustrated in the voltammetry below (figure 35) by the blue arrow.

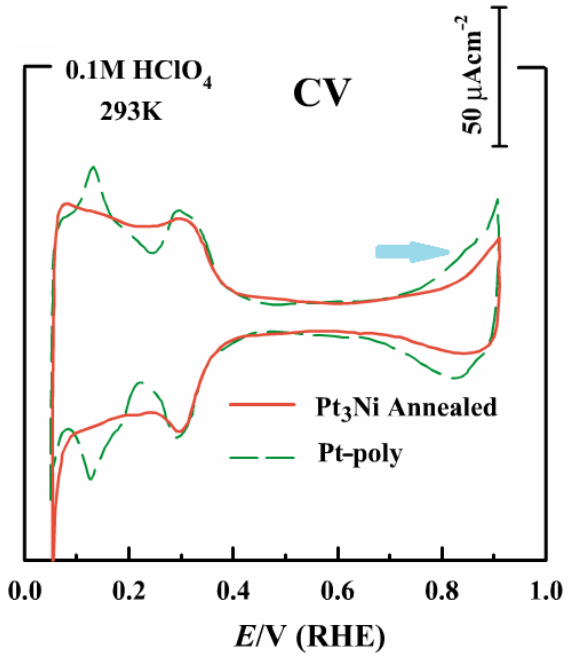

Figure 35. Cyclic voltammetry of annealed Pt_3Ni, 'Pt-skin', surface vs. polycrystalline Pt at 293 K. The blue arrow highlights the shift in OH adsorption. Adapted from [132]

A later study by Markovic *et. al.* on Pt-skin Pt_3Ni single crystal electrodes found that the weaker interaction with OH for these surfaces is attributed to a downshifted *d*-band centre relative to the same single crystal pure platinum electrodes [122]. Other studies have found that many alloys of platinum exhibit this skin structure and that the *d*-band centre is tuneable by the choice of alloying metal [30]. Figure 36, below, shows the electronic effect of alloying platinum with metals such as Ni, Co, Fe, V and Ti and also the activity enhancements possible for the ORR. A negative shift in d-band centre compared to polycrystalline platinum of approximately 0.3eV corresponded in this study to the top of the volcano curve of activity. It is unclear how close to the top of the volcano curve current state of the art catalysts are. Studies on alloys of platinum with early transition metals such as Y or Sc have shown even higher ORR activity than platinum-late transition metal alloys [123, 133]. These results indicate that the optimum *d*-band centre shift is closer to 0.2eV [133]. It is also unclear how much activity increase is possible through focussing solely on the *d*-band centre property of alloy catalysts.

The surface segregation effects described so far have been found not only to occur in UHV-prepared extended alloy surfaces, but also in alloy nanoparticles. As such, the synthesis of stable, active Pt-skin nano-structures which have low Pt usage (and hence low cost) for the oxygen reduction reaction has been the focus of recent work.

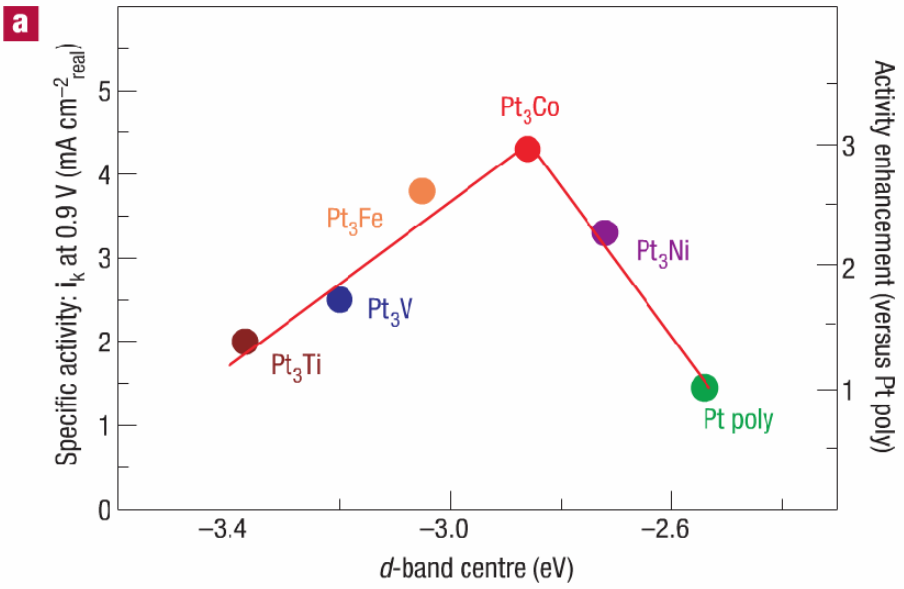

Figure 36. Relationship between experimentally measured specific activity for the ORR on Pt_3M surfaces in 0.1 M $HClO_4$ at 333K versus the d-band centre position for the Pt-skin surfaces. [30]

1.5.2 Preparing Surface Alloys

The selvedge region (the few atomic layers below the metal surface that are affected by the presence of the surface) of an alloy may be investigated by the use of bulk alloys or by the use of surface alloys. Surface alloys are those present in either the first or first few atomic layers of an otherwise singular metal. Whereas bulk alloy surfaces are prepared by cutting and polishing a bulk single crystal alloy, surface alloys are prepared by the deposition of one metal, the solute, onto another, the primary metal. After deposition of the solute metal, some alloying may occur spontaneously through diffusion at room temperature, but usually an annealing step at a particular temperature is required for the surface alloy to form. The simplified process of deposited metal film to multilayer surface alloy transformation is depicted in the illustration below. By taking the multi or single layer surface alloy that is formed to a temperature higher than that used for annealing, the solute atoms can diffuse into the bulk of the base metal due to

the entropic driving force for this process, forming a dilute bulk alloy (process illustrated below) [116]. If the base metal sink is large enough, then diffusion of the solute atoms from the surface alloy into the bulk metal forms a bulk alloy so dilute as to essentially become monometallic in its properties. [116]

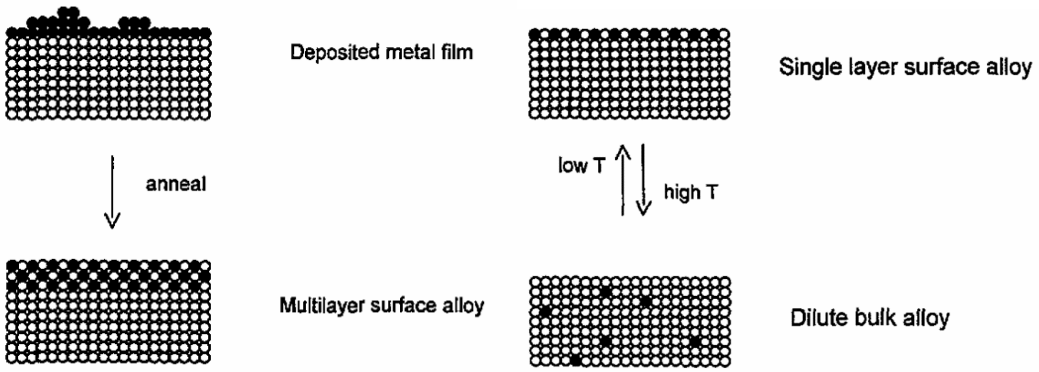

Figure 37. Schematic illustration of the mechanism of formation of multilayer surface alloys, left. At high temperatures entropic effects may favour the formation of a dilute bulk alloy, right. [116]

Sandwich surface structures can also be formed by alternative deposition: a secondary metal is deposited onto a bulk metal substrate and then another layer of atoms is deposited on top of this layer. To form a real sandwich structure the second metal deposition has the same identity as the bulk metal. Using the techniques here a wide variety of near-surface compositions may be created and their properties and catalytic activity analysed. For the first step (deposition of the metal film), a number of methods may be used. High quality deposition may be performed by chemical vapour deposition (CVD) under UHV conditions, forced deposition, electrochemical deposition, or other methods such as spontaneous deposition. CVD involves the transport of a volatile precursor (a molecule containing the target metal with supporting ligands) to the substrate surface [134]. Through absorption and reaction at the surface, the metal becomes free of its supporting ligands and may then go on to form a stable nucleus for metal growth on the surface [134]. The process is illustrated below.

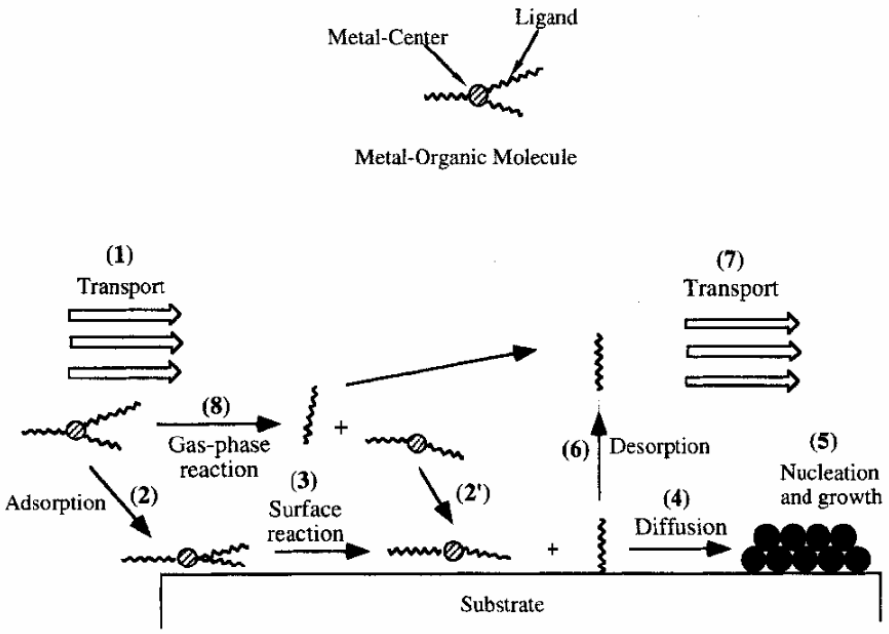

Figure 38. Key steps involved in chemical vapour deposition [134].

Spontaneous deposition occurs by immersion of a clean metal surface into a metal cation-containing solution, producing an ad-layer which is strongly bound without the application of an external potential [135]. Forced deposition occurs by a similar method, but instead of anions being reduced and adsorbed spontaneously, a reducing chemical species is required to react with the metal ions, for example hydrogen gas. Electrochemical deposition uses an external potential, which is applied to the metal surface to reduce the cations in solution. A potential must be applied that is thermodynamically sufficient to reduce the solution species, although in some cases metal adsorption may occur below the anion's reduction potential (a phenomenon known as underpotential deposition, UPD). The reduced metal ions then become adsorbed. An example of electrochemical deposition of palladium layers on Pt{111} [136] is shown below, performed by the reduction of PdO by cyclic voltammetry. For this ad-layer/support system, cyclic voltammetry can be used to deduce the sub-monolayer coverage of palladium and also to determine when exact mono-layer growth has been reached. A single sharp peak is observed at low potentials for sub-monolayer coverages and a second peak only appears upon the start of multilayer growth.

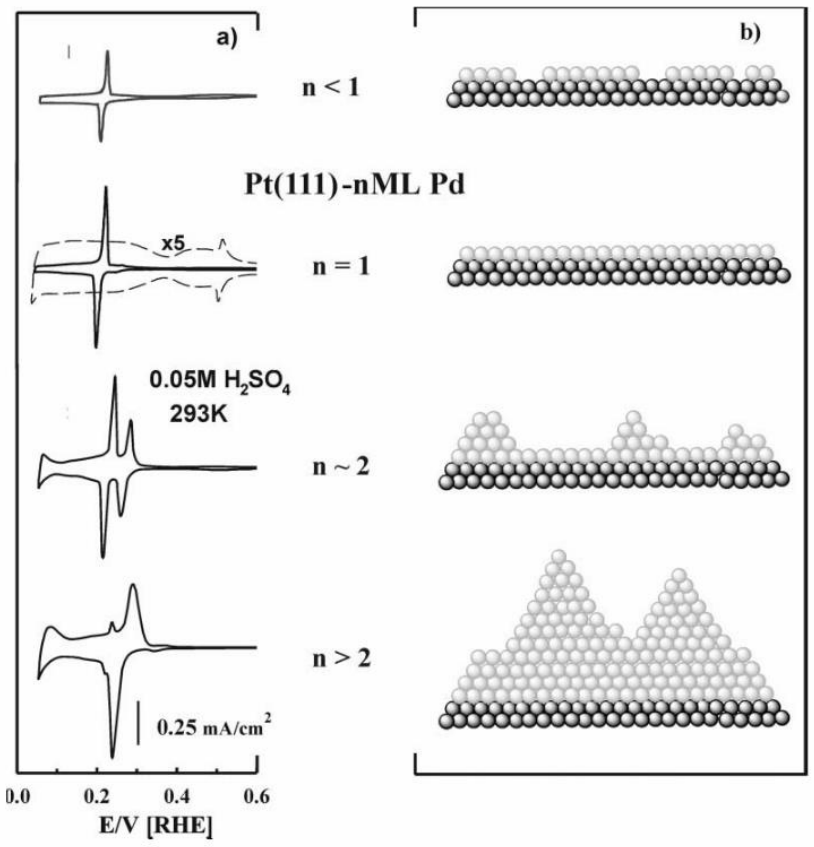

Figure 39. (a) CVs of a Pt{111}surface at different coverage levels of palladium depicted in (b). [136]

The annealing stage in surface alloy formation (figure 39) can be performed by heating the over-layer in UHV or in the presence of low gas pressures. Recently a method has been developed which enables this step to be carried out at room temperature, at ambient pressure, with simple apparatus and great control over temperature [137-139]. This is the resistive heating procedure, also known as induction heating. An example of the resistive heating apparatus is shown in figure 40.

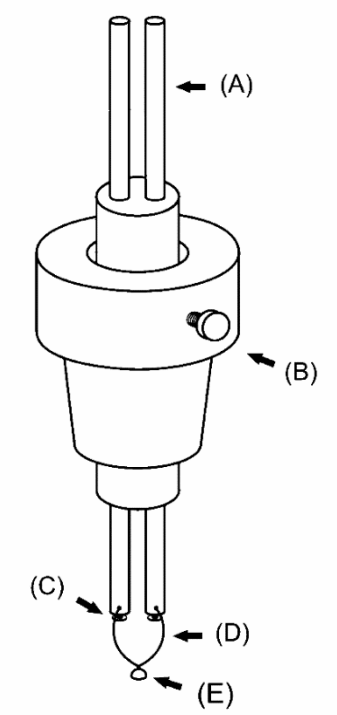

Figure 40. Diagram of the holder used to resistively heat the single crystal electrode. (A) steel rods for electrical contact with the crystal, (B) Teflon screw and holder to vary length of crystal above electrolyte, (C) steel screws to secure the Pt wires, (D) Pt wire for making contact with the crystal and to complete the electrical circuit, (E) single crystal. [137]

The single crystal electrode is attached at point (E) in the diagram above and the electrodes are attached at point (A). High currents are driven through the crystal and resistance between the single crystal and the contacting Pt wire causes the crystal to heat up. The temperature reached at the single crystal can be controlled by the current. The resistive heating apparatus can be placed in the electrochemical cell with an atmosphere that can be controlled by different gas feeds.

This piece of apparatus was first used by our research group in order to prepare Ru overlayers on [Ptn{111}x{100}] and [Ptn{100}x{111}] surfaces [137]. Chorkendorff *et. al.* have since used this type of apparatus to create near-surface alloys of platinum-copper and investigated the oxygen reduction reaction as a function of surface composition [140]. In this thesis, surface alloys of platinum created using this resistive heating apparatus, and their oxygen reduction activities are discussed.

1.6 Ex-Situ Techniques

Electrochemical techniques can be used to gain a great amount of information about the activity of oxygen reduction catalysts but do not give information about the condition of the electrode surface. Much greater insight into catalysts may be gained by using electrochemistry in combination with in-situ and ex-situ spectroscopic and imaging techniques. In-situ techniques (also known as operando techniques as operando is latin for working) are those that are implemented during the operation of a catalyst. Such techniques are difficult to perform in comparison to ex-situ techniques (where the catalyst is analysed before or after use, not under working conditions) due to the need to interface the analytic technique with the reaction vessel. In this thesis, X-ray photoelectron spectroscopy (XPS) and scanning tunnelling microscopy (STM) were used ex-situ for the study of bimetallic surfaces.

1.6.1 X-ray Photoelectron Spectroscopy (XPS)

X-ray photoelectron spectroscopy (XPS) is a quantitative technique that analyses surface atomic composition as well as the surface's chemical and electronic state. The technique is carried out by targeting a focussed monochromatic beam of x-rays (e.g. Al K_α x-rays, wavelength 8.3386nm, photon energy 1486.7eV) onto the sample and measuring the kinetic energy of electrons that are ejected from the atoms in the surface layer (<10nm). It is carried out under a minimum of a high vacuum (pressure $<10^{-8}$ Torr) so that the x-ray photons and ejected electrons have minimal interaction with atoms or molecules on their path through the apparatus. [141] A pressure of 10^{-9} Torr was used in the XPS experiments carried out in this work.

The kinetic energy of an ejected electron is unique to the element that it came from, as every element has electrons with their own binding energy. It is common in XPS experiments to consider electrons ejected from the innermost orbitals, i.e. 1s, 2s and 2p, as these are least affected by the chemical environment of the atom and therefore can reliably identify the element. Nevertheless the technique is not limited to inner electrons; outer orbitals may be examined also. For example, it is common to use electrons ejected from the 4f shell of platinum at 70.9eV (Pt $4f_{7/2}$ peak) to identify this element.

Figure 41, below, illustrates the process of photoemission that occurs in XPS. In this schematic, photoemission of a Ni $2p_{3/2}$ electron from a nickel atom is shown. The Ni $2p_{3/2}$ electron adsorbs energy from the x-ray photon, which has more than enough energy to eject the electron from the atom. The excess energy becomes the kinetic energy of the ejected electron as it travels through the vacuum and it is directed towards the detector in a controlled electrostatic field. The electron is then detected and its kinetic energy recorded. The photon energy (hv) is known, the kinetic energy of the electron (E_k) has been measured and therefore the electron's binding energy (E_B) must be deduced. This is done by subtracting E_k from hv according to equation (1).

$$E_B = hv - E_k - \phi \qquad (1)\ [141]$$

Where ϕ is an experimental constant (the spectrometer's work function, i.e. the energy lost from the electron as it is detected), which is a few eV. [141]

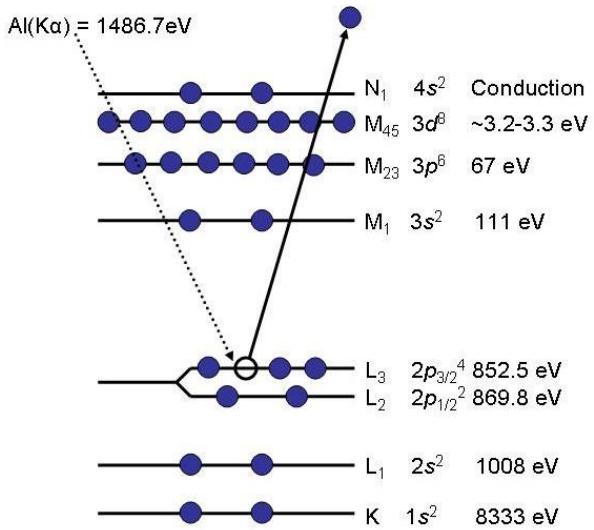

Figure 41. Schematic of the photoemission of a Ni $2p_{3/2}$ electron from a nickel atom. [141]

Figure 41 shows that E_B values can range from a couple of eV for weakly bound electrons in the outer-most orbitals, to many keV for strongly bound electrons in the L or K levels.

Figure 42 shows a typical wide (survey) scan XPS spectrum of metallic silver (Ag^0). Although the electron's kinetic energy is detected, the calculated binding energy is displayed on the x axis. The number of electrons is shown on the y axis. Therefore XPS can be used to detect the number of each element type present in the surface of the sample.

In the process of XPS, electrons may also be ejected via Auger emission. This occurs when the exited atom, with its electron hole, undergoes one or a series of internal relaxation steps before releasing a secondary electron with lower energy than the original photo-emitted electron. An atom with a core electron hole formed by photoemission is unstable and an electron from an outer orbital may fall into this hole. The energy released by this transition can be transferred to a secondary electron, ejecting it from the atom if the energy is bigger than the secondary electron's binding energy [142]. Due to the internal relaxation events, the kinetic energy of this secondary ejected electron is low and will therefore appear to have high binding energy in an XPS spectrum due to the application of equation (1) to all electrons detected. The kinetic energy of an Auger electron is calculated from difference between the core level energy and the total of the energies of the electrons that are involved in the relaxation process. Electrons ejected via these processes are investigated via Auger electron spectroscopy (AES) and will not be discussed further. Peaks for Auger emission in Ag^0 are shown in figure 42 at >1120eV binding energy.

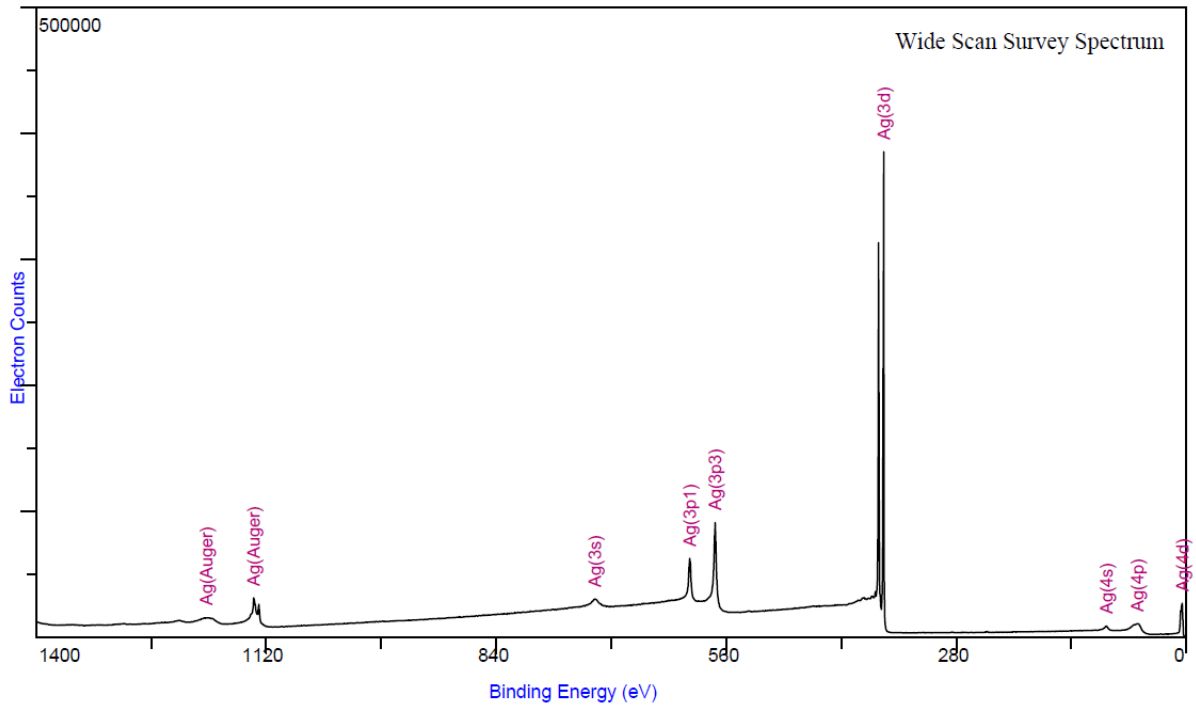

Figure 42. Survey XPS spectrum of metallic silver, Ag^0. Pass energy of analyser = 150eV, x-ray beam size = 250 x1500 μ ellipse, step size = 0.1eV/step (i.e. 0.1 eV/data point), operating pressure = 1.6 x 10^{-9} torr. [143]

Information on the surface's oxidation state may be gained by looking in detail at the area of the XPS spectrum around each peak. For example figure 43(a), below, shows the Ni $2p_{3/2}$ and $2p_{1/2}$ region of a Ni metal surface that is covered by a thin NiO film. The largest peaks, at

852.6eV and 870eV, are the Ni $2p_{3/2}$ and $2p_{1/2}$ photoemissions respectively for metallic nickel [144]. There are smaller peaks at higher binding energy, which, when metallic spectral components are removed, can be seen more clearly (figure 43(b)). These occur between 855eV and 865eV for Ni $2p_{3/2}$ and between 872eV and 885eV for Ni $2p_{1/2}$ and were assigned to the presence of Ni^{2+} in the form of NiO [144]. Metals with higher oxidation state exhibit a positive shift in the binding energy peaks compared to the metallic form due to the higher positive charge on the atom, which holds the electrons more strongly.

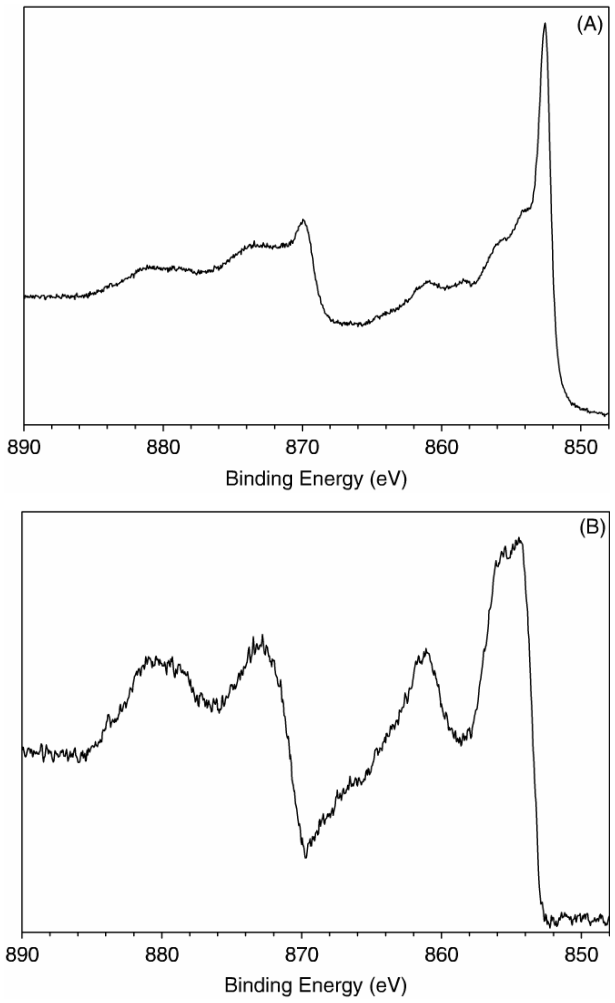

Figure 43. Ni 2p spectra from (A) Ni metal surface covered by a thin NiO film: (B) after subtraction of the metal spectral components. [144]

XPS may also be carried out as a function of depth in order to elucidate the selvedge composition of a sample. In the case of the work reported in this thesis, this has been done by a process where high energy Ar^+ ions are fired at the sample to "sputter" away the surface atoms in a controlled manner. XPS spectra are obtained between sputtering steps and a depth profile is obtained.

1.6.2 Scanning Tunnelling Microscopy (STM)

Scanning tunnelling microscopy (STM) is an atomic imaging technique invented in 1982 by IBM scientists Gert Binnig and Heinrich Rohrer [52, 145, 146]. The scanning tunnelling microscope has evolved to serve other purposes, for example to probe local electronic structure, manipulate atoms and molecules, and monitor chemical reactions occurring at singular particles or molecules, as well as many others. A schematic of the STM apparatus is shown below.

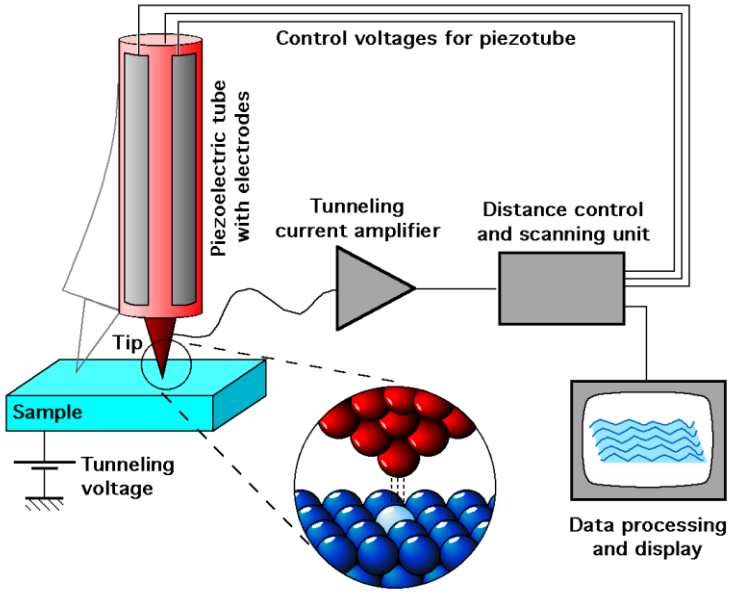

Figure 44. Basic schematic for a scanning tunnelling microscope.
http://commons.wikimedia.org/wiki/File:ScanningTunnelingMicroscope_schematic.png

A single sharp tip is brought towards the surface of a sample under investigation whilst a potential difference, controlled by a bipotentiostat, is applied between the sample and tip. The sharpness of the tip determines the ultimate resolution of the STM image and atomic resolution is only possible with an atomically sharp tip. (Forming such a tip is not an experimentally difficult process. For example simply cutting a platinum wire with wire cutters may suffice. Another method involves electrochemically etching a tungsten wire in sodium hydroxide solution.)

Initially, coarse control of the tip brings it within a few nanometres of the sample, where quantum tunnelling may occur. At this point the tip is said to have “engaged” the sample. The

process of quantum tunnelling is depicted in figure 45. Here the barrier for traditional electron transfer is given by eV_b and is the difference between the higher of the two Fermi levels and the vacuum level electron energy, i.e the work function. Quantum tunnelling is where electron transfer can occur across the "free space", d_b, between the sample and tip, rather than surmounting this activation energy barrier for electron transfer. This occurs due to overlapping of the sample and tip's atomic orbitals at short distances and the electron is said to "tunnel" the barrier [52].

The direction of current flow in STM depends on the potential bias applied, if the tip is held at a positive potential relative to the sample, then current flows from the sample to the tip. Current flows the opposite way (tip to sample) if the tip is held negative relative to the sample. Quantum tunnelling is a very short range effect and decays exponentially with distance. Therefore tunnelling current can give very accurate information on the tip-sample distance.

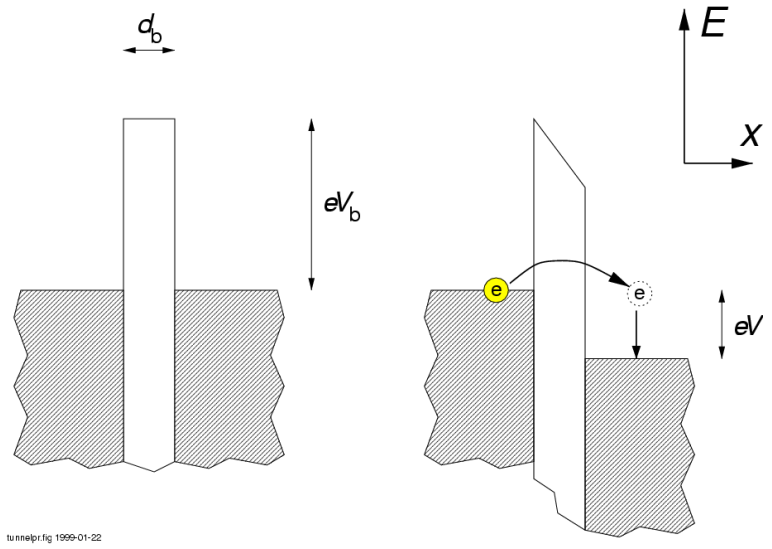

Figure 45. Schematic representation of an electron (e, right) tunnelling through a barrier of "height" (vertical dimension is energy) eV_b and thickness (horizontal dimension is spatial) d_b. e is the elementary charge, -1.6×10^{-19} C, V is the bias voltage leading to a current flowing between the right and the left "electrode" (side of the barrier). http://commons.wikimedia.org/wiki/File:TyTunnelling.png

The tunnelling current (I) is described by the following equation.

$$I = Ce^{(-W\sqrt{\phi})} \qquad (1)[52]$$

Here, C is a constant, W the sample to tip distance and ϕ the work function of the sample. This equation shows that different metals will have different tunnelling currents at the same sample-tip distance due to their unique work function values. This is important in STM as an increase

in tunnelling current may be caused by either encountering a metal in the sample with a lower work function or by a protrusion of atoms on the surface, shortening the tip-sample distance. In STM, the quantum tunnelling effect is exploited in order to gain topographical information on the sample surface by scanning the tip parallel across the sample.

One method of gaining topographical information is by carrying it out in constant current mode. In this mode, as the tip is scanned parallel to the sample surface, its height is free to move perpendicular to the surface (in the z axis) so that a chosen tunnelling current is maintained (see figure 46, left). In this mode, the tip will withdraw from the surface when approaching higher topography and extend towards the surface upon approaching lower topography. An image obtained from STM in constant current mode is that of height vs the x and y axis position.

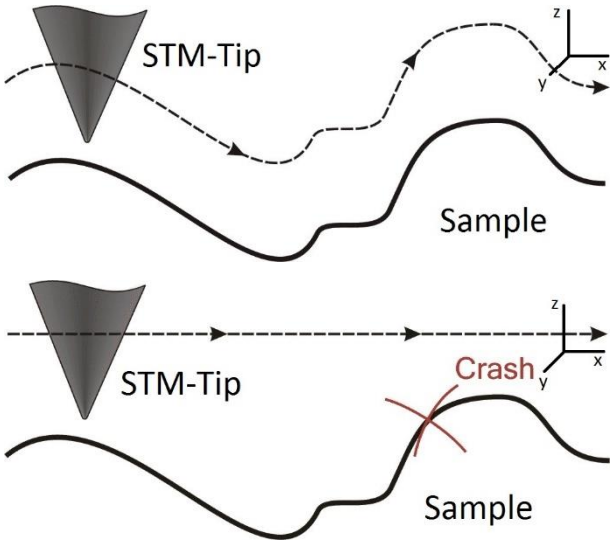

Figure 46. Comparative schematic of constant current, left, vs. constant height, right, STM. The risk of crashing the STM tip in constant height mode is shown in red. Adapted from images. http://commons.wikimedia.org/wiki/File:Constant_current.jpg

The shape of the tip formed via the methods described previously has an effect on the topography perceived whilst scanning. Figure 47, shows how the sample may be perceived to have three different topographies when T-shaped (red), V-shaped (green) and U-shaped (blue) tips are scanned across the surface in constant current mode.

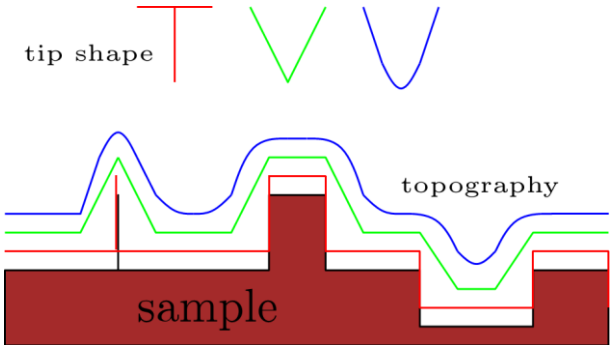

Figure 47. Illustrative description of the effect of tip shape on the perceived topography of a sample surface according to STM. http://commons.wikimedia.org/wiki/File:Tipsample.png

The second main mode of STM operation is known as constant height mode. In this mode the position of the tip is locked in the z axis and scanned across the surface (see right, figure 46, right). The increase or decrease in tunnelling current caused by the different sample-tip distance is measured and the readout is of tunnelling current vs the x and y axis position. As the height of the tip is locked, there is no feedback between the tunnelling current and tip position and therefore fast rastering of the tip across the surface is possible. In this mode there is a risk of the tip crashing into the sample upon approaching higher topography, causing damage to the tip and/or the sample.

To gain accurate information on the topography of the sample, the absolute position of the tip must be controlled finely and, for constant current mode, there must be feedback between the tip position and the tunnelling current. This is done by mounting the tip in a piezoelectric scanner; a device which utilizes a material which expands or contracts when a voltage is applied across it, enabling manipulation of the tip's position on the angstrom scale in the x, y and z axis. In combination with the piezoelectric scanner, a current amplifier is used so that the minute quantum tunnelling current is magnified to a usable level. The amplified current is measured and interpreted by a computer, which then changes the voltages for the x, y and z components of the piezoelectric scanner. This is the basis of the current feedback loop in STM.

The above description covers the five basic components of a STM; the metal tip, bipotentiostat, piezoelectric scanner, current amplifier and the hardware/software controlled current feedback loop.

1.7 Objectives of the Current Investigation

The general objective of this investigation is to elucidate the effect that surface species such as OH_{ads}, O_{ads} and the interfacial water layer have on the oxygen reduction reaction activity of active catalysts in perchloric acid electrolyte. To that end, these are the investigations that shall be carried out:

- CV and ORR of [Ptn{111}x{100}] and [Pt{100}x{111}] surfaces. These surfaces exhibit OH_{ads}/O_{ads} formation at terrace and step sites in the potential range relevant to loss in ORR activity.
- Hydrogen peroxide oxidation/reduction reaction activity of [Ptn{111}x{100}] and [Pt{100}x{111}] surfaces. Hydrogen peroxide is an ORR intermediate which exhibits a switch-over from reduction to oxidation in the potential range relative to oxygen reduction and OH_{ads}/O_{ads} processes.
- CV and ORR of kinked surfaces which have previously not been studied. These exhibit low coordination sites with potential high activity and unique OH_{ads}/O_{ads} features.
- CV and ORR of alloys of platinum with other transition metals, to investigate OH_{ads} binding strength and surface site availability on alloys with different electronic structure. These shall be created via the resistive heating procedure.
- XPS and STM of the previously created alloys in order to gain surface structural, compositional and electronic information which may aid in interpreting ORR and CV trends.
- CV and ORR studies of the most active basal platinum surface, Pt{110}, with an aim to create and analyse the 1x1 unreconstructed surface.

1.8 References

[1] J.E. Cohen, Science, 302 (2003) 1172-1175.
[2] S. Dalby, Geography Compass, 1 (2007) 103-118.
[3] S.A. Marcott, J.D. Shakun, P.U. Clarke, A.C. Mix, Science, 339 (2013) 1198-1201.
[4] S.F.B. Tett, P.A. Stott, M.R. Allen, W.J. Ingram, J.F.B. Mitchell, Nature, 399 (1999) 569-572.
[5] J.E. Harries, H.E. Brindley, P.J. Sagoo, R.J. Bantges, Nature, 410 (2001) 355-357.
[6] D. Lüthi, M.L. Floch, B. Bereiter, T. Blunier, J.M. Barnola, U. Siegenthaler, D. Raynaud, J. Jouzel, H. Fischer, K. Kawamura, T.F. Stocker, Nature, 453 (2008) 379-382.
[7] J.D. Shakun, P.U. Clark, F. He, S.A. Marcott, A.C. Mix, Z. Liu, B. Otto-Bliesner, A. Schmittner, E. Bard, Nature, 484 (2012) 49-54.
[8] A.K. Tripati, C.D. Roberts, R.A. Eagle, 326 (2009) 1394-1397.
[9] K.A. Giles, S.W. Laxon, A.L. Ridout, Geophys. Res. Lett., 35 (2008).
[10] J.A. Church, N.J. White, Geophys. Res. Lett., 33 (2006).
[11] O. Hoegh-Guldberg, P.J. Mumby, A.J. Hooten, R.S. Steneck, P. Greenfield, E. Gomez, C.D. Harvell, P.F. Sale, A.J. Edwards, K. Caldeira, N. Knowlton, C.M. Eakin, R. Iglesias-Prieto, N. Muthiga, R.H. Bradbury, A. Dubi, M.E. Hatziolos, Science, 318 (2007) 1737-1742.
[12] G. Shaffer, S.M. Olsen, J.O.P. Pedersen, Nat. Geosci., 2 (2009) 105-109.
[13] D. Coumou, S. Rahmstorf, Nat. Clim. Change, 2 (2012) 491-496.
[14] C.D. Thomas, A. Cameron, R.E. Green, M. Bakkenes, L.J. Beaumont, Y.C. Collingham, B.F.N. Erasmus, M.F. de Siqueira, A. Grainger, L. Hannah, L. Hughes, B. Huntley, A.S. van Jaarsveld, G.F. Midgley, L. Miles, M.A. Ortega-Huerta, A. Townsend Peterson, O.L. Phillips, S.E. Williams, Nature, 427 (2004) 145-148.
[15] D.B. Lobell, W. Schlenker, J. Costa-Roberts, Science, 333 (2011) 616-620
[16] M. Jiang, W.M. Griffin, C. Hendrickson, Environ. Res. Lett. 6 (2011).
[17] R.W. Howarth, R. Santoro, A. Ingraffea, Clim. Change, 106 (2011) 679-690.
[18] R.G. Newell, D. Raimi, Environ. Sci. Technol., 48 (2014) 8360-8368.
[19] B. van der Zwaan, I. Keppo, F. Johnsson,, Energy Policy, 61 (2013) 562-573.
[20] E. Robert, H. Heinz, L. Laura, M. Heiko, R. David, WELL-TO-WHEELS Report version 4. a: JEC WELL-TO-WHEELS ANALYSIS, (2014).
[21] M.G. Waller, E.D. Williams, S.W. Matteson, T.A. Trabold, Appl. Energy, 127 (2014) 55-63.
[22] M. Wang, J. Power Sources, 112 (2002) 307-321.
[23] R. Faria, P. Marques, P. Moura, F. Freire, J. Delgado, A. T. de Almeida, Renewable Sustainable Energy Rev., 24 (2013) 271-287.
[24] T.W. Frederick, L. Balasubramanian, F.M. Mark, J. Phys. Chem. Lett., 1 (2010) 2204-2219.
[25] M. Wang, T. Weber, T. Darlington, Well-to-wheels analysis of advanced fuel/vehicle systems: A North American study of energy use, greenhouse gas emissions, and criteria pollutant emissions, Well-to-Wheels Analysis of energy use, greenhouse gas emissions and criteria pollutant emissions, (2005).
[26] T.W. Frederick, L. Balasubramanian, F.M. Mark, J. Phys. Chem. Lett., 1 (2010) 2204-2219.
[27] W. Tang, Y. Zhu, Y. Hou, L. Liu, Y. Wu, K.P. Loh, H. Zhang, K. Zhu, Energy Environ. Sci., 6 (2013) 2093-2104.
[28] C.H. Dharmakeerthi, N. Mithulananthan, T.K. Saha, International Journal of Electrical Power & Energy Systems, 57 (2014) 241-249.
[29] D. van der Vleit, C. Wang, M. Debe, R. Atanasoski, N.M. Markovic, V.R. Stamenkovic, Electrochim. Acta, 56 (2011) 8695-8699.
[30] V.R. Stamenkovic, B.S. Mun, M. Arenz, K.J.J. Mayrhofer, C.A. Lucas, G. Wang, P.N. Ross, N.M. Markovic, Nat. Mater., 6 (2007) 241-247.
[31] A. Morozan, B. Jousselme, S. Palacin, Energy Environ. Sci., 4 (2011) 1238-1254.
[32] I.-Y. Jeon, H.-J. Choi, S.-M. Jung, J.-M. Seo, M.-J. Kim, L. Dai, J.-B. Baek, J. Am. Chem. Soc., 135 (2013) 1386-1393.
[33] J.V. Mierlo, G. Maggetto, Ph. Lataire, Energy Convers. Manage., 47 (2006) 2748-2760.
[34] W.R. Grove, Philos. Mag. Series 3, 14 (1839) 127-130.
[35] W.R. Grove, Philos. Mag. Series 3, 13 (1838) 430-431.
[36] W.R. Grove, Philos. Mag. Series 3, 21 (1842) 417-420.

[37] J. Zhang, PEM fuel cell electrocatalysts and catalyst layers: fundamentals and applications, PEM fuel cell electrocatalysts and catalyst layers: fundamentals and applications, (2008).
[38] A.E. Lutz, R.S. Larson, J.O. Keller, Int. J. Hydrogen Energy, 27 (2002) 1103-1111.
[39] K.C. Neyerlin, W. Gu, J. Jorne, H.A. Gasteiger, J. Electrochem. Soc., 154 (2007) B631-B635.
[40] J.K. Nørskov, J. Rossmeisl, A. Logadottir, L. Lindqvist, J.R. Kitchin, T. Bligaard, H. Jónsson, J. Phys. Chem. B, 108 (2004) 17886-17892.
[41] T. Takaishi, A. Numata, R. Nakano, K. Sakaguchi, Mitsubishi Heavy Industries Ltd. Technical Review, 45 (2008) 21-24.
[42] B. Lindstrom, L.J. Petterson, CATTECH, 7 (2003) 130-138.
[43] J.T. Stock, M.V. Orna, In Electrochemistry, Past and Present, Am. Chem. Soc. Symp. Ser., 390 (1989).
[44] R.G. Ehl, A.J. Ihde, J. Chem. Educ., 31 (1954) 226.
[45] D. Pletcher, F.C. Walsh, Industrial Electrochemistry, Springer (1990).
[46] J.J. Berzelius, Årsberättelse om framstegen i fysik och kemi, Norstedt (1835).
[47] S.H. Jordanov, P. Paunovic, O. Popovski, A. Dimitrov, D. Slavkov, Bull. Chem. Technol. Maced., 23 (2004) 101-112.
[48] J.N Armor, Catal. Today, 163 (2011) 3-9.
[49] H.H. Carl, H. Andrew, V. Wolf, Electrochemistry, Wiley (2007).
[50] D. Pletcher, A First Course in Electrode Processes, 2nd Edition ed., Royal Society of Chemistry, RSC Publishing, (2009).
[51] IUPAC Gold Book Version 1.0.0, (2006).
[52] G. Attard, C. Barnes, Surfaces, Oxford University Press, (1998).
[53] J.E. Lennard-Jones, Trans. Faraday Soc., 28 (1932) 333-359.
[54] M. Shiraiwa, Y. Sosedova, A. Rouvière, H. Yang, Y. Zhang, J.P.D. Abbatt, M. Ammann, U. Pöschl, Nat. Chem., 3 (2011) 291-295.
[55] G. Calingaert, F.E. Huggins, J. Am. Chem. Soc., 45 (1923) 915-920.
[56] J.P. Hobson, J. Phys. Chem., 73 (1969) 2720-2727.
[57] H.M.F. Freundlich, J. Phys. Chem, 57 (1906) 1100-1107.
[58] Y.S. Ho, J.F. Porter, G. McKay, Water, Air, Soil Pollut., 141 (2002) 1-33.
[59] I. Langmuir, J. Am. Chem. Soc., 40 (1918) 1361-1403.
[60] H.A. Asiri, A.B. Anderson, J. Phys. Chem. C, 117 (2013) 17509-17513.
[61] S. Brunauer, P.H. Emmett, E. Teller, J. Am. Chem. Soc., 60 (1938) 309-319.
[62] M.I. Temkin, V. Pyzhev, Acta physiochim. URSS, 12 (1940) 217-222.
[63] K.Y. Foo, B.H. Hameed, Chem. Eng. J., 156 (2010) 2-10.
[64] S. Srinivasan, Fuel Cells, Springer, (2006) 27-92.
[65] H. Helmholtz, Ann. Phys., 165 (1853) 211--233.
[66] D.L. Chapman, London, Edinburgh Dublin Philos. Mag. J. Sci., 25 (1913) 475-481.
[67] O. Stern, Z. Elektrochem. Angew. Phys. Chem., 30 (1924) 508-516.
[68] D.C. Grahame, Chem. Rev., 41 (1947) 441-501.
[69] J.O'M. Bockris, M.A.V. Devanathan, K. Muller, Proc. R. Soc. London, Ser. A, 274 (1963) 55-79.
[70] M.T.M. Koper, Nanoscale, 3 (2011) 2054-2073.
[71] M.A. Van Hove, G.A. Somorjai, Surf. Sci., 92 (1980) 489-518.
[72] N. Tian, Z.-Y. Zhou, S.-G. Sun, J. Phys. Chem. C, 112 (2008) 19801-19817.
[73] R.G. Compton, C.E. Banks, Understanding Voltammetry 2nd Edition, Imperial College Press, (2010).
[74] D. Harvey, Analytical Chemistry 2.0, Springer-Verlag, (2010).
[75] D. Harvey, Modern Analytical Chemistry, McGraw-Hill, (1999).
[76] A. Fick, Ann. Phys., 170 (1855) 59-86.
[77] J. Wang, Analytical Electrochemistry, Wiley (2006).
[78] C. Amatore, S. Szunerits, L. Thouin, J.-S. Warkocz, J. Electroanal. Chem., 500 (2001) 62-70.
[79] T. Pajkossy, D.M. Kolb, Electrochim. Acta, 46 (2001) 3063-3071.
[80] N. Garcia-Araez, V. Climent, E. Herrero, J.M. Feliu, J. Lipkowski, Electrochim. Acta, 51 (2006) 3787-3793.
[81] K.E. Toghill, P. Voyame, D. Momotenko, A.J. Olaya, H.H. Girault, Phys. Chem. Chem. Phys., 15 (2013) 972-978.

[82] N. Lopez, D.J. Graham, R. McGuire, G.E. Alliger, Y. Shao-Horn, C.C. Cummins, D.G. Nocera, Science, 335 (2012) 450-453.
[83] O. Reynolds, Proc. R. Soc. London, 35 (1883) 84-99.
[84] M.D. Macia, J.M. Campina, E. Herrero, J.M. Feliu, J. Electroanal. Chem., 564 (2004) 141-150.
[85] N.M. Markovic, H.A. Gasteiger, P.N. Ross, J. Phys. Chem., 99 (1995) 3411-3415.
[86] N.M. Markovic, H.A. Gasteiger, N. Philip, J. Phys. Chem., 100 (1996) 6715-6721.
[87] V. Stamenkovic, N.M. Markovic, P.N. Ross, J. Electroanal. Chem., 500 (2001) 44-51.
[88] N.M. Markovic, H.A. Gasteiger, B.N. Grgur, P.N. Ross, J. Electroanal. Chem., 467 (1999) 157-163.
[89] M.W. Breiter, Electrochim. Acta, 8 (1963) 925-935.
[90] H. Angerstein-Kozlowska, B.E. Conway, W.B.A. Sharp, J. Electroanal. Chem. Interfacial Electrochem., 43 (1973) 9-36.
[91] V. Climent, J.M. Feliu, J. Solid State Electrochem., 15 (2011) 1297-1315.
[92] B.E. Conway, H. Angerstein-Kozlowska, W.B.A. Sharp, E.E. Criddle, Anal. Chem., 45 (1973) 1331-1336.
[93] S. Trasatti, O.A. Petrii, J. Electroanal. Chem., 327 (1992) 353-376.
[94] B.E. Conway, B. Barnett, H. Angerstein-Kozlowska, B.V. Tilak, J. Chem. Phys., 93 (1990) 8361.
[95] A. Wieckowski, Interfacial Electrochemistry: Theory: Experiment, and Applications, Taylor & Francis (1999).
[96] F.G. Will, J. Electrochem. Soc., 112 (1965) 451-455.
[97] J. Clavilier, R. Faure, G. Guinet, R. Durand, J. Electroanal. Chem., 107 (1980) 205-209.
[98] J. Clavilier, J. Electroanal. Chem., 107 (1980) 211-216.
[99] A. Al-Akl, G.A. Attard, R. Price, B. Timothy, J. Electroanal. Chem., 467 (1999) 60-66.
[100] L.A. Kibler, A. Cuesta, M. Kleinert, D.M. Kolb, J. Electroanal. Chem., 484 (2000) 73-82.
[101] A. Al-Akl, G. Attard, R. Price, B. Timothy, J. Chem. Soc., Faraday Trans., 91 (1995) 3585-3591.
[102] N.M. Marković, B.N. Grgur, C.A. Lucas, P.N. Ross, Surf. Sci., 384 (1997) L805-L814.
[103] A. Kuzume, E. Herrero, J.M. Feliu, J. Electroanal. Chem., 599 (2007) 333-343.
[104] J. Solla-Gullon, P. Rodriguez, E. Herrero, A. Aldaz, J.M. Feliu, Phys. Chem. Chem. Phys., 10 (2008) 1359-1373.
[105] T. Yu, D.Y. Kim, H. Zhang, Y. Xia, Angew. Chem., Int. Ed., 50 (2011) 2773-2777.
[106] F.J. Vidal-Iglesias, J. Solla-Gullón, P. Rodríguez, E. Herrero, V. Montiel, J.M. Feliu, A. Aldaz, Electrochem. Commun., 6 (2004) 1080-1084.
[107] C. Sánchez-Sánchez, J. Solla-Gullón, F. Vidal-Iglesias, A. Aldaz, V. Montiel, E. Herrero, J. Am. Chem. Soc., 132 (2010) 5622-5624.
[108] F.J. Vidal-Iglesias, N. García-Aráez, V. Montiel, J.M. Feliu, A. Aldaz, Electrochem. Commun., 5 (2003) 22-26.
[109] N.M. Markovic, R.R. Adzic, B.D. Cahan, E.B. Yeager, J. Electroanal. Chem., 377 (1994) 249-259.
[110] C. Chen, Y. Kang, Z. Huo, Z. Zhu, W. Huang, H.L. Xin, J.D. Snyder, D. Li, J.A. Herron, M. Mavrikakis, M. Chi, K.L. More, Y. Li, N.M. Markovic, G.A. Somorjai, P. Yang, V.R. Stamenkovic, Science, 343 (2014) 1339-1343.
[111] N. Fan, Y. Yang, W. Wang, L. Zhang, W. Chen, C. Zou, S. Huang, ACS nano, 6 (2012) 4072-4082.
[112] W. Yu, M. Porosoff, J. Chen, Chem. Rev., 112 (2012) 5780-5817.
[113] M. Wakisaka, S. Mitsui, Y. Hirose, K. Kawashima, H. Uchida, M. Watanabe, J. Phys. Chem. B, 110 (2006) 23489-23496.
[114] J. Rodriguez, Surf. Sci. Rep., 24 (1996) 223-287.
[115] C.T. Campbell, Annu. Rev. Phys. Chem., 41 (1990) 775-837.
[116] U. Bardi, Rep. Prog. Phys., 57 (1994) 939.
[117] A. Cuesta, Chemphyschem, 12 (2011) 2375-2385.
[118] R. Burch, Acc. Chem. Res., 15 (1982) 24-31.
[119] J. Kitchin, J. Nørskov, M. Barteau, J. Chen, Phys. Rev. Lett., 93 (2004) 156801.
[120] Y.G.Shen, D.J.O'Connor R.J. MacDonald, J. Phys.: Condens. Matter, 9 (1997) 8345-8358.
[121] R. Baudoing, Y. Gauthier, M. Lundberg, J. Rundgren, J. Phys. C: Solid State Phys., 19 (1986) 2825-2831.

[122] V.R. Stamenkovic, B. Fowler, B.S. Mun, G. Wang, P.N. Ross, C.A. Lucas, N.M. Markovic, Science, 315 (2007) 493-497.
[123] S.J. Hwang, S.-K. Kim, J.-G. Lee, S.-C. Lee, J.H. Jang, P. Kim, T.-H. Lim, Y.-E. Sung, S.J. Yoo, J. Am. Chem. Soc., 134 (2012) 19508-19511.
[124] J.K. Norskov, J. Rossmeisl, A. Logadottir, L. Lindqvist, J.R. Kitchin, T. Bligaard, H. Jonsson, J. Phys. Chem. B, 108 (2004) 17886-17892.
[125] S. Deckers, F.H.P.M. Habraken, W.F. van der Weg, A.W. Denier van der Gon,, J.F. van der Veen, J.W. Gues, Appl. Surf. Sci., 42 (1990) 121-129.
[126] Y. Gauthier, R. Baudoing, Y. Joly, J. Rundgren, J.C. Bertolini, J. Massardier, Surf. Sci., 162 (1985) 342-347.
[127] M.P. Humbert, J.G. Chen, J. Catal., 257 (2008) 297-306.
[128] J.R. Kitchin, N.A. Khan, M.A. Barteau, J.G. Chen, B. Yakshinskiy, T.E. Madey, Surf. Sci., 544 (2003) 295-308.
[129] C.A. Menning, J.G. Chen, J. Chem. Phys., 128 (2008) 164703.
[130] C.A. Menning, J.G. Chen, J. Chem. Phys., 130 (2009) 174709.
[131] V. Stamenković, T.J. Schmidt, P.N. Ross, N.M. Marković, J. Phys. Chem. B, 106 (2002) 11970-11979.
[132] V. Stamenković, T.J. Schmidt, P.N. Ross, N.M. Marković, J. Electroanal. Chem., 554–555 (2003) 191-199.
[133] J. Greeley, I. Stephens, A. Bondarenko, T. Johansson, H. Hansen, T. Jaramillo, J. Rossmeisl, I. Chorkendorff, J. Nørskov, Nat. Chem., 1 (2009) 552-556.
[134] M.J. Hampden-Smith, T.T. Kodas, Chem. Vap. Deposition, 1 (1995) 8-23.
[135] S.R. Brankovic, J. McBreen, R.R. Adžić, J. Electroanal. Chem., 503 (2001) 99-104.
[136] M.J. Ball, C.A. Lucas, N.M. Markovic, V. Stamenkovic, P.N. Ross, Surf. Sci., 518 (2002) 201-209.
[137] S.E. Huxter, G.A. Attard, Electrochem. Commun., 8 (2006) 1806-1810.
[138] G.A. Attard, J.-Y. Ye, A. Brew, D. Morgan, P. Bergstrom-Mann, S.-G. Sun, J. Electroanal. Chem., 716 (2014) 106-111.
[139] G.A. Attard, A. Brew, J.-Y. Ye, D. Morgan, S.-G. Sun, Chemphyschem, 15 (2014) 2044-2051.
[140] I.E.L. Stephens, A.S. Bondarenko, F.J. Perez-Alonso, F. Calle-Vallejo, L. Bech, T.P. Johansson, A.K. Jepsen, R. Frydendal, B.P. Knudsen, J. Rossmeisl, I. Chorkendorff, J.Am. Chem. Soc., 133 (2011) 5485-5491.
[141] An Overview of XPS Spectroscopy, http://www.xpsfitting.com/2012/08/an-overview-of-x-ray-photoelectron.html.
[142] D. Brune, R. Hellborg, H.J. Whitlow, O. Hunderi, Surface Characterization, Wiley, (2008).
[143] B.V. Crist, Handbook of Monochromatic XPS Spectra: The elements and native oxides, Wiley (2000).
[144] M.C. Biesinger, B.P. Payne, L.W.M. Lau, A. Gerson, R.St.C. Smart, Surf. Interface Anal., 41 (2009) 324-332.
[145] G. Binnig, H. Rohrer, IBM J. Res. Dev., 44 (2000) 279-293.
[146] G. Binnig, H. Rohrer, Ch. Gerber, E. Weibel, Phys. Rev. Lett., 49 (1982) 57-61.

2 Chapter Two - Experimental

2.1 Introduction

Platinum single crystal electrodes used in these studies were prepared in-house, via the technique of Clavilier and Durand [1]. Briefly, high purity platinum wire (99.999% Goodfellows) was melted in an oxygen/gas flame until a bead of 2-3mm diameter was obtained. The quality of the platinum poly-orientated bead was checked by laser alignment in a goniometer. It was then aligned to the angle required for the crystal being made and set in epoxy resin. Using a combination of grit paper of decreasing particle size and diamond sprays (from 20μm down to 0.25 μm), the bead was cut to its circumference and polished to a mirror finish.

All glassware such as the electrochemical cell and stoppers had to be removed of all contaminants before use. A series of cleaning steps were carried out to ensure this. Firstly, a dilute permanganic acid was prepared by adding a few grains of potassium permanganate to pure sulphuric acid and all glassware was immersed in this overnight. The permanganic acid was then decanted and the glassware was rinsed thoroughly with ultrapure water (>18.2MΩ•cm resistivity from the Milli-Q water purification system). Any plastic apparatus which were not compatible with permanganic acid were rinsed with ultrapure water at this stage. All components to be used were then either boiled or steam cleaned with ultrapure water and rinsed thoroughly a final time before use. Due to the sensitivity of the work carried out, only the most pure of reagents and solvents were used.

2.2 Cyclic Voltammetry (CV)

CV described in detail in section 1.4, was the main electrochemical technique used in the studies presented in this thesis. Principally it was used to characterise single crystal electrode surfaces in degassed 0.1 mol dm^{-3} perchloric acid and 0.1 mol dm^{-3} sodium hydroxide electrolytes prior to ORR activity analysis. Single crystals were flame-annealed and cooled in hydrogen and meniscus contact was made with the electrolyte in an electrochemical cell, as described previously [2] and illustrated in figure 1.

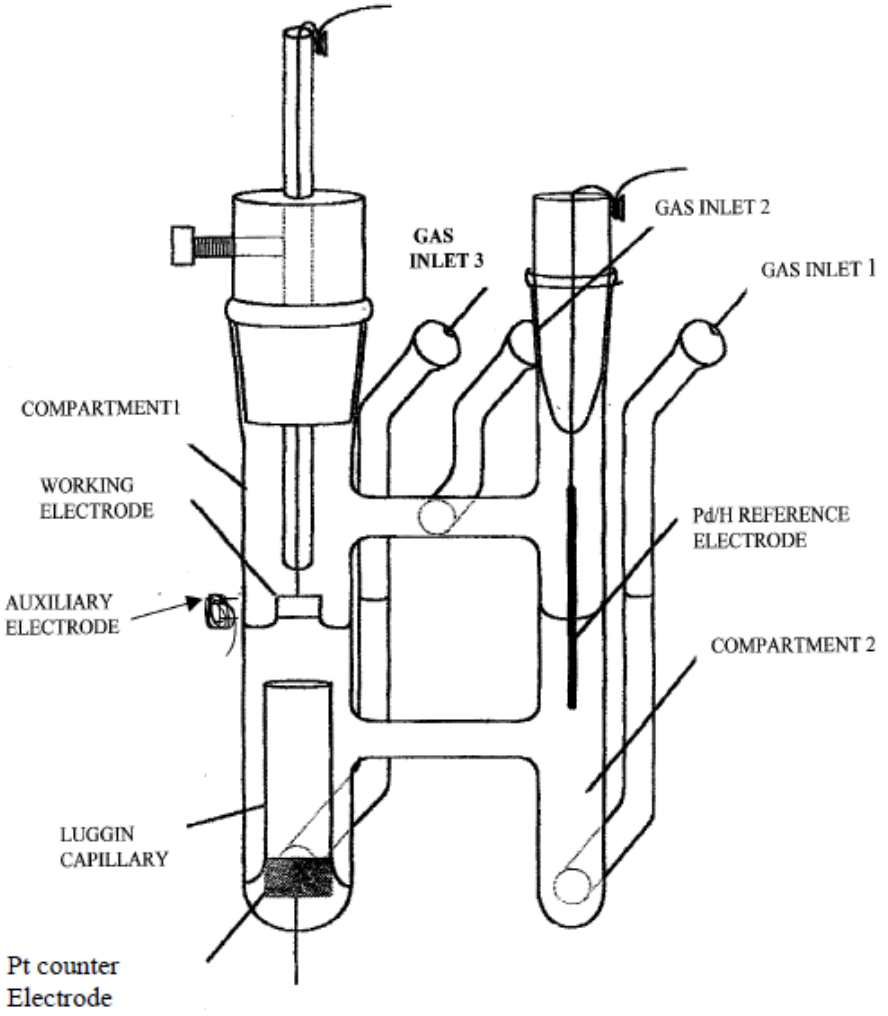

Figure 1. The electrochemical cell used for cyclic voltammetry in these studies.

$HClO_4$ (70% Suprapur® supplied by Merck) and NaOH (Sigma-Aldrich Z99.9995%), were used to prepare all aqueous electrolyte solutions by diluting in ultra-pure water. Electrolytes were degassed by bubbling through with nitrogen gas for 30 min. A palladium hydride reference electrode was used for $HClO_4$ electrolyte and a Ag/AgCl(sat) reference electrode was used when collecting the aqueous NaOH data. However, all potentials are reported with reference to the palladium hydride reference electrode. All CV data employed a potential sweep rate of 50 mV s^{-1} unless stated otherwise and contact with electrolyte was made at the lowest potential, e.g. 0V vs PdH. A CHi 800 potentiostat interfaced with a PC using proprietary software was employed to collect all voltammetric data. This digital potentiostat approximates linear voltammetry by the use of a staircase with a stepping potential of 1mV. This approximation is accurate for the electrode sizes and scan rates used in this study.

For some experiments, CO gas was used for cooling in the flame annealing and cooling procedure. Where this gas was used the crystal was left in the CO atmosphere for 5 minutes, resulting in a CO covered surface. This was then transferred to the electrochemical cell protected by CO and contacted with the electrochemical cell electrolyte under potential control at 0 V (vs. PdH). A positive going potential sweep was engaged to remove the CO ad-layer.

2.3 Rotating Disc Electrode (RDE)

CV in combination with a RDE was used to analyse oxygen reduction reaction (ORR) activity of prepared surfaces in both the aforementioned electrolyte solutions. The RDE was also utilised in the analysis of the hydrogen peroxide oxidation-reduction reaction (HPORR).

ORR measurements were collected using a Basi RDE-2 rotating disc electrode system controlling the hydrodynamics of the reaction in the hanging meniscus configuration [3]. The cell used for RDE measurements contained a reference electrode within a luggin capillary containing degassed aqueous electrolyte. Oxygen of purity 99.999% from BOC was bubbled through the RDE electrochemical cell for 30 minutes at 1atm pressure prior to performing any ORR measurement. After saturating the electrolyte with oxygen, bubbling into the electrolyte was discontinued and a positive pressure of oxygen was maintained across the electrolyte during all ORR measurements. The ORR activity of single crystal surfaces was measured by potential controlled contact with the electrolyte at 0 V, before applying a linear, positive potential sweep of 30 mV s^{-1} up to 1 V (versus Pd/H) in order to exclude possible structural perturbations associated with the rather positive open circuit potential corresponding to oxygen saturated electrolyte.

For the HPORR, the experimental setup was similar to that used for examining the ORR. Differences included the electrolyte used (10^{-3} mol dm^{-3} H_2O_2, 0.1moldm^{-3} $HClO_4$) and that this was degassed with nitrogen. Further information on the experimental setup of used for the HPORR can be found in reference [4].

The error in $E_{1/2}$ values for all HPORR and ORR results was found to be +/-2mV.

2.4 Preparation of Bi-metallic Surfaces by Resistive Heating

The design of the resistive heating holder utilised to prepare bimetallic electrode surfaces has been described previously [5]. It was used in this thesis to prepare bimetallic Pt{111} surfaces.

After flame-annealing, cooling in hydrogen and checking that the CV response was that of a well-ordered Pt{111} electrode, the bimetallic surfaces were prepared. The platinum crystal was first dipped into a solution of metal ions and removed with a droplet of the aqueous metal solution still attached to the crystal surface (0.01m $NiCl_2$, $Fe(NO_3)_3$ and $Co(NO_3)_2$ were used to create PtNi, PtFe and PtCo electrodes, respectively). The electrode was then returned to the electrochemical cell, taking care not to touch the electrolyte contained within the electrochemical cell at this stage. The flow of nitrogen through the cell ensured that oxygen was removed from the attached aqueous droplet. An electric current of approximately 8A was then passed through the Pt stem wires attached to the single-crystal bead electrode and these began to glow. The temperature reached by the bead crystal was estimated using an optical pyrometer. Once a particular temperature had been reached (1100 K), the temperature was maintained for approximately 10s and then the electric current was switched off and the crystal allowed to cool in the nitrogen/water atmosphere of the electrochemical cell. In order to examine changes in the selvedge brought about by cooling in a more reducing atmosphere, the electrode would be removed from the electrochemical cell after this resistive heating stage, re-annealed in a Bunsen flame to 900 K and then transferred quickly to a hydrogen bubbler where it would cool back to room temperature and its surface protected with a droplet of ultra-pure water. The electrode would then be returned to the electrochemical cell and CV characterisation undertaken.

2.5 X-Ray Photoelectron Spectroscopy (XPS) and Scanning Tunnelling Microscopy (STM) of Bimetallic Single Crystal Electrodes

Two ex-situ techniques were utilised for the further analysis of Pt-M(where M=Ni, Co or Fe) single crystal electrodes; X-ray photoelectron spectroscopy (XPS) and scanning tunnelling microscopy (STM).

Single-crystal electrodes were transferred for XPS analysis with a droplet of ultrapure water attached to protect the bimetallic surface from the ambient atmosphere and maintain surface

cleanliness. XPS measurements were performed on a Kratos Axis Ultra- DLD photoelectron spectrometer, using monochromatic AlKa radiation operating at 120 W. The base pressure during acquisition was $1x10^{-9}$ Torr. Spectra were collected from a 110 mm diameter spot at a pass energy of 80 eV and 160 eV for high resolution and survey scans respectively. Sputtering was performed using a Kratos minibeam-1 rastering ion source operated at 4 keV and an argon pressure of $1x10^{-6}$ Torr. The beam was rastered over an approximately 4 mm^2 area. The spectra were subsequently analysed through CasaXPS v.2.3.16 software using modified Wagner sensitivity factors as supplied by the manufacturer.

Scanning tunnelling microscopy measurements were performed using a Molecular Imaging STM incorporating a Nanoscope E controller described in detail elsewhere[6]. STM images are presented using WSxM software. [7]

2.6 Formation of (1x1)-Pt{110} Single Crystal Electrode Surface

The Pt{110} crystal was flame annealed and cooled in CO gas, left in the CO atmosphere for 5 minutes, resulting in a CO covered surface. This was then transferred to the electrochemical cell protected by a droplet of the CO saturated electrolyte and contacted with the electrochemical cell electrolyte under potential control at 0 V (vs. PdH). After dispersing the excess CO by bubbling with argon, a positive going potential sweep from 0 V to 0.85 V was engaged to remove the CO adlayer leaving behind the pristine (1x1) surface. In the case of the preparation of the disordered Pt{110}-(1x2) phase, the CO cooling ambient was replaced by either pure hydrogen or pure nitrogen.

2.7 Reagents

Chemical Reagents			
Chemical	**Formula**	**Grade**	**Supplier**
Perchloric Acid	$HClO_4$	Aristar	VWR
Sulphuric Acid	H_2SO_4	Aristar	VWR
Sulphuric Acid	H_2SO_4	Reagent	Fischer Scientific
Potassium Permanganate	$KMnO_4$	Reagent	BDH, Poole

Platinum Wire	Pt	99.999%	Goodfellows & Johnson Matthey
Palladium Wire	Pd	99.99%	Advent Research Materials
Sodium Hydroxide	NaOH	99.9995% TraceSELECT ® for trace analysis	Fluka Analytical
Hydrogen Peroxide	H_2O_2	50%wt in H_2O	Sigma-Aldrich
Nitrogen Gas	N_2	Pureshield	BOC
Hydrogen Gas	H_2	High Purity 99.995%	BOC
Oxygen Gas	O_2	High Purity N6.0	BOC
Iron Nitrate	$Fe(NO_3)_2$	99.9%	Sigma-Aldrich
Cobalt Nitrate	$Co(NO_3)_2$	99.9%	Aldrich Chemical Company
Nickel Chloride Hexahydrate	$NiCl_2$ $6H_2O$	99.9%	Sigma-Aldrich

2.8 References

[1] J. Clavilier, R. Faure, G. Guinet, R. Durand, J. Electroanal. Chem., 107 (1980) 205-9.
[2] N. Markovic, M. Hanson, G. McDougall, E. Yeager, J. Electroanal. Chem. Interfacial Electrochem., 214 (1986) 555-566.
[3] B.D. Cahan, H.M. Villullas, J. Electroanal. Chem. 307 (1991) 263-8.
[4] I. Katsounaros, W.B. Schneider, J.C. Meier, U. Benedikt, P.U. Biedermann, A.A. Auer, K.J.J. Mayrhofer, Phys. Chem. Chem. Phys., 14 (2012) 7384-91.
[5] S.E. Huxter, G.A. Attard, Electrochem. Commun. 8 (2006) 1806-10.
[6] C.M. Whelan, M.R. Smyth, C.J. Barnes, G.A.Attard, X. Yang, , J. Electroanal. Chem., 474 (1999) 138-146.
[7] I. Horcas, R. Fernández, J.M. Gómez-Rodríguez, J. Colchero, J. Gómez-Herrero, A.M. Baro, Rev. Sci. Instrum. 78 (2007) 13705.

3 Chapter Three – Results

3.1 The Oxygen Reduction and Hydrogen Peroxide Oxidation/Reduction Reactions on Pt{hkl} Surfaces in Perchloric Acid

Parallels have been discovered and investigated between the oxygen reduction reaction (ORR) and the hydrogen peroxide oxidation-reduction reaction (HPORR) on the stepped [Pt n{111}x{100}] and [Pt n{100}x{111}] surfaces. Changes in Tafel slope for oxygen reduction correlate with similar changes in the Tafel slopes for the HPORR in the same potential ranges. Platinum oxide species are found to be responsible for these changes. In the ORR, platinum oxide causes a sharp decline in activity, whereas for HPORR, the presence of platinum oxide causes a switch from reduction to oxidation of peroxide molecules. Stepped platinum surfaces exhibit electrosorption oxide peaks at more negative potentials than their basal plane counterparts, leading to more negative potentials for hydrogen peroxide electrooxidation. These results can be interpreted in two ways; the HPORR results could indicate that once H_2O_2 is formed in the ORR it is instantly oxidised over a platinum oxide surface so that zero current is passed. An alternative explanation is that platinum oxide species inhibit H_2O_2 formation in the ORR, which could be a key step if the reaction is believed to proceed via the series pathway at these potentials.

3.1.1 Introduction

Understanding the origin of the overpotential for the oxygen reduction reaction (ORR) on real nanoparticles catalysts requires at first an understanding of the reaction at “ideal” surfaces. These ideal surfaces are well defined single crystal electrodes which exhibit predefined, long range atomic order. The method for producing these crystals, known as the Clavilier method [1], exposes only a surface with the desired atomic arrangement to a given electrolyte so that structure-activity relationships can be obtained between crystal faces and electrochemical reactions under investigation. In the 90’s, the Clavilier method was used to create platinum basal plane single crystal electrodes and to investigate their activity for the ORR [2-4]. It was found in this initial work that the order of ORR activity of the basal planes of platinum in

perchloric acid, an electrolyte which exhibits negligible or very weak anion adsorption, is {110}>{111}>{100} [4]. More recent work, presented in chapter 3.4 in this thesis, suggests that the true order of activity for atomically perfect base plane surfaces in this electrolyte is actually {111}>{110}>{100}. In sulphuric acid the activity of Pt{111} is found to be greatly diminished [3] due to the strong ordered adsorption of (bi)sulphate on {111} terraces at low potentials [5], which acts to block the surface towards oxygen adsorption.

The activity of stepped platinum crystal surfaces (in relation to the ORR) was studied by Feliu et al [6, 7] in aqueous perchloric and sulphuric acid electrolytes. [Pt n{111}x{100}], [Pt n{100}x{111}] and [Pt n{111}x{111}] vicinal surface electrodes were investigated in both studies. It was found that surfaces with short {111} terraces exhibited the highest activity for oxygen reduction in both electrolytes. For {111} terraced surfaces [Pt n{111}x{100}] and [Pt n{111}x{111}] in sulphuric acid, the presence of steps was suggested to break up the ordered (bi)sulphate adlayer associated with extended Pt{111} terraces so that this site blocking effect is diminished. In perchloric acid, only a relatively small increase in activity with step density were found. This was understood in terms of a subtle balance of higher adsorption energy at step sites for O_2 (increasing ORR activity) together with an increased strength of adsorption of oxygen species such as OH_{ads} or O_{ads} (decreasing activity) at these sites, typical of the Sabatier principle in action. Oxygen molecules were therefore speculated to access free metal sites vacated by OH_{ads} and O_{ads} surface species in order to undergo reaction. It must be noted that the exact role of such oxide species in inhibiting the ORR is not well understood (they may well be involved in coupled systems [8]) and the identity and arrangement of OH/O_{ads} species on Pt{hkl} surfaces is a topic of current research [8-10].

Hydrogen peroxide is an intermediate in the oxygen reduction reaction that can be detected using a rotating ring disc electrode (RRDE) under certain conditions [2-4, 11-13]. Single crystal studies in acid and alkaline electrolytes show that hydrogen peroxide is detectable in the H_{upd} region where hydrogen peroxide is produced upon reduction of oxygen over a Pt-H surface which then undergoes no further reduction to water [2-4]. It has also been detected at more positive potentials when there are halogen ions present in the electrolyte solution [12, 13]. Studies on well-defined nanoparticle arrays indicate that H_2O_2 is produced during the ORR and may desorb from its reaction site before further reduction to water [14, 15]. Sparse Pt nanoparticle arrays exhibit greater H_2O_2 yields than dense arrays and increasing the electrolyte flow rate increases the H_2O_2 yield at potentials up to 0.8 V (vs. RHE) [14, 15]. Lower density

arrays and increased flow rate therefore act to decrease the chance of hydrogen peroxide re-adsorbing and completing the 4 electron reduction.

The stepwise mechanism of oxygen reduction, which proceeds at first by reduction to hydrogen peroxide and then on to water, is known as the "series" pathway (k_2 and k_3, below).

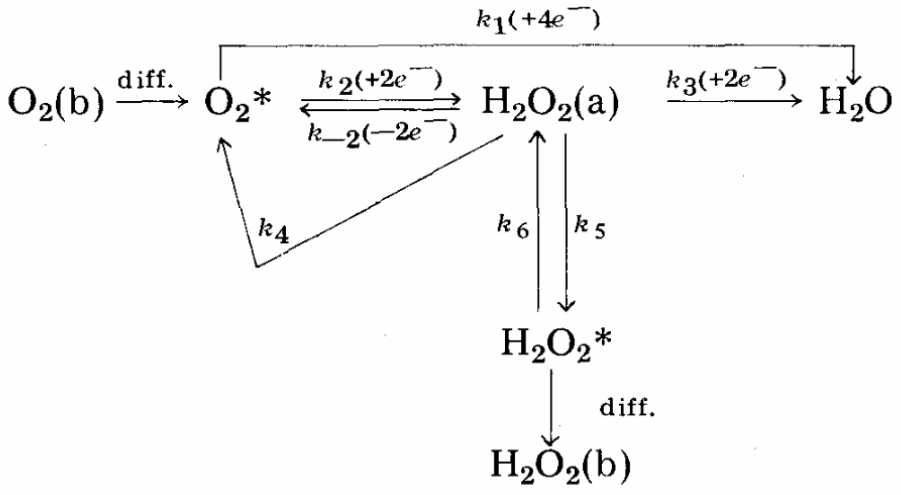

A general scheme of electrochemical oxygen reduction [16].

Steps k_2 and k_3 may be written;

$$O_2 + 2H^+ + 2e^- \rightarrow H_2O_2 \quad (1)$$

$$H_2O_2 + 2H^+ + 2e^- \rightarrow 2H_2O \quad (2)$$

The mechanism by which hydrogen peroxide is not considered to be formed, or at least where it is not detected experimentally, is known as the "direct" mechanism (k_1, above) and may be written;

$$O_2 + 4H^+ + 4e^- \rightarrow 2H_2O \quad (3)$$

The general scheme of oxygen reduction does not consider every elementary, single electron transfer, step. ORR mechanisms that take these into account have different nomenclature, as summarised below. The mechanisms are:

(i), the "dissociative" mechanism, where bond breaking precedes the reduction (and protonation),

(ii), the "associative" mechanism where a one electron reduction step precedes the bond breaking, and

(iii), the "peroxo"-mechanism (or 2nd associative mechanism) where two reduction steps precede the bond breaking, and which can proceed with or without desorption of the H_2O_2 intermediate [17].

DFT simulations indicate that the reaction activity is limited by two factors, OH_{ads} removal and OOH_{ads} formation [18, 19]. Therefore ideally it would be desirable to have weaker OH binding and stronger OOH binding to the surface [19].

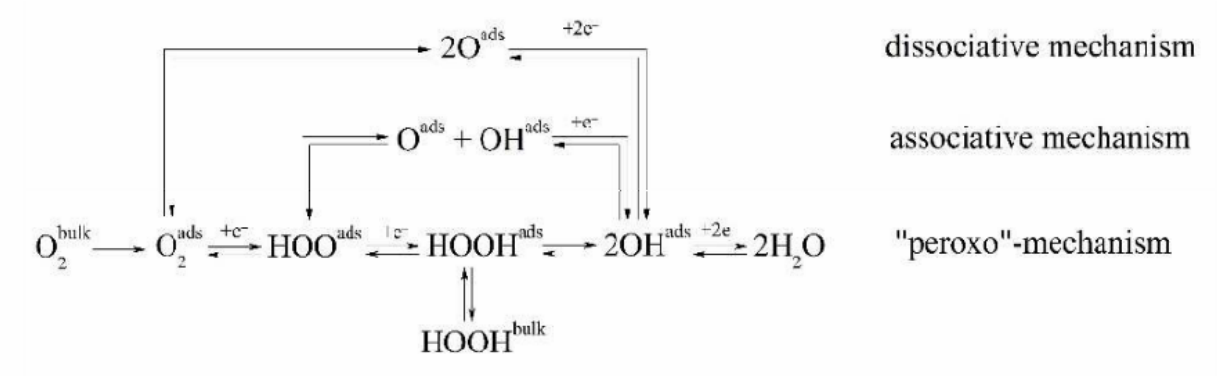

Elementary steps in the electrochemical oxygen reduction reaction [17].

Recently the interaction of hydrogen peroxide with platinum has been investigated over a polycrystalline platinum surface in order to understand the reactivity of this ORR intermediate species [17]. A diffusion limiting 2 electron reduction current was observed below 0.9 V vs. RHE, quickly switching to a diffusion limiting 2 electron oxidation current above 1.0 V. The switchover occurs in the potential region of OH formation. The authors explained that hydrogen peroxide is reduced to water over bare platinum metal sites and oxidised to oxygen over Pt-OH sites, which are present at most positive potentials. Feliu *et. al.* have examined this reaction over Pt{111} and found that O_2 is the product of the hydrogen peroxide oxidation reaction through online electrochemical mass spectrometry (OLEMS) [20].

These results have important implications for oxygen reduction reaction studies. If hydrogen peroxide is created as an intermediate at potentials other than those corresponding to H_{upd} during ORR, it would not be detected at the ring of a RRDE due to the fast kinetics of its subsequent reaction (either reduction or oxidation).

The potential and extent of PtOH and PtO coverage on a crystal surface depends on the surface atomic arrangement and is therefore unique for basal and stepped platinum single crystal surfaces. Hence, investigating the hydrogen peroxide oxidation/reduction reaction (HPORR)

as a function of crystal arrangement may give further insights into the effect of these surface species on the HPORR. As hydrogen peroxide is an oxygen reduction intermediate, insight into the ORR may also be gained.

In this study, stepped surfaces in the non-specifically adsorbing electrolyte perchloric acid shall be investigated, looking in more detail at the effect of the high potential oxide/hydroxide region on the HPORR and ORR.

3.1.2 Results

3.1.2.1 CV and ORR

3.1.2.1.1 CV and ORR of stepped [Pt n(111)x(100)] electrodes

Figure 1 shows the voltammetric profiles of [Pt n{111}x{100}] stepped surfaces in 0.1 mol dm^{-3} aqueous perchloric acid. The potential was swept from immersion of the electrode at 0 V to the positive potential limit of 1 V. This single excursion to a higher potential caused minimal structural change to the surfaces, as was seen by cycling the electrodes within a smaller potential range (0 - 0.8 V) before and after the 1 V excursion. This enabled electrodes to be characterised in a wide potential range relevant to oxygen reduction. The voltammetry reported here matches those reported previously [21, 22].

The features at potentials between 0.6 V and 1 V are relevant to the potential range of activity loss in ORR. The butterfly peak that occurs in this potential range on Pt{111} is a feature which has a number of interpretations [23, 24]. Feliu has attributed the sharp component to OH_{ads} as originating from isolated water interacting with the perchlorate anion and attributed the broad component to OH originating from bulk, ice-like structured water that does not interact with the anion [23]. Koper has associated the butterfly peak to a transition from OH adsorption occurring in a disordered manner (broad feature) to OH adsorption occurring in an ordered $(\sqrt{3}\times\sqrt{3})R30°$ ad-layer (sharp feature) [24, 25], a structure which has been observed over Pt{111} [26]. Presently, a complete description of this feature is the focus of much research.

Figure 1 shows that incorporating steps decreases the intensity of both the broad and sharp components of the butterfly peak. Using Koper's interpretation of this feature [24], the diminishing sharp component could be understood as disruption of the terrace $(\sqrt{3}\times\sqrt{3})R30°$

OH structure and the strong hydrogen bond network that DFT predicts it shares with bulk water [19, 27, 28].

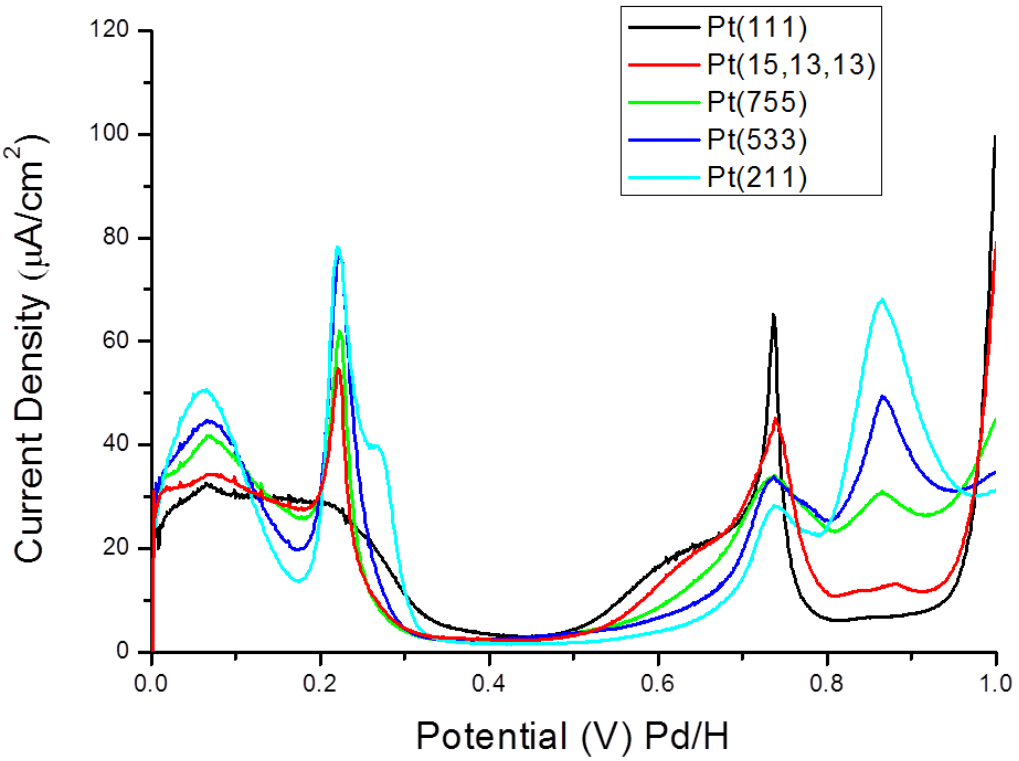

Figure 1. Voltammetry of [Pt n{111}x{100}] surfaces in contact with 0.1M perchloric acid electrolyte, sparged with N_2 and an applied scan rate of 50 mVs^{-1}.

Figure 2 shows the ORR profiles of [Pt n{111}x{100}] surfaces in perchloric acid. The voltammetry was again recorded up to 1 V and the whole change from diffusion limiting to zero current can be seen for all surfaces. Voltammetry obtained after oxygen reduction up to 1 V performed here showed small changes but were still characteristic of the initial surface structure.

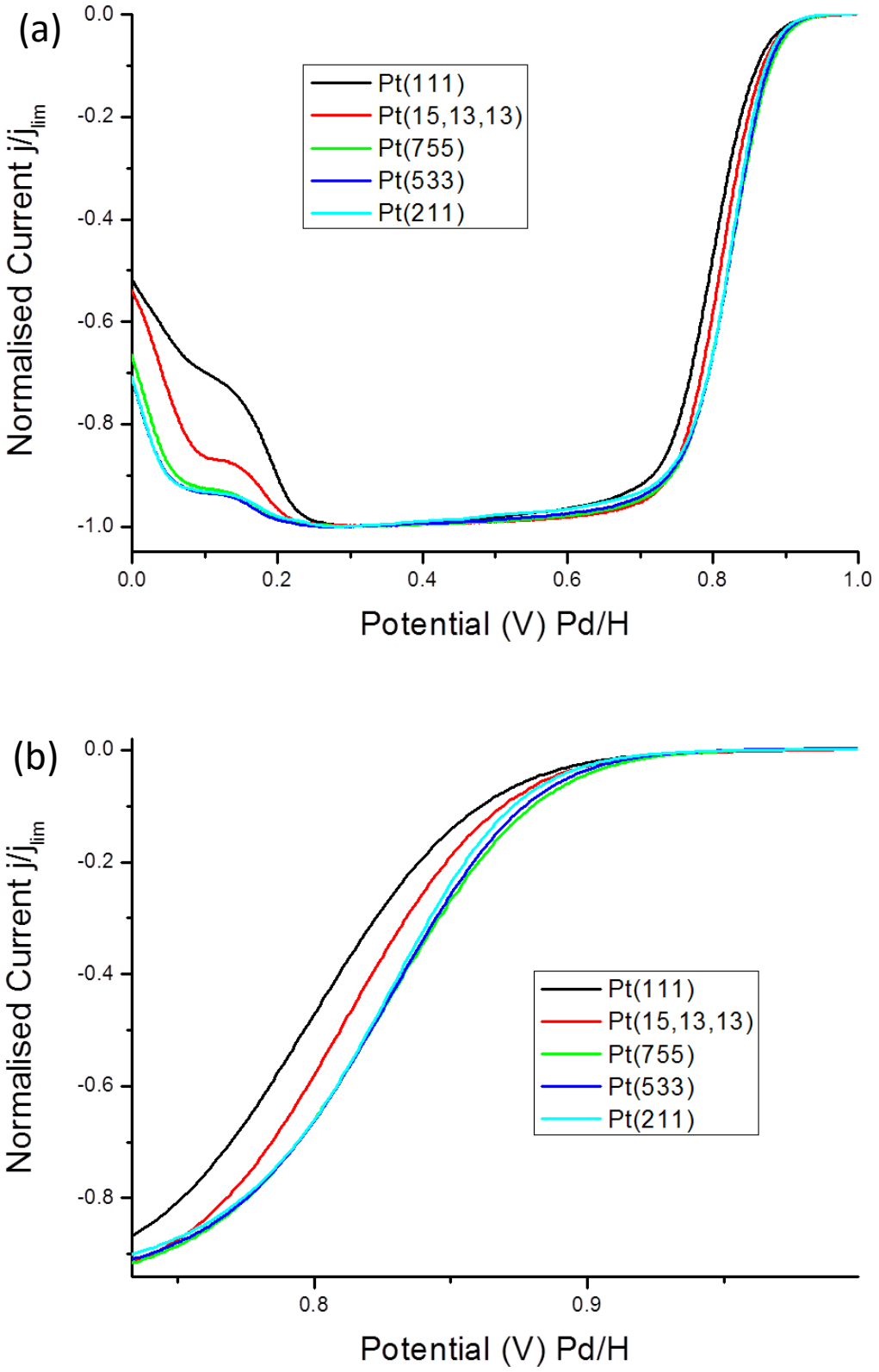

Figure 2. Rotating disc electrode oxygen reduction voltammetry in 0.1 M perchloric acid of [Pt n{111}x{100}] surfaces shown in figure 1. A 1600rpm rotation rate, 30 mVs^{-1} scan rate and 1 atm oxygen pressure were implemented. (a), top, shows the whole potential range used, whereas (b), bottom, shows a close up of the kinetic/mixed kinetic diffusion regimes.

The ORR of the [Pt n{111}x{100}] surfaces in figures 2(a) and (b) show that the Pt{111} surface has the lowest activity for this series, as has been reported previously [7]. A jump in activity is seen for the Pt{15,13,13} surface, which has a 14 atom wide average {111} terrace and another jump is seen for the 6 atom average terrace width Pt{755} surface. The activity levels off at this terrace width and no further activity increase is seen upon increasing step density when using $E_{1/2}$ as a measure of activity. A general increase in activity with step density for this same series was observed in reference [7], but no levelling off of activity was observed, where the exchange current density was used to define the activity. Hoshi *et. al.* have also looked at [Pt n{111}x{100}] ORR activity and their results very closely match those obtained here [22]. Using the current density at 0.9 V (vs. RHE) as a measure of activity, they found that activity increases between n = ∞ and n = 5 average atomic terrace width, and activity decreases between n = 5 and n = 2. The turning point for activity in Hoshi *et. al.*'s work of n = 5 is close to the turning point of n = 6 that we observe and indicates that there may be a true turning point for activity at this point in this series.

For Pt{111}, the activity for ORR begins to diminish above 0.7 V, which corresponds to just before the sharp component of the butterfly peak. The formation of a stable extended OH/H_2O over-layer structure, as described above, may block O_2 adsorption and could be responsible for the decline of activity over Pt{111}. It is postulated that steps destabilise this structure, weakening its interaction with platinum and therefore increasing ORR activity by allowing O_2 adsorption to occur at more positive potentials. This may explain the initial increase in activity observed between Pt{111} and Pt{755}.

As well as disrupting the terrace OH feature, the voltammetry in figure 1 shows that increasing step density results in a growth of peaks at 0.22 V and 0.85 V (vs. Pd/H). The peak at 0.22 V occurs in the potential range where H_{upd} is also occurring at Pt{111} terrace sites and therefore this peak is thought of as step sites for H_{upd}. Koper *et. al.* have stated that the sharpness of this peak indicates attractive interactions between the adsorbates which would seem unlikely between hydrogen atoms alone [25]. They also noted that the formation of H_{ads} at the step is a reaction which should not shift with pH on the RHE scale, whereas a large pH dependency is observed experimentally. To take into account these factors, it was suggested that the sharp peaks that occur at low potentials over stepped {111} surfaces are due to the replacement of H_{ads} with O_{ads} and/or OH_{ads} and therefore O/OH_{ads} are present at the step sites of [Pt n{111}x{100}] surfaces at low potentials [25, 29]. The O/OH_{ads} ratio at the step is not known

and there is no direct spectroscopic evidence for the above description, nevertheless this interpretation does account for the observed voltammetry.

After initial oxidation of the step site at 0.22 V, it is further oxidised at 0.85 V. According to the interpretation given above, this oxidation is occurring at steps which already have OH/O_{ads} present. Therefore further oxidation at 0.85 V would lead to formation of a step with greater O_{ads}, either by oxidation of OH_{ads} or by oxidation of platinum sites not already covered by OH/O_{ads}.

Figure 1 shows that the 0.85 V peak is the largest for the most stepped surface, Pt{211}. Figure 2(b) shows that in the potential range of this peak 0.8 - 0.9V, the activity for ORR is affected. At the foot of this peak, at 0.8 V, the Pt{211} surface has the highest activity, equivalent to Pt{755} and Pt{533}. After this peak, at 0.9 V, the Pt{211} surface now exhibits lower ORR activity than either Pt{755} and Pt{533}. The surface process responsible for this peak seems to affect the oxygen reduction reaction detrimentally. The Pt{755} surface, which has a smaller peak for this process, has the highest activity for the ORR at potentials above 0.8 V. This negative relationship between step oxide formation and the ORR has also been mentioned previously in reference [22].

These results imply that the ORR activity on [Pt n{111}x{100}] surfaces is a balance of disrupting the long range OH/H_2O over-layer structure on terraces, which increases the activity, and the high potential oxidation of step sites, decreasing activity at high potentials. The Pt{755} surface has the optimum balance of these competing effects, moderate disruption of the terrace over-layer structure and moderate step oxidation at high potentials, explaining its high activity throughout the kinetic and mixed kinetic-diffusion controlled regime.

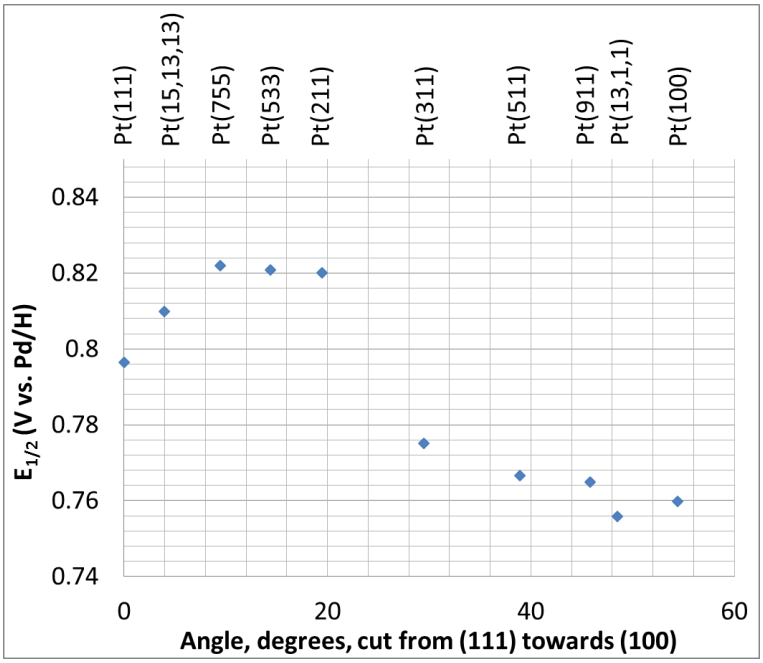

Figure 3. $E_{1/2}$ of [Pt n{111}x{100}] and [Pt n{100}x{111}] surfaces vs. the angle of the cut used in their creation. Error in $E_{1/2}$ = +/-2mV.

3.1.2.1.2 CV and ORR of [Pt n(100)x(111)]

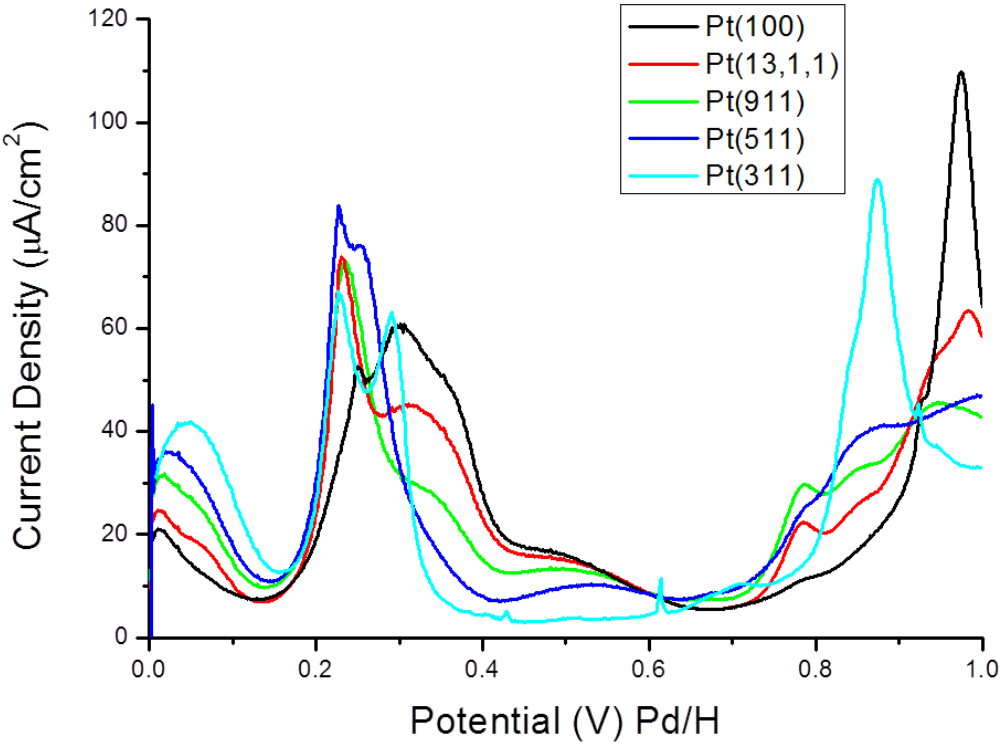

Figure 4. Voltammetry of [Pt n{100}x{111}] surfaces in contact with 0.1 M perchloric acid electrolyte, sparged with N_2 and an applied scan rate of 50 mVs^{-1}.

Figure 4 shows the voltammetric profiles of [Pt n{100}x{111}] stepped surfaces in 0.1 mol dm^{-3} perchloric acid. The most stepped surface, {311}, lies on the turning point in the zone and therefore could equally be considered as belonging to both the [Pt n{100}x{111}] and [Pt n{111}x{100}] series of surfaces (where n = 2). Here though, it shall be considered as a Pt[2{100}x{111}] as its ORR activity will be shown to fit in with the [Pt n{100}x{111}] trend. The voltammetry of this series matches previous reports [30, 31].

The features of the voltammetry of the basal plane Pt{100} surface, as well as the other voltammetry in the series are summarised in reference [31]. With regards to the Pt{100} surface shown in black in figure 4, charge displacement studies indicate that peaks below 0.4 V are associated with H_{ads} formation and the 'bump' between 0.4 - 0.6 V being ascribed to anion adsorption, most likely OH_{ads} in perchloric acid [31, 32]. In contrast to Pt{111}, where there is separation of these two process, Pt{100} exhibits significant overlap of H_{ads} and OH_{ads} [33]. Much less work theoretical has been carried out concerning the structure of the Pt{100}-OH_{ads}/H_2O interface in comparison to Pt{111}. Nevertheless, DFT predicts a complex OH_{ads}-H_2O interfacial layer exhibiting long-range interactions, despite the mismatch between Pt{100}'s square atomic arrangement and water's preferred hexagonal arrangement [34]. This interfacial layer was found to be important in modelling Pt{100}'s ORR activity [34].

Increasing the step density in this series causes many changes in voltammetry. Firstly, H_{ads} occurring at Pt{100} terraces diminishes at 0.3 V and a new peak (relating to the step) grows at 0.22 V, the same potential observed in the [Pt n{111}x{100}] series. As the symmetry of the Pt{100}x{111} step is also the same, the explanation used in the previous section will be used for the nature of this peak. Namely, the replacement of step H_{ads} with OH/O_{ads}. Increasing step density also diminishes the charge associated with OH_{ads} at {100} terraces and shifts it to more positive potentials. This results in separation of previously overlapping H_{ads} and OH_{ads} features, as also noticed in reference [31]. This separation becomes obvious at Pt{911}, where n = 5, and complete separation of the two features is observed in the voltammetry from the Pt{511} surface, where n = 3. These two surfaces exhibit a current minimum at ~0.4 V, between the H_{ads} and OH_{ads} terrace features. This positive shift in OH_{ads} could be interpreted as disruption of an ordered {100}-OH_{ads}/H_2O terrace interfacial layer by the presence of steps, as was the case for the [Pt n{111}x{100}] series discussed previously. Even if an ordered

interfacial layer is not present, the positive potential shift still implies weaker OH_{ads} binding upon increasing step density. The onset potential of OH_{ads} formation has been shown in many studies to be a determining factor in ORR activity [35, 36].

The large peak at ~0.95 V is associated with the electrooxidation of OH_{ads} at {100} terrace sites and therefore, diminishes with step density. O_{ads} is the likely product of this oxidation. This feature will not be considered in great detail as it occurs at a potential where the oxygen reduction activity has already diminished to zero. The peak centred at 0.85 V (again the same oxidation potential observed in the [Pt n{111}x{100}] series) grows with step density and is due to further oxidation of the step site. As this step site is considered to be already covered by OH/O_{ads}, further oxidation should increase the O_{ads} coverage.

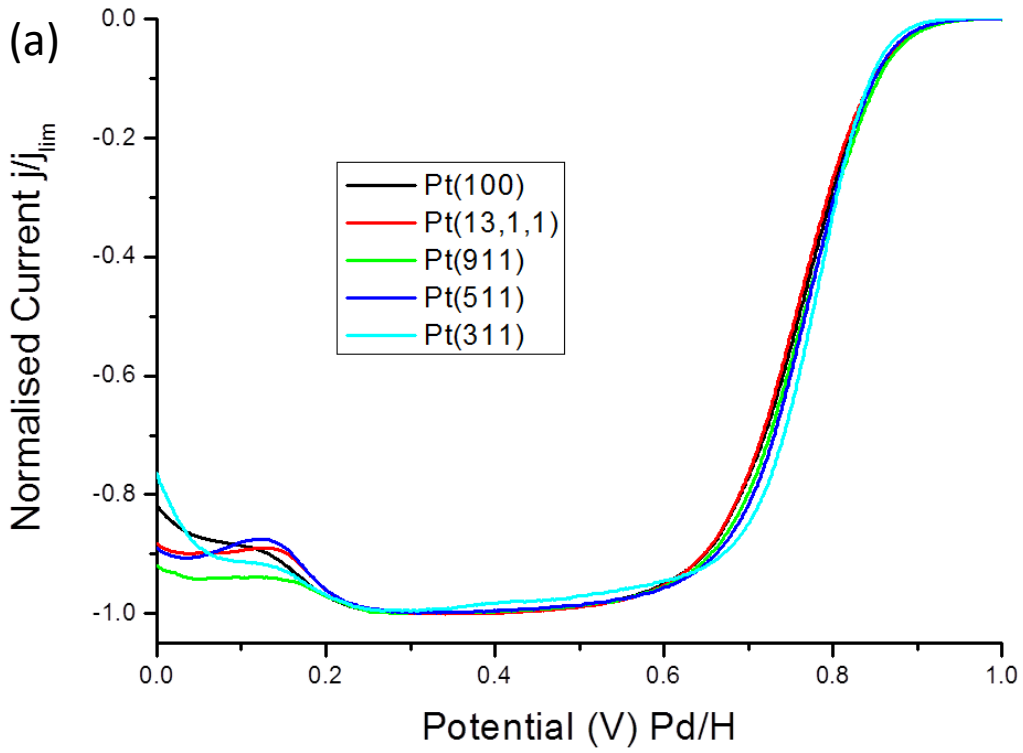

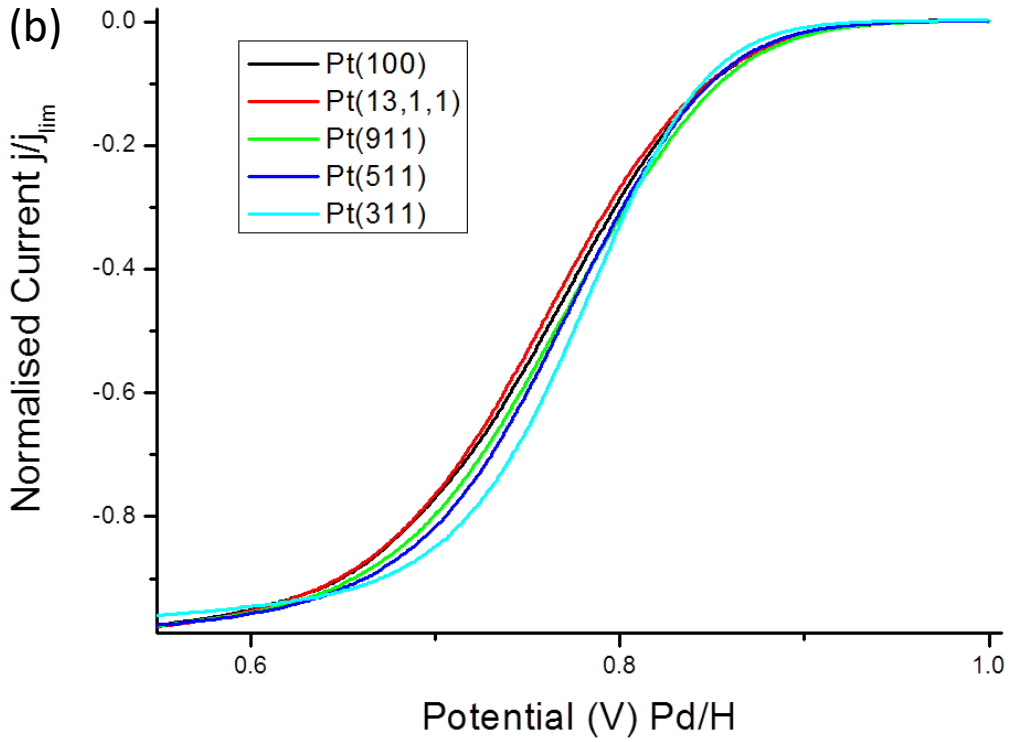

Figure 5. Rotating disc electrode oxygen reduction reaction voltammetry in 0.1 M perchloric acid of [Pt n{100}x{111}] surfaces shown in figure 4. A 1600 rpm rotation rate, 30 mVs^{-1} scan rate and 1 atm oxygen pressure were implemented. (a), top, shows the whole potential range used, whereas (b), bottom, shows a close up of the kinetic/mixed kinetic diffusion regimes.

[Pt n{100}x{111}] surfaces give rise to lower ORR activity in perchloric acid than the [Pt n{111}x{100}] and [Pt n{111}x{111}] series, as seen from figure 3 and in other studies [6, 7, 22]. The activity of the [Pt n{100}x{111}] series (see figure 5, above) also diminishes over a larger potential range than [Pt n{111}x{100}], ~ 0.6 - 0.9 V in comparison with ~ 0.7 - 0.9 V. Figure 4 shows that 0.6 V corresponds with completion of the OH_{ads} layer on Pt{100}. Therefore, OH_{ads} electrosorption at terraces is concurrent with the initial decrease in activity, as was observed with Pt{111}. Pt{13,1,1} shows negligible change in ORR activity and activity begins to increase at Pt{911}, where n = 5 is the average terrace width. At potentials less than 0.8 V, a general increase in activity is observed upon increasing step density which correlates well with the positive shift in OH_{ads} formation discussed above. Therefore, a bond strength weakening of site blocking {100}-OH_{ads} and/or the disruption of a stable {100} terrace OH_{ads}/H_2O interfacial layer are consistent explanations for the increase in activity observed at these potentials.

Between 0.8 - 0.9 V, the electrooxidation at step sites exerts a substantial effect on ORR activity and the general increase in activity with step density is no longer seen. In this potential range the Pt{311} surface displays the lowest activity, lower even than Pt{100}, and also the largest oxidation peak at ~0.85 V. Again it is shown that oxidation at steps causes this great decrease in activity at low overpotentials.

An alternative explanation for the trends observed in ORR activity over both the [Pt n{100}x{111}] and [Pt n{111}x{100}] electrode surfaces is that the step sites are more active than terraces. Increasing step density increases would then increase the amount of high activity step sites, resulting in a positive shift of the ORR curve. These high activity steps sites are then blocked as they are oxidised at larger potentials. It is currently not known whether either terrace or step sites dominate the ORR activity, or whether they exhibit comparable activity.

3.1.2.1.3 Tafel Plots

Changes in Tafel slope are traditionally interpreted as changes in reaction mechanism or rate determining step. For the ORR over Pt{*hkl*}, it has been shown that changes in Tafel slope are not explained by mechanistic effects, but by the interference of OH/O_{ads} [6, 37]. These species interfere with the reaction within the potential range where Tafel analysis is performed, between the kinetic and the mixed kinetic-diffusion controlled region. OH/O_{ads} may completely block O_2 adsorption or may let O_2 reduction proceed, but with a greatly reduced rate compared to the clean platinum surface. OH/O_{ads} may also affect neighbouring platinum sites electronically. The effects of adsorbed species on Tafel slopes have been described by Markovic *et. al.* [37]. In that work, the interference of OH adsorption on Tafel analysis on Pt{111} was modelled in perchloric and sulphuric acid. It was shown that when Tafel analysis of the ORR is performed on Pt{111} in sulphuric acid, a single slope is observed over a large potential range (> 550 mV) due to the constant coverage of sulphate. As the underlying surface is constant, this enabled a valid Tafel analysis. However on Pt{111} in perchloric acid, the range at which Tafel analysis is performed does not correspond to an unchanging surface. OH_{ads} coverage was shown to increase from 10% at 0.7 V to 45% at 0.9 V. The potential dependence of adsorbate coverage on Pt{111} was used in this study to model the kinetic parameters of ORR on an adsorbate free surface and to estimate electronic effects of adsorbates on the neighbouring sites. It was suggested that the Tafel slope of around 80 – 90 mV found on

Pt{111} in perchloric acid deviates from the intrinsic value of 120 mV found in sulphuric acid due to the site blocking and electronic effects of OH_{ads} in the potential range of Tafel analysis. In this study it was concluded that a 1 electron reduction is the rate determining step in both sulphuric and perchloric acid when these effects are taken into consideration. An intrinsic j_0 for an adsorbate free Pt{111} of 8 – 20 μAcm^{-2} was obtained. Although this process has given good results for Pt{111} applying the same process to stepped surface would be more complicated as OH_{ads} adsorption often overlaps with O_{ads} and the identity of species at the steps is not certain. [37]

Tafel plots were utilised by Feliu *et. al.* in order to extrapolate exchange current density (j_0) values for [Pt n{100}x{111}] and [Pt n{111}x{100}] surfaces [7]. These j_0 values were then used as a measure of activity for these surfaces. Tafel slope values of approximately 90 mV were obtained for the [Pt n{111}x{100}] series and ~120 mV for [Pt n{100}x{111}]. Although these values are higher than those found in this study (see figures 6(a)-(d)), the [Pt n{100}x{111}] series did exhibit consistently higher Tafel gradient values than the [Pt n{111}x{100}] surfaces. It is not clear from Feliu's work from which part of the curve the Tafel slopes were taken.

Figures 6(a)-(d) show that the Tafel slope is very sensitive to the potential range chosen. The results below are therefore split into two regions where markedly different Tafel slopes were observed, the high and low overpotential regimes (relating to the potential range before and during step OH/O_{ads}, formation observed in the deoxygenated voltammetry, respectively). Gradients are highlighted for the basal plane (Pt{100} and Pt{111}) and most stepped surfaces (Pt{211} and Pt{311}) for ease of comparison. The gradients were chosen where the best linear fit was observed over a wide potential range. Wider potential ranges resulted in significant deviation from linearity and narrower potential ranges did not improve the fit.

The results below show that the basal plane electrodes, Pt{111} and Pt{100}, match a straight line fit best, at both low and high overpotentials. This is because they exhibit no step OH/O_{ads}, which would interfere with Tafel analysis at low overpotentials. For Pt{111}, in the low overpotential region (-235→-335 mV overpotential = 945-845 mV vs. PdH), a Tafel slope of 54 mV/decade is seen. As the step density increases the value of the slope in this potential systematically decreases, to 43 mV/decade for the most stepped Pt{211} surface. Tafel slope changes are also seen on [Pt n{100}x{111}] surfaces. In contrast, Pt{100} exhibits a Tafel

slope of 85 mV/decade in the -270 mV→-400 mV overpotential range (910-780 mV vs. PdH) and Pt{311} exhibits a Tafel slope of 55 mV/decade.

The most stepped surfaces were difficult to fit to a straight line and exhibited very low Tafel slope values at low overpotentials. As stated previously [7], low Tafel slopes are not taken to signify that the rate determining step occurs later in the reaction mechanism over stepped surfaces, they signify the interference of OH/O_{ads}. Therefore, the low slope values observed at low overpotentials over the most stepped surfaces are due to increasing $\theta_{OH/O}$ at step sites which have either no or very low oxygen reduction activity. The effect of OH/O_{ads} on oxygen reduction is most obvious for Pt{311}, as the potential range at which it turns from most active in the [Pt n{100}x{111}] series to least active is 0.8 - 0.85 V (see figure 5), which correlates exactly to the potential range of formation of step oxide. The effect that this has on its Tafel plot is shown in Figures 6(c) and (d), where it is seen that this surface dislays the greatest deviation from linearity. Its rapid diminution of activity at low overpotentials is demonstrated by its low Tafel slope value.

The interference of OH/O_{ads} described here makes extrapolation to find j_0 very subjective and therefore j_0 values are not reported. The same conclusion was arrived at in reference [6], where j_0 values were found to be unreliable and instead $E_{1/2}$ values were used as an indicator of activity.

(a)

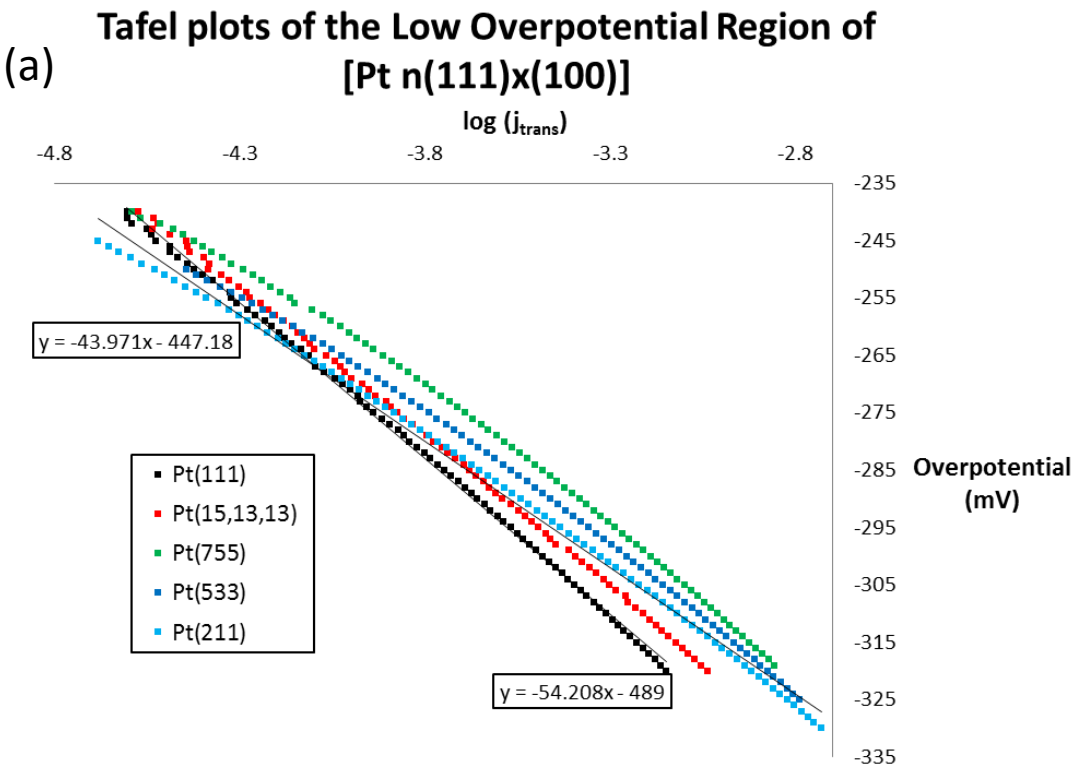
Tafel plots of the Low Overpotential Region of [Pt n(111)x(100)]
log (j_trans)
-4.8
-4.3
-3.8
-3.3
-2.8
-235
-245
-255
-265
-275
-285
-295
-305
-315
-325
-335
Overpotential (mV)
y = -43.971x - 447.18
y = -54.208x - 489
Pt(111)
Pt(15,13,13)
Pt(755)
Pt(533)
Pt(211)

(b)

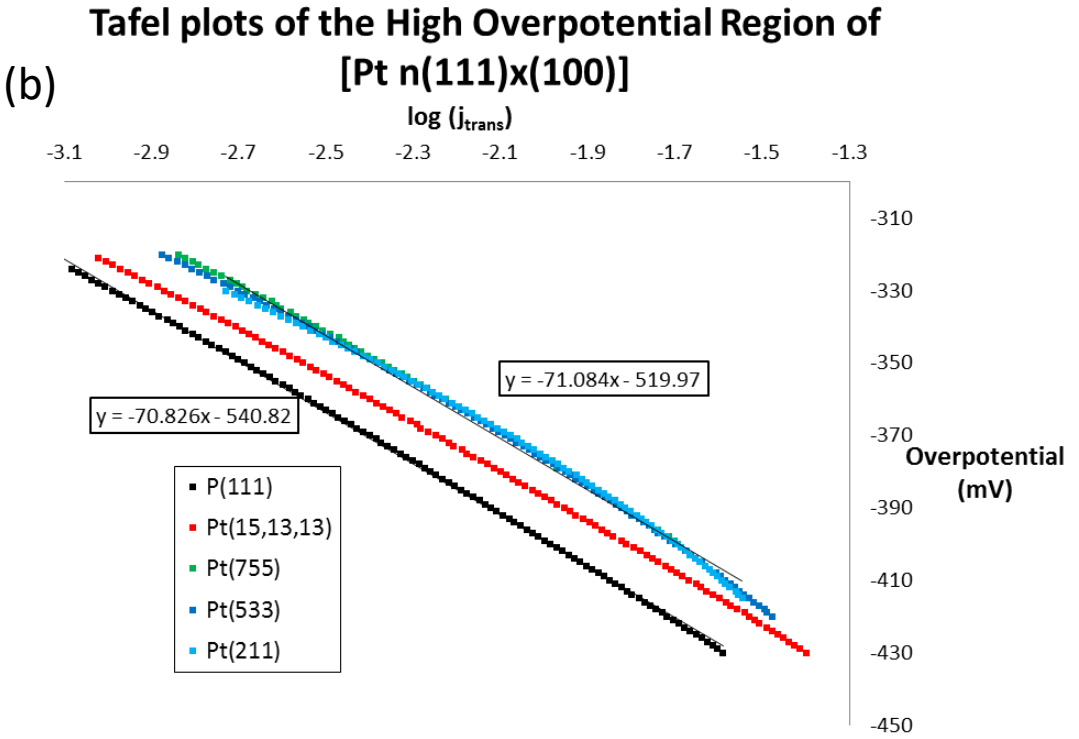
Tafel plots of the High Overpotential Region of [Pt n(111)x(100)]
log (j_trans)
-3.1
-2.9
-2.7
-2.5
-2.3
-2.1
-1.9
-1.7
-1.5
-1.3
-310
-330
-350
-370
-390
-410
-430
-450
Overpotential (mV)
y = -71.084x - 519.97
y = -70.826x - 540.82
P(111)
Pt(15,13,13)
Pt(755)
Pt(533)
Pt(211)

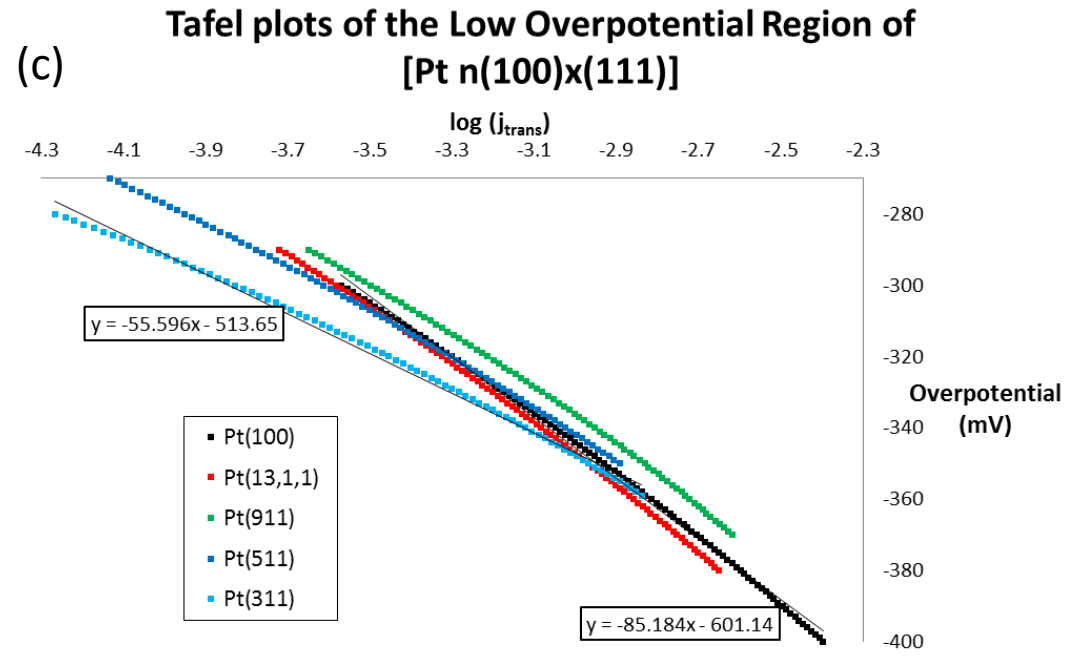

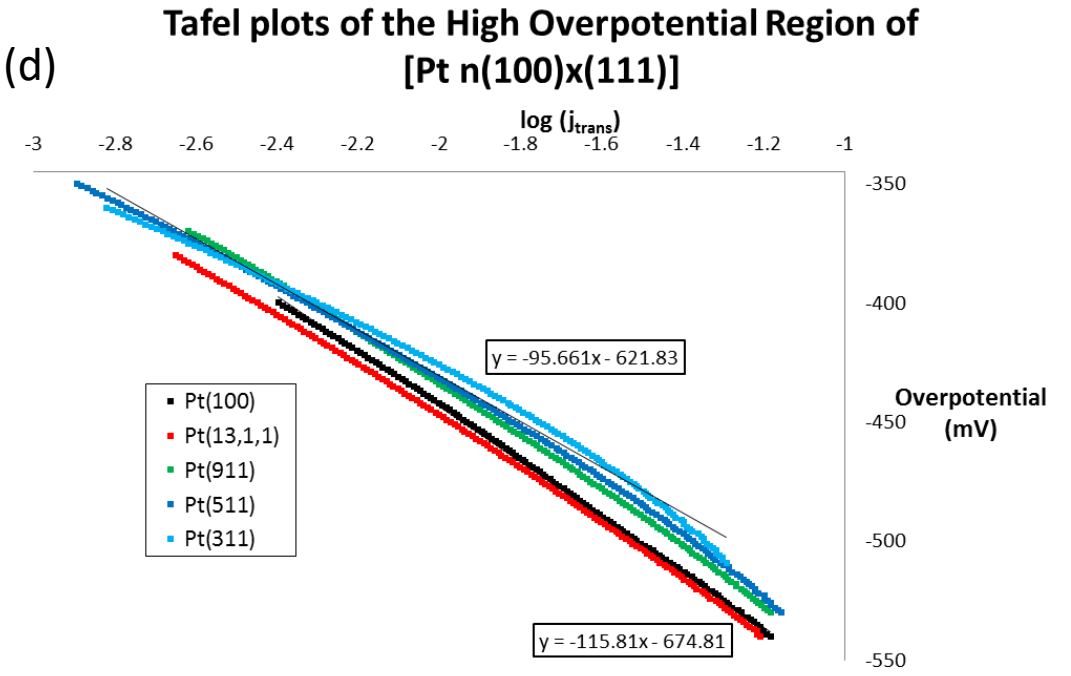

Figure 6(a) - (d), top to bottom. Tafel plots for the ORR activity of [Pt n{111}x{100}] and [Pt n{100}x{111}] surfaces in the high and low overpotential regimes.

3.1.2.2 Hydrogen Peroxide Oxidation/Reduction Reaction (HPORR)

3.1.2.2.1 HPORR of [Pt n(111)x(100)] and [Pt n(100)x(111)]

The results for the activity of [Pt n{111}x{100}] and [Pt n{100}x{111}] single crystal surfaces towards hydrogen peroxide oxidation/reduction show that at potentials below 0.85 V the 2 electron reduction of hydrogen peroxide occurs, validated by the variation of limiting current with rotation rate (Koutecky-Levich analysis).. In the low potential H_{upd} region (0 - 0.3 V) of the [Pt n{111}x{100}] series of surfaces the changes observed are similar to those observed in the ORR. The current drops most for Pt{111} and less so the more stepped the surface. Oxygen reduction at a H_{upd} covered surface has been shown to form hydrogen peroxide in a two electron process [38]. Therefore at low potentials, the oxygen reduction heads towards half of the liming current due to the switch from 4 electron reduction to 2 electron reduction process (see figure 2). For hydrogen peroxide reduction, the Pt-H formed by H_{upd} over [Pt n{111}x{100}] surfaces seems to act as a site blocking species, with the current tending towards 0 at lowest potentials. The HPORR of the [Pt n{100}x{111}] series of surfaces show little change in the H_{upd} region, with only a small reduction in the limiting current compared to potentials above 0.3 V. Clearly, H_{upd} formation is less detrimental to peroxide reduction over Pt{100} terraced surfaces than over Pt{111} terraced surfaces.

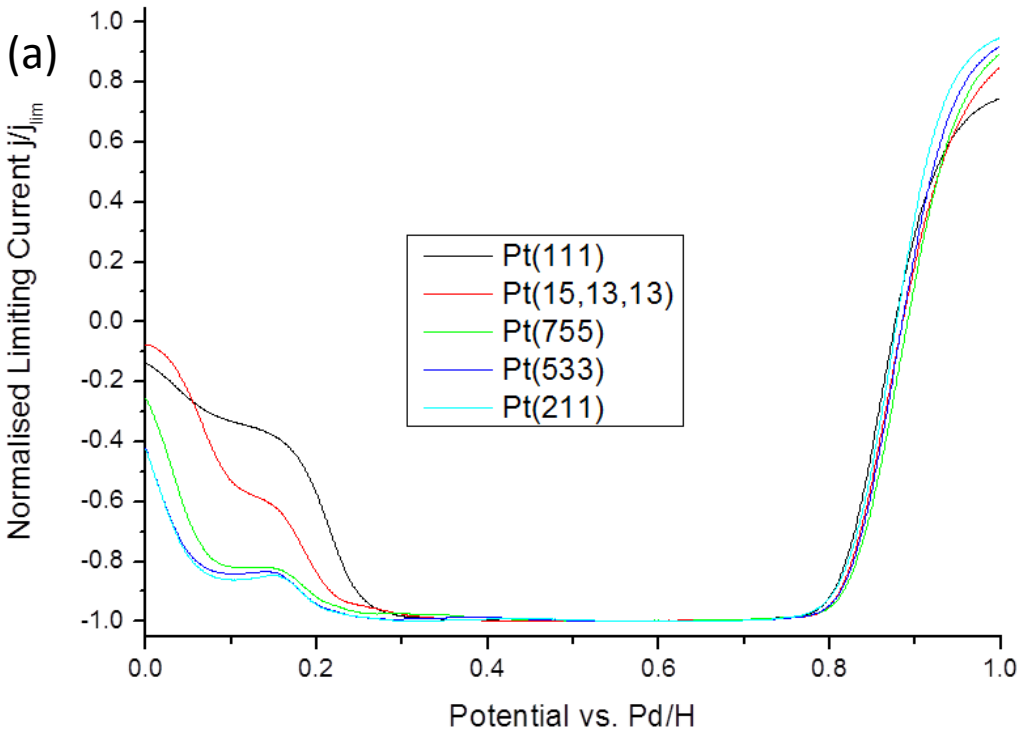

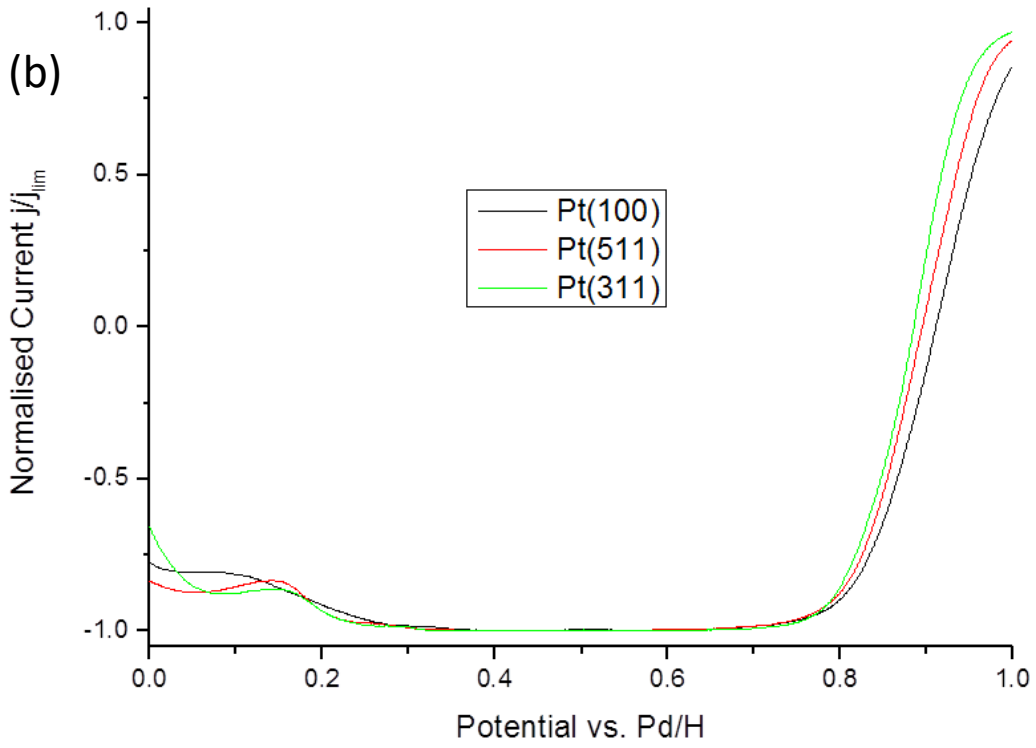

Figure 7(a) and (b). Rotating disc electrode hydrogen peroxide oxidation/reduction voltammetry in 0.1 M perchloric acid of (a), [Pt n{111}x{100}], and (b), [Pt n{100}x{111}] surfaces. A 1600 rpm rotation rate, 30 mVs^{-1} scan rate and a 10^{-3} M hydrogen peroxide concentration were used. The electrolyte was sparged with nitrogen.

It has been shown that under standard conditions the two electron reduction of peroxide to produce water according to the reaction below has an equilibrium potential of 1.763 V (vs. RHE) [17, 20].

$$H_2O_2 \xrightarrow{+(2H^+ + 2e^-)} H_2O$$

Therefore the potentials where hydrogen peroxide reduction occurs in figure 7 are far below the equilibrium potential and the reaction should proceed very quickly. Hydrogen peroxide oxidation to oxygen, below, occurs with an equilibrium potential of 0.695 V [17, 20] and therefore this reaction should occur at potentials greater than this.

$$H_2O_2 \xrightarrow{-(2H^+ + 2e^-)} O_2$$

A study of the HPORR over polycrystalline platinum showed that at potentials between 0 - 1.5 V there is always a massive thermodynamic driving force for either the reduction or oxidation of hydrogen peroxide in solution [17]. Whether oxidation or reduction does proceed depends

on the state of the platinum surface, with hydrogen peroxide reduction theorised to only occur over platinum with no OH_{ads} present. At potentials greater than 0.695 V, hydrogen peroxide oxidation only proceeds when oxidised platinum sites are present on the surface and therefore these act as oxidation catalysts. When OH_{ads} is formed at the surface, a diffusion limiting oxidation current is quickly reached as the potential of their formation is far above the hydrogen peroxide oxidation equilibrium potential. The 'switch over' potential between both states was therefore found to be a probe of the oxidation state of the platinum electrode. [17]

Over [Pt n{111}x{100}] surfaces, the $E_{1/2}$ for hydrogen peroxide reduction (normalised limiting current = - 0.5 in figure 7(a)) moves positive upon increasing the step density. Pt{15,13,13} exhibits a reduction curve that is more positive than Pt{111}. Pt{755} has the most positive reduction curve in the series. Upon further increasing the step density the $E_{1/2}$ for hydrogen peroxide reduction then moves negative and therefore Pt{533} and Pt{211} give rise to more negative values than Pt{755}. This trend mirrors the $E_{1/2}$ changes observed with step density for oxygen reduction observed previously. Therefore the same mechanism may be responsible for the hydrogen peroxide reduction changes: i.e. a breaking up of a protecting $(\sqrt{3}\times\sqrt{3})R30°$ OH ad-layer by the presence of steps enables adsorption and reduction of hydrogen peroxide at higher potentials. This effect is present at low step density. Upon further increasing the step density, formation of step PtO decreases reduction activity.

Between 0.8 and 1V, the hydrogen peroxide reaction switches from reduction to oxidation over all the stepped and basal plane surfaces examined. [Pt n{111}x{100}] surfaces exhibit increasing oxidation current between 0.9 - 1V as step density is increased. Figure 7(a) shows that the most stepped surfaces approach the limiting current for oxidation at lower potentials than Pt{111}, which does not reach the limiting current for oxidation within the potential window used. It has been shown that PtO has to form on Pt{111} at > 1V for the limiting oxidation current to be reached [20, 39]. Surface oxides show greater activity for oxidation of hydrogen peroxide, as seen by the fact that stepped surfaces form oxides at lower potentials and show greater current at around 1 V. The workers in the study of hydrogen peroxide on polycrystalline platinum mentioned above [20, 39] attributed the switch as a change from peroxide reduction over bare platinum to peroxide oxidation over Pt-OH. These results show that peroxide oxidation occurs over Pt-O and reduction can still occur over Pt-OH sites. Feliu has recently reported that Pt oxides play a role in hydrogen peroxide oxidation on Pt{111} [20] and this work also showed that it is these species that are more important for the switch from hydrogen peroxide reduction to oxidation than OH. This is not to say that OH species do not

play some part in peroxide oxidation. Figure 7(a) shows that Pt{111} oxidises peroxide below 1V, at potentials where only Pt-OH is present on this surface.

The [Pt n{100}x{111}] series of surfaces exhibit a HPORR wave which is more positive in potential than [Pt n{111}x{100}] surfaces. This is in contrast with the ORR, where the waves for [Pt n{100}x{111}] surfaces are significantly more negative with respect to [Pt n{111}x{100}]. This highlights a fundamental difference between the oxygen reduction and hydrogen peroxide reduction reaction. Different surface species are also shown to affect these reactions over Pt{111} and Pt{100} surfaces. To elaborate, it was concluded that the same surface species, Pt-OH, inhibits both oxygen and hydrogen peroxide reduction. Over Pt{100} however, oxygen reduction begins to attenuate after Pt-OH formation and hydrogen peroxide reduction is unaffected by this surface process. It is only when Pt{100} oxide formation begins that hydrogen peroxide reduction current decreases.

This is made more obvious when the ORR and HPORR reactions are compared directly. Figures 8(a) and (b) below show ORR, HPOR and CV on the same scale. Raw data for the HPORR is used, CVs are scaled (20x) and the ORR is modified so that its limiting current matches double that of the hydrogen peroxide reduction reaction due to the 2 vs 4 electron processes. These figures show clearly that for Pt{111}, oxygen and hydroxide reduction die off after OH_{ads} formation at 0.74V and that hydrogen peroxide reduction over Pt{100} is unaffected by OH_{ads}. The current for oxygen reduction is already close to zero when O_{ads} formation begins over Pt{100}. This illustrates the different inhibiting species for these reactions. The reason that Pt-OH acts as an inhibiting species in the reduction of oxygen but not peroxide over Pt{100} is not known.

These results indicate that if hydrogen peroxide is an intermediate in the ORR then it would immediately be consumed at the electrode surface, either through reduction to water or oxidation to oxygen. At high potentials in the ORR, two electron reduction of oxygen to form hydrogen peroxide would be then followed by two electron oxidation to oxygen and therefore zero overall current would be observed. This is a possible explanation for the low activity of Pt surfaces for the ORR.

Other experiments have shown that a soluble intermediate is formed during oxygen reduction at high potentials [8, 40]. It is unlikely that hydrogen peroxide is responsible for this due to its instability to oxidation at the electrode surface at these potentials. The $OOH^{\bullet}$ radical has been suggested for its origin, which may then be reduced aqueously via the reaction

$$OOH^{\bullet} + \mathrm{H}^{+} + \mathrm{e}^{-} \leftrightarrow PtH_2O_2$$

This has been suggested as the reaction which connects the HPORR to the ORR, where formation of the $OOH^{\bullet}$ species is the rate determining step of the ORR [8, 40].

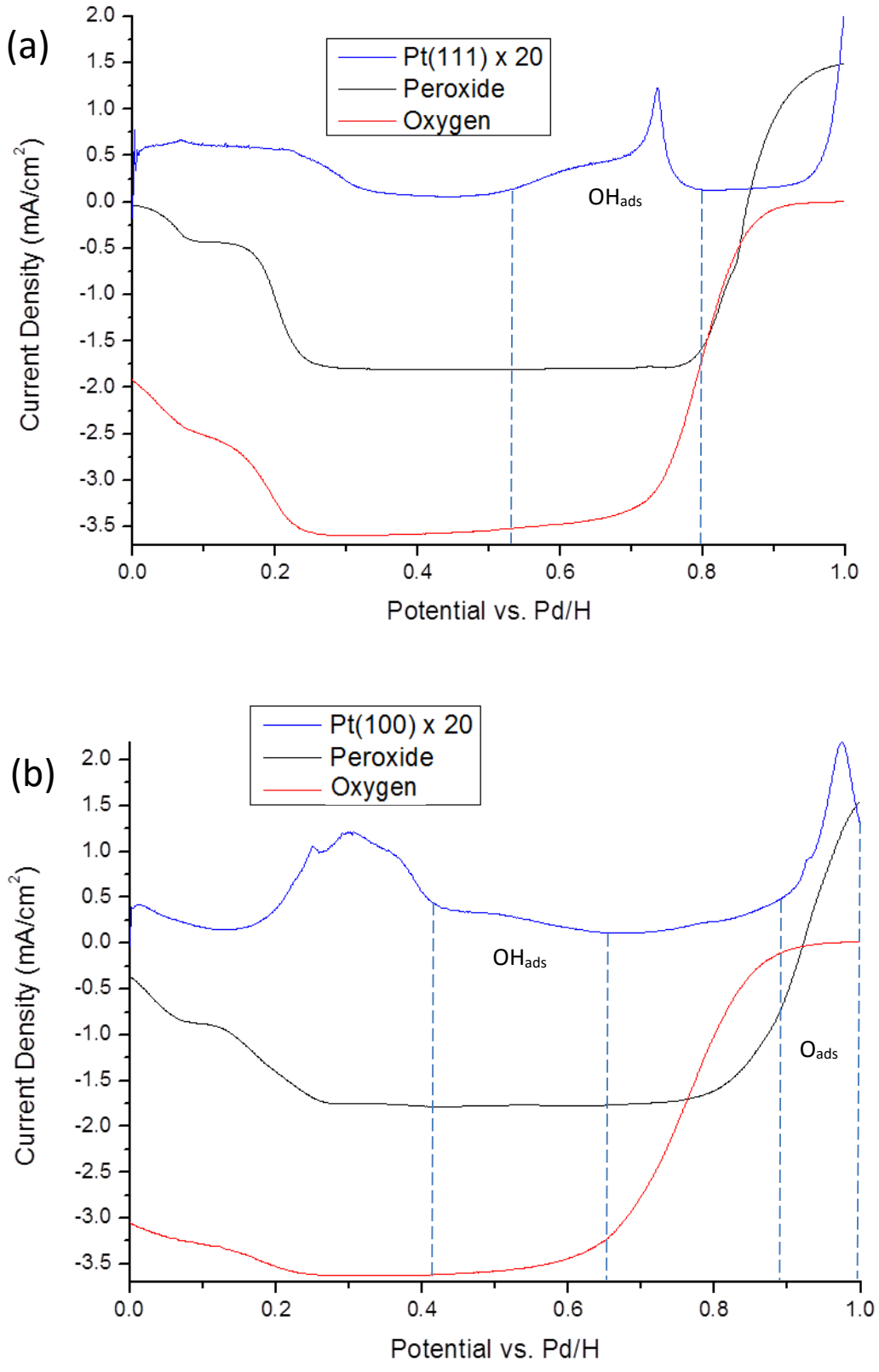

Figure 8(a) and (b). Cyclic voltammetry, ORR and HPORR profiles of the, (a), Pt{111} and, (b), Pt{100} surfaces. Experimental parameters are identical to those shown in previous figures. CV current has been multiplied by 20 and ORR current divided to match double the limiting current of the HPORR curve so that all data can be compared on the same graph. Raw data of the HPORR results were used.

Figures 9(a)-(d) show the Tafel slopes for the HPORR. Approximately the same Tafel slope was observed for all [Pt n{111}x{100}] surfaces at low potentials, 60 mV/dec, where hydrogen peroxide reduction takes place (60 mV/dec was also found to be a good fit to experimental data found in reference [39]). At this potential range only small changes are observed in Tafel slopes as the changes in OH_{ads} coverage over stepped surfaces have little effect on the reaction. This should be compared with figure 6(b), where all [Pt n{111}x{100}] surfaces exhibited a similar Tafel slope (~70 mV/dec) for oxygen reduction. At high potentials (hydrogen peroxide oxidation), figure 9(b) shows that greater changes in Tafel slope occur with step density. The gradient of these slopes becomes smaller with increasing step density, as was the case for oxygen reduction at low overpotentials (see figure 6(a)). Pt oxide species are clearly responsible for the changes in slope observed for these surfaces.

The [Pt n{100}x{111}] series of surfaces show smaller changes in Tafel slope with increasing step density. Tafel slopes of between 80 – 90 mV/dec are observed for hydrogen peroxide reduction and 60 - 80 mV/dec observed for oxidation. The smaller slope values obtained at high potentials indicate the effect of Pt oxide.

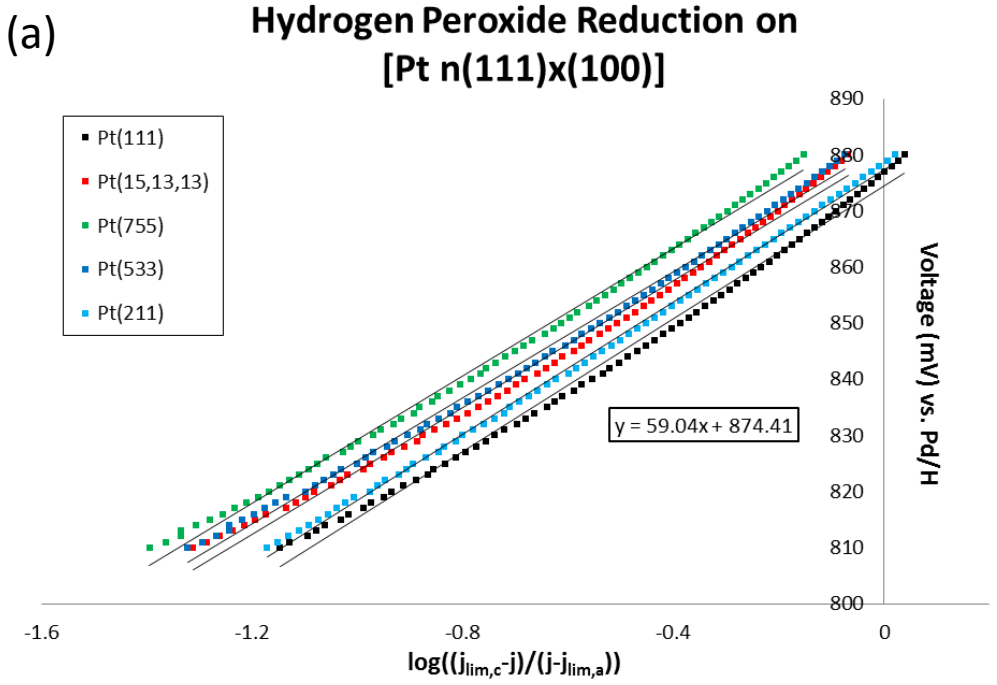

(b)

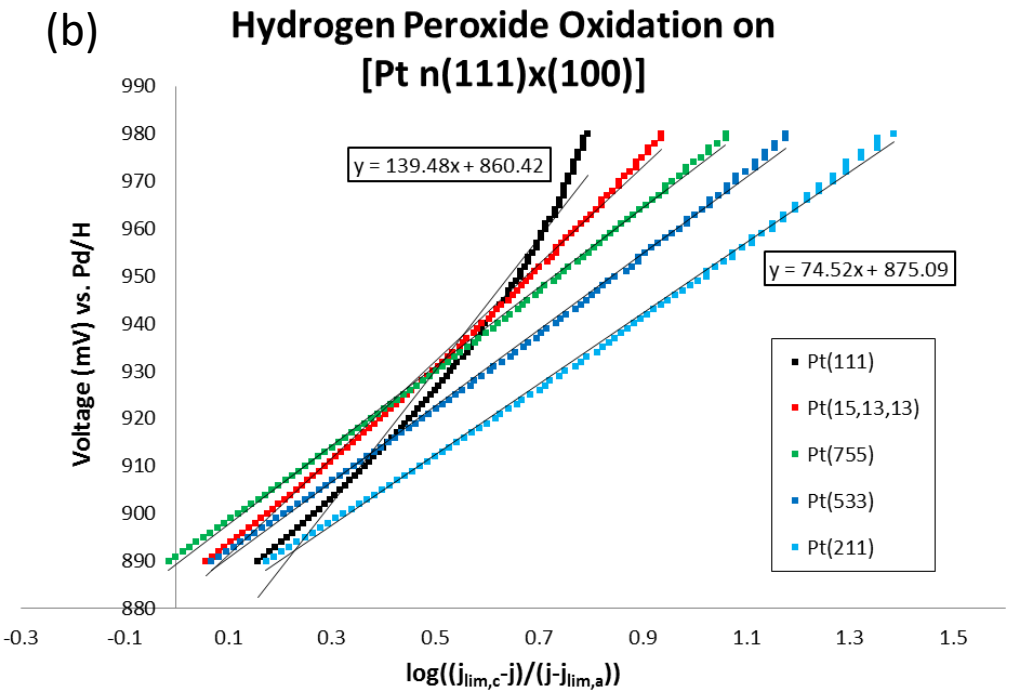
Hydrogen Peroxide Oxidation on [Pt n(111)x(100)]
y = 139.48x + 860.42
y = 74.52x + 875.09
Pt(111)
Pt(15,13,13)
Pt(755)
Pt(533)
Pt(211)
Voltage (mV) vs. Pd/H
log((j_lim,c-j)/(j-j_lim,a))

(c)

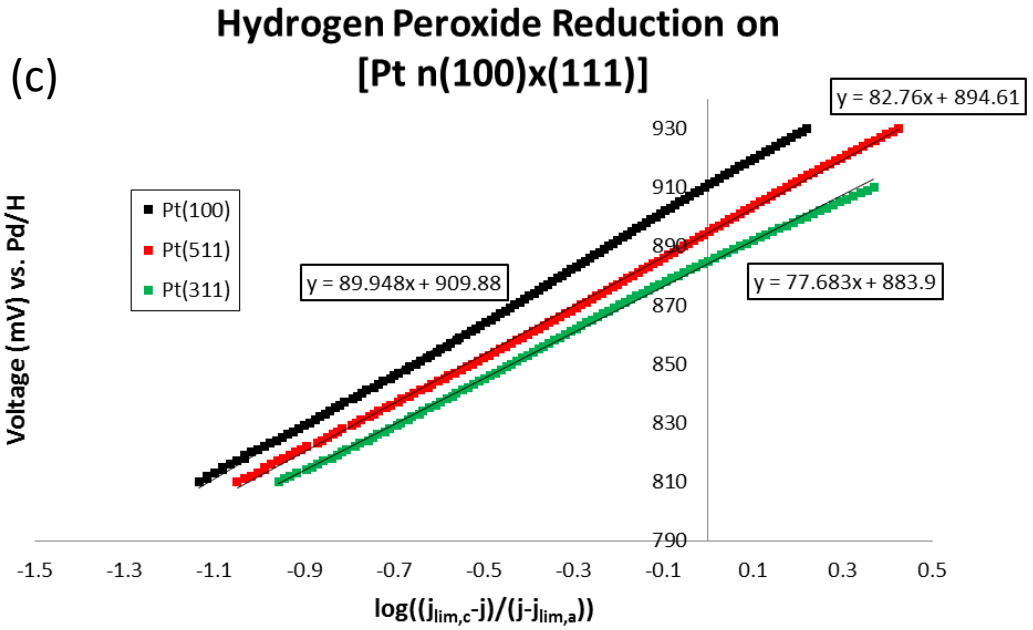
Hydrogen Peroxide Reduction on [Pt n(100)x(111)]
y = 82.76x + 894.61
y = 89.948x + 909.88
y = 77.683x + 883.9
Pt(100)
Pt(511)
Pt(311)
Voltage (mV) vs. Pd/H
log((j_lim,c-j)/(j-j_lim,a))

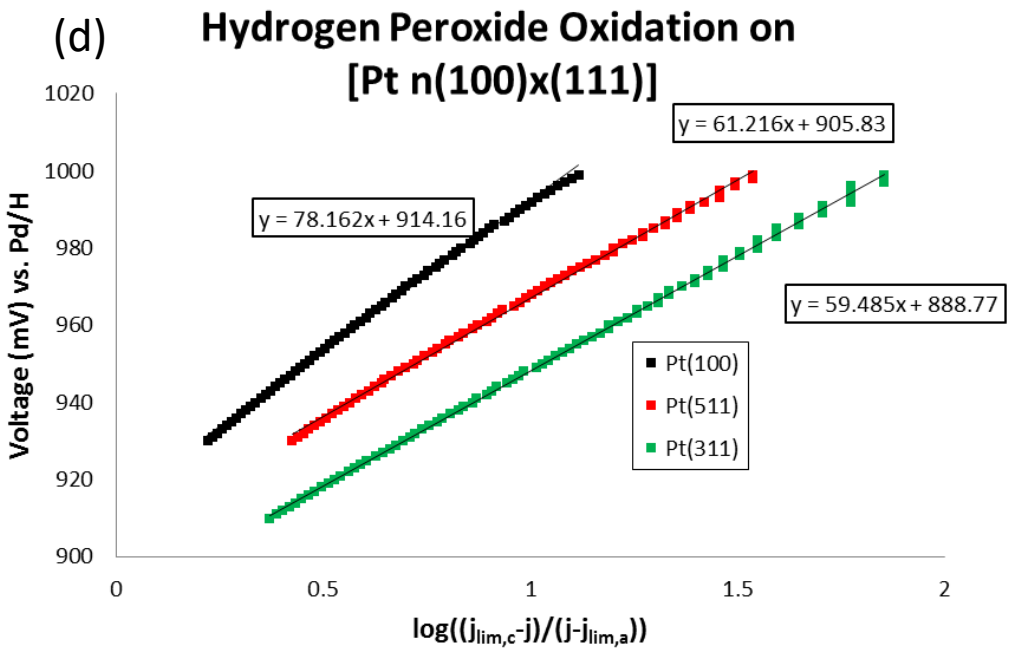

Figure 9(a) - (d), top to bottom. Tafel analysis of the HPORR activity of [Pt n{111}x{100}] and [Pt n{100}x{111}] surfaces in reduction and oxidation potential regimes.

3.1.3 Conclusions

This work has shown parallels between the ORR and the hydrogen peroxide (an intermediate in the ORR) oxidation/reduction reaction, HPORR, over the [Pt n{100}x{111}] and [Pt n{111}x{100}] series of surfaces. It is found that steps' disruption of terrace OH increases ORR activity at large over-potentials over both series of surfaces. PtO species on step sites, which gives rise to a peak at ~0.85 V on both [Pt n{100}x{111}] and [Pt n{111}x{100}], are found to be responsible for the sharp decline in activity for the ORR at low overpotentials. With [Pt n{111}x{100}] surfaces, hydrogen peroxide reduction is shifted to positive potentials with increasing step density and oxidation current increases at potentials above 0.9 V. Although the HPORR results here do not prove that hydrogen peroxide is an intermediate in the ORR, some comments can be made. Firstly, HPORR results indicate that if hydrogen peroxide were formed in the ORR over [Pt n{111}x{100}] and [Pt n{100}x{111}] surfaces, its subsequent reduction to water would attenuate between 0.75 and 0.9 V. Secondly, above 0.9 V, hydrogen peroxide would rapidly oxidise to oxygen, resulting in zero net current overall. These results also indicate that different surface species influence the ORR and HPORR activity over the [Pt n{111}x{100}] and [Pt n{100}x{111}] series.

3.2 Single Crystal Pt{111}-M Bimetallic Surfaces for ORR (Where M=Ni, Co, or Fe)

PtM overlayers (where M = Fe, Co or Ni) supported on Pt{111} were prepared via the thermal annealing in either a nitrogen/water or hydrogen ambient with a dilute aqueous droplet containing M^{Z+} cations attached directly to the electrode. Two different PtM phases were detected depending on the nature of the cooling environment post-anneal. The first of these consisted of small (< 20 nm), closely packed microcrystals comprised of a central metallic core and a shell several monolayers thick of mixed metal oxides/hydroxides. The second type of PtM phase was prepared by cooling in a stream of hydrogen gas. Although this second phase also consisted of numerous microcrystals covering the Pt{111} electrode surface, these were both flatter than before and moreover were entirely metallic in character. A positive shift in the onset of PtM oxide formation correlated with increased activity towards ORR which we ascribe to the greater availability of platinum metallic sites under ORR conditions.

3.2.1 Introduction

In recent years, platinum bimetallic surfaces have been found to exhibit high activity for the oxygen reduction reaction (ORR) [41-49]. PtNi [35, 50, 51], PtCo [50, 51], PtFe [43, 52] and alloys of platinum with early transition metals such as Pt_3Y [49, 53] and Pt_3Sc [53] in particular have all been shown to exhibit significantly higher activity than pure platinum. Such alloys exhibit weaker OH/oxide binding than pure platinum and this increases the upper potential limit at which metallic platinum sites are available to react with oxygen [35, 43, 47]. As a consequence, the overpotential for the ORR is decreased and for proton exchange membrane (PEM) fuel cells utilising such catalysts, greater energy conversion efficiency results. The weakening of oxide binding is caused by the unique surface structure that these alloys exhibit in that they form a singular selvedge region containing only platinum atoms in the first atomic layer covering an underlying bimetallic phase [35, 43, 47]. This sub-surface phase electronically modifies the topmost surface platinum layer such that its d-band centre is downshifted compared to that of pure Pt [35]. Such an electronic perturbation facilitates weaker oxide adsorption compared to pure platinum.

The method of ORR electrocatalytic enhancement described above has been shown to reduce the overpotential for the ORR of alloy catalysts compared to pure platinum by up to ~100 mV

[47]. Nonetheless, such bimetallic catalysts still require approximately 0.3 V of overpotential to run the ORR at an appreciable rate. Hence, there is much scope in exploring further the change in overpotential of the ORR on platinum as a function of alloying and surface structure in order to optimise electrode activity and stability. In fact much effort is being exerted in growing nanoparticles of specific shape and composition [44, 46, 54-59] based on the original, single crystal alloy results [35, 47, 51] but the systematic control of alloy structure and composition is often still quite challenging. In an effort to bring about a reliable and simple method of controlling both surface structure and composition, Attard *et. al.* had previously introduced a method of thermally annealing aqueous solutions of metal ions attached to a Clavilier bead electrode in the electrochemical cell to facilitate the formation of quasi-crystalline epitaxial thin films supported on Pt{hkl} [60, 61]. Identical results to bulk single crystal alloys could be reproduced using this method [62]. Simple flame-annealing removed all traces of the alloy in most cases allowing for rapid turnaround in surface composition exploration. Using this same procedure, it was envisaged that Pt-M (where M is the second metal) alloys could be created with varying degrees of metal composition in the hope to understand in more detail the effect of alloying on the increase in ORR activity.

In this study the Pt{111}-M (where M = Ni, Co or Fe) systems are investigated using CV, STM, RDE and XPS in order both to reproduce previous studies and to investigate different cooling environments on the M/Pt selvedge region in terms of surface segregation and oxide formation [63]. It is found that the cooling environment of the electrode surface plays a crucial role in determining ORR activity.

3.2.2 Results

3.2.2.1 PtNi{111}

3.2.2.1.1 CV and ORR

In Fig. 10(a) is shown a series of experiments reporting changes in the voltammetric response of a Pt{111} electrode in aqueous perchloric acid as the number of nickel chloride droplet additions/resistive heating treatments is increased up to four. The steady accumulation of a chemisorbed adlayer is revealed via two aspects, namely the gradual attenuation in the intensity of the sharp Pt{111} OH peak at 0.72 V together with electrosorption features ascribable to the

clean surface between 0.5 V and 0.7 V and the emergence of electrosorption states positive of 0.72 V which we assign to the presence of nickel. A slight diminution in hydrogen underpotential deposition (H UPD) intensity between 0.2 V and 0.35 V is also a feature of increased nickel loading on the electrode surface. Fig. 10(b) shows that in fact the increase in electrosorption charge above 0.72 V corresponds to a symmetric, broad peak at 0.87 V. Fig. 10(c) reveals that this peak will continue to increase in intensity as the number of nickel chloride additions is increased although interestingly, the H UPD features associated with the reduced surface remain almost unchanged. We speculated that this behaviour corresponds to the growth of particles of nickel oxide/hydroxide that grow in size (leading to the increase in 0.87 V peak intensity) but that these do not block the underlying Pt{111} surface completely. From Fig. 10(c), small remnants of the sharp 0.72 V clean surface peak may still be discerned indicating that some regions of the electrode surface are ostensibly clean and well ordered. It may be that the nickel adlayer is not uniformly covering the electrode surface after resistive heating and that this phenomenon may be giving rise to the residual, clean Pt{111} voltammetric features reported even at the highest loadings of nickel.

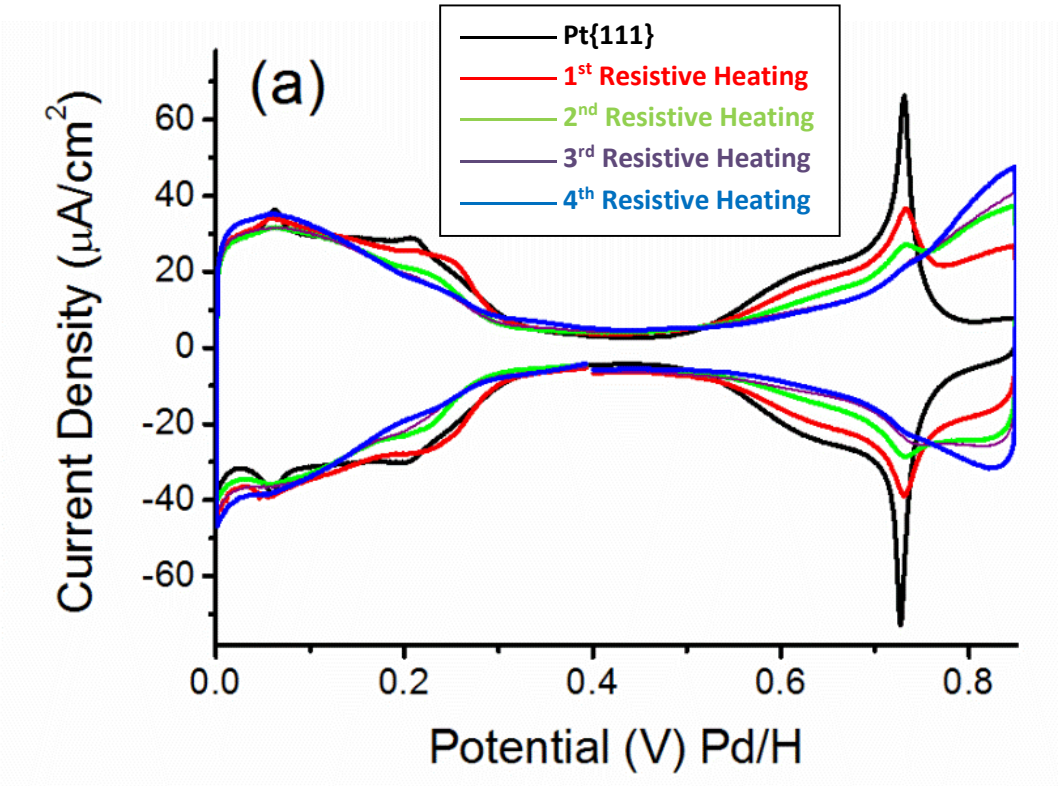

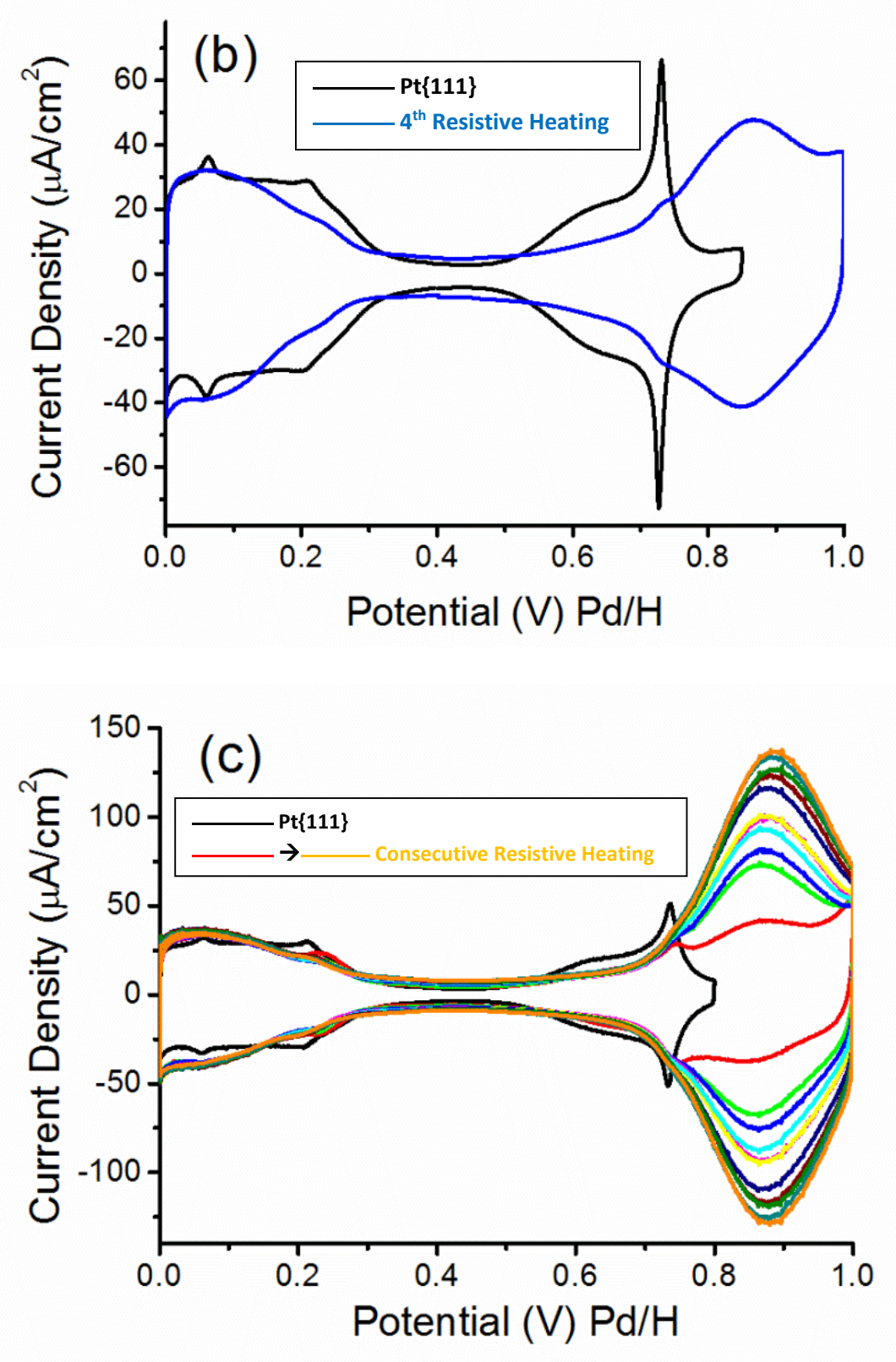

Fig. 10. (a) Cyclic voltammograms of Pt{111} (black) in 0.1 M $HClO_4$ with increasing resistive heating treatments in water/nitrogen ambient of the electrochemical cell (1st, red, 2nd, green, 3rd, purple and 4th, blue). (b) shows a 0 – 1 V scan of the 4th resistive heating treatment. (c) CVs of multiple resistive heating treatments

showing growth in reversible nickel oxide/hydroxide phase after 5th and higher additions of nickel. Sweep rate = 50 mV/s.

In Fig. 11, we compare the electrocatalytic activity towards ORR of Pt{111} and the nickel-modified electrode formed via resistive heating. In contrast to clean Pt{111}, a negative shift in the half-wave potential of the ORR of 150 mV indicates a strong inhibition of the ORR although on both surfaces, a four electron reduction is reported. This is a surprising result since previous work by Markovic and co-workers [35] emphasised that a shift of the OH adsorption peak of Pt{111} to more positive potentials as a result of alloying Ni with Pt should result in a marked increase in ORR activity whereas we observe the complete opposite. Hence, it is unlikely that the PtNi adlayer phase formed by resistive heating corresponds to a metallic PtNi alloy phase although superficially, the 0.87 V feature does appear similar to the feature reported by Markovic and co-workers as OH adsorption but shifted positive relative to the clean surface [35].

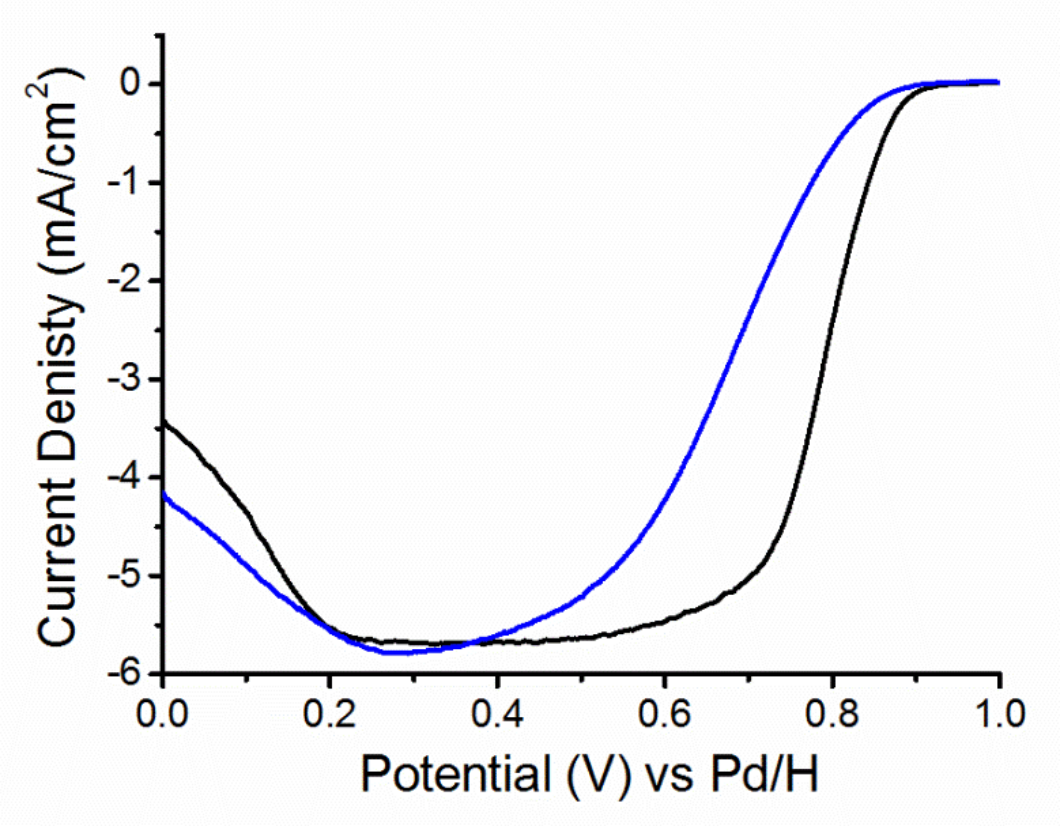

Fig. 11. ORR activity of a clean, well ordered Pt{111} electrode (black) compared with the PtNi oxidised surface depicted in the 4th treatment (blue) of figure 10(a). 0.1 mol dm^{-3} $HClO_4$, scan rate = 30 mV/s, 1 atm O_2, 1600 rpm rotation rate.

In order to try to reproduce the results of ref. [35], it was thought useful to try and reduce the nickel adlayer chemically using hydrogen gas. Clearly, the electrode surface produced above did not possess the electrocatalytic characteristics of a well-ordered $Pt_3Ni\{111\}$ alloy surface and it was necessary to find out why. Therefore, after washing the electrode carefully with ultra-pure water (previously treated with four resistive heating cycles), it was subsequently flame annealed in a Bunsen flame to approximately 900 K and cooled in hydrogen. Fig. 12 shows changes in the nickel adlayer as a result of flame-annealing and cooling in hydrogen. The most obvious change compared to Fig. 10 is that the peak ascribable to increasing nickel loading above 0.7 V is no longer symmetric about the potential axis. In addition, attenuation of all features associated with clean Pt{111} is much more obvious with no trace of the sharp peak at 0.72 V after only four resistive heating treatments for example (signifying break up/blocking of any Pt{111} long range order present at the surface consistent perhaps with greater wetting of the Pt{111} surface by the nickel after the hydrogen exposure). Rather, a greater resemblance to the CV behaviour of $Pt_3Ni\{111\}$ [35] albeit with an increased measure of disorder being present perhaps compared to ref. [35] (as signified by the more asymmetric OH adsorption peaks at potentials >0.7 V).

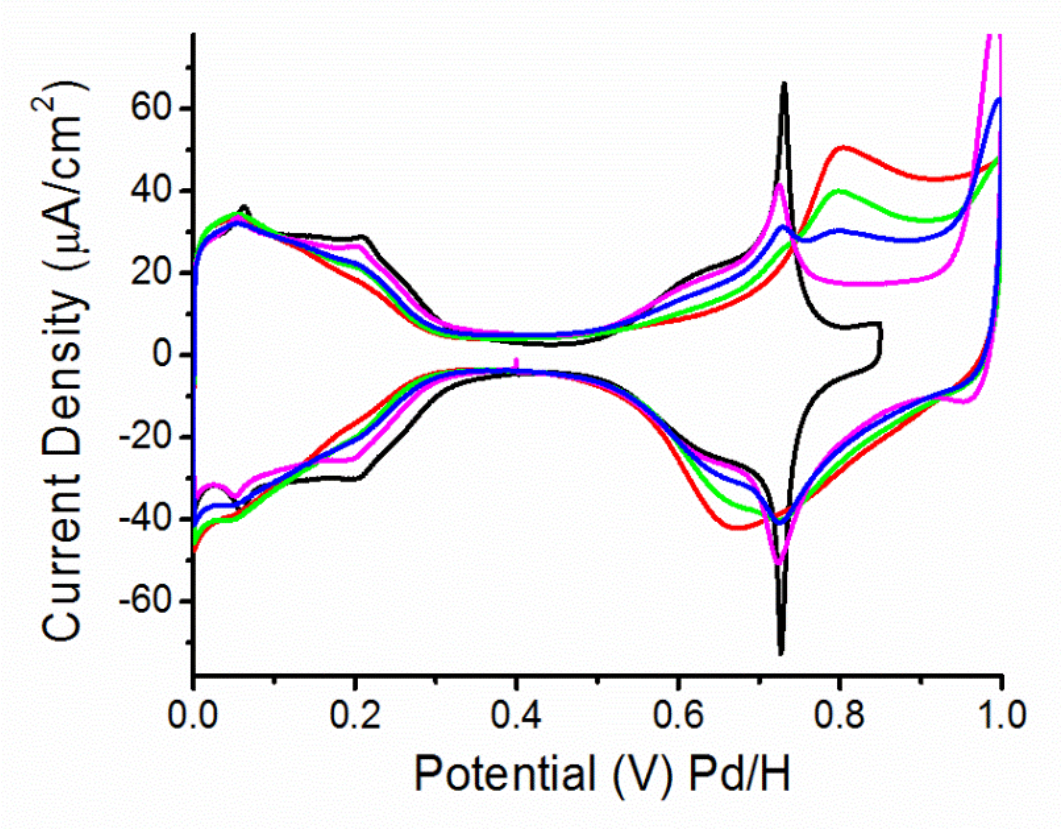

Fig. 12. CVs of Pt{111} electrode surface (black) after consecutive flame annealing to 900 K and cooling in hydrogen of the resistively heated electrodes shown in Fig. 10(b), (1^{st} flame anneal, red, 2^{nd}, green, 3^{rd}, blue and 4^{th}, purple). 0.1 mol dm^{-3} $HClO_4$ scan rate = 50 mV/s.

Continued flaming and cooling in hydrogen recovered the underlying Pt{111} crystal CV response completely demonstrating both the lability of nickel when exposed to air at high temperature and the ease and rapidity with which samples of differing nickel loadings may be prepared. The electrocatalytic activity of the hydrogen reduced nickel adlayer towards ORR was also tested at this stage (Fig. 13) corresponding to the ‘‘4th heating’’ in Fig. 12 whereby the electrosorbed OH peak on the positive-going scan at 0.8 V is at its maximum intensity. It is evident from this result that this time, a marked increase in ORR activity relative to the clean Pt{111} surface is observed with a shift in the half-wave potential towards more positive potentials of 75 mV and a times 10 increase in current density at 0.9 V. This value is commensurate with results obtained by Markovic et al. for well-ordered Pt_3Ni{111} electrodes which exhibited a platinum skin structure [43]. Therefore it is likely that, in contrast to data reported in Fig. 10, the hydrogen reduced surface corresponds to a platinum skin structure also, although this cannot be deduced directly from the ORR overpotential and the CV.

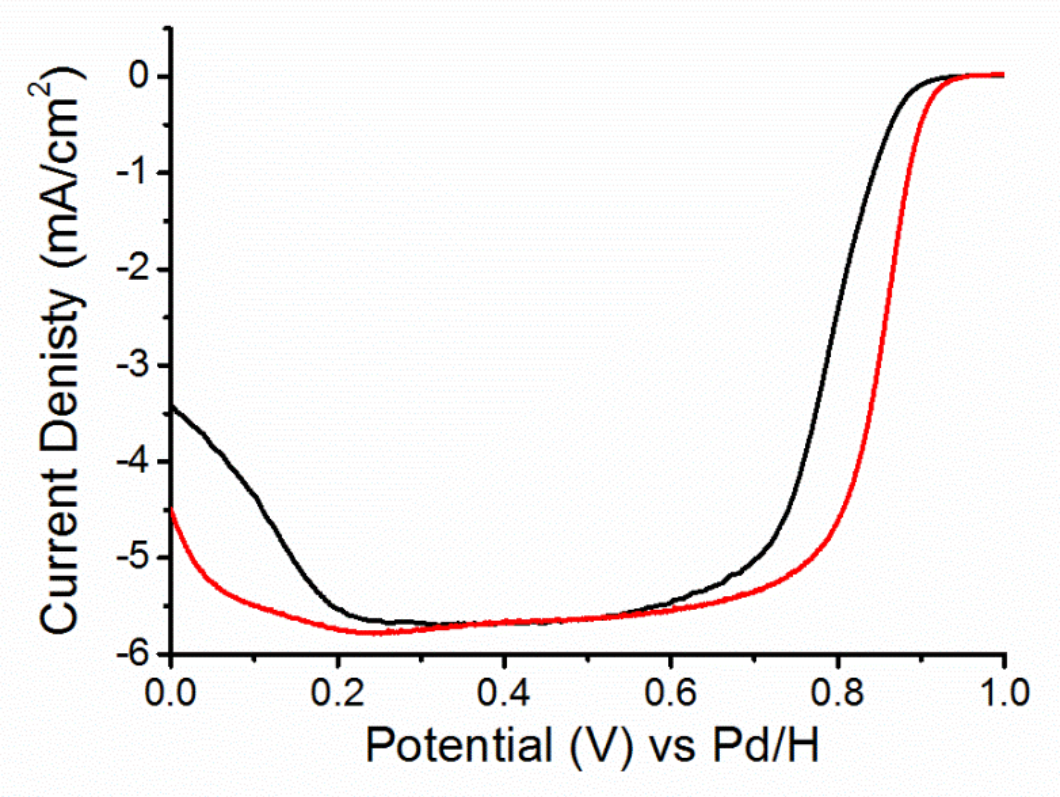

Fig. 13. ORR activity of Pt{111} (black) compared with the PtNi adlayer prepared by flame annealing and cooling in hydrogen of the resistively heated catalyst (1st treatment) in Fig. 12 (red). 0.1 mol dm^{-3} $HClO_4$, scan rate = 30 mV/s, 1 atm O_2, 1600 rpm rotation rate.

Moreover, we deduce that annealing the Pt{111}/ nickel adlayer in a nitrogen/water vapour mixture almost certainly results in surface segregation of nickel rather than Pt followed by the formation of a nickel oxide/hydroxide phase which is much less active for ORR. However, we note here that according to Markovic and co-workers [64], the presence of pure nickel oxide/hydroxide islands on Pt{111} gives rise to redox peaks in the CV (under alkaline conditions) at potentials just negative of the OH peak of Pt{111}. We examined our thermally prepared oxidised PtNi surface in 0.1 M sodium hydroxide and once again, observed the symmetric nickel oxide/hydroxide peak at potentials positive of the Pt{111} OH adsorption peak (not shown). Therefore, we must conclude that the nickel oxide/hydroxide phase in our study is remarkably less oxophillic than pure nickel oxide/ hydroxide. Furthermore, the nickel oxide/hydroxide phase reported in the present study is quite stable towards dissolution in acidic aqueous electrolyte. This behaviour is reminiscent of previous findings by Kibler [63] who demonstrated a difference in the segregation behaviour of PtRu{111} alloy electrodes depending on the annealing environment of the electrode with preferential segregation of Ru under oxidising conditions. The ORR that was observed in Fig. 11 may therefore be ascribed to residual Pt{111} sites that are not covered by the nickel oxide/hydroxide phase. This interpretation also suggests that the nickel oxide/hydroxide phase formed is not reducible electrochemically at room temperature and potentials of 0 V due to a large activation energy barrier. It should be noted that repeated flame-annealing of the electrode surface corresponding to Fig. 13 caused a gradual shift in the ORR wave to more negative potentials as mentioned above (not shown). This suggested the gradual removal of all nickel from the selvedge and the eventual recovery of the clean Pt{111} CV. It was also noticed that a gradual attenuation in the magnitude of the 0.8 V OH electrosorption peak alluded to earlier in Fig. 12 was correlated with this effect such that the maximum intensity reached in the 0.8 V peak coincided precisely with the most positive potential of the ORR wave. Hence, the amount of nickel present could be systematically changed using this procedure in order to tune electrocatalytic behaviour.

3.2.2.1.2 STM

STM was performed to image the surface of the two PtNi modified Pt{111} electrodes formed by resistive heating and flame annealing/cooling in hydrogen. Fig. 14(a) shows an STM image of the PtNi surface prepared via resistive heating and cooling in the water/nitrogen ambient of the electrochemical cell together with a typical height profile. From previous CV data, this is postulated to be largely a nickel oxide/hydroxide surface terminated phase. But, due to the low oxophilicity observed for this surface (discussed in the previous section), we suggest that the islands observed by STM are actually PtNi alloy particles with preferentially segregated surface nickel that subsequently has undergone oxidation. The size of the islands in Fig. 14(a) is typically 3 – 6 nm with a height of about 0.2 nm commensurate with monolayer islands of nickel oxide/hydroxide sitting proud of a PtNi alloy (see later for XPS support of this interpretation). Fig. 14(b) shows STM images of the catalyst prepared after flame annealing and cooling in hydrogen together with a typical height profile. Steps and terraces are much more clearly observed in this image and the nickel adlayer is much more discernable with the surface exhibiting a ‘‘smoother’’ profile with regular structures being observed over the entire surface. A typical island size this time is 3 nm with a height of 0.3 nm consistent with a 1–2 monolayer average height if the surface consisted of a PtNi metallic phase.

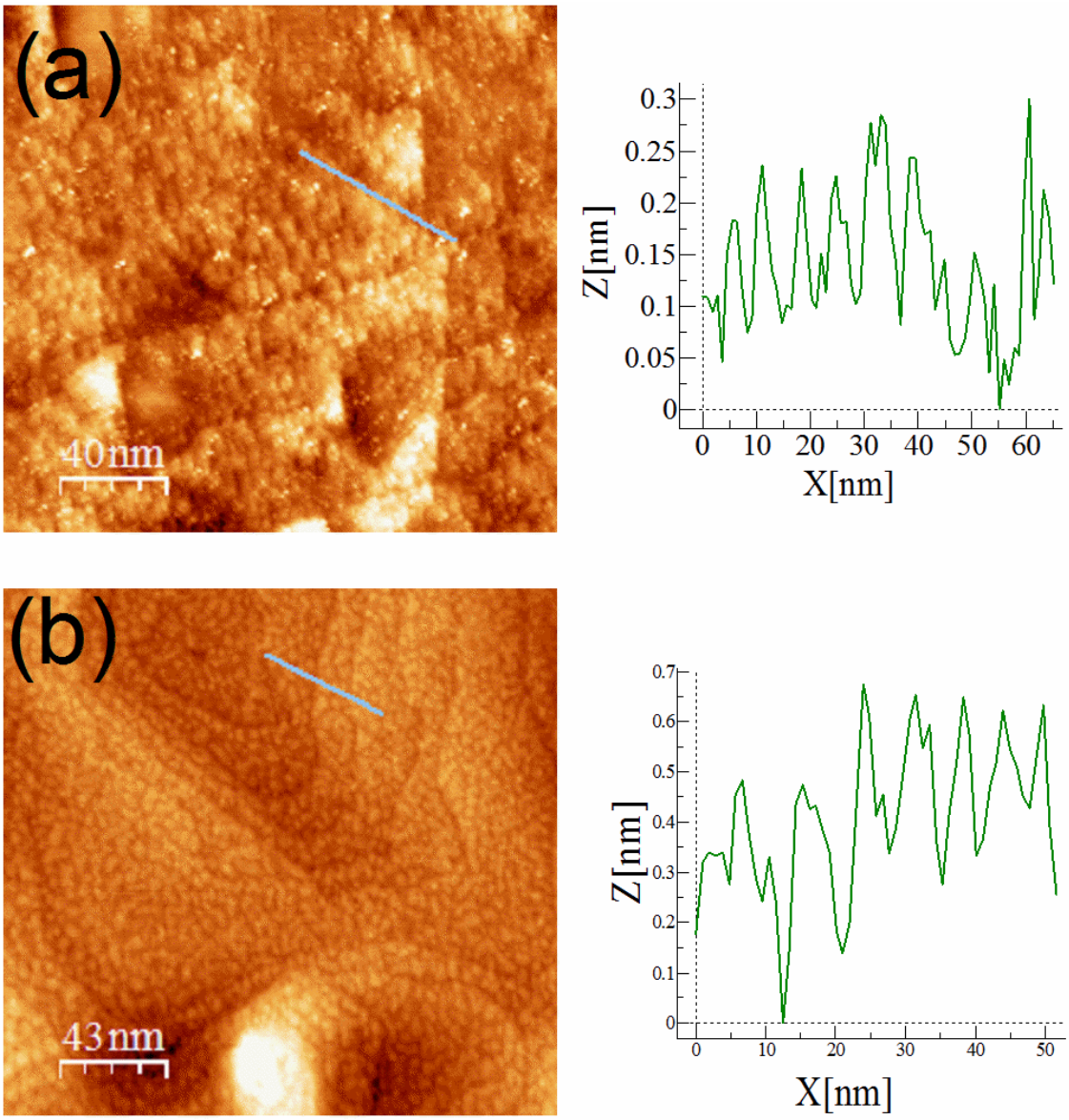

Fig. 14. (a) Shows the STM image of the PtNi modified Pt{111}surface prepared by resistive heating in the electrochemical cell together with a typical height profile. Tunnelling current = 30 nA, tip bias = - 500 mV, scan rate = 4.52 Hz. 14(b) Same except for sample that was subsequently flame annealed at 900 K and cooled in hydrogen. Tunnelling current = 30 nA, tip bias = - 500 mV, scan rate = 5.55 Hz.

3.2.2.1.3 XPS

XPS data were collected ex situ and an argon ion etch profile of each transferred nickel modified electrode surface performed. The data in relation to the resistively heated nickel films is outlined in Fig. 15 which shows the Pt 4f and Ni 2p regions of the XPS peaks after every 30 s of etch together with a plot of surface composition versus time. For the first 30 s of etch, there is always a large jump in the intensities of all peaks which we ascribe to removal of adventitious

impurities on the surface collected during transfer of the samples and pump down of the UHV system (which took several hours). Nonetheless, XPS confirms that the binding energies of the Pt 4f peaks are consistent with metallic platinum whereas those associated with nickel are mainly emblematic of nickel oxide/hydroxide phases. These higher binding energy peaks between 854 and 858 eV are consistent with Ni^{2+}/Ni^{3+} $2p_{3/2}$ states and are ascribed to a mixture of NiO, $Ni(OH)_2$ and NiOOH species [65, 66]. In fact the ratio of oxygen 1s intensity to nickel 2p intensity reveals a range of O/Ni surface stoichiometry for the oxide adlayer of Ni/O of 1.7 ± 0.3 as a function of etch time consistent with the above. What is also noticeable is a gradual increase in the intensity of the Ni(0) peak at 852.6 eV as a function of etch time which indicates that below the oxide surface layer there exists nickel in its metallic state. The results of peak fitting of the oxygen 1s XPS peak corresponding to the etch data is shown in Table 1. After initial argon sputtering, the majority contribution to the overall O 1s region was the 530 eV peak at 70% with minor contributions at 531.5 and 532.5 eV. The 530 eV peak would be consistent with NiO, the 531.5 eV peak to a defective oxide or hydroxide (or both) and the 532.5 eV peak to Ni_2O_3 phase [65, 66]. Hence, the majority phase is almost certainly nickel II oxide/hydroxide with smaller amounts of nickel III oxides being present consistent with the interpretation given previously.

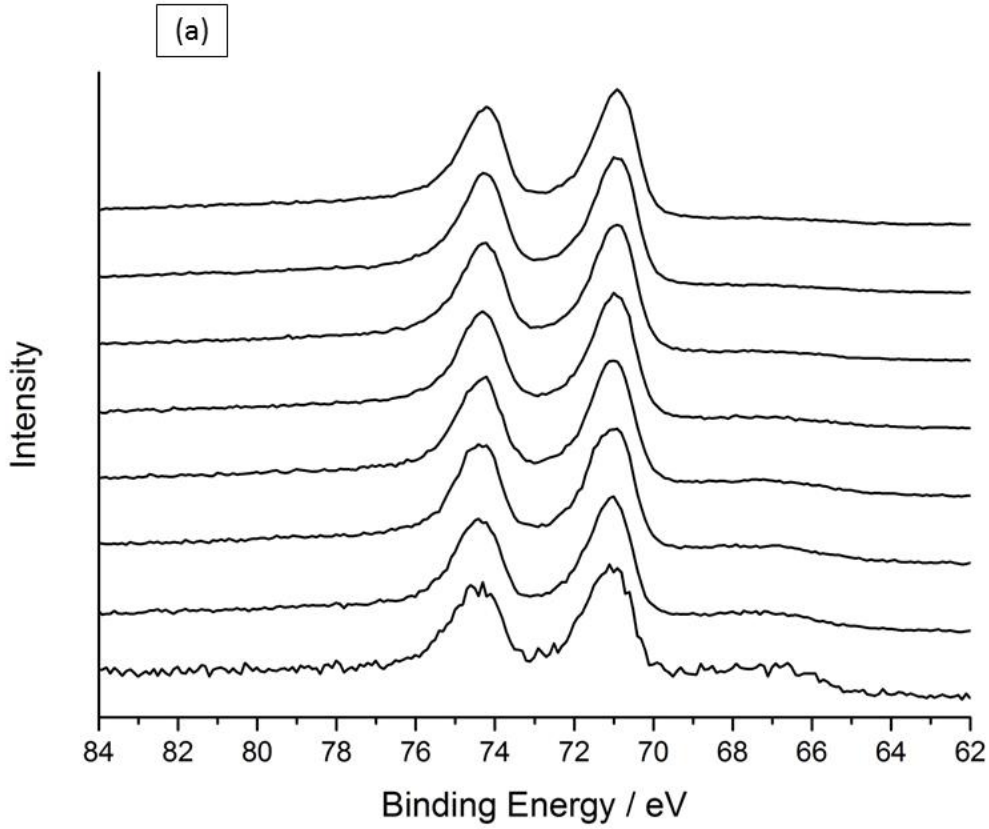

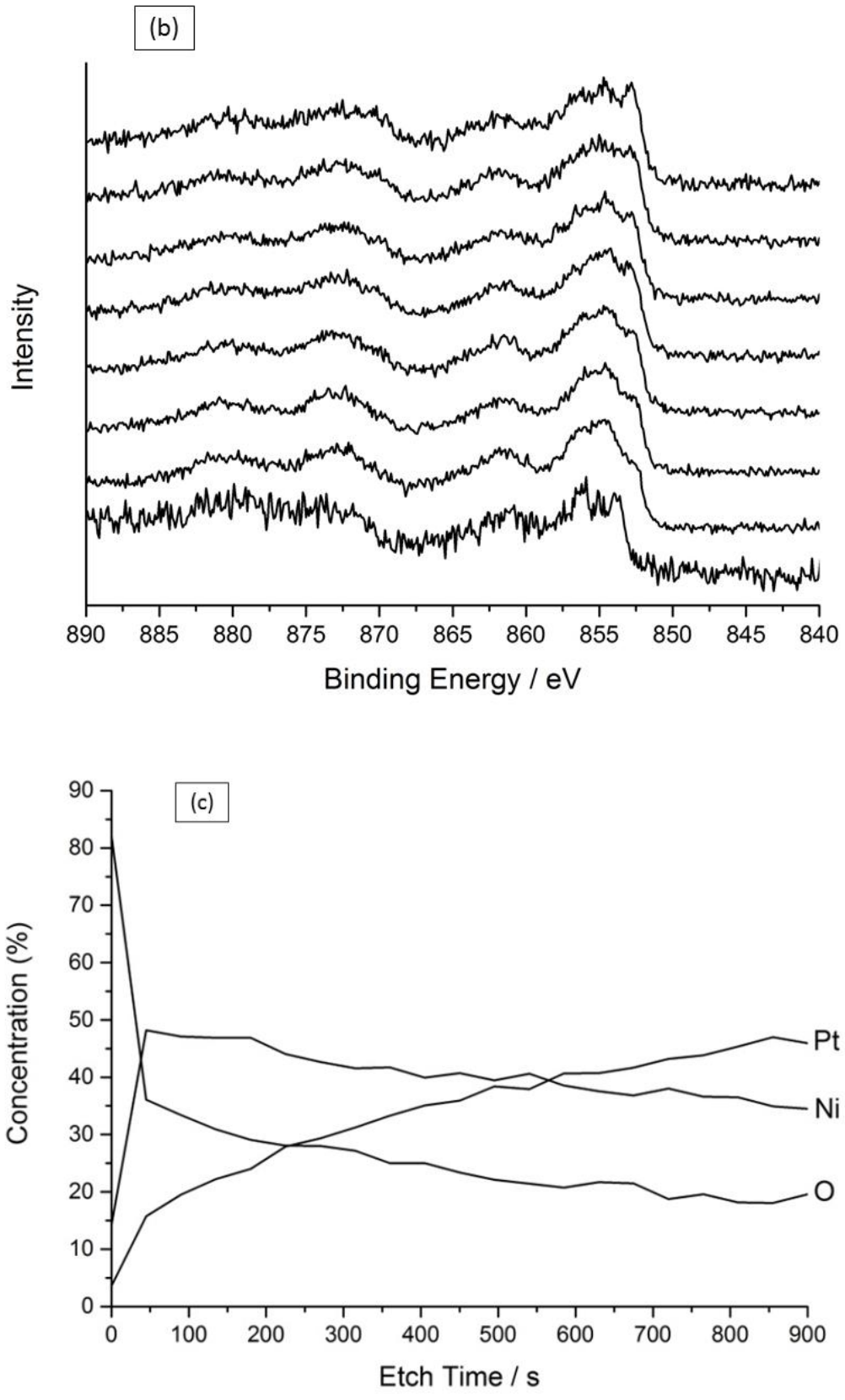

Fig. 15. XPS results for the resistively heated PtNi modified Pt{111} electrode. Figure (a) is of the Pt 4f region as a function of argon etching time. (b) Shows the Ni 2p XPS region as a function of argon etching time. Both

(a) and (b) show spectra normalised to the same intensity. Time intervals for surface etch are 0, 30, 60, 90, 180, 300, 600 and 900 s. (c) Shows how surface composition changes as a function of argon etching time.

In contrast to the XPS results obtained for the resistively heated nickel–modified platinum electrode, when flame-annealed and cooled in hydrogen, inspection of Fig. 16 reveals that both nickel and platinum are reduced to their metallic state. An intense Ni(0) $2p_{3/2}$ peak at a binding energy of 852.5 eV is the major feature of the XPS spectra observed throughout the argon etching process with a constant PtNi composition being observed almost immediately indicating a homogeneous alloy. After sputtering, a constant alloy surface composition of Pt-90%/Ni-10% is observed. Hence, the XPS results confirm our initial hypothesis concerning the nature of the active phase in the ORR for the two types of PtNi adlayer on Pt{111}. The most active phase is the platinum-rich PtNi alloy in which all elements are in their metallic state.

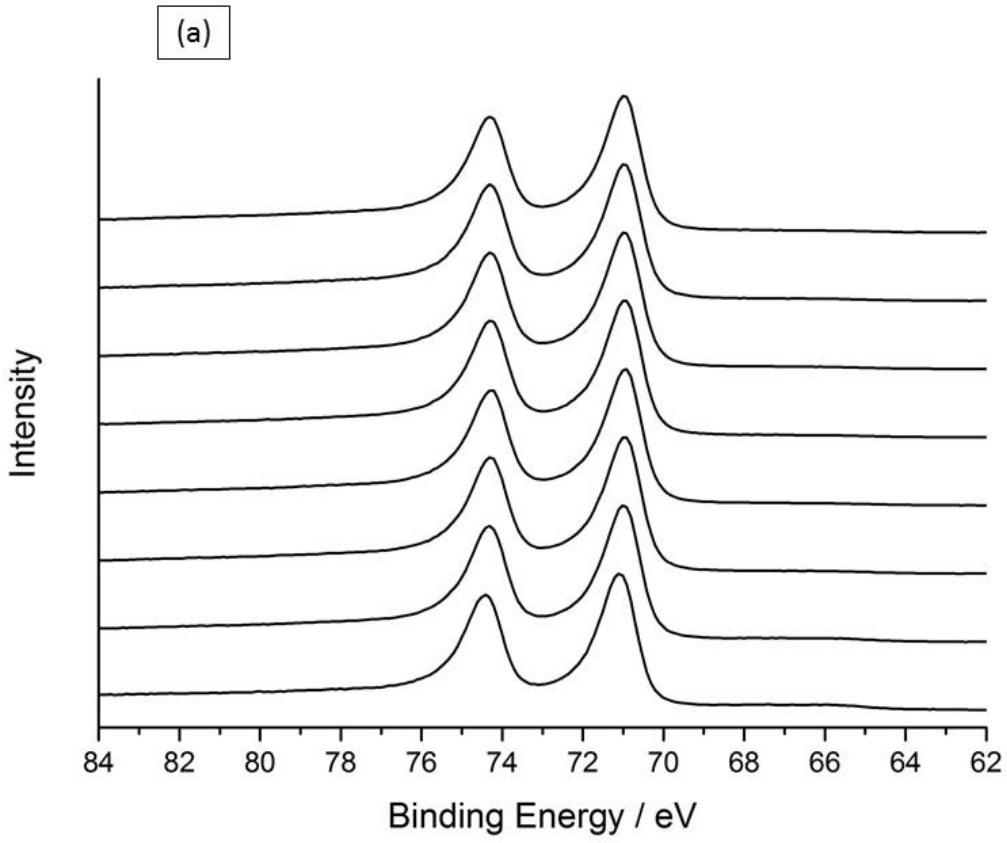

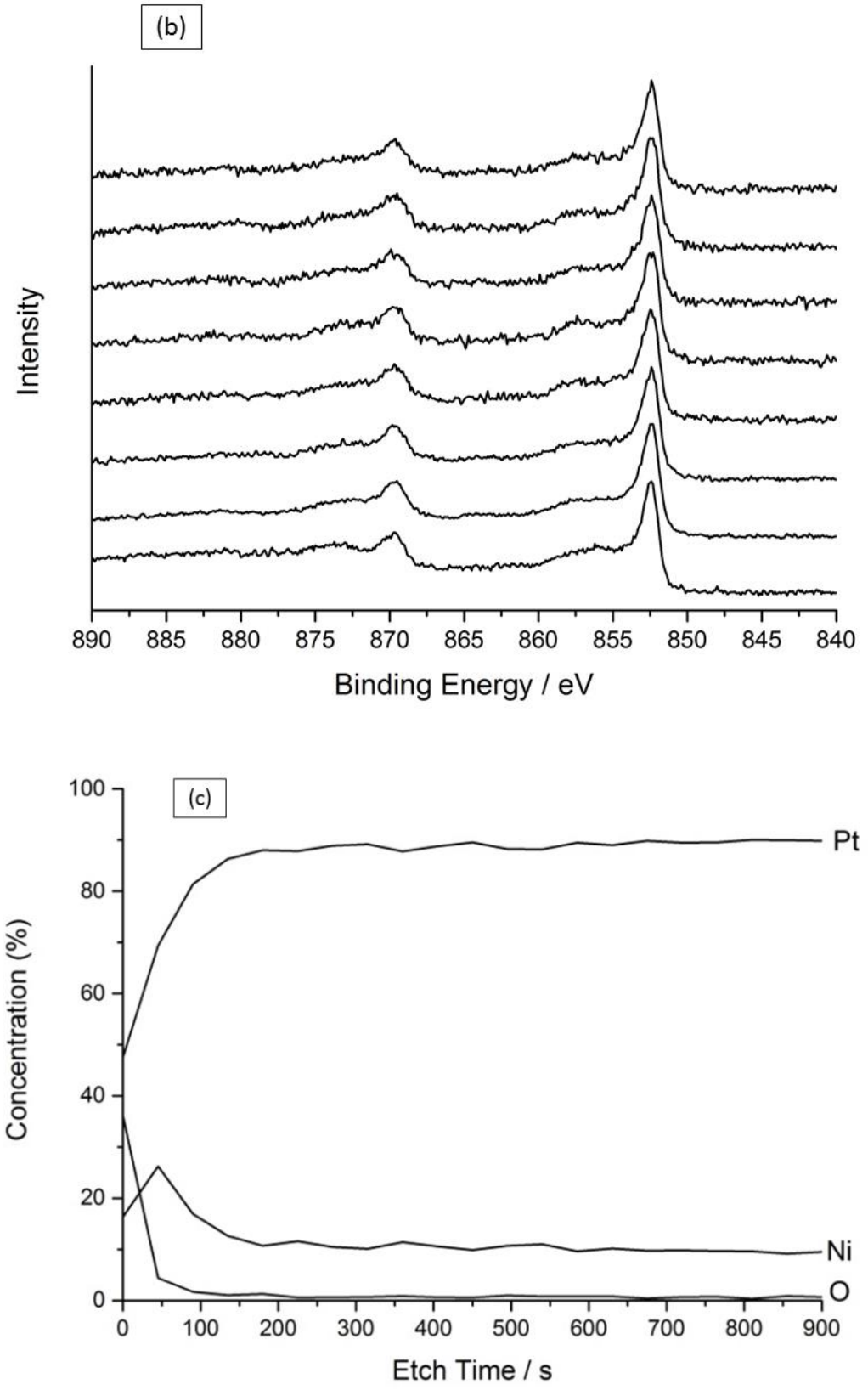

Fig. 16. XPS results for the resistively heated PtNi modified Pt{111} electrode but after flame annealing and cooling in hydrogen. Figure (a) is of the Pt 4f region as a function of argon etching time. (b) Shows the Ni 2p XPS region as a function of argon etching time. Both (a) and (b) Show spectra normalised to the same intensity.

Time intervals for surface etch are 0, 30, 60, 90, 180, 300, 600 and 900 s. (c) Shows how surface composition changes as a function of argon etching time.

3.2.2.2 PtCo{111} and PtFe{111}

3.2.2.2.1 CV and ORR

Resistive heating of a Pt{111} single crystal was carried out in the electrochemical cell with droplets of 0.01 M $Fe(NO_3)_3$ and $Co(NO_3)_2$ attached in order to investigate the PtCo and PtFe selvedge region as a function of cooling environment. The experimental parameters, concentration, resistive heating current, temperature etc. were identical to those utilised for the creation of a PtNi surface, as detailed in the previous section. Fig. 17(a) and 8(b) show the CV results corresponding to resistive heating for Co^{2+}(aq) and Fe^{3+}(aq) solutions respectively. The CV responses for both of these metals are quite distinct (and very different to Ni whereby a well-defined, reversible, broad surface redox peak at 0.85V was observed together with only a marginal increase in double layer charging current). After the first resistive heating procedure (fig. 17(a)), a large increase in the capacitive current associated with the double layer region of the PtCo phase between 0.3 and 0.5 V was observed which increased still further with a second resistive heating treatment (second Co^{2+}(aq) droplet applied). The underlying OH_{ads} and H_{upd} peaks of Pt{111} may still be seen, albeit diminished in magnitude, even after the second resistive heating treatment. There is clearly an adsorbed layer present over the Pt{111} electrode that exhibits a substantial increase in pseudocapacitance and higher resistance to electron transfer (as reflected by irreversibility in the electrosorption features as cobalt loading increases) reminiscent of an adsorbed oxide phase. The CVs for this adlayer were also stable upon potential cycling, indicating that the unknown adsorbed adlayer was stable to repeated CV cycles in perchloric acid electrolyte.

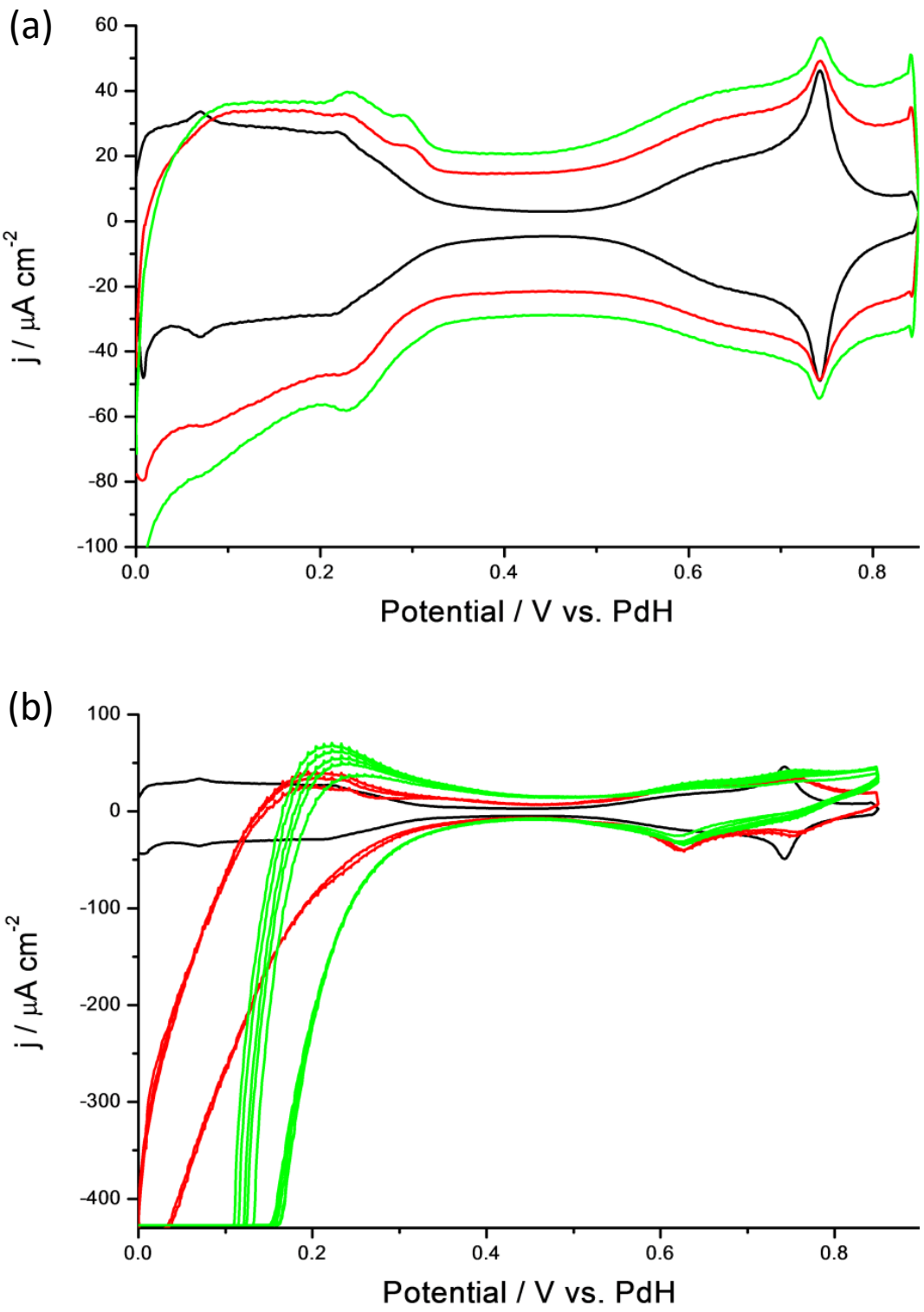

Fig. 17. (a), Cyclic voltammogram of Pt{111} in 0.1 M $HClO_4$ (black), and after 1st $Co(NO_3)_2$ resistive heating treatment in water/nitrogen ambient of the electrochemical cell (red). 2nd treatment (green). Sweep rate = 50 mV/s. (b), Cyclic voltammogram of Pt{111} in 0.1 M $HClO_4$ (black), and after 1st $Fe(NO_3)_3$ resistive heating treatment in water/nitrogen ambient of the electrochemical cell (red). 2nd treatment (green). Sweep rate = 50 mV/s.

In contrast, although resistive heating of a 0.01 M $Fe(NO_3)_3$ droplet attached to Pt{111} (fig. 17(b)) also showed an increase in the capacitance of the interface, under repetitive potential cycling, large cathodic currents negative of 0.3 V were obtained. We ascribe such behaviour to Fe or Fe oxide phases dissolving at low pH together with the generation of hydrogen gas. The magnitude of the dissolution current diminished with successive potential cycles, presumably because Fe was lost to the electrolyte from the surface. This suggestion was confirmed since dissolution current increased following successive resistive heating treatments (increase in Fe loading).

Because of instabilities associated with the Fe adlayer and the main thrust of this investigation being to compare ORR for Ni, Co and Fe when these components were 'stable' on Pt{111}, attempts were made to stabilise the Fe adlayer by reference to previous platinum-nickel results. In this way, re-annealing of the (presumed) oxided PtCo and PtFe phases was carried out in the reducing ambient of a hydrogen/water gas stream. In contrast to results shown in fig. 17 whereby distinctly different cyclic voltammetric responses were reported, upon heating in a Bunsen flame to approximately 900K and subsequently cooling in hydrogen gas, fig. 18(a) shows that CV results for all bimetallic systems investigated were remarkably similar (PtNi included). In our previous study, the PtNi phase formed after this treatment was wholly metallic suggesting that this was also the case for the PtCo and PtFe electrodes. That the H_{upd} region resembled strongly previous results by Markovic et al for Pt_3Ni{111} points to significant ordering of the surface towards a {111} structure. Even the electrosorbed oxide peaks at potentials positive of 0.7 V reflect this point, as was achieved with PtNi{111} in our previous study. For all three metals Fe, Co and Ni, the H_{upd} regions between 0 - 0.3 V overlap almost exactly, and the double layer regions between 0.3 - 0.6 V are also very similar. The only notable difference between the three metals is in the electrosorbed oxide region. XPS results have demonstrated that the flame annealed PtNi surface was consistent with a metallic $Pt_{90}Ni_{10}$ alloy phase being formed. As PtCo and PtFe flame annealed electrode surfaces show very similar CV responses to PtNi{111}, it suggests that metallic PtCo{111} and PtFe{111} alloy phases seem to have been formed (this will be confirmed later). A key point to notice in comparing the CVs for the flame annealed surfaces is how the onset of oxide adsorption changes. As the number of d-electrons in the metallic adsorbate decrease, the onset for oxide adsorption moves to more positive potentials, with the PtFe{111} phase exhibiting the highest onset potential for surface oxidation of all three metals studied. There also actually seems to be at least two oxide

electrosorption peaks for the FePt system on the positive going sweep with the highest potential oxide peak occurring at 0.9 V.

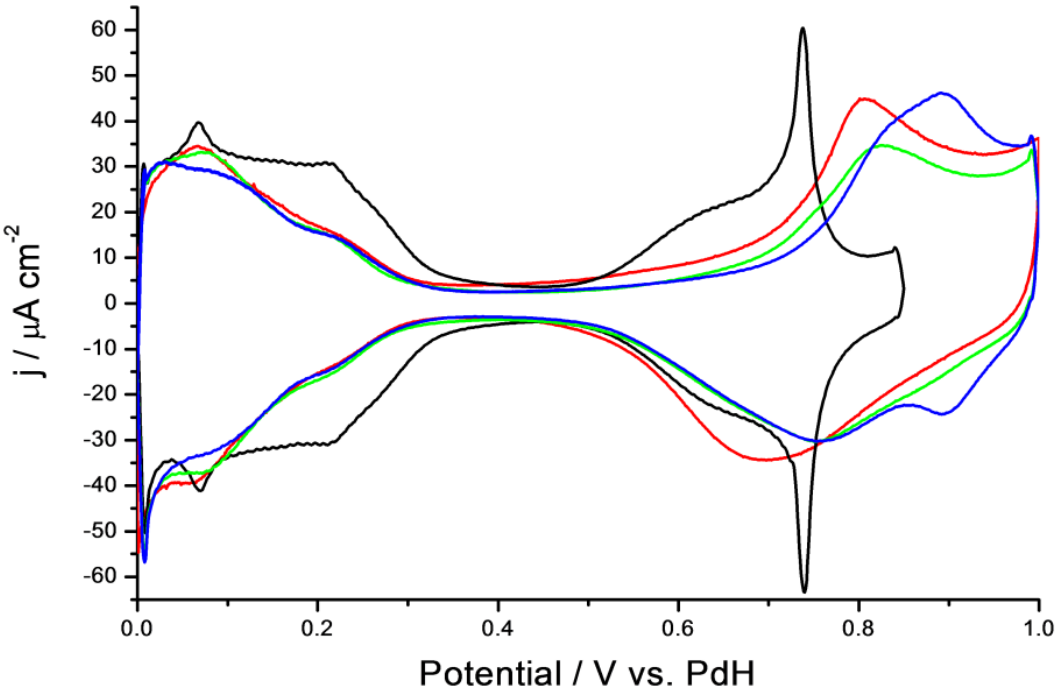

Fig. 18(a). CVs obtained after flame annealing and cooling in hydrogen the resistively heated bimetallic electrodes. (red) $NiCl_2$, $Co(NO_3)_2$ (green), $Fe(NO_3)_3$ (blue). CV of Pt{111} electrode surface (black). 0.1 mol dm^{-3} $HClO_4$ scan rate = 50 mV/s.

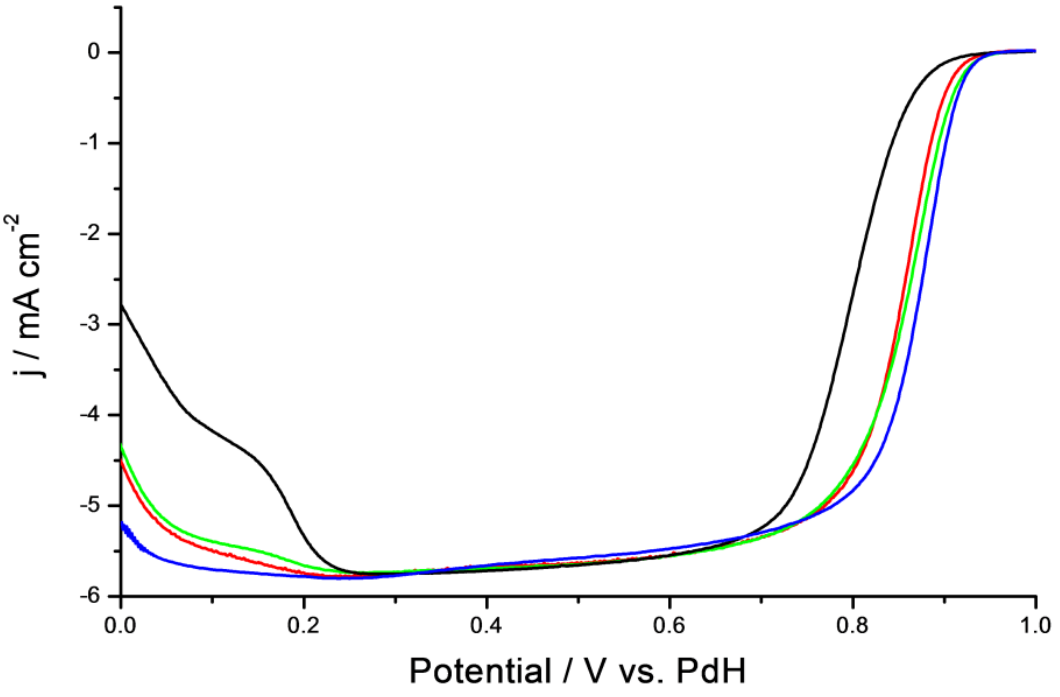

Fig. 18(b) ORR activity of Pt{111} electrode surface (black) compared with the electrodes shown in figure 18(a). Ni (red), Co (green) and Fe (blue). 0.1 mol dm^{-3} $HClO_4$ scan rate = 30 mV/s, 1 atm O_2, 1600 rpm rotation rate.

Trends in the onset of oxide formation shown in fig. 18(a) can be directly correlated with ORR activity results shown in fig. 18(b). Here the $E_{1/2}$ for PtNi{111} is just under 70 mV more positive than for pure Pt{111} and the $E_{1/2}$ for PtFe{111} is ~ 80 mV more positive (PtCo{111} lies in between these two). The link between the potential of surface oxidation and ORR activity has been discussed in previous work [35, 43, 47]. Alloying platinum with another metal has been shown to weaken the Pt-OH bond strength [35, 47] so that Pt-OH layers, which inhibit oxygen reduction activity, are formed at more positive potentials compared to Pt{111}. There is then an increased availability of metallic platinum surface sites, with inherently high oxygen reduction activity, at more positive potentials. The present results are in accord with these ideas for a Pt{111} single crystal surface.

3.2.2.2.2 STM

STM was used to image the surfaces of the PtCo and PtFe modified Pt{111} electrodes formed by either the resistive heating method or after the flame annealing/cooling in hydrogen procedure. Fig. 19(a) and 20(a) show STM images of the PtCo and PtFe surfaces prepared by resistive heating whereas 19(b) and 20(b) show the corresponding flame annealed electrodes. It was demonstrated that the PtNi surface prepared by resistive heating consisted of islands of Ni oxide/hydroxide terminated PtNi covering the entire surface. The size of these islands was typically 3 – 6 nm with a height of approximately 0.2 nm. In combination with XPS results it was suggested that the islands were monolayers of nickel oxide/nickel hydroxide sitting proud of a PtNi alloy. In contrast, a smoother surface with Pt{111} terraces and linear steps clearly visible was seen in the STM image of the flame annealed/hydrogen cooled PtNi{111} electrode. In this case, the islands were 3 nm in diameter and 0.3 nm in height and these were interpreted as being due to monolayers of a metallic PtNi phase adsorbed on Pt{111}.

For the PtCo surface, fig. 19(a) shows a significantly rougher profile compared to fig. 19(b). Similar to the situation with nickel, the STM image of the resistively heated PtCo electrode in fig. 19(a) gives rise to a range of rounded microcrystallites ranging in diameter from 3 to 8 nm with little ordering of the microcrystallites themselves being apparent. There is also little

contrast across the surface for any of the microcrystallites and certainly there is no evidence of atomic surface superstructures being formed. However, upon flame-annealing and cooling in hydrogen, the topology of the bimetallic PtCo microcrystallites changes markedly becoming smoother and with individual rows of atoms becoming apparent, ordered along particular directions. The island size has also become more uniform (typically 7 +/- 1 nm). The islands in both the resistively heated and flame annealed PtCo surfaces are larger than those observed previously with PtNi.

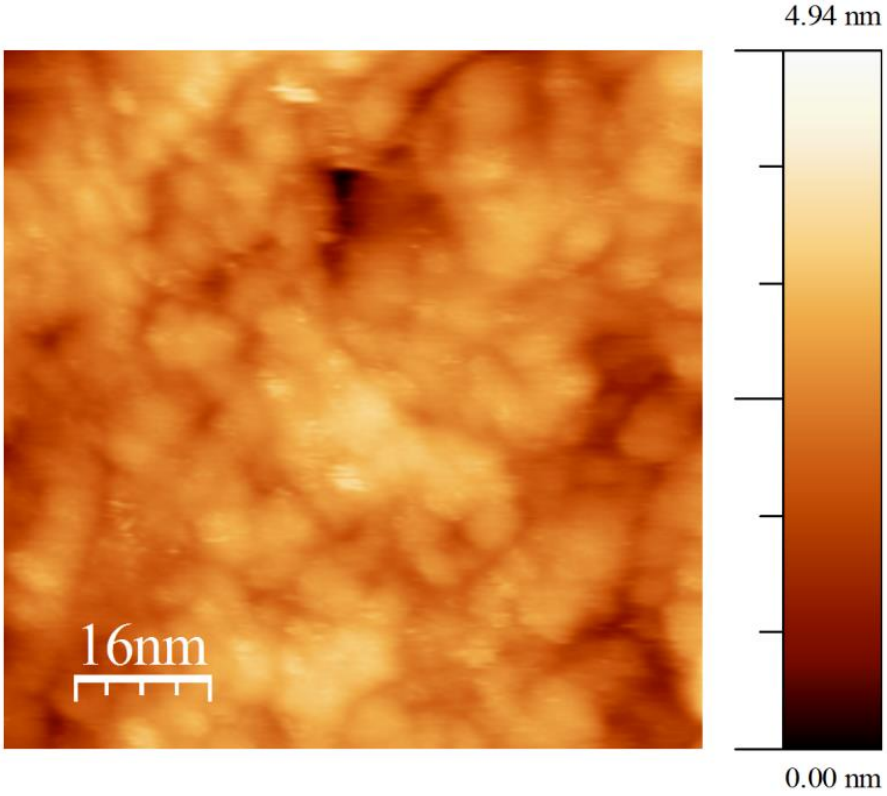

Fig. 19(a). STM image of the PtCo modified Pt{111} surface prepared by resistive heating in the electrochemical cell. Tunnelling current = 30 nA.

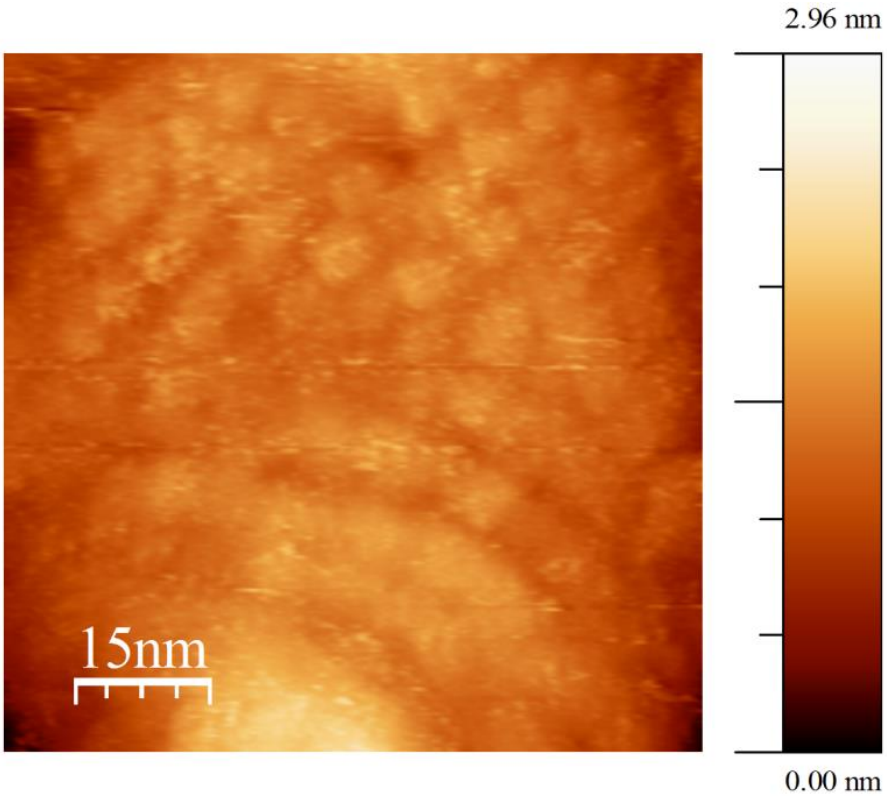

Fig. 19(b). STM image of the PtCo modified Pt{111} after flame annealing the electrode prepared by resistive heating to 900 K and cooling in hydrogen. Tunnelling current = 30 nA.

The PtFe resistively heated and flame annealed surfaces in fig. 20(a) and 20(b) respectively also show the same basic features as observed for the Ni and Co systems. The resistively heated PtFe surface, (fig. 20(a)) exhibits the largest, most irregular islands of all the systems studied with sizes ranging from 4-20 nm. After heating and cooling in hydrogen, the PtFe appearance is transformed into one exhibiting a much more uniform, regular array of large islands (relative to Co and Ni), again with a smoother, flatter topology than before. These results show that the bimetallic, microcrystallite structures formed consist of islands with ever increasing average sizes as one changes the adatom from Ni to Co to Fe.

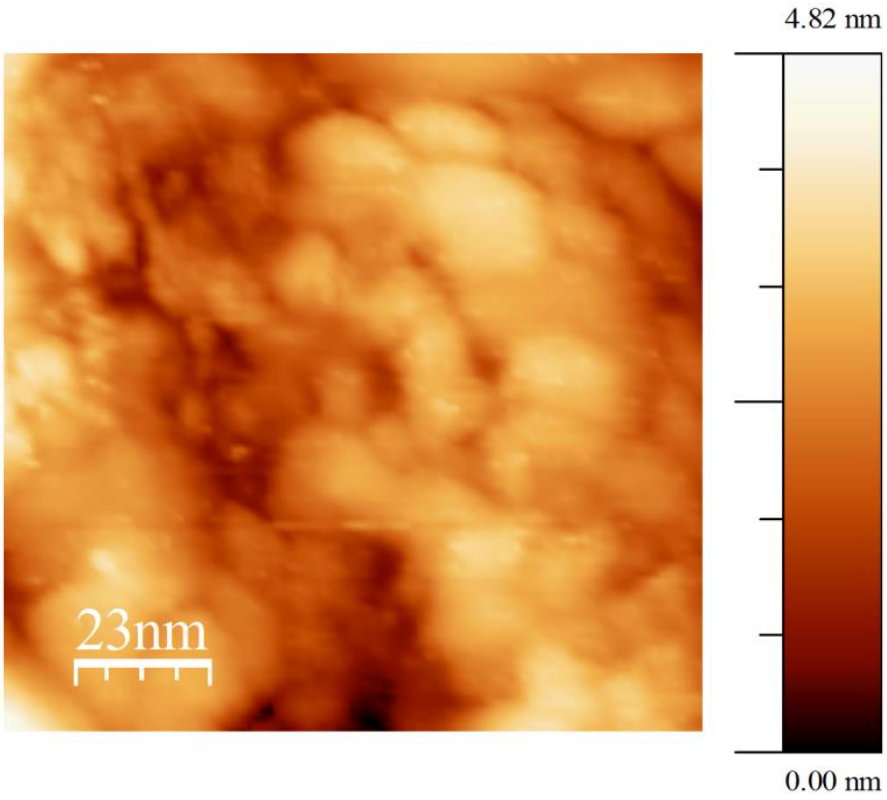

Fig. 20(a) STM image of the PtFe modified Pt{111} surface prepared by resistive heating in the electrochemical cell. Tunnelling current = 30 nA.

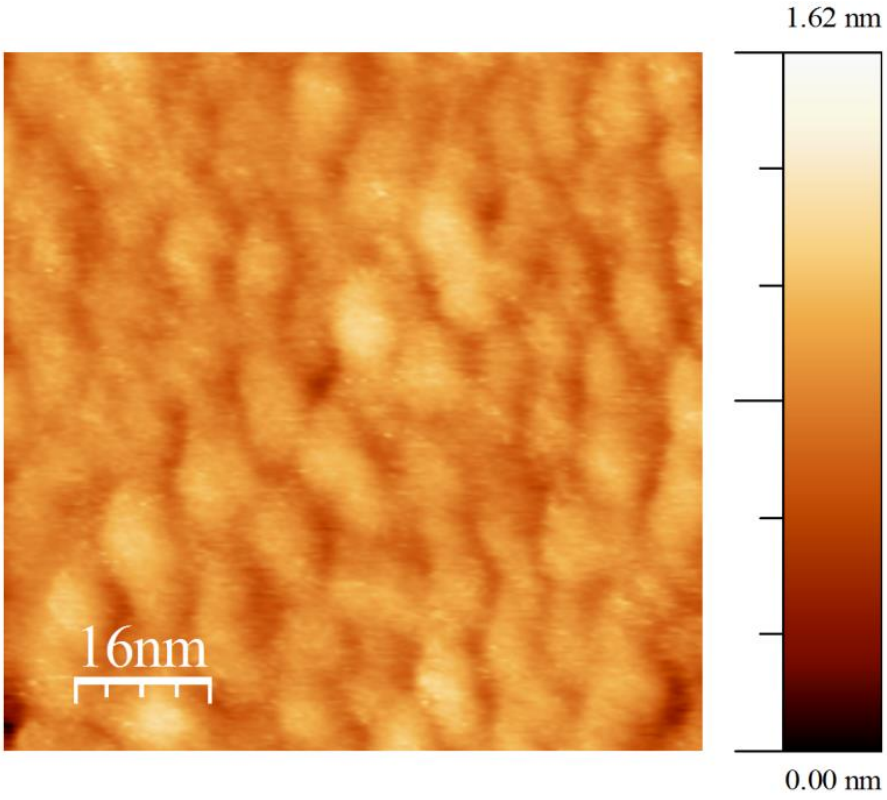

Fig. 20(b) STM image of the PtFe modified Pt{111} after flame annealing the electrode prepared by resistive heating to 900 K and cooling in hydrogen. Tunnelling current = 30 nA.

These STM results may also be used to suggest an explanation as to why the CVs shown in fig. 17 and 18 do not correspond in every detail to those of the bulk PtM{111} single crystal electrodes [35, 67]. Although close in CV profile to PtM{111}, the presence of some surface defects such as (110) steps at the surface may be gleaned from inspection of figure 18(a) for example. According to STM, only small islands of the bimetallic phase are formed on Pt{111}. This precludes long range {111} order being developed over distances of more than perhaps 6-10 nm and hence, deviations from bulk PtM{111} CV behaviour are observed. It is suggest that if annealing temperatures were increased and moreover that heating for extended periods of time in a hydrogen ambient were undertaken, surface (and bulk) diffusion would be promoted and therefore, larger areas of single crystalline phase would develop on the Pt{111} surface. In spite of this however, the CV profiles of all PtM{111} surfaces are sufficiently close to those of the bulk PtM{111} surface that it is highly probable that the quasicrystalline overlayer exhibits a mostly {111} surface texture.

3.2.2.2.3 XPS

XPS depth profile analysis was performed for each of the PtM (M = Ni, Co or Fe) Clavilier bead samples following CV characterisation. For all samples, regardless of the alloying metal, for the first 20 seconds of argon etching, XPS revealed a large increase in the intensity of the Pt and M XPS core-levels, consistent with the removal of adventitious impurities from the electrode surfaces which had accumulated during transfer from the electrochemical cell to the vacuum system. Furthermore, for all samples investigated the Pt($4f_{7/2}$) photoelectron peak (not shown) was found at a binding energy of 70.9 eV, consistent with metallic Pt. For the resistively heated PtM systems (fig. 21(a) and 22(a)) all showed a high degree of oxidation for the alloying metal. This was also seen for the PtNi sample. In this case, the Ni(2p) region revealed a broad feature between 851 and 867 eV, which could be resolved into three peaks ca. 853.5 and 856.5 eV indicating the presence of NiO and $Ni(OH)_2$ [68]. This interpretation was supported by the broad satellite structure above 860 eV, consistent with the presence of Ni(II). For the total etching time utilised (900s), the Ni overlayer was oxidic in nature, with little change in either the magnitude or the binding energies of Ni(2p) XPS peaks other than for small changes in the ratio of the various Ni(II) species due to preferential sputtering of adsorbed oxygen.

Equally, for the PtCo sample, inspection of the Co(2p) core-level (fig. 21(a)) revealed a heavily oxidised surface. The Co(2p) level prior to sputtering was measured at 780.0 eV, consistent with a hydroxylated Co species. Support for this assertion may be gleaned by considering also the large O(1s) signal at 531.8 eV, a binding energy consistent with hydroxide species. Argon ion etching reveals a much larger satellite to higher binding energy of the Co(2p) level at ca. 786 eV, consistent with spectra for CoO [69]. After ca. 180 seconds of sputtering, a broadening of the peak on the lower binding energy side is observed. Increased sputtering time allows this peak, centred at 778.3 eV to increase in magnitude and, after 750 seconds of sputtering, it is noted to be sharper than the other Co peaks with a binding energy indicative of metallic Co. Fig. 21(b) records how the XPS peak intensities for Pt, Co and O change with argon etching. It is evident that although a gradual increase in Co intensity is matched by a corresponding decrease in O intensity (consistent with preferential depletion of oxygen compared to cobalt as previously remarked upon discussing the change in the ratio of the oxide/hydroxide surface components), the Pt XPS peak intensity remains very low indicating that the cobalt oxide/hydroxide layer formed following resistive heating is several monolayers thick. How thick exactly can only be gauged by knowing a priori the number of monolayers of material sputtered away per unit time. We roughly estimated this value by noting sputtering rates for metal overlayers such as gold and lead as being around a couple of nm per minute, tested internally under our sputter conditions. Consideration of XPS data shown in fig. 21 and 22 corresponding to hydrogen cooled PtM samples demonstrates that a rapid removal of the oxygen overlayer takes place in the first 60 s of sputtering. Clearly, if this is assumed to be a whole surface atomic layer, it gives a lower bound of approximately 1 monolayer per 60 s as a nominal sputtering rate, i.e. of the same order of magnitude as the previous estimation using metals. Hence, if CoO type species are still present at the surface after 600 s, it means a thickness of at least 10 monolayers still remains consistent also with the low intensity of the Pt 4f XPS peak after this time. We shall utilise this rough estimation of sputtering rate below. It is also noted that the overall stoichiometry as etch time increases is towards a 1:1 Co:O ratio consistent with a CoO phase at the end of the sputtering period and CoOx or Co(OH)x where $1 < x < 2$ at the beginning.

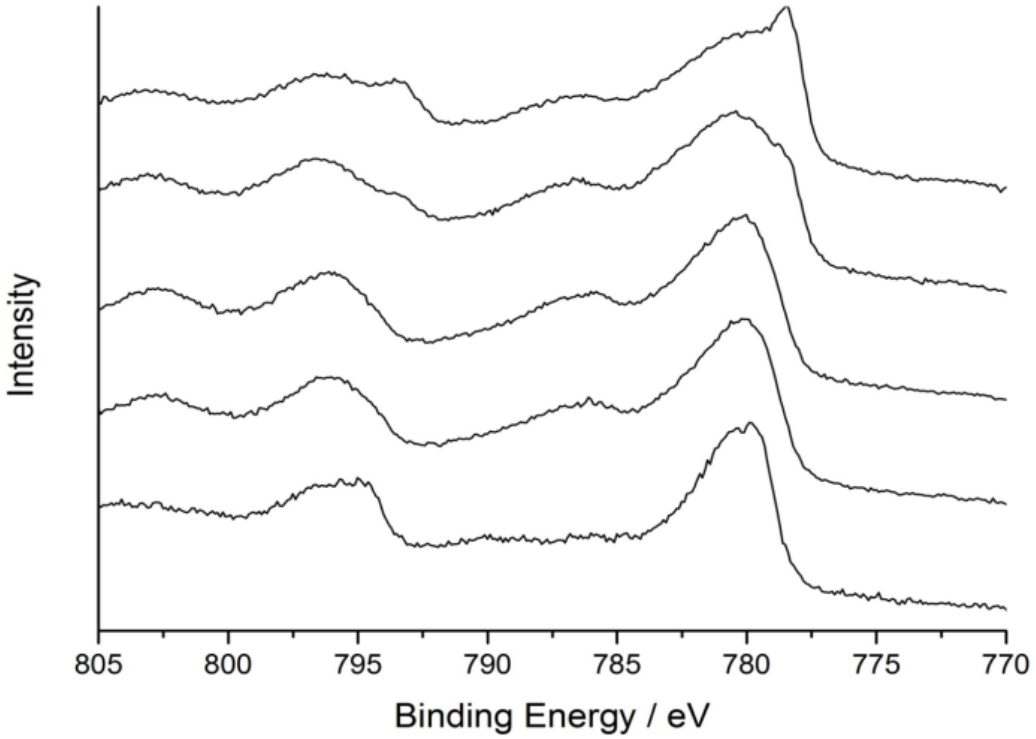

Figure 21(a) XPS results for the resistively heated PtCo modified Pt{111} electrode showing the Co 2p XPS region as a function of argon etching time. Time intervals for surface etch are, from bottom to top, 0, 30, 60, 300 and 750 s.

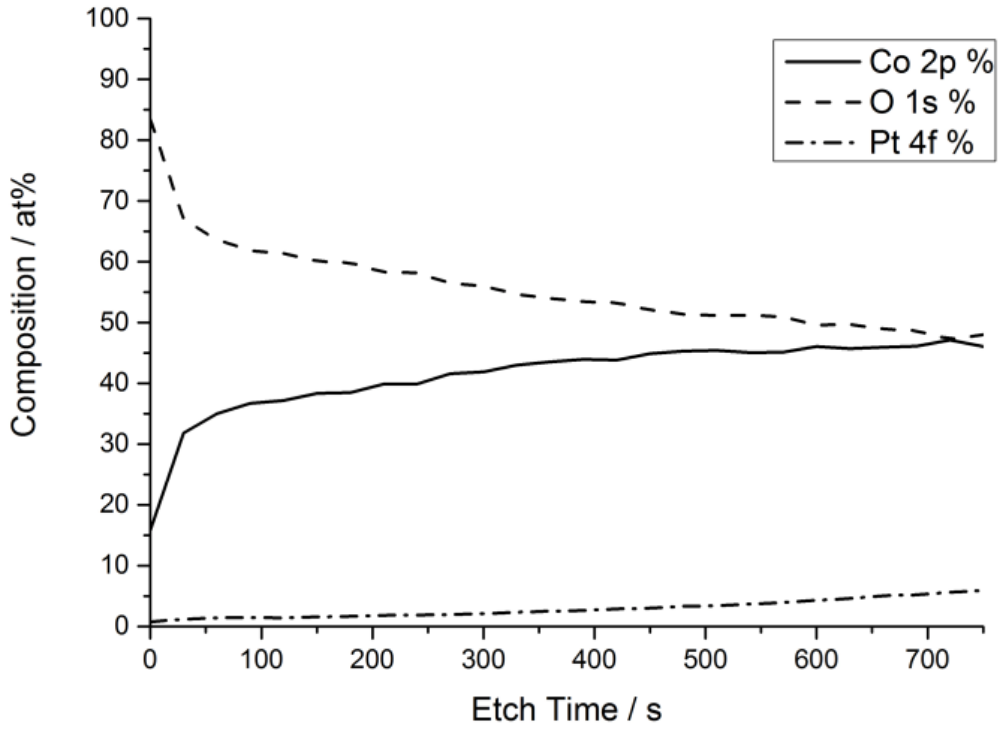

Figure 21(b) XPS peak intensities for Pt, Co and O as a function of etch time for the resistively heated PtCo modified Pt{111} electrode. Surface composition changes as a function of argon etching time are plotted.

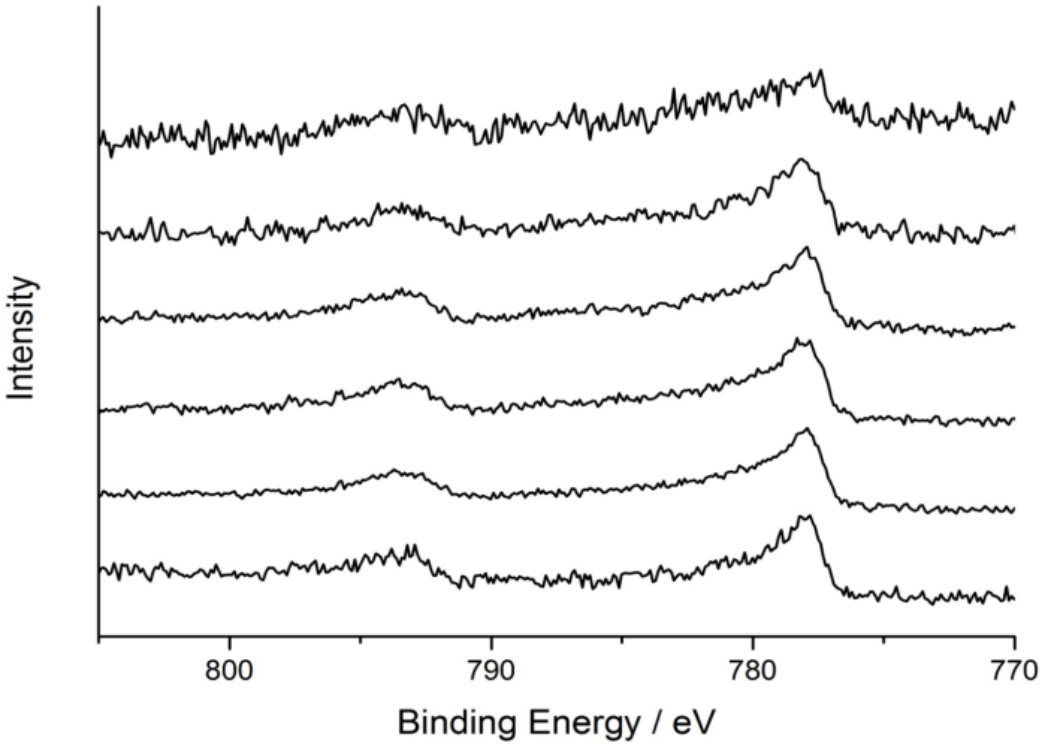

Figure 21(c) XPS results for the resistively heated PtCo modified Pt{111} electrode but after subsequent flame annealing and cooling in hydrogen. The Co 2p XPS region as a function of argon etching time is shown. Time intervals for the surface etch are, from bottom to top, 0, 30, 60, 90, 300 and 600 s.

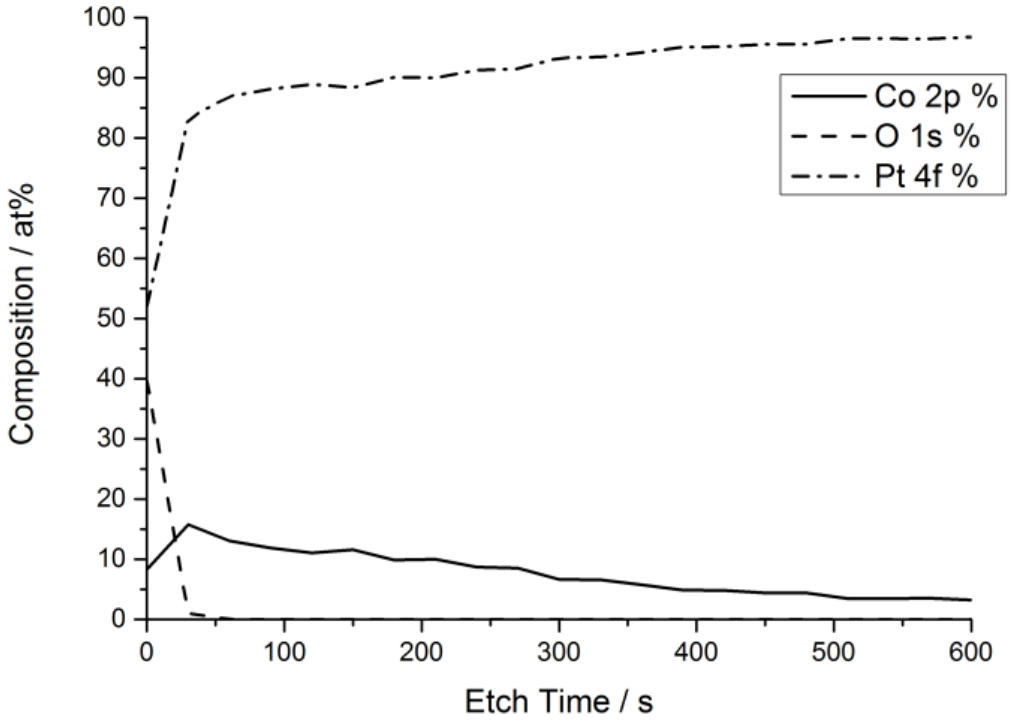

Figure 21(d) XPS results for the resistively heated PtCo modified Pt{111} electrode but after flame annealing and cooling in hydrogen. Surface composition changes as a function of argon etching time for Pt, Co and O surface atoms are shown.

Compared to fig. 21(a), fig. 21(c) shows a much simpler Co 2p spectral region with a single peak being observed for both the $2p_{3/2}$ and $2p_{1/2}$ features at a binding energy consistent with metallic cobalt. Hence, as for PtNi, flame annealing and cooling in hydrogen of the metal oxide/hydroxide phase produced by annealing in water vapour leads to chemical reduction of the selvedge giving rise to a completely metallic PtCo overlayer. XPS peak intensities as a function of sputtering time also reveal that an initial $Pt_{85}Co_{15}$ phase is formed (see Co2p % after 30 seconds of etching in fig. 21(d)) covered with a superficial oxide layer which is readily removed within the first 60 seconds of sputtering as discussed earlier. After 250 seconds of etching, the relative intensities of Pt to Co correspond more to a $Pt_{92}Co_8$ phase consistent with either preferential sputtering of cobalt versus Pt or a gradual enrichment in Pt as one moves away from the topmost layer of metal atoms towards the bulk. In either case, it is confirmed that two distinct phases of the bimetallic PtCo surface may be prepared depending on the cooling ambient following annealing. Hence, the ORR activity reported in fig. 18 is confirmed as arising from a purely metallic PtCo electrode surface.

The resistively heated PtFe system (fig. 22(a)), again revealed a heavily oxidised surface after transfer to the XPS system. The Fe(2p) region exhibiting a Fe($2p_{3/2}$) peak centred at 710.8 eV, together with weak satellite structure ca. 719 eV, indicated the presence of an Fe_2O_3 surface layer [70]. Even after only 30 seconds of sputtering, the Fe($2p_{3/2}$) binding energy is downshifted to 709.9 eV and satellite structure appears at ca 715 eV, indicating a Fe(II) oxide environment [70]. Continued etching reveals further broadening of the iron peak, with a shoulder developing at ~707 eV, indicative of metallic Fe, although this is only beginning to be resolved after 600 s of etching. Fig. 22(b) shows the surface composition as a function of etch time. Unlike for Co, the underlying Pt surface gives rise to moderated electron emission from the $4f_{7/2}$ state from the start showing that either the Fe_2O_3/Fe(II) layer is very thin or incompletely wets the Pt surface giving rise to 'cracks' through which electron emission takes place. The former explanation appears unlikely since at the estimated sputter rate, a thin iron oxide layer should be removed rather quickly. Therefore, we ascribe the sputtering behaviour reported in fig. 22(b) to large islands of iron oxide/hydroxide sitting proud of the Pt{111} electrode with patches of 'bare' Pt giving rise to all Pt emission features. Again, consideration

of the atomic abundances of Fe and O as a function of sputtering confirms a FeO_x stoichiometry for the surface layer with $1 < x < 2$.

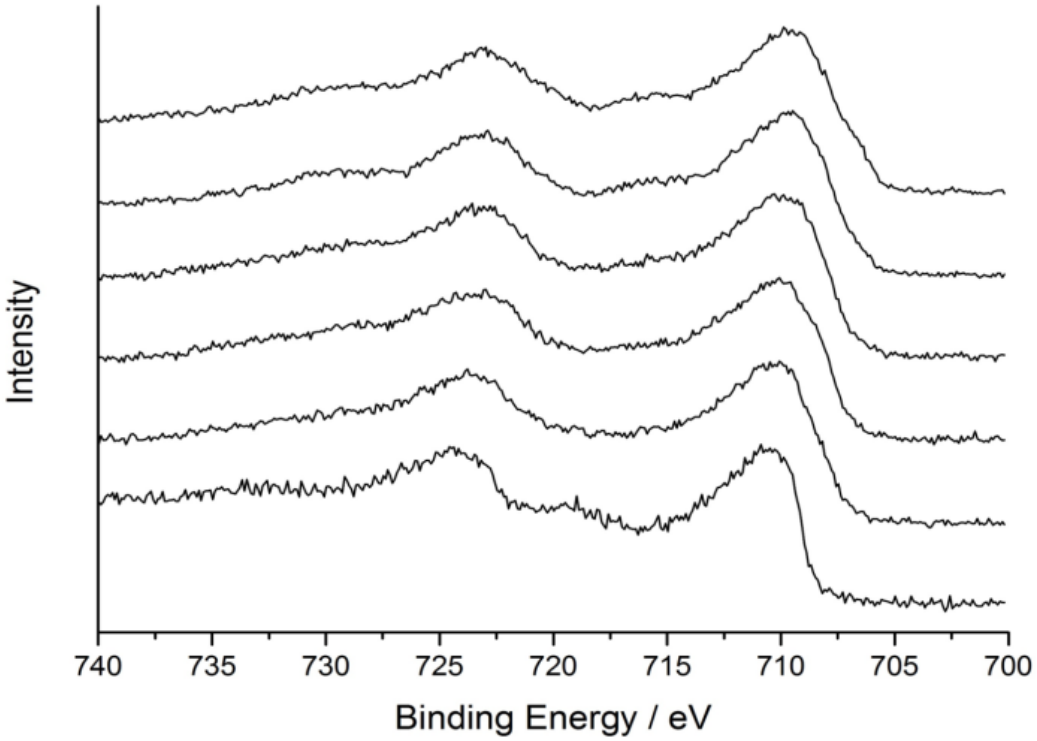

Figure 22(a) XPS results for the resistively heated PtFe modified Pt{111} electrode showing the Fe 2p XPS region as a function of argon etching time. Time intervals for surface etch are, from bottom to top, 0, 30, 60, 90, 300 and 600 s.

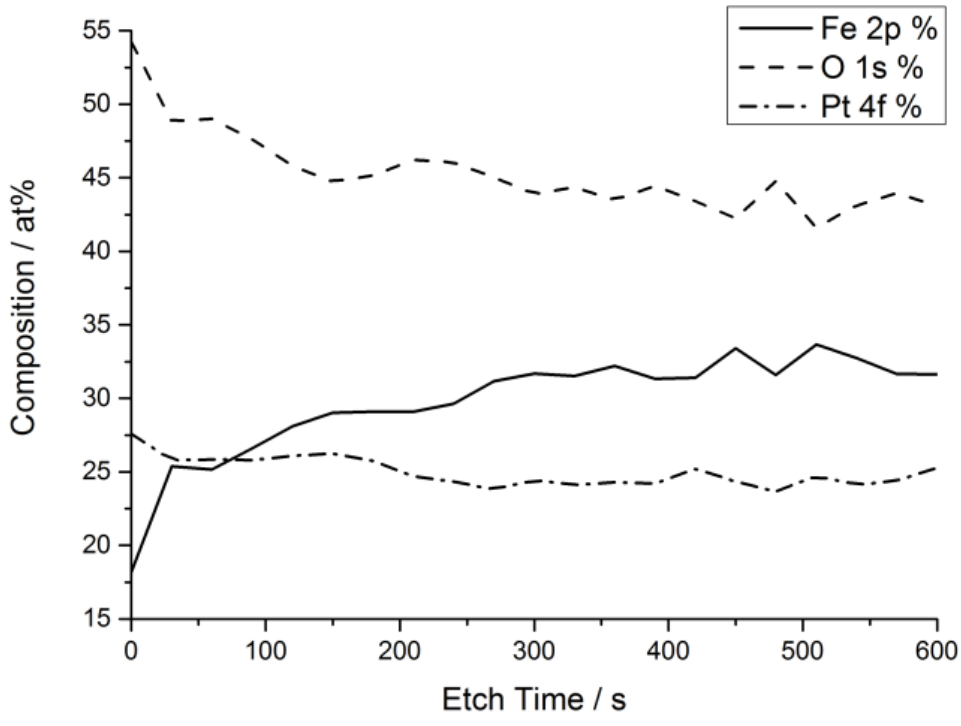

Figure 22(b) XPS results for the resistively heated PtFe modified Pt{111} electrode. Shows how surface composition changes as a function of argon etching time.

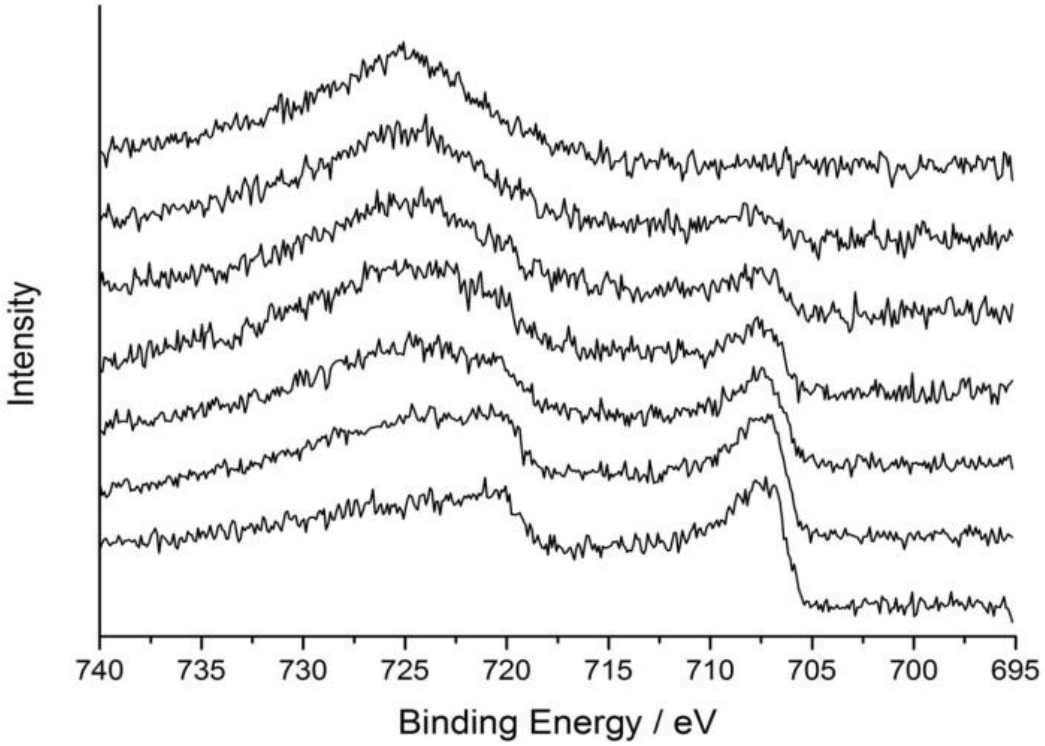

Figure 22(c) XPS results for the resistively heated PtFe modified Pt{111} electrode but after flame annealing and cooling in hydrogen. The Fe 2p XPS region as a function of argon etching time is shown. Time intervals for surface etch are, from bottom to top, 0, 30, 60, 90, 120, 150 and 180 s.

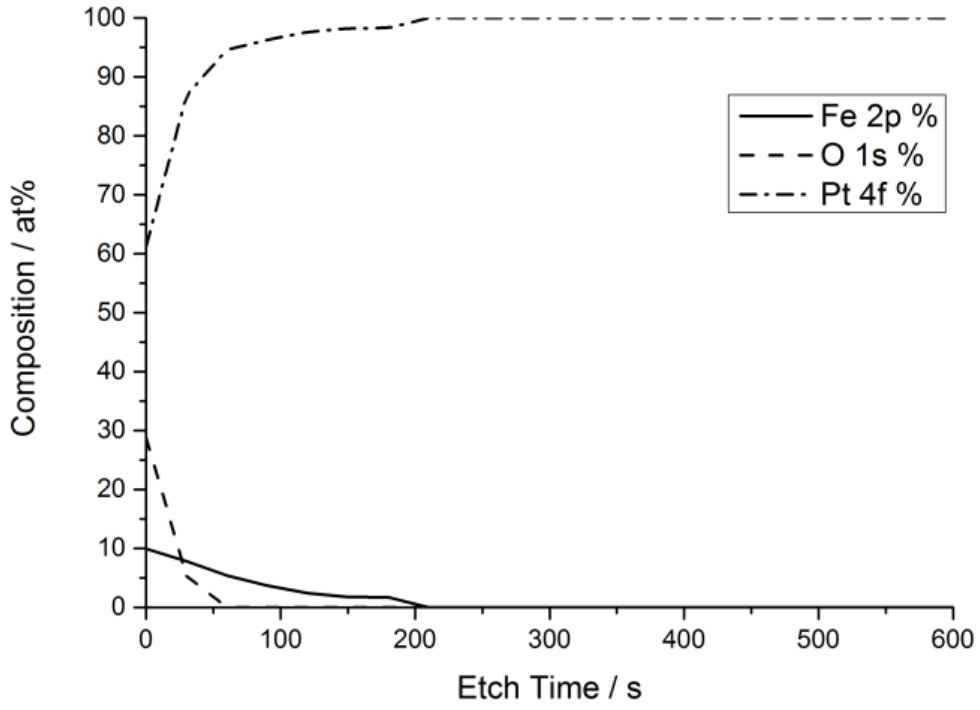

Figure 22(d) XPS results for the resistively heated PtFe modified Pt{111} electrode but after flame annealing and cooling in hydrogen. Shows how surface composition changes as a function of argon etching time.

Fig. 22(c) shows the XPS data obtained for the PtFe system after flame annealing and cooling in hydrogen. It is evident that all Fe 2p features now correspond to the binding energy of metallic Fe [70]. Again, the surface is covered by a hydroxide layer (O(1s) = 532.2 eV; not shown) which is quickly removed after 30 sec of etching. The Fe($2p_{3/2}$) signal is centred at 707.6 eV, consistent with metallic Fe. However, unlike the PtNi and PtCo systems, the Fe is removed more rapidly from the Pt surface with depletion of the Fe(2p) signal occurring after only 210 sec (fig. 22(d)). This points to the nature of the metallic PtFe{111} surface as being quite different to both NiPt and CoPt{111} in that the selvedge region is largely depleted of iron after flame annealing and cooling in hydrogen. It is suggested that exposure to any significant flame treatment rapidly removes iron from the Pt{111} surface.

In spite of its rather low surface concentration, the PtFe{111} surface still exhibited the most active behaviour towards ORR and it is concluded therefore that although PtM bimetallic surfaces have been prepared, greater control of how the final surface composition of the selvedge region is obtained is required before full understanding of this phenomena is obtained. There is clearly a relationship between the electronic perturbation afforded by surface alloying of Pt with Fe, Co and Ni such that a decrease in the number of d-electrons in the adsorbate seems to favour greater ORR activity. However, the composition of the selvedge region may also be a factor in controlling ORR activity and this will be the subject of future work.

3.2.3 Conclusions

Nickel, cobalt and iron modified Pt{111} electrodes have been prepared and investigated as a function of two annealing and cooling environments. A combination of cyclic voltammetry (CV), scanning tunnelling microscopy (STM) and X-ray photoelectron spectroscopy (XPS) have confirmed the presence of two distinct PtM phases depending on surface preparation conditions. It is found that when these electrodes are resistively heated and cooled in the nitrogen/water atmosphere of the electrochemical cell the surface is covered with PtM (M=Ni, Co, Fe) islands which are terminated with surface oxides/hydroxides. The islands increase in size in the order Ni, Co, Fe. The second series of catalysts were created by flame annealing the resistively heated surfaces in a Bunsen flame and subsequently cooling them in a stream of

hydrogen. This procedure reduced the oxides/hydroxides to metallic Ni, Co or Fe and formed surface alloys. CV for these surfaces show that the onset of electrochemical oxide formation shifts positive in the order Ni, Co, Fe. This shift correlated with increased activity towards the oxygen reduction reaction (ORR) which we ascribe to the greater availability of highly active metallic sites for oxygen reduction at ORR potentials.

3.3 ORR of a Series of Kinked Surfaces Based Upon Pt{332}

The effect of kink sites on the oxygen reduction reaction (ORR) in perchloric acid has been investigated. The series of kinked surfaces used were based upon Pt{332}, within the [Pt n(111)x(111)] series (where n = 6), for this investigation due to this surface's high activity. Pt{10,9,6}, Pt{764} and Pt{864} surfaces were chosen based upon their increasing density of isolated {100} kink sites, enabling a study which singled out the effect of {100} kinks on the ORR in this series. The voltammetry and ORR activity of these surfaces was compared to Pt{332}. The voltammetric trend observed upon increasing kink density was that expected from the ball models of the surfaces, i.e. growth of a {100} voltammetric response at ~ 0.2 V with increasing surface density of kink sites. Subtle changes in the oxide region were also observed and their significance discussed. ORR activity was found to decrease with increasing {100} kink density, with the most kinked surface Pt{864} approaching the activity of Pt{755}, a surface which contains linear {100} step sites. These results show that {100} kinks have ORR activity that is identical to {100} step sites. These results may be useful in understanding the activity of platinum nanoparticles which almost certainly exhibit high surface concentrations of such low coordination sites.

3.3.1 Introduction

The oxygen reduction reaction has been examined extensively for a variety of metals [71-74], either by the use of nanoparticles [72, 74, 75] or by employing well-defined single crystal electrodes [6, 7, 22, 76-78]. A wealth of information about the reaction has been achieved from both of these approaches. Early work on platinum single crystal electrodes investigated the effect of electrolyte and anion adsorption on the ORR with platinum basal plane surfaces [2-4, 12, 79] and later work showed the activity of Pt stepped surfaces, [Pt n{111}x{100}] [7, 22], [Pt n{100}x{111}] [7, 22] and [Pt n{111}x{111}] [6]. As Pt nanoparticles exhibit a high density of low coordination step and kinks sites, investigations examining stepped and kinked single crystal electrodes can afford insight into NP activity. Stepped surfaces have been investigated for their ORR activity in the references given above and a series of stepped surfaces have also been investigated in chapter 3.1 of this thesis. Although there has been much work reported on the ORR activity of stepped surfaces, it is surprising that there is no literature on the ORR activity of kinked surfaces, which may emulate the activity of NP catalysts more

accurately. Compared to their stepped counterparts, kinked surfaces offer low coordination sites for stronger binding of reactant, intermediate, product and spectator species and may therefore have activity that is different to sites explored thus far. In this work the unexplored effect of kink sites on the oxygen reduction reaction was investigated. A series of kinked surfaces centred on the Pt{332} crystal plane were investigated. Pt{332} was chosen as it is part of the most active, [Pt n{111}x{111}], series of surfaces and in microfacet notation may be denoted Pt 6{111}x{111}.

A {332} Miller index plane is one that intercepts the face-centred cubic unit cell of platinum on the x, y and z unit cell axes at 1/3, 1/3, 1/2 the length of a unit cell side respectively. A slightly smaller fractional value in the intercept of the x axis creates a surface with kinked sites, specifically those of {100} orientation. Smaller x intercepts create surfaces with more of these sites. In preparing these single crystal surfaces, {100} kink sites were introduced by firstly aligning the goniometer holding a Pt single crystal to the angle required to create a Pt{332} plane (containing linear steps). Next, the crystal was rotated by an appropriate angle towards the 100 zone. A greater number of kinks were introduced by increasing the rotation angle towards the 100 zone. The Pt{332}, {10,9,6}, {7,6,4} and {864} surfaces were created via this method and are illustrated below. The Pt{10,9,6}, {7,6,4} and {864} surfaces have a {100} kink every 4, 3 and 2 atoms along the step respectively. The location of these surfaces on the stereographic triangle is illustrated below.

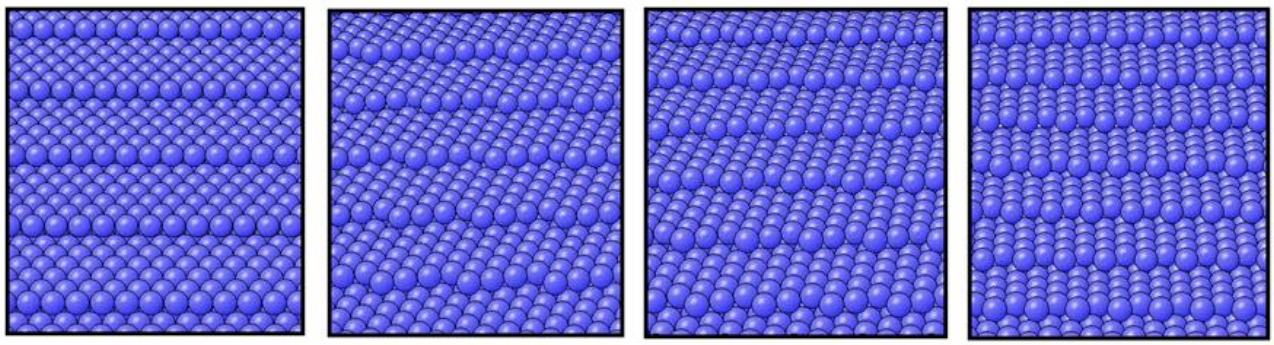

From left to right: Pt{332}, Pt{10,9,6}, Pt{764}, Pt{864}.

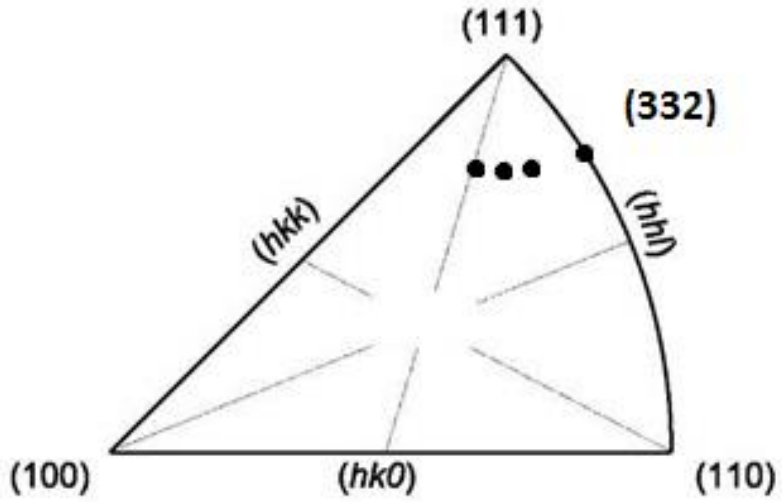

The stereographic triangle of an fcc system. Spots indicate, from right to left, the locations of Pt{332}, Pt{10,9,6}, Pt{764}, Pt{864} surfaces.

3.3.2 CV and ORR Results

The CVs of the crystals under examination in perchloric acid are illustrated in fig. 23. The response for Pt{322} matches voltammetry reported previously [80]. The voltammetry of the series of kinked surfaces examined have not been reported in the literature previously. Nevertheless, it is expected that voltammetric {110} response would diminish and a response for the {100} kinks would grow. Fig. 23 corroborates this idea: the voltammetric response from the {110} step at 0.1 V diminishes with increasing kink density as {110} step sites are replaced with {100} kinks and a very broad peak appears at ~ 0.22 V, indicating electrosorption reactions occurring at the kink site. The potential of this peak is at the same potential as the peak for anion adsorption at {111} x {100} steps, as seen from the voltammetry of [Pt n{111}x{100}] surfaces [7]. We attempted to create surfaces that were less kinked than Pt{10,9,6}, but the voltammetry obtained from these were indistinguishable from Pt{332}: i.e. Pt{10,9,6} was the lowest kink density surface which exhibited unique voltammetry and thus established a lower limit on the kink density we were able to investigate.

The 0.1 V peak from these surfaces is attributed to H_{ads}/OH_{ads} co-adsorption on {110} step sites and the broad feature at potentials < 0.3V is attributed to H_{ads} at terrace sites. The increase in current at ~ 0.2 V (and in the case of Pt{864}, the presence of a peak in current) shall be attributed to the replacement of H_{ads} at kink sites with O_{ads} and/or OH_{ads}, based on the current

understanding of [Pt n{111}x{100}] surfaces outlined in chapter 3.1 (section 3.1.2.1.1). The onset of H_{ads} terrace formation on the stepped surfaces is negative relative to Pt{111}, indicating weaker Pt-H bond strength, which is also concluded from DFT studies [80]. At potentials greater than 0.6 V, OH_{ads} formation begins at the terrace sites of all the surfaces examined and as stated in reference [80] the PtOH bond is weaker on the {111} terraces of stepped surfaces compared to those of flat Pt{111}. For Pt{332}, this process is completely reversible in the potential range used. Increasing kink density pushes this process to positive potentials (indicated by the arrow at high potentials in fig. 23) and results in slightly lower charge for OH_{ads} terrace formation. This is due to the small decrease in terrace width for the more kinked surfaces, as is shown in the ball models above. Increasing kink density also results in the appearance of an irreversible process at ~ 0.7V. This feature is usually prominent in the [Pt n{111}x{100}] series of surfaces and represents the formation of O_{ads} at {111}x{100} step sites by the diffusion of OH_{ads} from terraces, as discussed in reference [81]. This feature is therefore further indication of the presence of {100} kinks in the surfaces created.

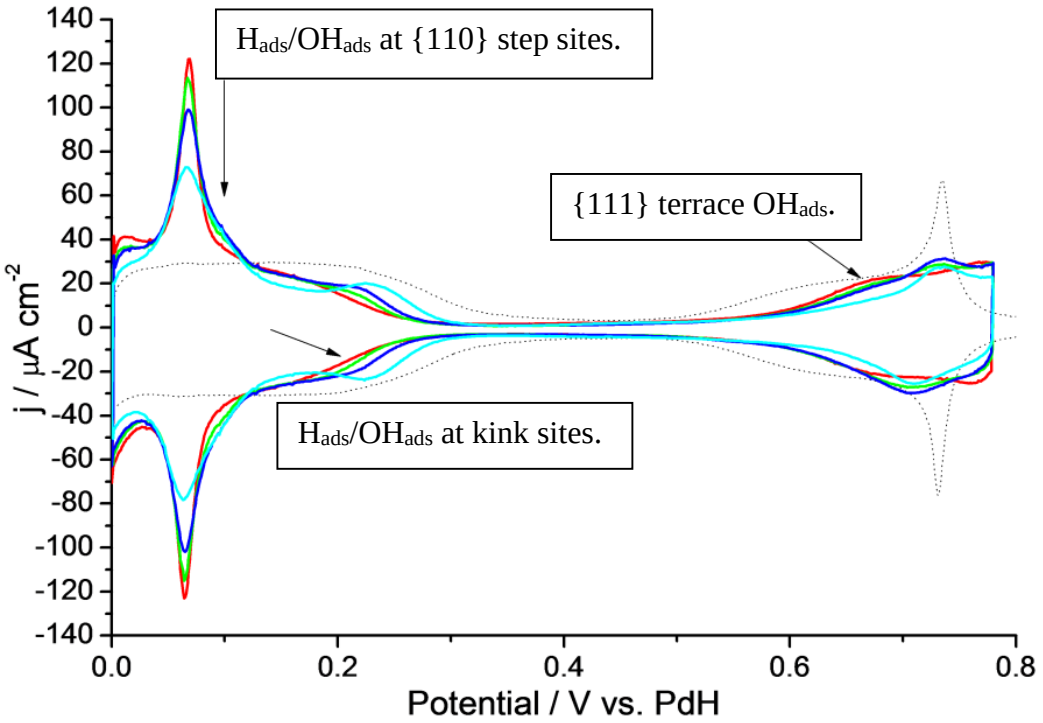

Figure 23. Cyclic voltammetry of Pt{111} (black dotted), Pt{332} (red), Pt{10,9,6} (green), Pt{764} (dark blue), Pt{864} (light blue) in contact with 0.1 M perchloric acid electrolyte, sparged with N_2 and an applied scan rate of 50 mVs^{-1}.

Fig. 24 shows the ORR results of the surfaces examined in perchloric acid and shows that the linearly stepped surface, Pt{332}, is the most active. This surface exhibits an $E_{1/2}$ value

approximately 50 mV positive of Pt{111}, in line with results shown in reference [6]. A drop in activity is observed upon examining the least kinked surface Pt{10,9,6}. Pt{764} has a further decrease in activity and the most kinked surface, Pt{864}, has the lowest activity. The activity of Pt{864} ($E_{1/2}$ = 0.824 V) approaches that of the Pt{755} surface ($E_{1/2}$ = 0.82 V) , which contains linear {100} steps (see table below). These results indicate that the presence of these types of kinks is detrimental to the ORR. As has been shown in previous work, [Pt n{111}x{100}] [7] surfaces are inferior to [Pt n{111}x{111}] [6] surfaces when equal terrace length is compared, indicating that the {100} step site has lower activity than the {110} step when present along with {111} terraces. These ORR RDE results show that {100}, even when present as kinks, lowers ORR activity on platinum surfaces.

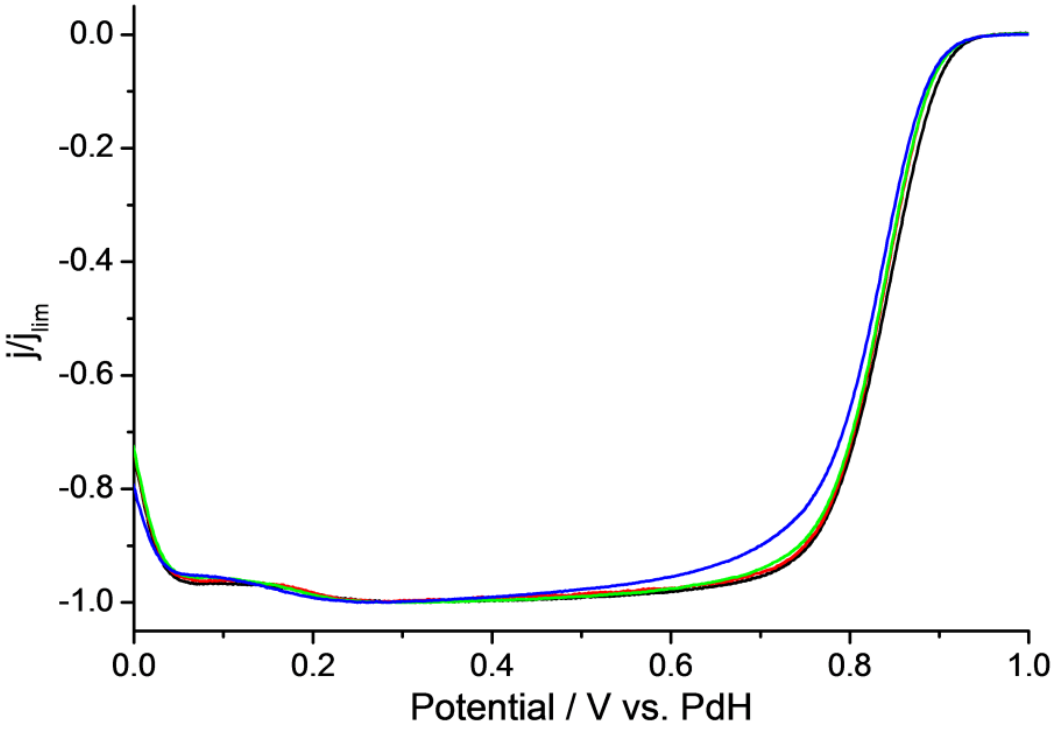

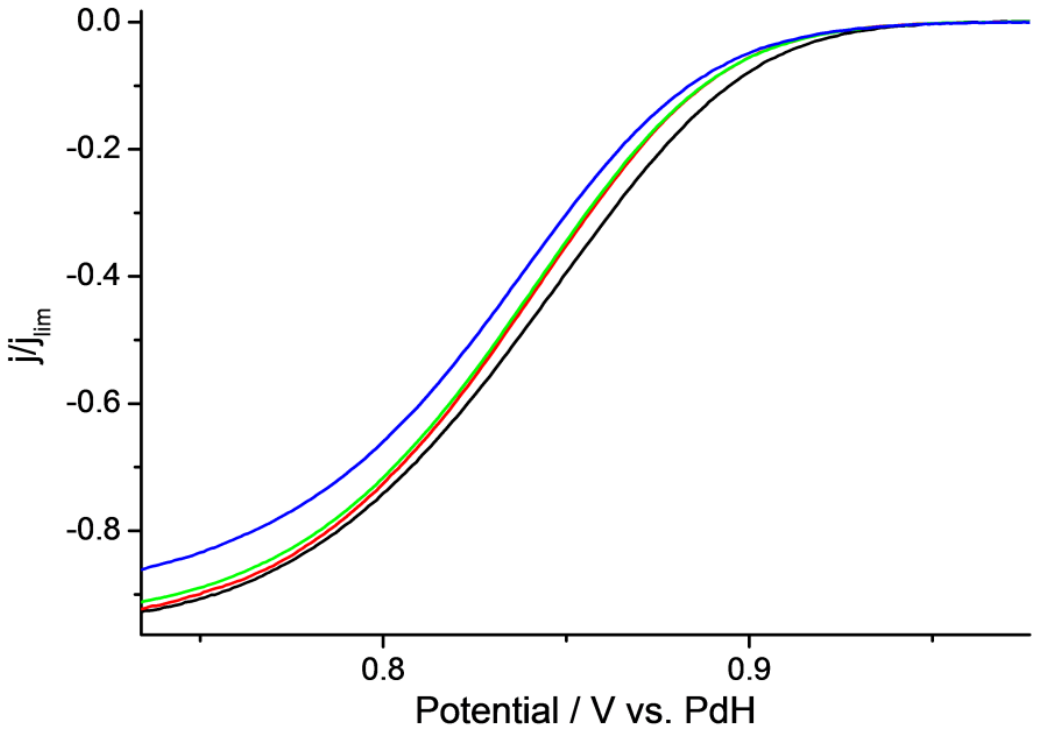

Figure 24. (a) above, ORR activity of Pt{332} (black), Pt{10,9,6} (red), Pt{764} (green) and Pt{864} (blue) surfaces. 0.1 mol dm^{-3} $HClO_4$ scan rate = 30 mV/s, 1 atm O_2, 1600 rpm rotation rate. (b), below, shows the mixed kinetic-diffusion controlled and kinetic regime of the results shown in figure (a).

Surface	$E_{1/2}$ (Volts)
Pt(332) [6(111)x(111)]	0.836
Pt(10,9,6)	0.834
Pt(764)	0.833
Pt(864)	0.824
Pt(755) [6(111)x(100)]	0.820

Table 2. Comparison of the $E_{1/2}$ values for the oxygen reduction reaction activity of selected surfaces. Experimental error of +/-2mV (0.002V) for all surfaces examined.

3.3.3 Conclusions

An ORR active surface, Pt{332}, has been compared to its kinked analogues. CVs of Pt{10,9,6}, {764} and {864}, with kinks every 4, 3 and 2 step atoms respectively, show that increasing the amount of {100} kinks on {110} steps decreases the activity of the surface

towards the ORR. The lowest activity, Pt{864}, surface approaches the activity of the non-kinked Pt{755} surface. This indicates that {100} kinks have the same reactivity as {100} steps and inhibit the ORR by the same process.

3.4 Cyclic Voltammetry and Oxygen Reduction Activity of the Pt{110}-(1x1) Surface

A Pt{110}-(1x1) single-crystal electrode surface was created by flame annealing and cooling of the electrode in gaseous CO. For the first time, the voltammetry of this unreconstructed surface is reported using aqueous perchloric acid and sodium hydroxide electrolytes. The voltammetric response for Pt{110}-(1x1) produces marked differences when compared with the reconstructed, H_2 – and N_2- cooled, disordered Pt{110}-(1x2) surface phases. Pt{110}-(1x1) exhibits as many as 6 individual peaks in the low potential region (0 - 0.25V vs. Pd/H), a singular sharp oxidation peak at 0.95 V (Pd/H) corresponding to the electrosorption of oxide and almost zero current associated with OH formation between 0.6 V (Pd/H) and 0.9 V (Pd/H). Charge density curves indicate that the total charge passed between 0 V (Pd/H) and 1.5 V (Pd/H) to be almost identical for both the (1x1) and the disordered (1x2) phases in perchloric acid, sulphuric acid and sodium hydroxide electrolyte. The oxygen reduction reaction (ORR) activity of the (1x1) surface phase was also examined using rotating disc electrode voltammetry in the hanging meniscus configuration. The half-wave ORR peak potential was found to be ~ 30 mV more negative than for the disordered reconstructed surface. This leads to the conclusion that the activity of the unreconstructed basal planes of platinum towards the ORR follows the order {100}<{110}<{111} when $E_{1/2}$ is used as a measure of activity and that the higher activity usually ascribed to Pt{110} over Pt{111} is actually a manifestation of the disordered (1x2) surface phase in which step sites and defects promote ORR.

3.4.1 Introduction

In surface electrochemical studies, a reproducible electrochemical interphasial region is of the utmost importance in order to clarify structure-sensitivity relationships in electrocatalysis. This is because electrode reactions may be catalysed by different surface sites to varying degrees [82]. For the case of solid metal electrodes, these sites could include terraces, steps or kinks. If the electrode surface structure and composition are not reproducible, structure activity relationships and a true understanding of any surface electrode process will be impossible to deduce. However, even when electrodes are prepared in such a way that the condition of the surface is well-defined and the same surface structure and composition obtained every time an adsorption experiment is performed, it is not necessarily the case that correlations between

reactivity and structure are unambiguous. For example, all (save for Ir{111}) of the basal planes of Pt, Ir and Au when clean may undergo surface reconstruction under appropriate conditions [83, 84] (The Pt{111} surface reconstructs only at high temperatures [85, 86], or in the presence of saturated Pt vapour [87, 88]). Hence, a fundamental question for electrocatalytic investigations would be how the reconstruction of a clean surface affects electrocatalytic activity? In the case of Pt{111} surfaces, the reconstructed state is not normally accessed under ambient electrochemical conditions. However, for Pt{100} differences in the reconstructive state of the electrode surface may be obtained by simply changing the ambient in which the electrode is prepared [89, 90].

Will was the first to use platinum single crystal electrodes for electrochemical analysis in the 1960's [91]. Although preparing these crystals involved potential cycling to high potentials, a procedure Will acknowledged may change the surface structure, electrosorption features in the H_{UPD} region (0.05-0.3V vs. RHE) in sulphuric acid electrolyte could be ascribed to particular adsorption sites using this procedure. The low potential H_{UPD} peak (0.12 V vs. RHE) was correctly assigned to the presence of {110} sites on the surface of polycrystalline platinum and the peak at more positive potentials (0.27 V vs RHE) to the presence of {100} sites.

The flame annealing procedure used to prepare well-defined Pt electrode surfaces was first reported by J. Clavilier and R. Durand leading to a great advance in our understanding of the relationships between surface structure and voltammetry [1]. In particular, the characteristic cyclic voltammetry of the clean and well-ordered Pt{111} surface in perchloric and sulphuric acid electrolytes was first reported [92].

It has since been shown that an intermediate cooling step in the flame annealing procedure may be instrumental in controlling surface reconstruction. A Pt{111}-(1x1) surface structure is obtainable using a cooling ambient of inert or reducing gases such as argon and hydrogen [93]. Similarly, cooling of a Pt{100} electrode after flame-annealing in a hydrogen ambient facilitates the formation of a Pt{100}-(1x1) surface structure [94]. In contrast, a reconstructed hex-R0.7° phase of Pt{100} is obtained when argon or nitrogen is employed as the cooling ambient with exclusion of all other gases [89]. Kolb *et al.* demonstrated that by flame annealing a Pt{110} electrode and cooling in a $CO + N_2$ atmosphere the (1x1) surface configuration would form whereas the Pt{110}-(1x2) "missing row" surface structure formed only when cooled in N_2 [93]. Markovic *et al.* using in situ surface X-ray diffraction (SXRD) also

demonstrated that either the (1x2) or (1x1) surface atomic arrangements could be formed by using the same cooling environment (3% H_2 in Ar) but by controlling the gas phase quenching temperature [95]. In their work, the (1x1) phase was formed by rapid gas phase quenching at high temperature, whereas to form the (1x2) structure the crystal was allowed to cool before quenching. In reference [95] it was also reported that the (1x2) reconstruction would remain stable so long as potential excursions into the electrochemical oxide potential region were avoided. This was in accordance with previous ex situ LEED studies [96]. Astonishingly, in situ SXRD measurements by these workers also revealed that the (1x2) reconstruction remained unperturbed after the Pt{110} electrode had been exposed to carbon monoxide [95]. This points to a marked stability being bestowed upon the reconstructed phase by the electrochemical environment since under UHV conditions, adsorbed CO immediately lifts the clean surface reconstruction of Pt{110} [97]. In contrast, studies on stepped surfaces vicinal to Pt{110} suggested that CO displaces adsorbed hydrogen amounts slightly higher [98, 99], but very close, to the theoretical (1x1) figure (147 $\mu C/cm^2$) hence, suggesting an unreconstructed state after hydrogen cooling.

Bittner *et al.* [100] showed by electrochemical scanning tunnelling microscopy (EC-STM) that for a Pt{110} surface cooled in iodine, at very negative potentials (in H_2SO_4 electrolyte), the iodine desorbs and gives rise to an unreconstructed (1×1) surface with a surface topography consisting of small rectangular and isotropic terraces [100]. However, recent work by Rodriguez *at al*. [101] using voltammetry and in situ surface infra-red studies supported the notion of both the (1x1) and (1x2) surface phases of Pt{110} coexisting to different extents depending on the cooling environment. Later, it will be shown that this model is indeed consistent with the data presented in the present study.

As mentioned earlier, many important electrocatalytic reactions carried out over platinum surfaces have been shown to be sensitive to the surface atomic arrangement. The oxygen reduction reaction (ORR) is one such reaction which shows not only increasing activity with surface step density but also different activities for the {100}, {110} and {111} basal planes. In some studies [4, 6, 7, 38, 102], Pt{110} exhibits high activity so that, when using the half-wave potential $E_{1/2}$ as a measure of ORR activity, the order of activity is {100}<{111}<{110}. Another study by Hoshi *et al*. has shown that, when using the current density at 0.9 V (vs. RHE) as a measure of activity, the {110} surface is approximately equal to {111} (0.59 vs 0.60 mA cm^{-2} respectively) but when using $E_{1/2}$ the order of activity is {100}<{110}<{111} [78].

Studies of the ORR usually utilise a H_2 or H_2/Ar cooling gas during the flame annealing procedure, producing the (1x1) unreconstructed surfaces of Pt{111} and {100}. As the Pt{110}-(1x1) surface requires stricter control over cooling conditions, it is likely that all previous studies have actually used a Pt{110}-(1x2) electrode or possibly a mixed (1x1)/(1x2) surface [95, 101]. This means that structure – reactivity trends in the case of the basal planes of platinum for ORR may not be being compared on a strictly similar basis since one of the surfaces would actually be reconstructed/disordered whereas the other two would not:

Pt{100}-(1x1) < Pt{111}-(1x1) < disordered/Pt(110}-(1x2) ?

No studies have looked at the ORR activity of the (1x1) unreconstructed Pt{110} surface, even though its voltammetry has been reported in sulphuric acid and has been shown to be quite distinct to that of the hydrogen-cooled surface [93]. In this section, the perchloric acid, sulphuric acid and sodium hydroxide voltammetry of the unreconstructed Pt{110} surface as well its ORR activity in perchloric acid will be reported. Also, the stability of Pt{110}-(1x1) towards potential cycling will be elucidated.

3.4.2 Results

3.4.2.1 Voltammetry

Fig. 25 shows cyclic voltammetry for an assumed Pt{110}-(1x1) single crystal electrode surface in aqueous 0.1 M sulphuric acid that was obtained by flame annealing and cooling in a CO ambient. Similarities in voltammetric response to Kolb *et al.* [93] can be seen here, namely the presence of a shoulder peak at 0.123 V which is not present in the voltammetry of the H_2 cooled Pt{110} surface. Although the peaks at ~ 0.1 V are larger for the CO-cooled electrode than for the hydrogen-cooled phase, the total charge passed in this region is approximately equal for both surfaces, 204 μC cm^{-2} for the hydrogen-cooled vs. 210 μC cm^{-2} for the CO-cooled (1x1) surface. Kolb and co-workers reported higher values of ~275 μC cm^{-2} for the (1x1) surface after CO + N_2 cooling. Our results agree more closely to those achieved by Markovic *et al.*, who also obtained sharper peaks for the (1x1) surface [95] and obtained approximately equal charges for the (1x1) and (1x2) surfaces of ~180 μC cm^{-2} [95] in the low potential electrosorption region.

Fig. 25 also shows the electrooxidation peak at ~ 1 V (ascribable to oxide formation) to be larger and sharper for the (1x1) phase compared to the hydrogen-cooled surface, implying a higher level of surface order for the (1x1) surface. This is also shown by the lower level of defect electrosorption peaks for the (1x1) surface at around 0.8 V. The total charge passed between 0 - 1.5 V is approximately equal for both surfaces.

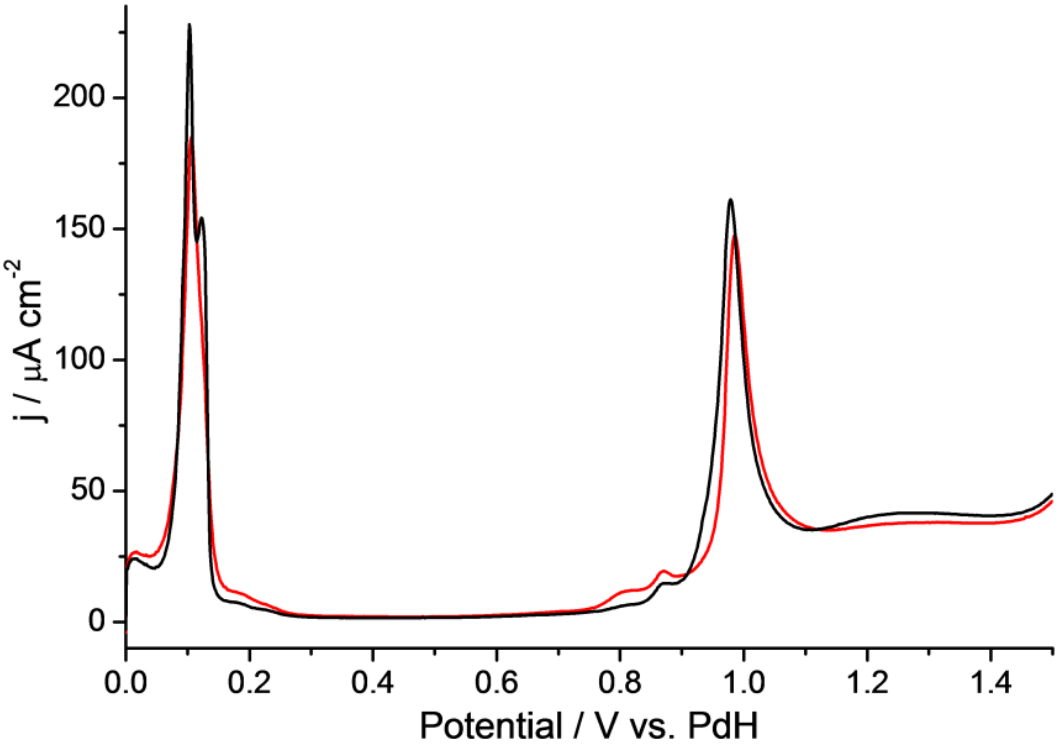

Figure 25. Voltammetry of the hydrogen cooled Pt{110} surface (red) and the CO cooled Pt{110}-(1x1) surface (black) in 0.1 mol dm^{-3} H_2SO_4. Sweep rate = 50 mV s^{-1}.

The voltammetry of the (1x1) surface in perchloric acid is shown in fig. 26(a). The first scan shows oxidation of the CO adlayer (~ 96% of charge in region 0 to 0.3 V blocked) to occur at 0.63 V. After removal of this adlayer, subsequent scans show peaks in the low potential region that are very different to those of the hydrogen-cooled and nitrogen-cooled surfaces (a direct comparison between all surfaces is shown in fig. 26(b)). As many as 6 peaks are seen in fig. 26(a) between 0 - 0.3 V in perchloric acid. The largest peak (P1) occurs at 0.09 V and has a shoulder (P2), which in some cases appears as a distinct peak, at 0.10 V. There is another pair of smaller peaks at slightly higher potentials, 0.135 V (P3) and 0.145 V (P4), and a final pair of peaks at 0.18 V (P5) and 0.20 V (P6). Peak fitting on the Pt{110}-(1x1) perchloric acid voltammetry in the 0.05-0.25 V potential range in order to elucidate the approximate charge associated with each of these peak processes was performed. From this analysis P1 was found

to have a charge of ~ 32 μC cm^{-2}, P2 a charge of ~ 5 μC cm^{-2}, P3 ~ 5.5 μC cm^{-2}, P4 ~ 6.5 μC cm^{-2}, P5 ~ 25 μC cm^{-2} and P6 a charge of ~ 43 μC cm^{-2}. The voltammetry reveals an extra 20 μC cm^{-2} to be associated with H_{ads} electrosorbed negative of 50 mV (vs. Pd/H), bringing the total to ~137 μC cm^{-2}. The remaining charge of ~ 60 μC cm^{-2} was associated with background current that could not be ascribed to peak processes listed above, reaching the total of ~ 200 μC cm^{-2} that is seen between 0 - 0.25 V in fig. 26(c). Since a theoretical charge of only 147 μC cm^{-2} is predicted for a perfect (1x1) surface and it is unlikely that this surface is defective based on its CV response, it is speculated that a second species is coadsorbed. As postulated using CO charge displacement studies, it is suggest that water splitting to form OH is the likeliest candidate here and that a PZTC value of around 0.18 V (Pd/H) is expected (potential where 147 μC cm^{-2} of H_{upd} charge is passed). This value would be close to the PZTC of a hydrogen-cooled Pt{110} electrode [103].

Despite the multitude of peaks in this low potential range, fig. 26(b) shows a single sharp oxidation peak at ~ 0.95 V for the (1x1) surface. The (1x1) surface's combination of a very sharp oxidation peak at 0.95 V and a multiplicity of peaks below 0.3 V implies an atomically perfect (1x1) surface with multiple and distinct energetic states in which H_{ads}/OH_{ads} can coadsorb as a function of potential. In fact we assert that only long range order giving rise to large domains of Pt{110}-(1x1) can generate such a multitude of sharp narrow peaks on Pt{110} in a similar manner to the so-called "butterfly" peaks on Pt{111} reflecting long range order being present in the surface.

In contrast, the hydrogen-cooled electrode voltammetric response exhibits only 2 peaks between 0 - 0.3 V, one at 0.09 V and another broad feature at 0.22 V (see red fig. 26(b)). This surface also exhibits an oxidation peak at 0.95 V which is half the height of the peak for the (1x1) surface and shows higher current responses for electrosorption of OH/oxide at defects between 0.6 and 0.9 V. We presume that (1x1) domains are actually present on this hydrogen-cooled electrode but that they are of lower surface density resulting in a 50% decrease in the magnitude of the {110}-(1x1) 0.95 V peak.

In a further manifestation of how the cooling environment influences the voltammetric response of a flame-annealed Pt{110} electrode, when nitrogen cooling is employed, the extent of 1x1 surface order (as signified by the intensity of the oxide electrosorption peak at 0.95 V)

is reduced still further and much greater peak intensity due to adsorption at defects (0.6 - 0.9 V) observed. It is noted that according to Kolb and co-workers [93], such treatment results in the generation of a reconstructed (1x2) phase (indeed according to Attard *et al.* the same is also true of Pt{100} whereby a reconstructed hex R0.7^{o} phase forms [89]). It should also be noted that the adsorption at "defects" occurs at rather negative potentials. Unpublished work from our group studying correlations between peak potential of electrosorbed OH species and step density/symmetry have shown that the small peaks between 0.84 and 0.87 V correspond to OH adsorbing at (111)x(100) and (100)x(110) linear steps respectively.

For the nitrogen-cooled sample, the large OH adsorption peak at 0.74 V is normally associated with the potential range ascribable to OH adsorption at{111} terraces rather than steps or kinks [24]. If this is the case, it would suggest that residual {111} adsorption sites, possibly from the (1x2) reconstructed phase, are still present under electrochemical conditions for the nitrogen-cooled surface.

Returning to the H_{upd} potential range, it is interesting that there is an exact correlation between the magnitude of the 0.2 V electrosorption feature and the oxide electrosorption peak situated between 0.95-1.0 V. Hence, as mentioned earlier, this 0.2 V peak profile must be arising from the degree of long range (1x1) order present at the surface. There is also an interesting lowering in intensity and broadening of the 0.09 V peak as surface disorder increases.

In order to visualise these changes, a schematic model of what might be happening as cooling environment is changed is shown in scheme 1. Here, we start with a pristine, reconstructed Pt{110}-(1x2) phase. In order to form regions of (1x1) (constituting an increase in the disorder of the (1x2) phase) surface diffusion perpendicular to the close packed atomic rows is envisaged. If this process continues, eventually the surface will transform continuously from a (1x2) to a (1x1) phase, especially if thermalizing of the surface is allowed (flame annealing). However, the thermodynamically stable clean surface of Pt{110} under UHV conditions is the (1x2) phase. Since chemical interactions between a Pt surface and molecular nitrogen are negligible, cooling in a nitrogen ambient should still result in a (1x2) phase being preserved (the same as found for Pt{100}hex R0.7^{o} [89]). However, as the interaction of Pt with the gas ambient increases, it is expected that a new thermodynamically stable state should result involving a lifting of the 1x2 reconstruction (as reported in UHV). Hence, since CO is a more strongly interacting chemisorbate compared to hydrogen, the extent of surface reconstruction

lifting should be greatest with CO-cooled samples with hydrogen-cooled surfaces displaying an intermediate behaviour between that of CO-cooled and N_2-cooled substrates. Therefore, according to scheme 1, we place the nitrogen-cooled electrode close to the top (more (1x2) reconstructed), hydrogen-cooled electrodes somewhere in the middle and CO-cooled samples close to the perfect (1x1) phase. This idea of "mixed" (1x2)/(1x1) surface structure is in accordance with previous IR studies of CO adsorption on Pt{110}by Paramaconi and coworkers [101].

By suitable peak deconvolution of the oxide electrosorption region in particular, it may be possible to quantify the extent of (1x1)/(1x2) mixing. In fact, we speculate that the very low potential for electrochemical oxide formation in the case of the nitrogen-cooled sample is consistent with electrosorption of OH at the highly unsaturated, close-packed chains of Pt atoms formed in the (1x2)-Pt{110} phase. These atomic sites should be highly oxophillic compared to even kink and step sites due to their very low surface coordination and are predicted to display unusual electrocatalytic behaviour towards electrooxidation reactions. Hence, we propose that the magnitude of the 0.74 V OH peak on Pt{110} is proportional to the extent of (1x2) surface reconstruction present under electrochemical conditions. These ideas will be examined further in future work.

Feliu *et al.* have speculatively ascribed the broad feature at 0.22 V formed from hydrogen-cooling to co-adsorption of hydrogen and OH species [33]. The 105 μC cm^{-2} charge of the low potential peak in their work was assigned solely to H_{ads} formation and the 90 μC cm^{-2} charge of the broad feature close to 0.2 V was assigned to coadsorption of adsorbed OH based on the value of the PZTC of the surface. The total charge of almost 200 μC cm^{-2} for the two peaks is the same as the charge obtained by ourselves and shown in fig. 26(c).

The many peaks that are observed below 0.3 V for the (1x1) surface suggest also that that co-adsorption of H and OH is occurring. If P1, P3 and P5 are thought to be H_{ads} and P2, P4 and P6 thought to be OH_{ads}, this would imply that between 0.09 and 0.2V the surface is covered by a mixed H_{ads}/OH_{ads} overlayer. With changing potential, the ratio of H to OH changes as new overlayer structures are preferred. It may be further concluded that the ordered (1x1) surface only has a couple of distinct stable overlayer structures, and that the peaks between 0 - 0.3V correspond to transformation between these structures. Further theoretical studies are required

to confirm this hypothesis. In all of these speculations, the existence of an OH species at such negative potentials is a vexatious and difficult concept. However, recent work supporting water splitting and surface pH values differing from the bulk might suggest a possible resolution of this conundrum [104].

In light of this idea some general conclusions can also be made about the disordered (1x2) surface as this surface exhibits current responses in the same potential range as the (1x1) surface. The broad feature of the disordered (1x2) surface, between 0.1 - 0.25 V, is ascribed to a changing H_{ads}/OH_{ads} over-layer, in a similar fashion to the (1x1) surface described above. P2 - P6 in the voltammetry of (1x1) may also be occurring in the voltammetry of the disordered (1x2) surface, but to a lesser extent, and combined with H_{ads} on the short (111) terraces of the (1x2) structure. The loss of long range order in the (1x1) phase would be consistent with both a broadening and decrease in intensity of electrosorption features similar to when the H UPD region of Pt{hkl} surfaces is strongly modified after potential cycles to high positive potentials [105].

Fig. 26(c) shows how charge varies as a function of potential for the voltammograms depicted in fig. 26(b). These have not been adjusted for the PZTC as this value has not been determined for the (1x1) surface as yet. Between 0 and 1.5 V the same total charge is passed for all surfaces. Also, the charge passed between 0 and 0.3 V is the same (~200 $\mu C\ cm^{-2}$) for the disordered (1x2) and (1x1) surfaces and is equal to the charge passed in this potential range in sulphuric acid. The charge passed in this range is greater than the theoretical charge that should be passed for pure H_{ads} formation at every surface atom, $147\mu C\ cm^{-2}$, as has been noted in a previous study [106]. Therefore the total charge of 200 $\mu C\ cm^{-2}$ must come from a combination of H_{ads} and OH_{ads} since voltammetry suggests strongly that the surface is atomically smooth (negligible OH/oxide adsorption at defect sites) as suggested earlier.

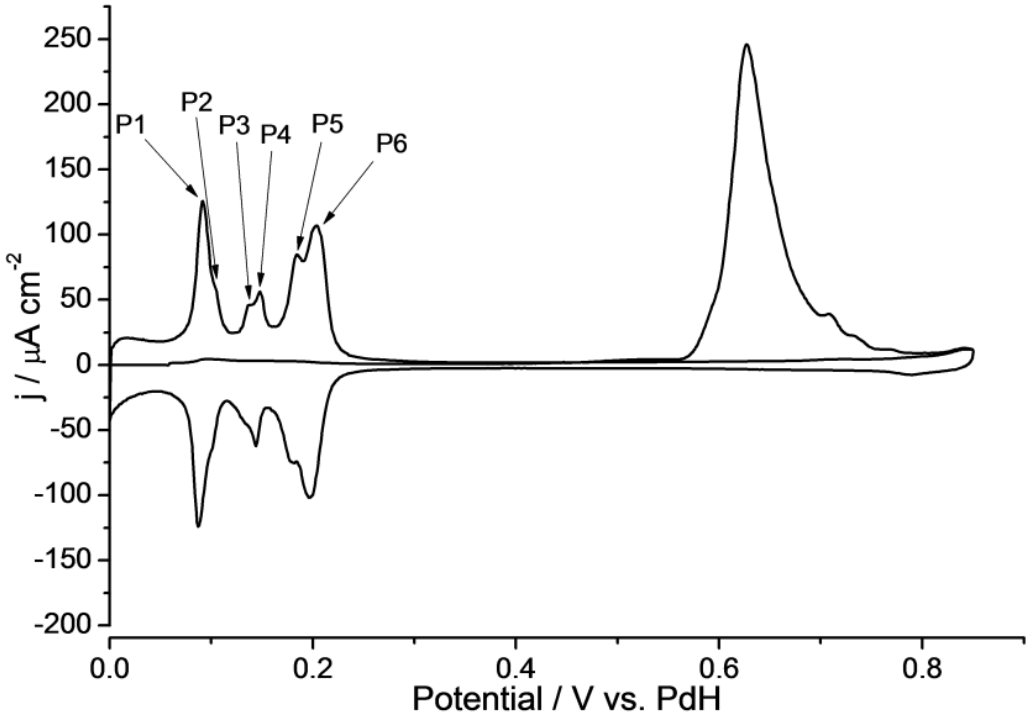
P1
P2
P3
P4
P5
P6
j / µA cm-2
Potential / V vs. PdH

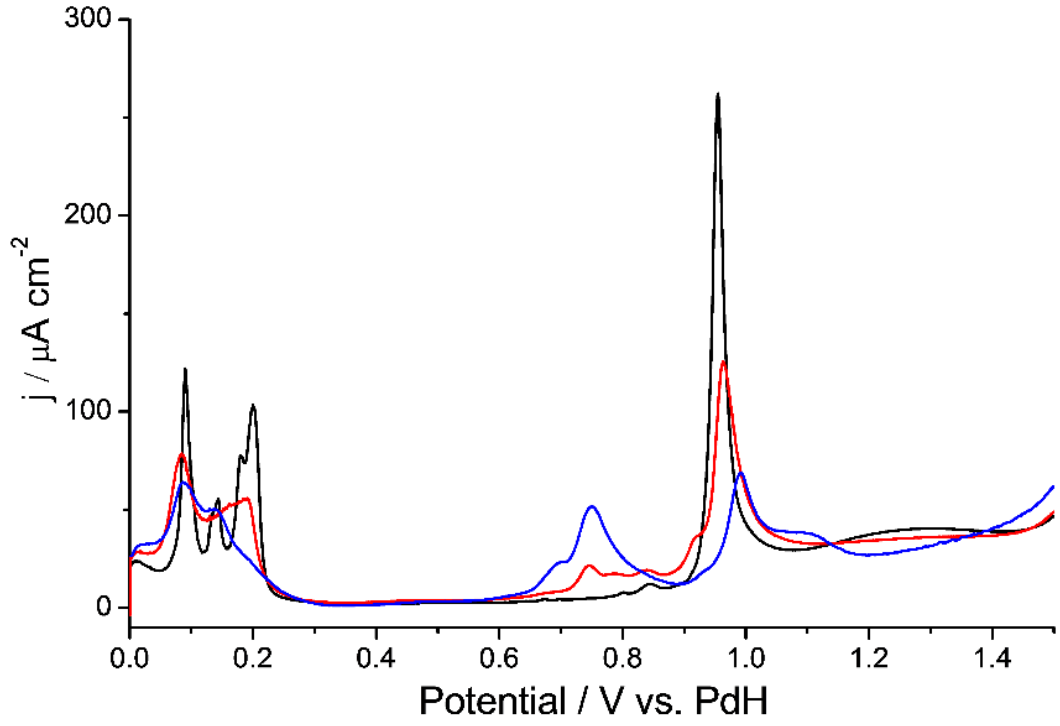
j / µA cm-2
Potential / V vs. PdH

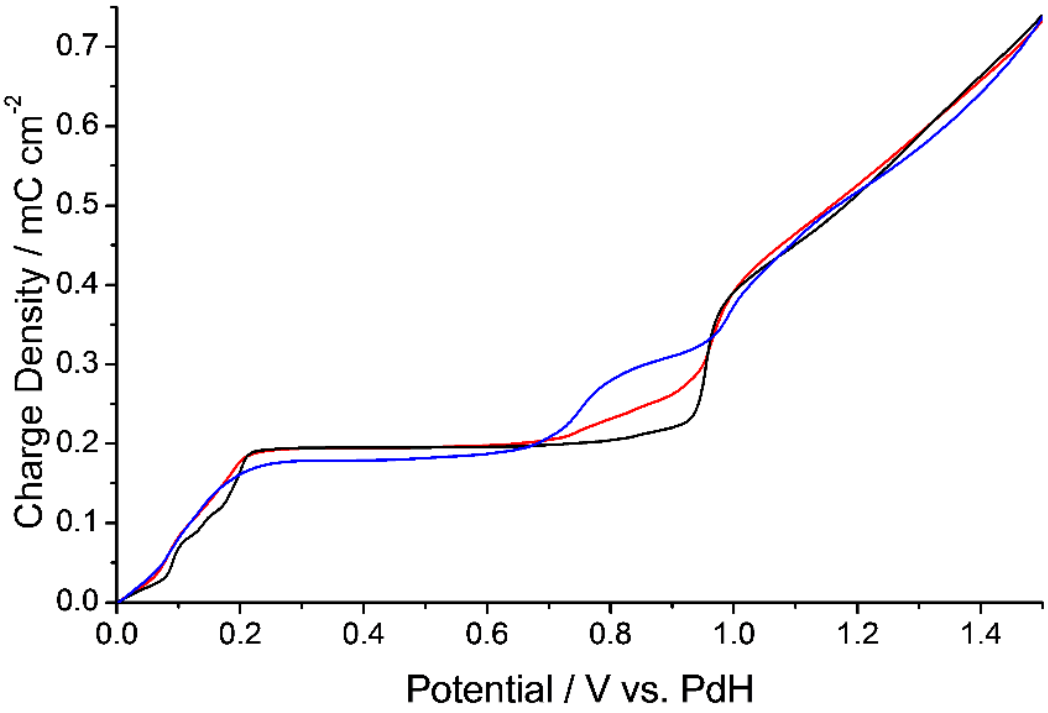

Figure 26(a) - (c). (a) CO stripping voltammetry of the CO cooled Pt{110}-(1x1) electrode in 0.1 mol dm^{-3} $HClO_4$. Sweep rate = 50 mV s^{-1}. (b) Voltammetry of the hydrogen-cooled Pt{110} surface (red), nitrogen-cooled Pt{110} (blue) and the CO cooled Pt{110}-(1x1) surface (black) in 0.1 mol dm^{-3} $HClO_4$. Sweep rate = 50 mV s^{-1}. (c) Charge density vs. potential for the (1x1), black, hydrogen-cooled, red, and nitrogen-cooled, blue, voltammetry shown in figure 26(b).

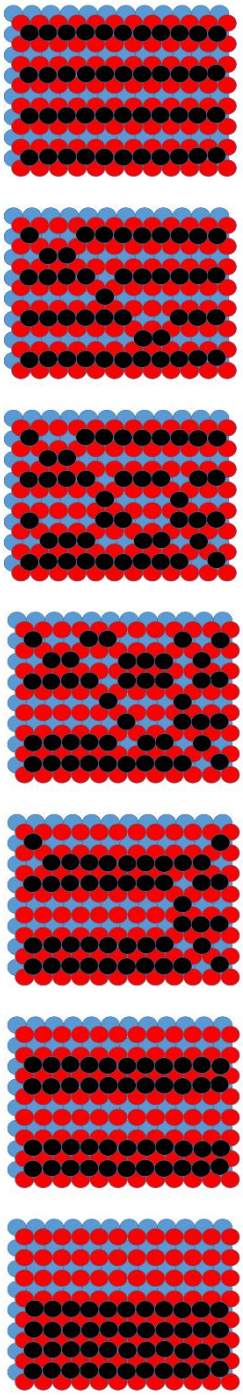

Scheme 1. An ordered (110)-(1x2), top, and (110)-(1x1) surface, bottom. The centre illustrations show disordered arrangements that are closer to (1x2) in nature near the top and close to (1x1) near the bottom.

Next, the stability of the Pt{110}-(1x1) surface was tested using potential window opening to high positive potentials in perchloric acid and the results of this procedure are shown in fig. 27(a)-(c). With an upper potential limit of 0.9 V (fig. 27(a)) the voltammetry of the (1x1) surface shows small but noticeable changes during five potential cycles. The peaks between 0 V and 0.3 V very gradually diminish with cycling and current density in the troughs between

the peaks increases at the same rate. This implies instability of the (1x1) surface even when the potential is set so that surface oxide is not formed. Nonetheless, 0.9 V does represent a rather positive potential for surface stability compared to all other Pt{hkl} electrodes save for Pt{111}. When the upper potential limit is increased to 0.95 V (fig. 27(b)), greater changes are seen in the voltammetry with cycling. At this potential limit surface oxide formation begins but is not completed. Within 5 potential cycles the voltammetry changes from that characteristic of the (1x1) surface and approaches the voltammetry usually observed after cooling in hydrogen (ascribable to the presence of disordered (1x2) domains). With an upper potential limit of 1 volt (fig. 27(c)), even after 1 cycle the voltammetry has changed dramatically and irreversibly. After 5 cycles within this potential limit, the voltammetry between 0 V and 0.3 V looks like the hydrogen cooled surface shown in fig. 26(a), implying a (1x1)→disordered (1x2) rearrangement after oxide formation and desorption (in scheme 1 corresponding to a movement in the opposite direction discussed for nitrogen-, hydrogen- and CO-cooled electrodes).

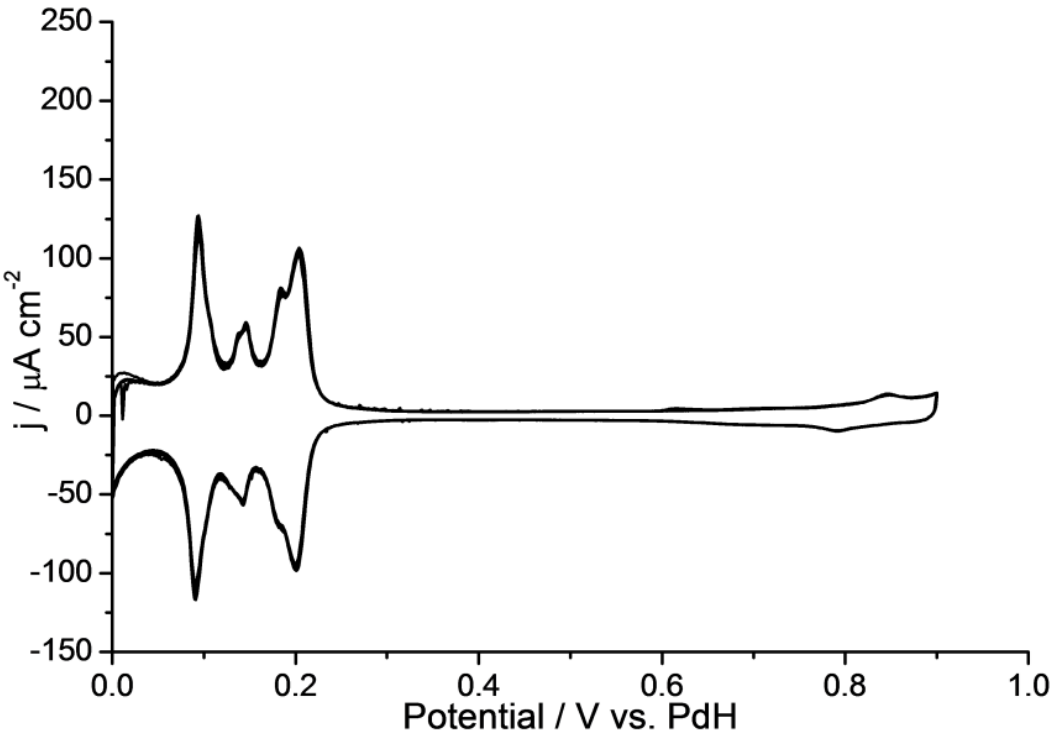

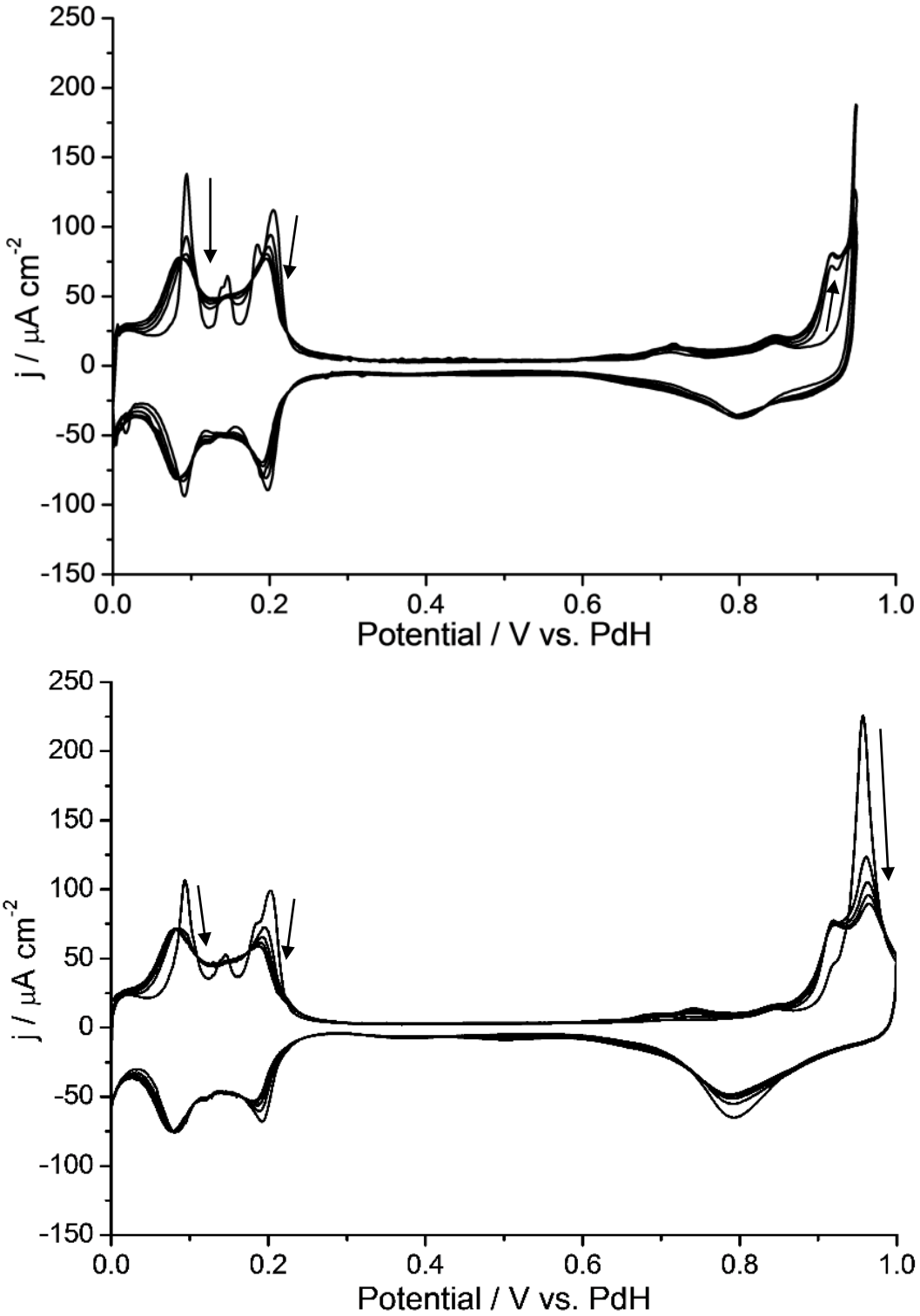

Figure 27(a)-(c). Test of increasing potential limits on the voltammetry of the Pt{110}-(1x1) surface in 0.1 mol dm^{-3} $HClO_4$. (a) 0-0.9 V. (b) 0-0.95 V. (c) 0-1 V. 5 cycles with sweep rate = 50 mV s^{-1}. Arrows indicate the direction of change in voltammetry, from first to last cycle.

The voltammetry of the CO- and H_2- cooled surfaces was then tested in 0.1 M NaOH and the results are shown in fig. 28(a). For Pt{110}- (1x1), at high potentials voltammetric behaviour

is similar to that found in perchloric and sulphuric acid whereby only limited electrosorption peaks for adsorption of OH/oxide at defects is observed. A large peak associated with oxide formation is observed at 1 V. At more negative potentials, the (1x1) surface exhibits a pair of peaks that have greater intensity than the hydrogen-cooled surface. The main peak is located at 0.22 V and exhibits a distinct shoulder at 0.25 V. Fig. 28(b) illustrates the charge density for the two surfaces. Between 0 V and 0.4 V, both (1x1) and hydrogen-cooled surfaces generate a charge of ~230 μC cm^{-2}. At ~0.7 V and above, surface defects of the hydrogen-cooled surface are responsible for its higher charge. The overall charge, between 0-1.5V, for both surfaces is approximately equal, as was seen in both sulphuric and perchloric acid electrolytes.

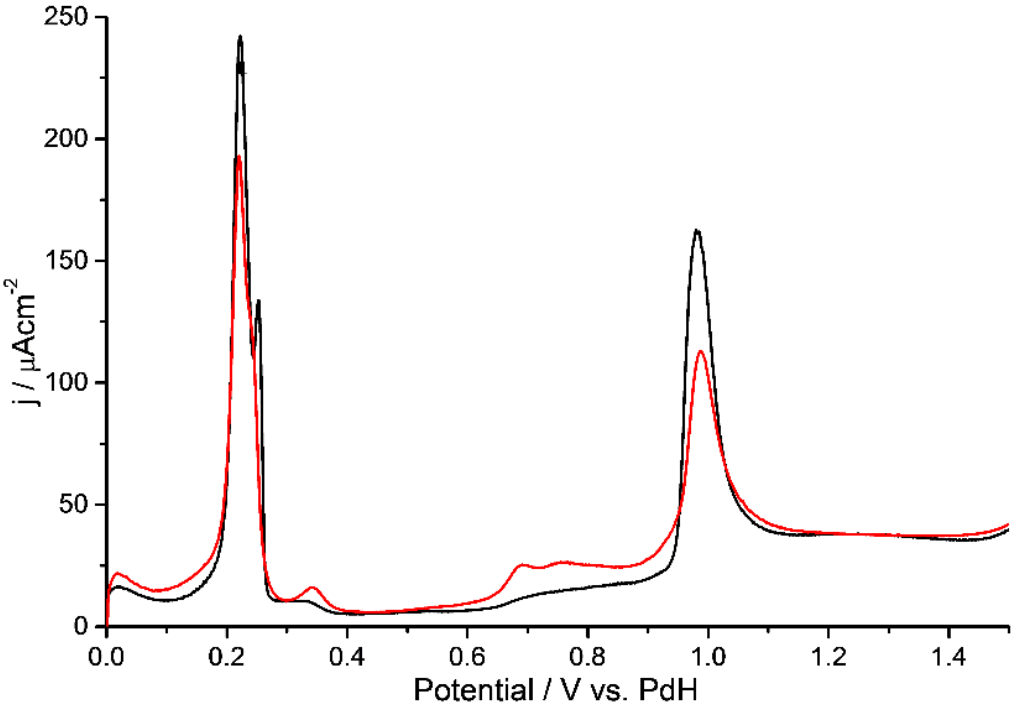

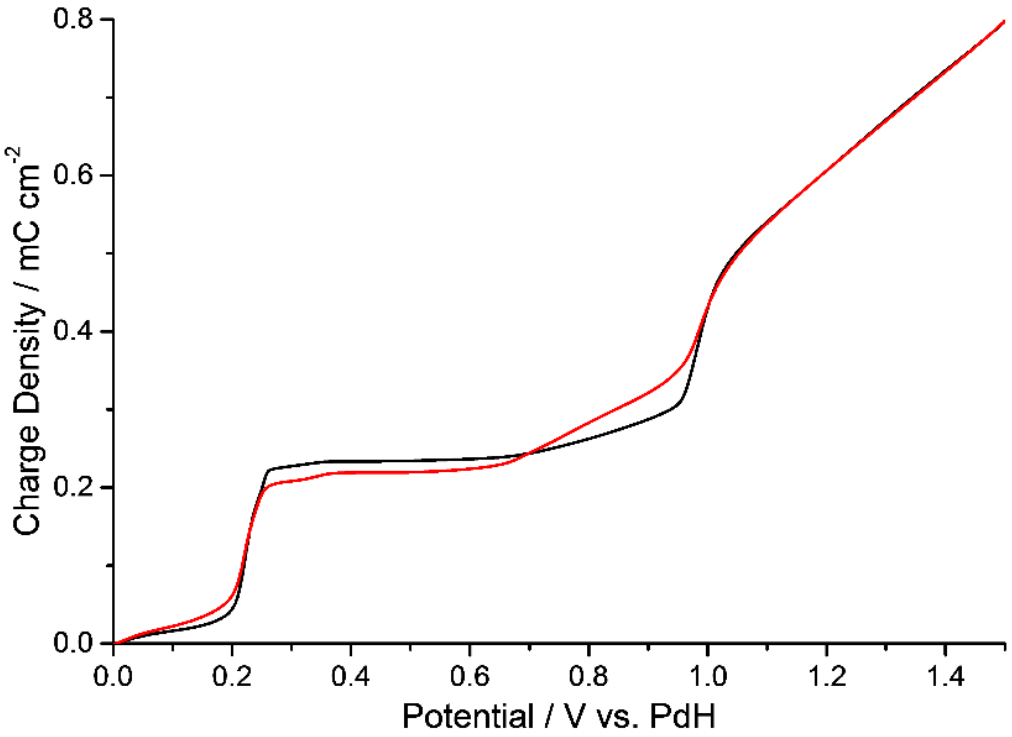

Figure 28(a) - (b). Voltammetry of the hydrogen cooled Pt{110} surface (red) and the CO cooled Pt{110}-(1x1) surface (black) in 0.1 mol dm^{-3} NaOH. Sweep rate = 50 mV s^{-1}. (b) Charge density vs. potential for the (1x1) and hydrogen-cooled electrode voltammetry shown in figure 28(a).

3.4.2.2 Oxygen Reduction

The ORR activity of the Pt{110}-(1x1), hydrogen- and nitrogen-cooled Pt{110} surface phases was tested using hanging meniscus rotating disc voltammetry and the results are shown in fig. 29. Oxygen reduction half wave potentials ($E_{1/2}$) of 0.795V and 0.765 V for the hydrogen-cooled and (1x1) surfaces respectively are noted. These results demonstrate that the disordered (1x2) surface phase of the hydrogen-cooled electrode exhibits the greater activity towards ORR. When using the current density at 0.85V as a measure of ORR activity, one observes the disordered Pt{110}-(1x2) surface to possess an even higher activity than the Pt{111} surface, ~1.1 mA cm^{-2} vs ~0.8 mA cm^{-2} respectively. The current density at 0.85V of the Pt{110}-(1x1) surface is ~ 0.8 mA cm^{-2}, a reduction of almost 30% in current compared to the hydrogen-cooled surface, bringing its activity in line with that of Pt{111}. Also shown in figure 29 is the ORR results for the nitrogen-cooled electrode. According to the voltammetric data this surface corresponds to the most "disordered" relative to the pristine (1x1) phase and we speculate, corresponds most closely to a reconstructed (1x2) phase. As expected, further disruption of the

(1x1) terraces results in still greater enhancement in ORR activity compared to the hydrogen-cooled sample. Therefore, comparing the ORR activity of the (1x1) platinum basal planes in their *unreconstructed state* results in the following order of activity:

$$\{100\} < \{110\} < \{111\}$$

It has been shown that in aqueous acidic media, stepped surfaces exhibit higher activity for oxygen reduction when compared to the basal planes [6, 7]. We conclude that the high activity usually observed for {110} is due to the predominantly disordered (1x2) structure being present. Imperfections in the (1x1) phase act to enhance electrocatalytic activity. We ascribe the mechanism by which this occurs to the break-up of a long range OH ordered structure present at the surface of Pt{110}-(1x1) which acts to prevent O_2 adsorbing, a model postulated originally by Markovic *et al.* for Pt{111} in perchloric acid [37].

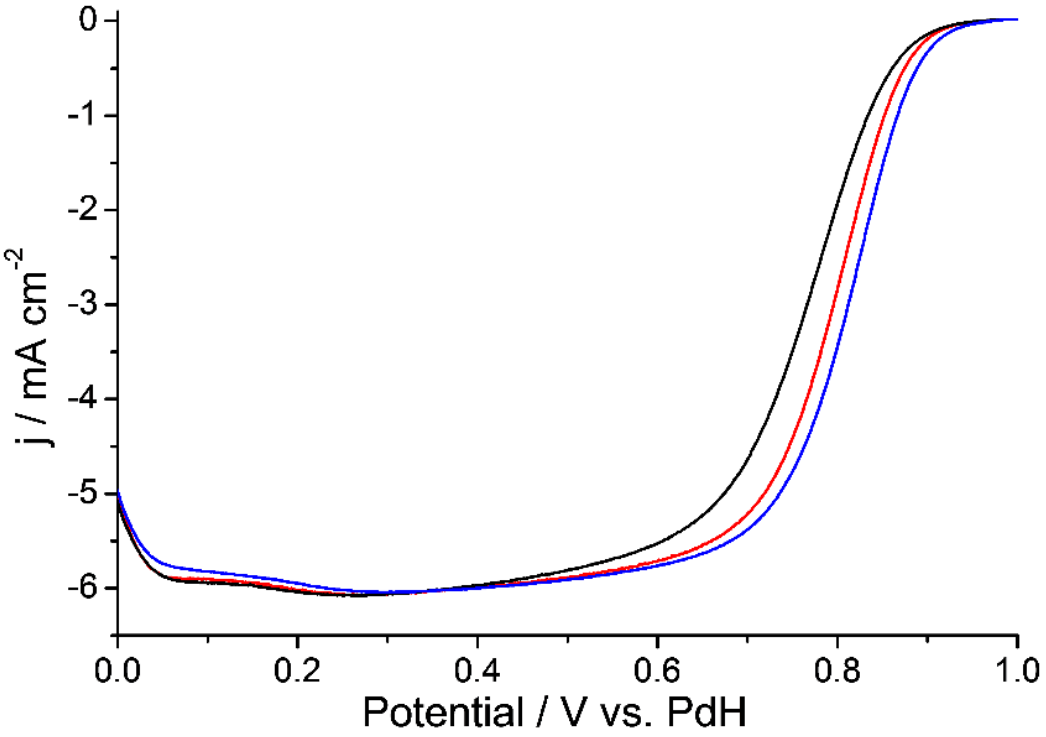

Figure 29. ORR data of Pt{110}-(1x1), black, hydrogen-cooled Pt{110}, red and nitrogen-cooled Pt{110}, blue in O_2 saturated 0.1 mol dm^{-3} $HClO_4$. A hanging meniscus rotating disc electrode configuration with sweep rate = 30 mV s^{-1}, 1atm O_2 pressure and 1600rpm rotation rate was utilised. The first positive going sweep is reported here.

3.4.3 Conclusions

The (1x1) and disordered (1x2) surface atomic arrangements of Pt{110} have been compared using their voltammetry in sulphuric acid, perchloric acid and sodium hydroxide. The voltammetry in sulphuric acid showed similarities to that reported by Kolb *et al.* and Markovic *et al.* For the first time, the voltammetry of the Pt{110}-(1x1) surface has been reported in perchloric acid and sodium hydroxide. Perchloric acid voltammetry of the (1x1) surface exhibited 6 peaks in the potential range 0 - 0.3 V, in stark contrast to the two broad peaks observed in the voltammetry of the disordered (1x2) surface. The (1x1) surface also exhibits a singular, large oxide electrosorption peak at 0.95 V and almost zero current associated with electrosorption at defects. This implies an atomically perfect Pt{110}-(1x1) surface. In contrast, the emergence of OH electrosorption peaks close to 0.75 V we ascribe to the generation of Pt{110}-(1x2) phases in which highly uncoordinated surface Pt atoms act as nucleation centres for oxide formation. It is concluded that the Pt{110} surface exhibits a mixed H_{ads}/OH_{ads} adlayer in the 0.09-0.2 V potential range and that the large number of peaks occurring are due to new adlayer structures, with differing hydrogen/OH ratios becoming stable at different potentials.

The activity of the Pt{110}-(1x1) surface for oxygen reduction was also tested and was found to be approximately 30-40 mV less active than any of the disordered (1x2) surfaces studied when $E_{1/2}$ values for ORR are compared.

3.5 References

[1] J. Clavilier, R. Faure, G. Guinet, R. Durand, J. Electroanal. Chem., 107 (1980) 205-209.
[2] N.M. Markovic, H.A. Gasteiger, P.N. Ross, J. Phys. Chem., 100 (1996) 6715-6721.
[3] N.M. Markovic, H.A. Gasteiger, P.N. Ross, J. Phys. Chem., 99 (1995) 3411-3415.
[4] N.M. Markovic, R.R. Adzic, B.D. Cahan, E.B. Yeager, J. Electroanal. Chem., 377 (1994) 249-259.
[5] K. Itaya, Prog. Surf. Sci., 58 (1998) 121-247.
[6] A. Kuzume, E. Herrero, J.M. Feliu, J. Electroanal. Chem., 599 (2007) 333-343.
[7] M.D. Macia, J.M. Campina, E. Herrero, J.M. Feliu, J. Electroanal. Chem., 564 (2004) 141-150.
[8] A.M. Gómez-Marín, J.M. Feliu, ChemSusChem, 6 (2013) 1091-1100.
[9] M.J.T.C. van der Niet, A. den Dunnen, L.B.F. Juurlink, M.T.M. Koper, Angew. Chem., Int. Ed., 49 (2010) 6572-6575.
[10] A.S. Bondarenko, I.E.L. Stephens, H.A. Hansen, F.J. Perez-Alonso, V. Tripkovic, T.P. Johansson, J. Rossmeisl, J.K. Norskov, I. Chorkendorff, Langmuir, 27 (2011) 2058-2066.
[11] K.L. Hsueh, E.R. Gonzalez, S. Srinivasan, Electrochim. Acta, 28 (1983) 691-697.
[12] N.M. Markovic, H.A. Gasteiger, B.N. Grgur, P.N. Ross, J. Electroanal. Chem., 467 (1999) 157-163.
[13] N.M. Marković, T.J. Schmidt, V. Stamenković, P.N. Ross, Fuel Cells, 1 (2001) 105-116.
[14] Y.E. Seidel, A. Schneider, Z. Jusys, B. Wickman, B. Kasemo, R.J. Behm, Faraday Discuss., 140 (2009) 167-184.
[15] A. Schneider, L. Colmenares, Y.E. Seidel, Z. Jusys, B. Wickman, B. Kasemo, R.J. Behm, Phys. Chem. Chem. Phys., 10 (2008) 1931-1943.
[16] H.S. Wroblowa, P. Yen Chi, G. Razumney, J. Electroanal. Chem. Interfacial Electrochem., 69 (1976) 195-201.
[17] I. Katsounaros, W. Schneider, J. Meier, U. Benedikt, P. Biedermann, A. Auer, K.J. Mayrhofer,, Phys. Chem. Chem. Phys., 14 (2012) 7384-7391.
[18] J. Rossmeisl, Z.W. Qu, H. Zhu, G.J. Kroes, J.K. Nørskov, J. Electroanal. Chem., 607 (2007) 83-89.
[19] V. Tripković, E. Skúlason, S. Siahrostami, J.K. Nørskov, J. Rossmeisl, Electrochim. Acta, 55 (2010) 7975-7981.
[20] A.M. Gómez-Marín, K.J.P. Schouten, M.T.M. Koper, J.M. Feliu, Electrochem. Commun., 22 (2012) 153-156.
[21] G. Roberto, C. Víctor, M.F. Juan, J.W. Michael, J. Phys. Chem. B, 104 (2000) 597-605.
[22] A. Hitotsuyanagi, M. Nakamura, N. Hoshi, Electrochim. Acta, 82 (2012) 512-516.
[23] A. Berná, V. Climent, J.M. Feliu, Electrochem. Commun., 9 (2007) 2789-2794.
[24] M.T.M. Koper, J.J. Lukkien, J. Electroanal. Chem., 485 (2000) 161-165.
[25] M.J.T.C. van der Niet, N. Garcia-Araez, J. Hernández, J.M. Feliu, M.T.M. Koper, Catal. Today, 202 (2013) 105-113.
[26] T. Schiros, L.Å. Näslund, K. Andersson, J. Gyllenpalm, G.S. Karlberg, M. Odelius, H. Ogasawara, L.G.M. Pettersson, A. Nilsson, J. Phys. Chem. C, 111 (2007) 15003-15012.
[27] G.S. Karlberg, G. Wahnström, Phys. Rev. Lett., 92 (2004) 136103.
[28] G.S. Karlberg, G. Wahnström, J. Chem. Phys., 122 (2005) 194705.
[29] K.J.P. Schouten, M.J.T.C. van der Niet, M.T.M. Koper, Phys. Chem. Chem. Phys., 12 (2010) 15217-15224.
[30] A. Rodes, M.A. Zamakhchari, K. El Achi, J. Clavilier, J. Electroanal. Chem. Interfacial Electrochem., 305 (1991) 115-129.
[31] K. Domke, E. Herrero, A. Rodes, J.M. Feliu, J. Electroanal. Chem., 552 (2003) 115-128.
[32] N. Garcia-Araez, J.J. Lukkien, M.T.M. Koper, J.M. Feliu, J. Electroanal. Chem., 588 (2006) 1-14.
[33] N. Garcia-Araez, V. Climent, J.M. Feliu, J. Electroanal. Chem., 649 (2010) 69-82.
[34] B. Han, V. Viswanathan, H. Pitsch, J. Phys. Chem. C, 116 (2012) 6174-6183.
[35] V.R. Stamenkovic, B. Fowler, B.S. Mun, G. Wang, P.N. Ross, C.A. Lucas, N.M. Markovic, Science, 315 (2007) 493-497.

[36] G.A. Attard, A. Brew, J.-Y. Ye, D. Morgan, S.-G. Sun, ChemPhysChem, 15 (2014) 2044-2051.
[37] J.X. Wang, N.M. Markovic, R.R. Adzic, J. Phys. Chem. B, 108 (2004) 4127-4133.
[38] J. Perez, H.M. Villullas, E.R. Gonzalez, J. Electroanal. Chem., 435 (1997) 179-187.
[39] E. Sitta, A.M. Gómez-Marín, A. Aldaz, J.M. Feliu, Electrochem. Commun., 33 (2013) 39-42.
[40] A.M. Gomez-Marin, Rubin Rizo, J.M. Feliu, Beilstein J. Nanotechnol., 4 (2013) 956-967.
[41] W. Yu, M. Porosoff, J. Chen,, Chem. Rev., 112 (2012) 5780-5817.
[42] C. Wang, M. Chi, D. Li, D. Strmcnik, D. van der Vliet, G. Wang, V. Komanicky, K.-C. Chang, A. Paulikas, D. Tripkovic, J. Pearson, K. More, N. Markovic, V. Stamenkovic, J. Am. Chem. Soc., 133 (2011) 14396-14403.
[43] V. Stamenkovic, B. Mun, M. Arenz, K.J. Mayrhofer, C. Lucas, G. Wang, P. Ross, N. Markovic, Nat. Mater., 6 (2007) 241-247.
[44] D. van der Vleit, C. Wang, M. Debe, R. Atanasoki, N.M. Markovic, V.R. Stamenkovic, Electrochim. Acta, 56 (2011) 8695-8699.
[45] S.J. Hwang, S.J. Yoo, S. Jang, T.-H. Lim, S.A. Hong, S.-K. Kim, J. Phys. Chem. C, 115 (2011) 2483-2488.
[46] L. Liu, E. Pippel, Angew. Chem., Int. Ed., 50 (2011) 2729-2733.
[47] I.E.L. Stephens, A.S. Bondarenko, F.J. Perez-Alonso, F. Calle-Vallejo, L. Bech, T.P. Johansson, A.K. Jepsen, R. Frydendal, B.P. Knudsen, J. Rossmeisl, I. Chorkendorff, J. Am. Chem. Soc., 133 (2011) 5485-5491.
[48] M.B. Vukmirovic, J. Zhang, K. Sasaki, A.U. Nilekar, F. Uribe, M. Mavrikakis, R.R. Adzic, Electrochim. Acta, 52 (2007) 2257-2263.
[49] S.J. Hwang, S.-K. Kim, J.-G. Lee, S.-C. Lee, J.H. Jang, P. Kim, T.-H. Lim, Y.-E. Sung, S.J. Yoo, J. Am. Chem. Soc., 134 (2012) 19508-19511.
[50] L. Rameshwori, L. Jin, H. Ting, C. Yongsheng, X. Zhichuan, N.N. Peter, N.W. Bridgid, F. Bin, M. Derrick, Y. Jun, K. Jonathan, P. Brian, Z. Chuan-Jian, J. Phys. Chem. C, 115 (2011) 1682-1694.
[51] U.A. Paulus, A. Wokaun, G.G. Scherer, T.J. Schmidt, V. Stamenkovic, N.M. Markovic, P.N. Ross, Electrochim. Acta, 47 (2002) 3787-3798.
[52] S. Jiang-lan, C. Chen, C.M.L. James, Adv. Funct. Mater., 21 (2011) 3357-3362.
[53] J. Greeley, I. Stephens, A. Bondarenko, T. Johansson, H. Hansen, T. Jaramillo, J. Rossmeisl, I. Chorkendorff, J. Nørskov, Nat. Chem., 1 (2009) 552-556.
[54] M. Shao, K. Shoemaker, A. Peles, K. Kaneko, L. Protsailo, J. Am. Chem. Soc., 132 (2010) 9253-9255.
[55] R. Yang, J. Leisch, P. Strasser, M.F. Toney, Chem. Mater., 22 (2010) 4712-4720.
[56] S. Guo, D. Li, H. Zhu, S. Zhang, N. Markovic, V. Stamenkovic, S. Sun, Angew. Chem., Int. Ed., 52 (2013) 3465-3468.
[57] S. Woo, I. Kim, J.K. Lee, S. Bong, J. Lee, H. Kim, Electrochim. Acta, 56 (2011) 3036-3041.
[58] H. Yang, Angew. Chem., Int. Ed., 50 (2011) 2674-2676.
[59] J. Wu, L. Qi, H. You, A. Gross, J. Li, H. Yang, J. Am. Chem. Soc., 134 (2012) 11880-11883.
[60] S.E. Huxter, G.A. Attard, Electrochem. Commun., 8 (2006) 1806-1810.
[61] N. Bogolowski, S. Huxter, A-E-A. A. Abd-Elf-Latif, G.A. Attard, H. Baltruschat, J. Electroanal. Chem., 646 (2010) 68-74.
[62] A.M. El-Aziz, L.A. Kibler, Electrochem. Commun., 4 (2002) 866-870.
[63] A. El-Aziz, R. Hoyer, L. Kibler, ChemPhysChem, 11 (2010) 2906-2911.
[64] S. Ram, N. Danilovic, P.P. Lopes, D. Tripkovic, D. Strmcnik, V.R. Stamenkovic, N.M. Markovic, J. Phys. Chem. C, 116 (2012) 22231-22237.
[65] A.P. Grosvenor, M.C. Biesinger, R. St.C. Smart, N.S. McIntyre, Surf. Sci., 600 (2006) 1771-1779.
[66] M.C. Biesinger, B.P. Payne, L.W.M. Lau, A. Gerson, R. St.C. Gerson, Surf. Interface Anal., 41 (2009) 324-332.
[67] M. Wakisaka, S. Morishima, Y. Hyuga, H. Uchida, M. Watanabe, Electrochem. Commun., 18 (2012) 55-57.
[68] H.W. Nesbitt, D. Legrand, G.M. Bancroft, Phys. Chem. Miner., 27 (2000) 357-366.
[69] C.R. Brundle, T.J. Chuang, D.W. Rice, Surf. Sci., 60 (1976) 286-300.
[70] M. Descostes, F. Mercier, N. Thromat, C. Beaucaire, M. Gautier-Soyer, Appl. Surf. Sci., 165 (2000) 288-302.

[71] J.K. Norskov, J. Rossmeisl, A. Logadottir, L. Lindqvist, J.R. Kitchin, T. Bligaard, H. Jonsson, J. Phys. Chem. B, 108 (2004) 17886-17892.
[72] Y. Gorlin, T.F. Jaramillo, J. Am. Chem. Soc., 132 (2010) 13612-13614.
[73] L. Xiao, L. Zhuang, Y. Liu, J. Lu, H.D. Abruna, J. Am. Chem. Soc., 131 (2009) 602-608.
[74] S. Guerin, B. Hayden, D. Pletcher, M. Rendall, J.-P. Suchsland, J. Comb. Chem., 8 (2006) 679-686.
[75] C.M. Sánchez-Sánchez, J. Solla-Gullón, F.J. Vidal-Iglesias, A. Aldaz, V. Montiel, E. Herrero, J. Am. Chem. Soc., 132 (2010) 5622-5624.
[76] A. Hitotsuyanagi, S. Kondo, M. Nakamura, N. Hoshi, J. Electroanal. Chem., 657 (2011) 123-127.
[77] Y. Takesue, M. Nakamura, N. Hoshi, Phys. Chem. Chem. Phys., 16 (2014) 13774-13779.
[78] S. Kondo, M. Nakamura, N. Maki, N. Hoshi, J. Phys. Chem. C, 113 (2009) 12625-12628.
[79] V. Stamenkovic, N.M. Markovic, P.N. Ross, J. Electroanal. Chem., 500 (2001) 44-51.
[80] R. Jinnouchi, K. Kodama, Y. Morimoto, J. Electroanal. Chem., 716 (2014) 31-44.
[81] A. Björling, E. Herrero, J.M. Feliu, J. Phys. Chem. C, 115 (2011) 15509-15515.
[82] N. Tian, Z.-Y. Zhou, S.-G. Sun, J. Phys. Chem. C, 112 (2008) 19801-19817.
[83] M.A. Van Hove, R.J. Koestner, P.C. Stair, J.P. Bibérian, L.L. Kesmodel, I. BartoŠ, G.A. Somorjai, Surf. Sci., 103 (1981) 189-217.
[84] M.A. Van Hove, R.J. Koestner, P.C. Stair, J.P. Bibérian, L.L. Kesmodel, I. Bartoš, G.A. Somorjai, Surf. Sci., 103 (1981) 218-238.
[85] A.R. Sandy, S.G.J. Mochrie, D.M. Zehner, G. Grübel, K.G. Huang, D. Gibbs, Phys. Rev. Lett., 68 (1992) 2192-2195.
[86] G. Grübel, K.G. Huang, D. Gibbs, D.M. Zehner, A.R. Sandy, S.G.J. Mochrie, Phys. Rev. B, 48 (1993) 18119-18139.
[87] M. Bott, M. Hohage, T. Michely, G. Comsa, Phys. Rev. Lett., 70 (1993) 1489-1492.
[88] M. Hohage, T. Michely, G. Comsa, Surf. Sci., 337 (1995) 249-267.
[89] A. Al-Akl, G.A. Attard, R. Price, B. Timothy, J. Electroanal. Chem., 467 (1999) 60-66.
[90] M.S. Zei, N. Batina, D.M. Kolb, Surf. Sci., 306 (1994) L519-L528.
[91] F.G. Will, J. Electrochem. Soc., 112 (1965) 451-455.
[92] J. Clavilier, J. Electroanal. Chem., 107 (1980) 211-216.
[93] L.A. Kibler, A. Cuesta, M. Kleinert, D.M. Kolb, J. Electroanal. Chem., 484 (2000) 73-82.
[94] A. Al-Akl, G. Attard, R. Price, B. Timothy, J. Chem. Soc., Faraday Trans., 91 (1995) 3585-3591.
[95] N.M. Marković, B.N. Grgur, C.A. Lucas, P.N. Ross, Surf. Sci., 384 (1997) L805-L814.
[96] R. Michaelis, D.M. Kolb, J. Electroanal. Chem., 328 (1992) 341-348.
[97] P. Hofmann, S.R. Bare, D.A. King, Surf. Sci., 117 (1982) 245-256.
[98] J. Souza-Garcia, V. Climent, J.M. Feliu, Electrochem. Commun., 11 (2009) 1515-1518.
[99] J. Souza-Garcia, C.A. Angelucci, V. Climent, J.M. Feliu, Electrochem. Commun., 34 (2013) 291-294.
[100] A.M. Bittner, J. Wintterlin, G. Ertl, J. Electroanal. Chem., 388 (1995) 225-231.
[101] P. Rodríguez, G. García, E. Herrero, J.M. Feliu, M.T.M. Koper, Electrocatalysis, 2 (2011) 242-253.
[102] H. Tanaka, Y. Nagahara, S. Sugawara, K. Shinohara, M. Nakamura, N. Hoshi, Electrocatalysis, 5 (2014) 354-360.
[103] V. Climent, G.A. Attard, J.M. Feliu, J. Electroanal. Chem., 532 (2002) 67-74.
[104] R. Rizo, E. Sitta, E. Herrero, V. Climent, J.M. Feliu, Electrochim. Acta, 162 (2015) 138-145.
[105] N. Furuya, M. Shibata, J. Electroanal. Chem., 467 (1999) 85-91.
[106] N.M. Markovic, B.N. Grgur, P.N. Ross, J. Phys. Chem. B, 101 (1997) 5405-5413.

4 Chapter Four - Conclusions

4.1 Introduction

The objective of this investigation was to understand the effect that oxygen containing species such as OH, O and H_2O, which are adsorbed on platinum and platinum alloy surfaces, have on the oxygen reduction reaction in perchloric acid media. Platinum based catalysts used in the ORR undergo changes in the amounts and identity of these species as a function of applied potential, especially at potentials relevant to loss of ORR activity. There is a fundamental need for such studies as there is a lack of adequate methods that may elucidate the structure of the electrode-electrolyte interface in-situ. An understanding of these effects will in turn inform the design of better fuel cell electrocatalysts.

The information gained in this thesis has enabled a more detailed understanding of the Pt{hkl} and PtM-electrolyte interface, the role of H_2O_2 in the ORR, the effect of alloying on the reaction and the true voltammetric response and activity of the (1x1)-Pt{110} surface. Therefore, the result of this work will be of benefit to the field of platinum electrochemistry in general, as well as our understanding of the ORR.

4.2 Conclusions

The voltammetric and ORR trends of the [Pt n{111}x{100}] and [Pt n{100}x{111}] series of surfaces in perchloric acid discussed in chapter 3.1 matched those reported previously by Feliu *et. al.* [1] In the present study, a wider potential range was used for the analysis of ORR activity, which enabled the effect of step and terrace oxidation on the reaction to be observed. The increase in activity observed at low step density was assigned to the disruption by steps of a long range ordered OH_{ads} terrace over-layer. This conclusion was reached for both series of surfaces, even though the structure of the over-layer differs over {100} [2] and {111} [3, 4] terraces. Very recently, Feliu *et. al.* have shown that even very large terraces ($20 < n < 50$) have increased activity relative to a perfect Pt{111} where $n = \infty$ [5]. The results of Feliu *et. al.* and those in this thesis are reminiscent of oxygen reduction in sulphuric acid [1], where the presence of even low step density disrupts the $\sqrt{3}$ x $\sqrt{7}$ (bi)sulphate terrace over-layer and enables the reaction to occur at much more positive potentials. Therefore, this effect is concluded to also

be present in perchloric acid, although it is much more prominent in sulphuric acid due to the stronger specific adsorption of (bi)sulphate relative to OH.

The identity of the surface species responsible for the oxidation peak that occurs between 0.8 and 0.9 V over both series of surfaces was discussed and remains still uncertain. From the voltammetry shown in chapter 3.1, it can be said that formation of species at the step sites ({111}x{100} or {100}x{111}) is responsible for this feature, as this peak grows with step density. Another peak, at approximately 0.2 V, also grows with increasing step density. Koper's theory for the identity of this low potential step peak was used to understand these results, as his interpretation is considered to account for a number of experimental observations.

It states that that the low potential "step" peak in the H_{upd} region is due to the replacement of H_{ads} at the step with an unknown ratio of O_{ads}/OH_{ads} [6, 7]. Following this interpretation, the high potential oxidation peak would be due to an increase in this ratio, as OH_{ads} is oxidised to O_{ads} or further O_{ads} is formed. Regardless of the identity of the surface species responsible for this peak, its formation is clearly detrimental to the ORR. The most stepped surfaces examined showed the largest step oxidation peak and this correlated exactly with low ORR activity in the potential ranges of its occurrence.

The reactivity of [Pt n{111}x{100}] and [Pt n{100}x{111}] surfaces towards hydrogen peroxide was then examined in the hope to understand the role that this intermediate has in the ORR. The idea for examining single-crystal surfaces came after reading reference [8], which discussed the reaction of this molecule over polycrystalline platinum. The results in this thesis give a possible reason as to why hydrogen peroxide is not detected at high potentials in clean single-crystal RRDE studies. If this molecule were to be formed in the ORR potential range, its subsequent reaction (either oxidation or reduction) would be very fast. Therefore, hydrogen peroxide is likely to be consumed at another platinum site before reaching the ring electrode in RRDE studies. The hydrogen peroxide reduction reaction over [Pt n{111}x{100}] surfaces follows a similar trend to the ORR. At low step density, an increase in the reduction wave potential is observed compared to Pt{111}, whereas at high step density the reduction wave is observed at more negative potentials. The best surface in the [Pt n{111}x{100}] series for hydrogen peroxide and oxygen reduction is the same, namely Pt{755}. These similarities imply that the same factors are instrumental in both reduction reactions; i.e. disruption of ordered OH_{ad}/H_2O terrace layer by steps enables higher potential hydrogen peroxide/oxygen reduction, whereas formation of O_{ads} at steps diminishes reduction activity. These results also imply that

if oxygen reduction proceeds via the series pathway the rate determining step lies in the later stages of the reaction, i.e. after H_2O_2 formation.

Hydrogen peroxide oxidation to oxygen occurs at high potentials (> 0.9 V) over all surfaces in this investigation. The activity towards this reaction increases with step density and it is asserted that O_{ads} at step sites is responsible for this trend. Thus, if hydrogen peroxide were produced in the ORR (through the series pathway), at these potentials it would be oxidised back to oxygen and therefore, zero net overall electrons would be transferred (zero current). This is a possible reason for the loss in ORR activity at high potentials rather than the more "classical" model of Markovic et al that metal sites are increasingly blocked by oxide (metallic sites being required for oxygen reduction) [9].

In results section 3.2, single crystal Pt{111}-M (where M=Ni, Co or Fe) surfaces were investigated as a function of two annealing and cooling environments. A combination of cyclic voltammetry (CV), scanning tunnelling microscopy (STM) and X-ray photoelectron spectroscopy (XPS) confirmed the presence of two distinct PtM phases depending on surface preparation conditions. It is found that when these electrodes are resistively heated and cooled in the nitrogen/water atmosphere of the electrochemical cell the surface is covered with PtM (M=Ni, Co, Fe) islands which are terminated with surface oxides/hydroxides. The islands increase in size in the order Ni, Co, Fe. The second series of catalysts were created by flame annealing the resistively heated surfaces in a Bunsen flame and subsequently cooling them in a stream of hydrogen. This procedure reduced the oxides/hydroxides to metallic Ni, Co or Fe and formed surface alloys. CV for these surfaces show that the onset of electrochemical oxide formation shifts positive in the order Ni, Co, Fe. This shift correlated with increased activity towards the ORR which we ascribe to the greater availability of highly active metallic sites for oxygen reduction at ORR potentials.

Chapter 3.3 was concerned with the investigation of a series of kinked surfaces based upon Pt{332}, with the goal of identifying the role of low-coordinate kink sites in the ORR. Pt{10,9,6}, Pt{764} and Pt{864} surfaces were chosen based upon their increasing density of isolated {100} kink sites, enabling a study which singled out the effect of {100} kinks on the ORR in this series. The voltammetric trend observed upon increasing kink density was that expected from the ball models of the surfaces, i.e. growth of a {100} electrosorption peak at ~ 0.2 V with increasing number of kinks. ORR activity was found to decrease with increasing {100} kink density, with the most kinked surface Pt{864} approaching the activity of Pt{755},

a surface which exhibits linear {100} steps. These results indicate that low-coordinate {100} kink sites do not have unique ORR activity, i.e. their activity is identical to {100} linear step sites.

The (1x1) and disordered (1x2) surface atomic arrangements of Pt{110} was compared in chapter 3.4. The voltammetry of these surface configurations in sulphuric acid, perchloric acid and sodium hydroxide was investigated. For the first time, the voltammetry of the Pt{110}-(1x1) surface has been reported in aqueous perchloric acid and sodium hydroxide. Perchloric acid voltammetry of the (1x1) surface exhibited 6 peaks in the potential range 0 - 0.3 V, in stark contrast to the two broad peaks observed in the voltammetry of the disordered (1x2) surface. The (1x1) surface also exhibited a singular, large oxide electrosorption peak at 0.95 V and almost zero current associated with electrosorption at defects. This implies an atomically perfect Pt{110}-(1x1) surface. In contrast, the emergence of OH electrosorption peaks close to 0.75 V was ascribed to the generation of Pt{110}-(1x2) phases in which highly uncoordinated surface Pt atoms act as nucleation centres for oxide formation. It is concluded that the Pt{110} surface exhibits a mixed H_{ads}/OH_{ads} adlayer in the 0.09 - 0.2 V potential range and that the large number of peaks occurring are due to new adlayer structures, with differing hydrogen/OH ratios becoming stable at different potentials. The activity of the Pt{110}-(1x1) surface for oxygen reduction was also tested and was found to be approximately 30 - 40 mV less active than any of the disordered (1x2) surfaces studied when $E_{1/2}$ values for ORR are compared.

4.3 Future Work

The voltammetric studies performed in this thesis and those performed by many other groups have led to a greater understanding of the ORR, but have not completely resolved the reaction mechanism. Therefore there is still great controversy as to the identity of many ORR intermediates and the rate determining step in the reaction.

The dissociative, associative and peroxo ORR mechanisms have been previously derived to account for various experimental observations, e.g. the detection of hydrogen peroxide intermediate. These were discussed in the introduction to chapter 3.1 and are thought to be simplifications of the real reaction mechanism. In these mechanisms only inner sphere electron transfer is considered via adsorbed species (i.e. outer sphere electron transfer between platinum and non-adsorbed solution species, is not usually considered in aqueous solutions [10]). In

aprotic solvents this is not the case and oxygen reduction has been shown to proceed via an outer sphere one electron reduction to produce the superoxide radical, $O_2^{\bullet-}$. The addition of acid to the solvent supplies protons, and the reaction then proceeds via a two electron reduction to produce H_2O_2, with $HO_2^{\bullet}$ as an intermediate [11].

The formation of solution species other than peroxide is not usually considered in aqueous media, even though there have been reports that aqueous radical species may be produced. There is spectroscopic evidence (Raman spectroscopy) for $O_2^{\bullet-}$ production in alkaline electrolyte [11, 12] and indirect evidence (scanning electrochemical microscopy, SECM) for OH• production [14] and for $O_2^{\bullet-}$ production in acid [15]. Recent electrochemical studies have shown unequivocally that a solution species is formed during the ORR, which is thought to be OOH• and may be involved in the r.d.s. [10]. The development of sensitive techniques which may directly identify intermediate ORR species is paramount to further understanding of this complex reaction. Due to its sensitivity to paramagnetic species, electron paramagnetic resonance (EPR) spectroscopy is one such technique which may be useful in detecting solution radical species produced during the reaction and elucidating these mechanistic problems. EPR has previously been used to detect paramagnetic solution ORR products in aprotic media [16]. A simple EPR compatible electrochemical cell is described in reference [17] and could be used as a starting point for designing experiments to address these issues.

In order to confirm, refute or expand upon the conclusions reached in chapter 3.1, further characterisation of the Pt{hkl}-electrolyte interface needs to be performed. A more detailed understanding of Pt{hkl}-OH_{ads}/O_{ads}/H_2O surface structures, their potential dependency, how the surface structures interface with bulk water and especially how they are affected by the presence of disturbances in surface order (i.e. steps which contain different amounts of OH_{ads} and O_{ads} to terrace sites), would help immensely in the understanding of ORR trends reported in this chapter.

As a continuation of the work in chapter 3.2, further work should be carried out on the role of the annealing and cooling environments on the formed surface. Resistive heating in a reductive atmosphere, H_2 or CO, may inhibit surface oxide formation and enable a single crystalline surface to be maintained upon alloying. Greater control of preformed alloys is a prerequisite to the understanding of the role of alloying metal on the ORR. Once this control is gained a range of alloy compositions may be investigated.

There is much further work that may be done in light of the results gained in chapter 3.4. The true voltammetry of the Pt{110}-(1x1) surface was shown to be quite unique to that reported previously. Therefore, there are many further investigations that may be performed on this surface which may also yield new results. For example, (1x1)-Pt{110} may have unique activity for important reactions such as methanol, ethanol and CO oxidation. In an effort to understand the (1x1)-Pt{110} electrode-electrolyte interface in more detail, surface sensitive techniques such as shell isolated nanoparticle surface enhanced Raman spectroscopy (SHINERS) may prove useful. The voltammetry of this surface may also prove key in elucidating the entropy and enthalpy of adsorption of surface species. This was attempted for Pt{110} previously by Feliu *et al*, but the overlapping of H_{ads} and OH_{ads} made the separation of the physical properties of these adsorbates impossible to achieve (unlike for Pt{111}) [18]. The sharp voltammetry observed in the present study may help in this regard. The final possible further investigation that will be mentioned is the voltammetry of stepped Pt{110} surfaces. By utilising the cooling method described in this thesis, accurate voltammetry of the stepped-Pt{110}-(1x1) terrace surfaces may be obtained. This is currently in progress in our group.

4.4 References

[1] M.D. Macia, J.M. Campina, E. Herrero, J.M. Feliu, J. Electroanal. Chem., 564 (2004) 141-150.
[2] B. Han, V. Viswanathan, H. Pitsch, J. Phys. Chem. C, 116 (2012) 6174-6183.
[3] M.T.M. Koper, J.J. Lukkien, J. Electroanal. Chem., 485 (2000) 161-165.
[4] T. Schiros, L.Å. Näslund, K. Andersson, J. Gyllenpalm, G.S. Karlberg, M. Odelius, H. Ogasawara, L.G.M. Pettersson, A. Nilsson, J. Phys. Chem. C, 111 (2007) 15003-15012.
[5] A.M. Gómez-Marín, J.M. Feliu, Catal. Today, 244 (2015) 172-176.
[6] M.J.T.C. van der Niet, N. Garcia-Araez, J. Hernández, J.M. Feliu, M.T.M. Koper, Catal. Today, 202 (2013) 105-113.
[7] M.J.T.C. van der Niet, A. den Dunnen, L.B.F. Juurlink, M.T.M. Koper, Angew. Chem., Int. Ed., 49 (2010) 6572-6575.
[8] I. Katsounaros, W. Schneider, J. Meier, U. Benedikt, P. Biedermann, A. Auer, K.J. Mayrhofer, Phys. Chem. Chem. Phys., 14 (2012) 7384-7391.
[9] V.R. Stamenkovic, B. Fowler, B.S. Mun, G. Wang, P.N. Ross, C.A. Lucas, N.M. Markovic, Sci. 315 (2007) 493-497.
[10] A.M. Gomez-Marin, R. Rizo, J.M. Feliu, Catal. Sci. Technol., 4 (2014) 1685-1698.
[11] C.P. Andrieux, P. Hapiot, J.M. Saveant, J. Am. Chem. Soc., 109 (1987) 3768-3775.
[12] M.-h. Shao, P. Liu, R.R. Adzic, J. Am. Chem. Soc., 128 (2006) 7408-7409.
[13] X. Li, A.A. Gewirth, J. Am. Chem. Soc., 127 (2005) 5252-5260.
[14] J.-M. Noël, A. Latus, C. Lagrost, E. Volanschi, P. Hapiot, J. Am. Chem. Soc., 134 (2012) 2835-2841.
[15] H.J. Forman, I. Fridovich, Science, 175 (1972) 339-339.
[16] D.L. Maricle, W.G. Hodgson, Anal. Chem., 37 (1965) 1562-1565.

[17] P.R. Murray, D. Collison, S. Daff, N. Austin, R. Edge, B.W. Flynn, L. Jack, F. Leroux, E.J.L. McInnes, A.F. Murray, D. Sells, T. Stevenson, J. Wolowska, L.J. Yellowlees, J. Magn. Reson., 213 (2011) 206-209.
[18] N. Garcia-Araez, V. Climent, J.M. Feliu, J. Electroanal. Chem., 649 (2010) 69-82.